Transverse Momentum Distributions and Nuclear Modification Factors in Heavy-Ion Collisions with ALICE at the Large Hadron Collider

Transversalimpulsverteilungen und Kernmodifizierungsfaktoren in Schwerionenkollisionen mit ALICE am Large Hadron Collider
Zur Erlangung des Grades eines Doktors der Naturwissenschaften (Dr. rer. nat.)
genehmigte Dissertation von Julius Gronefeld aus Bonn
Tag der Einreichung: 9.4.2018, Tag der Prüfung: 31.5.2018
Darmstadt — D 17

1. Gutachten: Prof. Dr. rer. nat. Anton Andronic
2. Gutachten: Prof. Guy Moore, Ph.D.

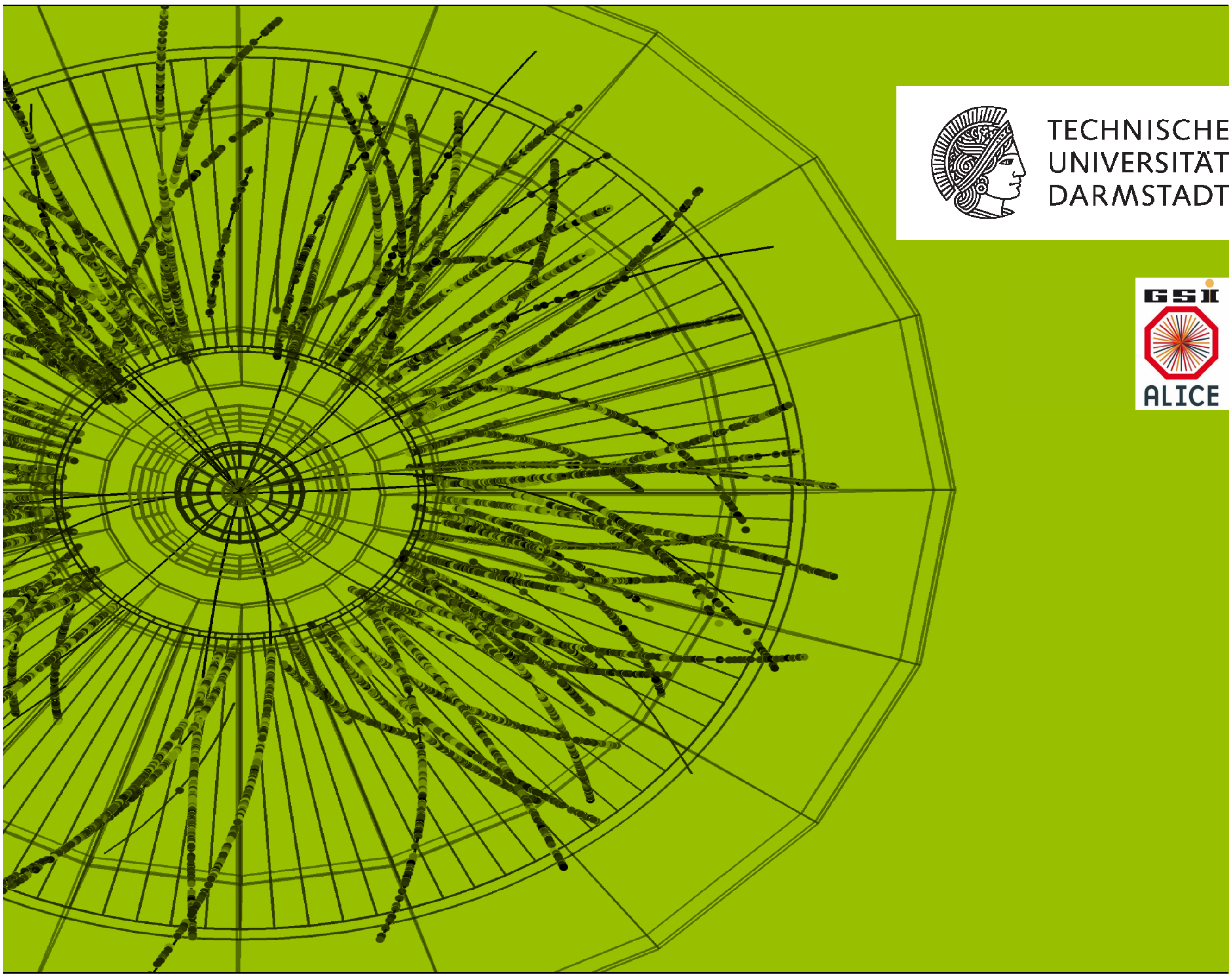

TECHNISCHE
UNIVERSITÄT
DARMSTADT

GSI
ALICE

Transverse Momentum Distributions and Nuclear Modification Factors in Heavy-Ion Collisions with ALICE at the Large Hadron Collider
Transversalimpulsverteilungen und Kernmodifizierungsfaktoren in Schwerionenkollisionen mit ALICE am Large Hadron Collider

Genehmigte Dissertation von Julius Gronefeld aus Bonn

1. Gutachten: Prof. Dr. rer. nat. Anton Andronic
2. Gutachten: Prof. Guy Moore, Ph.D.

Tag der Einreichung: 9.4.2018
Tag der Prüfung: 31.5.2018

Darmstadt — D 17

Abstract

In this work, Pb–Pb collisions measured in 2010 during the first data taking period (Run 1) at a centre-of-mass energy of $\sqrt{s_{\mathrm{NN}}} = 2.76\,\mathrm{TeV}$ and data taken in 2015 during Run 2 at $\sqrt{s_{\mathrm{NN}}} = 5.02\,\mathrm{TeV}$ are analysed. In November 2017, the LHC brought xenon ions to collision for the first time; this data set that was taken at $\sqrt{s_{\mathrm{NN}}} = 5.44\,\mathrm{TeV}$ is also analysed.

Transverse momentum (p_{T}) distributions at high p_{T} of charged particles have shown that particle yields in heavy-ion (AA) collisions are suppressed compared to a superposition of independent nucleon-nucleon collisions (binary collision scaling). This observation is related to parton energy loss in the Quark Gluon Plasma (QGP).

To obtain the charged-particle yield as a function of p_{T}, corrections are made for tracking efficiency and acceptance, for contamination by secondary particles from weak decays or secondary interactions and for the p_{T} resolution. To circumvent differences in the particle composition of event generators and data, the charged-particle reconstruction efficiency is calculated from the particle-dependent efficiencies weighted by the relative abundances of each particle measured during Run 1. The correction for contamination with secondary particles is usually obtained from Monte-Carlo (MC) simulations. The abundances of secondary particles in data and MC is estimated by analysing the distance of closest approach of tracks to the event vertex. It is found that the contamination correction from MC has to be scaled up by $\sim 50\%$ to match the data.

The improvement of the analysis methods resulted in a reduction of the total relative systematic uncertainties by about 50% compared to previous analyses due to an improved reconstruction and calibration procedure in Run 2, as well as to improved track selection methods.

The transverse momentum distribution of charged particles from Pb–Pb and Xe–Xe collisions were measured for nine classes of centrality. The measurement was performed for particles within $|\eta| < 0.8$ in pseudo-rapidity and for a transverse-momentum range of $0.15 < p_{\mathrm{T}} < 50\,\mathrm{GeV}/c$.

The nuclear modification factor (R_{AA}) is defined as the p_{T}-differential yield in a AA collision divided by the cross section in pp collisions, scaled by the nuclear overlap function calculated in a Monte-Carlo Glauber approach. Any suppression of particle yields in AA compared to a superposition of individual pp collisions results in a nuclear modification factor below unity.

All measurements exhibit a moderate suppression for peripheral collisions. With increasing collision centrality, a pronounced suppression with $R_{\mathrm{AA}} \approx 0.13$ at intermediate p_{T} develops. At higher p_{T}, a significant rise of the nuclear modification factor is observed.

The comparison of R_{AA} as a function of the charged particle density per unit of rapidity ($d\mathrm{N}_{\mathrm{ch}}/d\eta$) shows a remarkable agreement of the observed suppression at high p_{T} in Xe–Xe and Pb–Pb collisions at both energies scales for $d\mathrm{N}_{\mathrm{ch}}/d\eta > 400$. This scaling does not hold for collisions with lower particle multiplicities.

This observation is consistent with a dependence of the partonic energy loss on the square of the path length in the medium. At lower transverse momenta a dependence of R_{AA} on the collision energy is observed, which might be due to the collision energy dependence of the bulk particle production.

Zusammenfassung

Im Rahmen dieser Arbeit wurden Kollisionen von Bleikernen ausgewertet, die während der ersten Messperiode (Run 1) bei einer Schwerpunktsenergie von $\sqrt{s_{\mathrm{NN}}} = 2.76\,\mathrm{TeV}$ und während Run 2 bei $\sqrt{s_{\mathrm{NN}}} = 5.02\,\mathrm{TeV}$ aufgezeichnet wurden. Im November 2017 brachte der LHC zum ersten Mal Xenonkerne mit einer Schwerpunktsenergie von $\sqrt{s_{\mathrm{NN}}} = 5.44\,\mathrm{TeV}$ zur Kollision. Diese Daten werden hier ebenfalls analysiert.

In der Vergangenheit wurde in Transversalimpulsverteilungen von geladenen Teilchen eine verringerte Teilchenausbeute im Vergleich zur Superposition unabhängiger Nucleon-Nucleon Kollisionen festgestellt. Diese Beobachtung steht im Zusammenhang mit dem Energieverlust hochenergetischer Partonen im Quark Gluon Plasma (QGP).

Um die Verteilung von geladenen Teilchen als Funktion des Transversalimpulses (p_{T}) zu erhalten, werden Korrekturen für Spurrekonstruktionseffizienz und Detektorakzeptanz, für Verunreinigung mit Sekundärteilchen, so wie für die p_{T}-Unschärfe angewendet. Um Unterschiede in der Zusammensetzung der Teilchensorten zwischen Daten und Kollisionssimulationen auszugleichen, wird die Rekonstruktionseffizienz aus den teilchensortenabhängigen Effizienzen entsprechend der relativen Gewichtung der jeweiligen Sorte in Run 1 Messungen bestimmt. Die Korrektur für die Verunreinigung mit Sekundärteilchen – aus Zerfällen und Detektorwechselwirkung – wird mit Hilfe einer Monte-Carlo (MC) Simulation bestimmt. Die Menge von Sekundärteilchen in Daten und MC wird abgeschätzt, in dem die maximale Annäherung der Spuren an den Ereignisursprung (Vertex) analysiert wird. Es stellt sich heraus, dass die Verunreinigung in MC erhöht werden muss um den Daten zu entsprechen.
Die Verbesserung der Analysemethoden führen gemeinsam mit einer verbesserten Kollisionsrekonstruktion und Kalibrierung des Detektors zu einer Verringerung der systematischen Unsicherheiten von 50% im Vergleich zu vorherigen Untersuchungen.

Die Transversalimpulsverteilungen von geladenen Teilchen in Pb–Pb und Xe–Xe Kollisionen wurde für neun Klassen von Kollisionszentralität gemessen. Die Messung wurde für Teilchen mit einer Pseudorapidität von $|\eta| < 0.8$ im Impulsbereich von $0.15 < p_{\mathrm{T}} < 50\,\mathrm{GeV}/c$ durchgeführt. Der Kernmodifizierungsfaktor (R_{AA}) ist das Verhältnis der p_{T} abhängigen Teilchenausbeute in Schwerionenkollisionen zu dem p_{T} abhängigen Wechselwirkungsquerschnitt in Proton-Proton Kollisionen, skaliert mit der Nuklearendichtefunktion, die durch eine Glauber Monte-Carlo Rechnung bestimmt wird. Jegliche Verringerung in der Teilchenausbeute in Schwerionenkollisionen drückt sich in einem R_{AA} kleiner als eins aus. Der R_{AA} wurde für alle Kollisionssysteme in neun Zentralitäten bestimmt. Alle Messungen zeigen dieselben Merkmale mit einer gering unterdrückten Teilchenausbeute in peripheren Kollisionen. Bei zunehmender Zentralität der Kollision entwickelt sich ein markantes Minimum mit $R_{\mathrm{AA}} \approx 0.13$ bei mittleren Transversalimpulsen. Bei höheren p_{T} wird ein signifikanter, linearer Anstieg des R_{AA} beobachtet.
Der Vergleich des R_{AA} der verschiedenen Systeme als Funktion der rapiditätsnormierten Teilchendichte ($d\mathrm{N}_{\mathrm{ch}}/d\eta$) zeigt, dass R_{AA} bei hohen p_{T} mit $d\mathrm{N}_{\mathrm{ch}}/d\eta$ skaliert sobald die mehr als 400 Teilchen pro Rapiditätseinheit erzeugt werden. Für geringere Teilchendichten gilt diese Skalierung nicht mehr. Dieses Verhalten deutet auf eine Abhängigkeit des Energieverlustes der Partonen im Medium mit dem Quadrat der Pfadlänge hin. Bei niedrigen p_{T} gilt dieser Zusammenhang ebenfalls nicht, jedoch wird eine Abhängigkeit von der Kollisionsenergie festgestellt.

Preface

In collisions of heavy ions at ultra-relativistic energies the properties of hot and dense matter are studied in which fundamental particles - the quarks and gluons - behave like quasi-free particles. In the early history of the universe, this state of matter, known as the Quark-Gluon Plasma (QGP), is believed to have filled the entire space. Due to its expansion, the energy density in the universe dropped and quarks and gluons were confined in hadrons for the first time a few microseconds after the Big Bang. The existence of such a phase is predicted by and can be understood through the theoretical framework of Quantum Chromodynamics (QCD), the fundamental quantum field theory describing the strong force.

To achieve the energies needed to create a drop of QGP in the laboratory, large accelerator facilities such as the Large Hadron Collider (LHC) at the European Organisation for Nuclear Research (CERN) are required. The LHC provides beams of heavy-ions such as lead (Pb) or xenon (Xe), as well as protons with the highest energies ever reached in an accelerator. While all four major experiments at the LHC are measuring collisions of heavy ions, ALICE is the experiment specifically built for the study of the QGP.

In this work the charged particle production in heavy-ion collisions is studied, as it provides a probe for the properties of the medium. Especially the suppression of the charged-particle yield at high transverse momenta is of interest, as it probes the energy loss of high energy partons in the QGP.
This *jet quenching* was proposed as a sign of QGP by Bjorken in 1982 [1].

This thesis is organised as follows:
In chapter 1 the theoretical background for this work is introduced. Chapter 2 gives an overview of experimental results concerning the production of charged particles. The LHC and the ALICE detector are introduced in chapter 3.
Chapter 4 introduces the analysis methods and the estimation of systematic uncertainties. Before coming to the results in chapter 6, the corresponding measurement in pp collisions is briefly summarised in chapter 5.
Finally the work is concluded in chapter 7.

Contents

1 Theoretical Background

1.1 The Standard Model

In the standard model, particles that make up matter are described by spin-half particles, the fermions. The strong, weak and electromagnetic interactions between the fermions are understood by the exchange of spin-one particles, the bosons. Fermions that do not interact with the strong interaction are called leptons l (e,μ,τ as well as ν_e, ν_μ and ν_τ). Hadrons on the other hand are particles that interact strongly and are made from the six quarks (q): up (u), down (d), strange (s),charm (c),bottom (often called beauty) (b) and top (t) (Figure 1.1). The bosons form a gauge symmetry group $SU_c(3) \times SU_L(2) \times U_Y(1)$. Here gluons which are the mediators of the strong force form the $SU_c(3)$, while $SU_L(2)$ is made up from three spin-one particles $W^{\pm}$ and Z^0 the mediators of the weak interaction. The exchange particle of the electromagnetic force is the photon which forms the $U_Y(1)$ group.

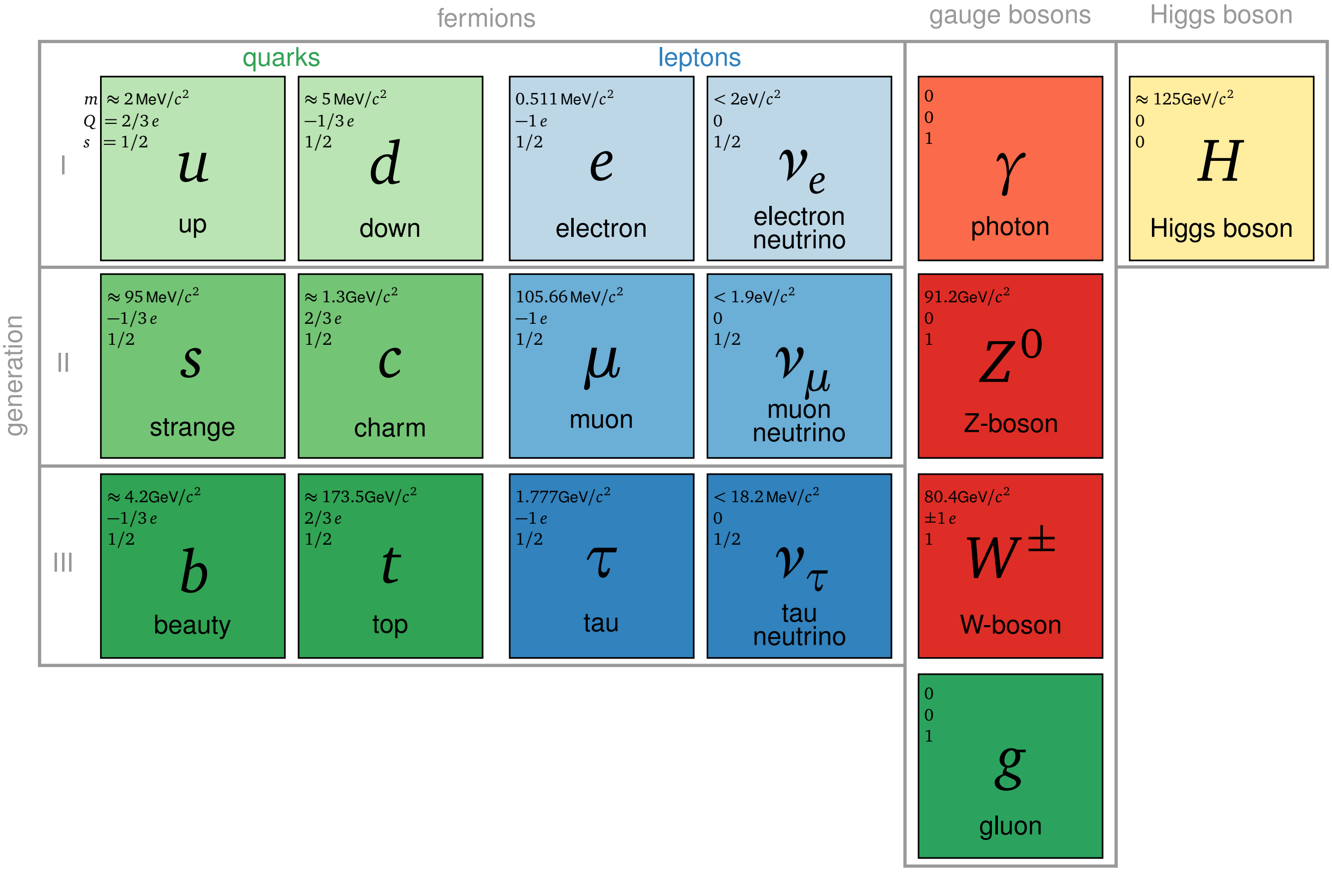

Figure 1.1.: The particles of the standard model. Two groups of fermions ($s = 1/2$) exist, quarks and leptons. The gauge bosons ($s = 1$) are the mediators of the interactions between the fermions. The Higgs boson is excitation of the Higgs field, which generates the masses of the elementary particles.

The different behaviour of the forces is understood by the differences in their mediators. While the boson corresponding to the electromagnetic force is massless and thus the electromagnetic force has a long range, the coupling of the electromagnetic force $\alpha_e \approx 1/137$ is smaller than the coupling of the weak force $\alpha_W \approx 1/30$ (eg. [2]). The short range of the weak interaction is explained by the heavy masses of its mediators, the $W^\pm$ and Z^0 boson. The range of the strong interaction however, is limited to a few fm (10^{-15} m) even though gluons are massless. The short range of the strong force is explained by gluon self interaction (see section 1.2). The coupling of the strong interaction is much larger than in the case of the other two forces $\alpha_s \approx 0.1 - 1$.

1.2 Quantum Chromodynamics

The theory which describes the strong force is called Quantum Chromodynamics (QCD). The strong force is the result of a new degree of freedom, the colour charge. Each quark can have the charge red, green or blue, as well as the corresponding anticolour for antiquarks. Colour however can not be observed directly, as composite hadrons are colour neutral and are either made up of three (anti-) quarks (qqq) that carry all three (anti-) colours, or consist of a pair of one quark and an antiquark ($q\bar{q}$). The triplets are called baryons, while the quark-antiquark pairs are referred to as mesons. The mediators of the strong force that couple to the colour charges are called gluons. Unlike photons, the gluons are not neutrally charged but also carry colour. The colour charge of the gluons consist of a colour and a different anticolour (there is no colour neutral gluon). A gluon exchange between two quarks therefore results in a colour change. As gluons are coloured particles, they too are bound to confinement, which results in the short range of the strong force. Confinement arises as the attractive force between quarks does not vanish with increasing distance, unlike QED, but stays constant. The energy in the field between the quarks rises until the threshold for quark-antiquark pair production is reached and a $q\bar{q}$-pair is created. Therefore quarks can never be observed individually - they are confined in mesons and baryons. The potential between a heavy quark-antiquark pair can phenomenological be described by the Cornell potential [3].

$$V(r) = -\frac{4}{3}\frac{\alpha_s}{r} + \kappa r \tag{1.1}$$

For short distances (r), the potential resembles a Coulomb like potential while towards higher r the linear increasing term becomes dominant. The latter is often referred to as the confinement term and the constant κ is often associated with a string tension between the two quarks in analogy with the constant force of a spring. The shape of this potential is verified by model calculations of the QCD, such as lattice QCD [4]. The string tension is found to be in the order of $\kappa = 1\,\mathrm{GeV/fm}$ [5].
In QCD the coupling constant α_s decreases with increasing energy (Figure 1.2). This can be understood in a schematic picture. From the uncertainty relation follows, that high energy partons (quark or gluon) will resolve a smaller volume around the colour charge, while low energy partons will resolve a larger volume. The colour charge however can not be assumed to be static. A quark for example is constantly emitting and absorbing gluons. Thereby the gluons spread the effective charge over a larger volume – the colour charge is diffused. A high energy parton will resolve a smaller colour charge. The decreasing coupling in QCD is known as asymptotic freedom. For its discovery David J. Gross, H. David Politzer and Frank Wilczek were awarded with the Nobel Prize in 2004. The running coupling constant implies that calculations of QCD can be performed using perturbation theory (pQCD) at high enough energies. Typically an energy larger than $\Lambda_{\mathrm{QCD}} \approx 200\,\mathrm{MeV}$ is required. The formation of particles, however, occurs at lower energy and therefore a process such as hadronisation can not be described perturbatively.

Parton distribution functions

The quantum numbers of a hadron are defined by its valence quark content, but quantum effects such as vacuum fluctuations result in additional quark and antiquark pairs as well as pairs of gluons present in the hadron. Indeed, individual partons carry a different fraction x of the nucleon's total momentum. This behaviour can be described by parton distribution functions (PDFs). The PDFs need to be determined by experiments, such as deep inelastic scattering (DIS) of electrons or positrons [7]. The PDF depend on

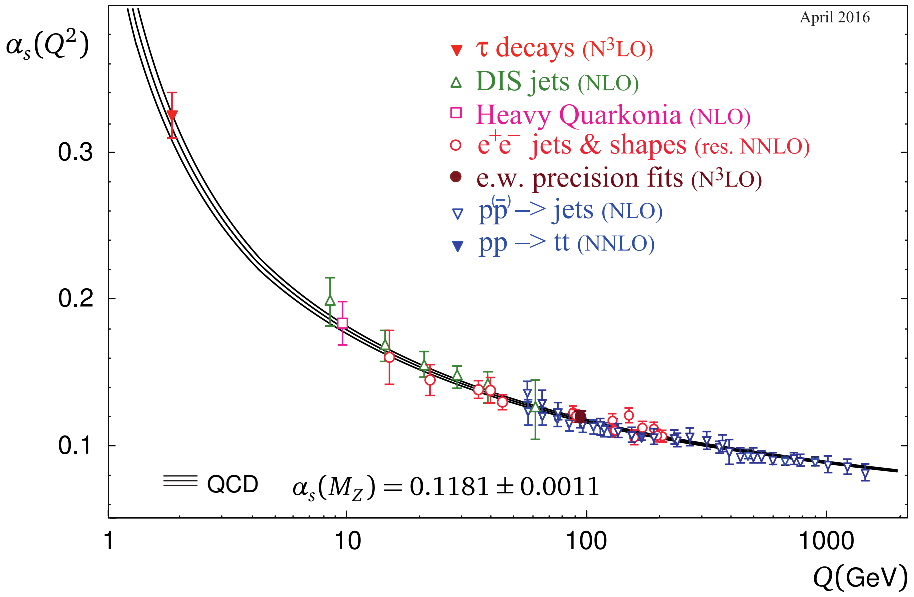

Figure 1.2.: The running coupling α_s is given at the mass scale of the Z^0 boson [6]

the energy scale Q^2 and their scale dependence is described by the DGLAP (Dokshitzer-Gribov-Lipatov-Altarelli-Parisi) equations [8–10].
A set of parton distribution functions is shown in Figure 1.3 as a function of Bjorken-x.
At large momentum fractions ($x \sim 1$) the PDF is dominated by the valance quarks up (xu_v) and down (xd_v). Towards smaller fractions (smaller x) their impact reduces and the the contribution from gluons (xg) as well as from the summed sea quarks (xS) rises. In nuclei the PDF's can be modified (see section 1.8).

1.3 The Quark-Gluon Plasma

Although quarks and gluons are not observed as free particles, one of the predictions of QCD is a hot and dense matter of quasi-free quarks and gluons, the Quark-Gluon Plasma (QGP).
This state can be reached by heating up nuclear matter above a critical temperature (T_c). Collisions of hadrons become frequent and partons of separated hadrons will interact with each other. In the high energy-density environment a large number of quark-antiquark pairs is produced, that conceals the colour charges of individual quarks. This phenomenon can be understood analogue to the *Debye screening* from classic electrostatic physics with colour charges instead of electric charges [11].
It is assumed that the early universe a few μs after the Big-Bang was filled by such a phase of deconfined quarks and gluons with a temperature well above T_c [12]. During its expansion the universe cooled down and quarks and gluons were bound into hadrons, about 10^{-5} s after the Big-Bang [13].

Today, lattice QCD is providing the most accurate predictions on T_c. As pQCD is not feasible at the energy scales targeted, the QCD equations are solved numerically using euclidean space-time on a discrete space-time lattice [14]. The critical temperature is found to be in the range of $T_c = 150-160\,\text{MeV}$ [15, 16]. This corresponds to a critical energy density of $\sim 0.5\,\text{GeV/fm}^3$ [14]. Figure 1.4 shows Lattice QCD calculations for normalised pressure $3p/T^4$, energy density ϵ/T^4 and entropy density $s/4T^3$ as a function of temperature T [16]. The calculations were performed with 2+1 quark flavours assuming two light quarks with equal mass and one heavier quark. At the value of T_c, the calculations feature a rapid increase, indicating a change in the state of matter due to a change in the degrees of freedom. At high T, the Stefan-Boltzmann limit for a non-interacting gas of quarks and gluons is shown, that is not reached by the calculations, indicating that quarks and gluons in the QGP are still interacting. At lower T, the

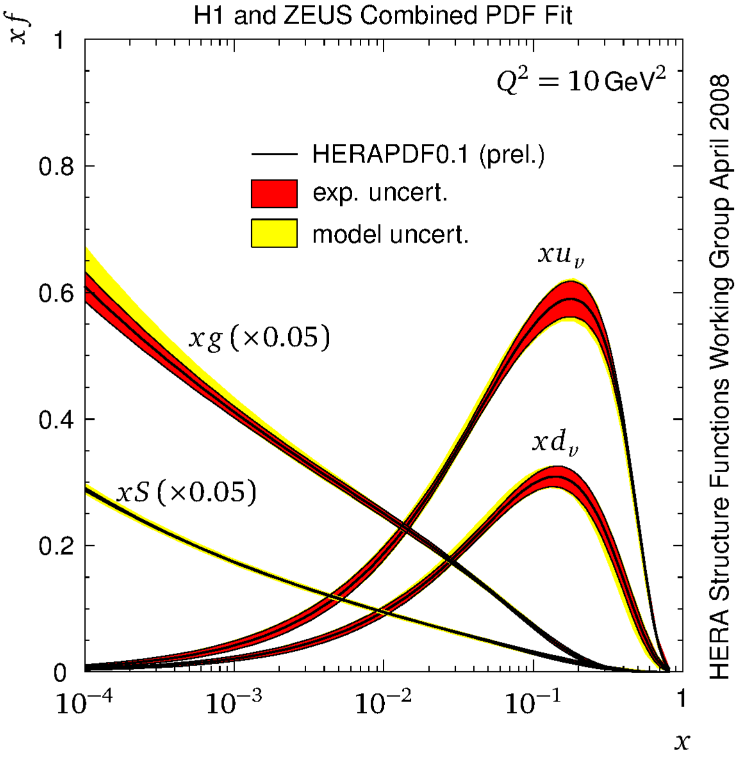

Figure 1.3.: The parton distribution functions of a proton for $Q^2 = 10\,\mathrm{GeV}^2$ [7]. Towards low x gluon densities increase rapidly.

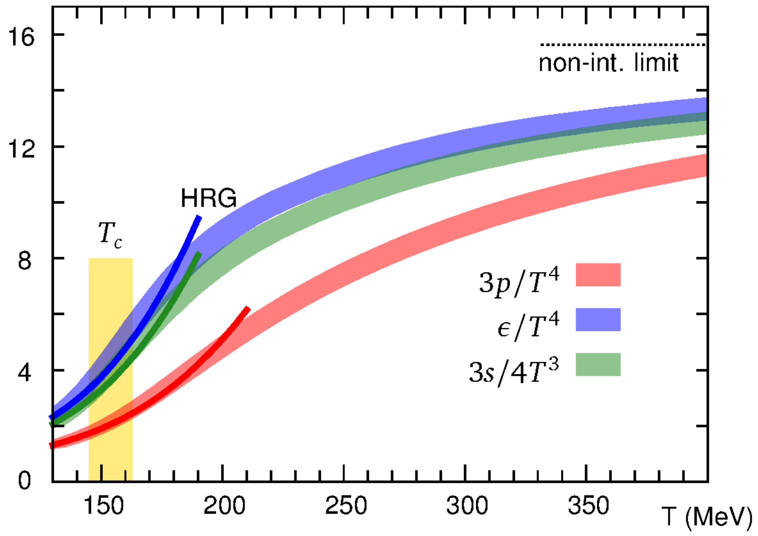

Figure 1.4.: Lattice QCD calculations of the pressure p (red), energy density ϵ (blue) and entropy density s (green) of hot QCD matter at thermal equilibrium as a function of T. At low T, calculations for a hadron resonance gas (HRG) are shown. At high T the Stefan-Boltzmann limit for non interacting particles is shown [16].

calculations of Lattice QCD are in agreement with calculations made for a Hadron Resonance Gas (HRG).

Lattice QCD calculations, however, are only feasible for vanishing baryo-chemical potential μ_B. The baryo-chemical is a measure for the excess of quarks over antiquarks, $\mu_B = 0$ implies the same number of quarks and antiquarks. A vanishing μ_B is a good approximation for both, heavy-ion collisions at the LHC and the evolution of the early universe. While the phase transition from a deconfined state of quarks and gluons to regular nuclear matter is of cross-over type for $\mu_B \approx 0$, a first order phase transition is assumed for larger μ_B. A schematic view of a possible phase diagram is shown in Figure 1.5. The investigation of QCD matter at higher μ_B, as well as the search for a possible critical point is the focus of current and future experiments at lower collision energies [17, 18].

Experimentally the phase diagram can also be constrained by measured particle yields. In the statistical hadronisation model the yields can be used to determine T and μ_B [19, 20]. The results obtained by this model are remarkably close to lattice calculations.

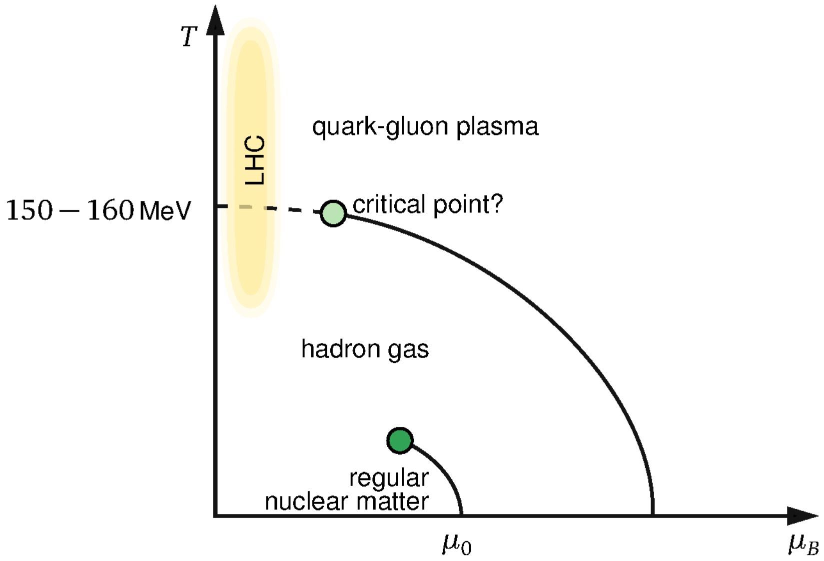

Figure 1.5.: A sketch of a possible phase diagram of strongly interacting matter. At low baryo-chemical potentials μ_B, the diagram is constrained by both lattice QCD predictions and experiment results, while its features for higher μ_B, including a possible critical point, are without experimental constraint.

1.4 Evolution of a Heavy Ion Collision

In ultra-relativistic heavy-ion collisions the Quark Gluon Plasma (QGP) can be created and observed through its remnants. The QGP however is not a stable system but disintegrates within less than $10-20\,\mathrm{fm}/c$ $(3-6\cdot10^{-23}\,\mathrm{s})$ [21]. At relativistic beam energies the nuclei form Lorentz contracted flat discs, their collision occurs at $\tau=0$. The first collisions to occur are hard collisions with a typical time scale of $\tau\sim1/p_\mathrm{T}\ll1/Q_0\sim0.1\,\mathrm{fm}/c$. Here, Q_0 is the scale of the momentum transfer resulting in particles with a high transverse momentum (p_T) or mass $p_\mathrm{T},m\gtrsim Q_0\gg\Lambda_\mathrm{QCD}$ ($Q_0=\mathcal{O}(1\,\mathrm{GeV})$) [22]. A typical space-time evolution of heavy-ion collisions is shown in Figure 1.6. The colliding nuclei are not stopped in the collision but rather penetrate each other leaving highly excited matter at very high densities in the overlap region. This medium is produced by soft collisions at larger time scales than the hard collisions. The medium is expected to reach a state of (local) thermal equilibrium within a very short time scale of $\tau\approx1\,\mathrm{fm}/c$ [24]. After the system has reached thermal equilibrium, the evolution of the system can be described by thermodynamic calculations.

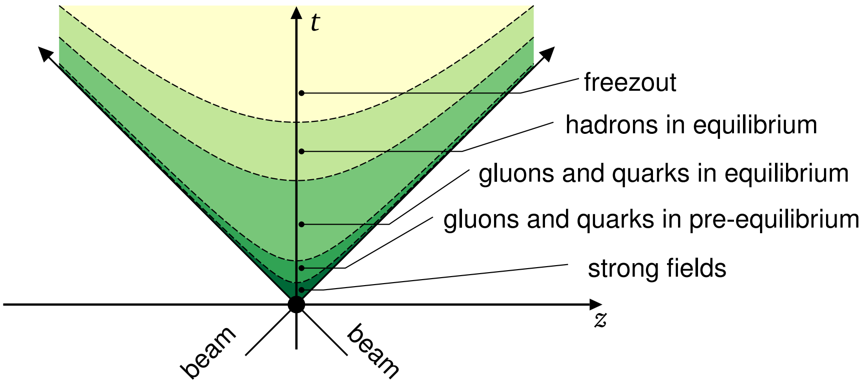

Figure 1.6.: Space-time diagram of the evolution of the heavy-ion collision. Adopted from [23].

The system will expand rapidly with a velocity close to the speed of light until energy densities reduce to $\epsilon_c\sim0.5\,\mathrm{GeV/fm}^3$. At that moment, temperatures have fallen below the critical temperature of the QGP - the quarks and gluons will combine to form hadrons. The evolution of the collision however does not stop at the hadronisation as the a mean free path in the hadron gas formed is still smaller than the system size. As the hadron gas continues to expand, the rate of inelastic collisions decreases until the chemical freezout is reached and the hadron composition no longer changes.

Along the transverse momentum, the pseudo rapidity η is an important variable, it is defined by the direction of the outgoing particle.

$$\eta=-\ln(\tan(\theta/2)) \tag{1.2}$$

Here, θ represents the polar angle. For relativistic particles $E\sim p$, the pseudo rapidiy η is a good approximation for the rapidiy.

$$y=\frac{1}{2}\ln\left(\frac{E+p_\mathrm{L}}{E-p_\mathrm{L}}\right) \tag{1.3}$$

Here, E is the particle's total energy, while p_L stands for the longitudinal momentum along the beam axis.

1.5 Particle Production in Hard Processes

In hadron collisions, hard processes with a large momentum transfer $Q \gg \Lambda_{\mathrm{QCD}}$ result in particles in the final state that posses a high transverse momentum (p_{T}), or have high masses m ($p_{\mathrm{T}}, m \gg \Lambda_{\mathrm{QCD}}$). In pp collisions, the underlying process can be regarded as a collision of partons in vacuum and the hard-scattering cross section ($d\sigma_{ab\to jd}$) is computable via pertubative QCD.
Together with the initial momentum fraction of the parton, given by the parton distribution functions (PDF, compare section 1.2), the overall particle-production cross section can be formulated (eg. [25]):

$$d\sigma_{\mathrm{pp}} \approx \sum_{abjd} \int dx_a \int dx_b \int dz_j f_{a/p}(x_a, \mu_f) \otimes f_{b/p}(x_b, \mu_f) \otimes d\sigma_{ab\to jd}(\mu_f, \mu_F, \mu_R) \otimes D_{j\to h}(z_j, \mu_F) \tag{1.4}$$

Here, $x_a = p_a/P_A$, $x_b = p_b/P_B$ are the initial momentum fractions carried by the interacting partons, while $z_j = p_h/p_j$ is the momentum fraction carried by the final observed hadron h. The two PDFs are given by $f_{a/p}(x_a, \mu_f)$ and $f_{b/p}(x_b, \mu_f)$. The differential cross section for a parton scattering process $ab \to jd$ is denoted as $d\sigma_{ab\to jd}(\mu_f, \mu_F, \mu_R)$. There are three different scales involved in the calculation: μ_f and μ_F are factorization scales and μ_R is the renomalisation scale. Usually they are taken to be the same $\mu_f = \mu_F = \mu_R$ as the typical hard scale Q involved in the process, such as the hadron p_{T}.
Finally $D_{j\to h}(z_j, \mu_F)$ is the fragmentation function that gives the probability of creating a hadron from the initial parton with a given fraction of the parton momentum. The process of fragmentation and hadronisation is – by its nature – a non perturbative process which can not be calculated from pQCD. Instead it has to be constrained by data, while its scale dependence is described by the DGLAP equations. This ansatz is often referred to as the factorisation theorem, as it separates the different scales of the total process. A schematic illustration of the factorisation is given in Figure 1.7

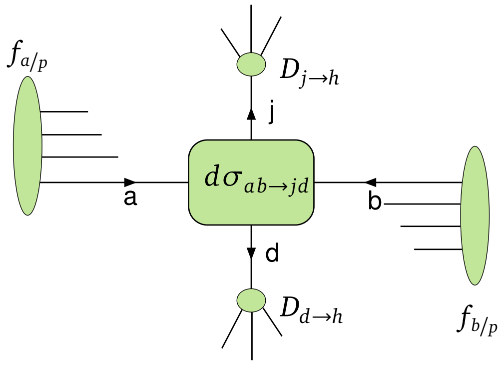

Figure 1.7.: Schematic illustration of a hard parton parton collision, resulting in the production of high p_{T} hadrons. The process may be factorised into parton distribution functions ($f_{a/p}$), hard partonic scattering cross section ($d\sigma_{ab\to jd}$) and fragmentation functions ($D_{j\to h}$). Adopted from [25].

The above considerations are valid for a vacuum, but need to be modified for heavy-ion collisions to account for nuclear and hot-medium effects. Here the behaviour of the scattered parton is influenced by parton energy loss (see following section 1.7). In vacuum a high energy parton would result in a spray of hadrons in the final state. In heavy-ion collisions the formation of such jets can be suppressed by parton energy loss. This phenomenon of jet-quenching was suggested as evidence for the formation of a deconfined state of matter by Bjorken as early as 1982 [1].
To account for parton-medium interaction, an additional term is introduced into the factorisation ansatz to account for parton energy loss. In addition, also the parton distribution function do not stay unchanged in the nucleus (nuclear PDFs are described in section 1.8).

1.6 Glauber Model

The Glauber model provides a tool to simulate the geometry of a heavy-ion collision. It is used to calculate the number of participating nucleons (N_{part}) and the number of binary collision (N_{coll}) of nuclei colliding with an impact parameter b. The likelihood of finding a nucleon in an infinitesimal area that is displaced from the nuclei's center by $\vec{s}$ is determined by $\hat{T}_A(\vec{s}) = \int \hat{\rho}_A(\vec{s}, z_A) dz_A$, with $\hat{\rho}_A(\vec{s}, z_A)$ being the probability to find a nucleon per unit volume, normalised to unity and z_A the nuclei's thickness (compare Figure 1.8). The probability $\hat{\rho}_A$ needs to be determined by experiments like low-energy electron scattering.

The product $\hat{T}_A(\vec{s})\hat{T}_B(\vec{s}-\vec{b})d^2s$ gives then the probability of having two nucleons in the overlapping area d^2s of the two colliding nuclei (A and B) with the impact parameter $\vec{b}$. The nuclear thickness function $\hat{T}_{AB}(\vec{b})$ is then obtained by integrating the total overlapping area.

$$\hat{T}_{AB}(\vec{b}) = \int \hat{T}_A(\vec{s})\hat{T}_B(\vec{s}-\vec{b})d^2s. \tag{1.5}$$

Multiplying this value with the inelastic cross section σ_{inel}^{NN} gives the probability of an interaction to occur. Here, the probability of n collisions occurring, ($P(n, \vec{b})$), can then be calculated using a binomial distribution.

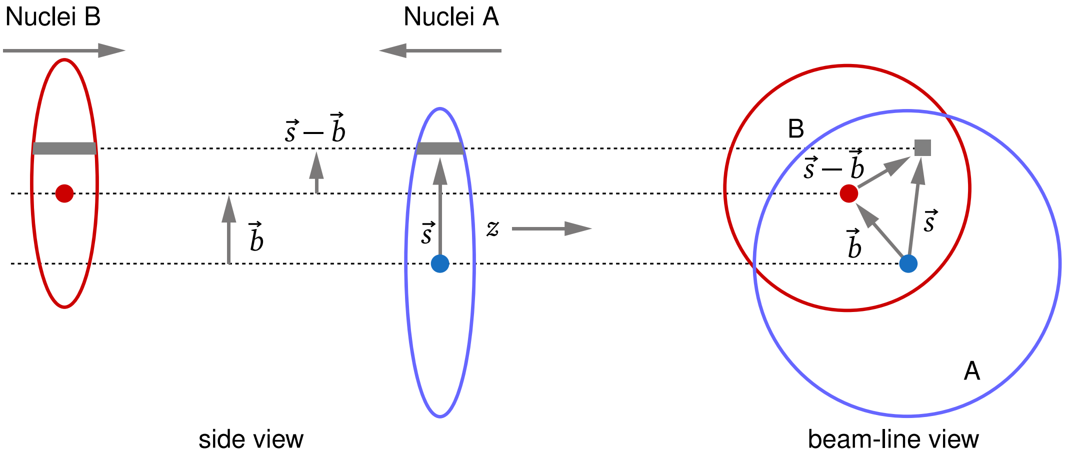

Figure 1.8.: Schematic of two nuclei colliding with an impact parameter $\vec{b}$ [26].

$$P(n, \vec{b}) = \binom{AB}{n}[\hat{T}_{AB}(\vec{b})\sigma_{inel}^{NN}]^n[1-\hat{T}_{AB}(b)\sigma_{inel}^{NN}]^{AB-n}. \tag{1.6}$$

The binomial factor $\binom{AB}{n}$ gives the number of combinations for finding n collisions out of $A \cdot B$ possible nucleon-nucleon interactions. The second term gives the probability of n collisions and the last term the probability of $(AB - n)$ misses.

The overall cross section is $\sigma_{inel}^{AB} = \int_0^\infty 2\pi b\, db \big(1 - [1 - \hat{T}_{AB}(b)\sigma_{inel}^{NN}]^{AB}\big)$ in the case of non-polarised nuclei.

The total number of nucleon-nucleon collisions (N_{coll}) is found as:

$$N_{coll}(b) = \sum_{n=1}^{AB} nP(n, b) = AB\, \hat{T}_{AB}(b)\, \sigma_{inel}^{NN}. \tag{1.7}$$

Often, a Glauber Monte-Carlo approach is chosen to simulate the collision. In this approach, the colliding nuclei are sampled from a Woods-Saxon distribution, as well as the impact parameter which is sampled from $0 < b < 2r$. Thereafter, the number of participants and collisions can be counted. Two nucleons are considered to collide if they have a minimum lateral distance $d \leq \sqrt{\sigma_{\text{inel}}^{NN}/\pi}$.

In general, the partonic energy loss depends both on properties of the parton (E, m, q) as well as on the properties of the medium (T, L). In the medium, the mean free path is given as $\lambda = 1/(\rho\sigma)$, with the medium density ρ and the particle-medium cross sections σ. For an ideal gas the medium density scales with the third power of the temperature $\rho \propto T^3$. The opacity $N = L/\lambda$ is given by the number of scatterings N, while traversing a medium with thickness L. The typical momentum exchange with the medium is given by the Debye mass $m_D(T) \sim gT$ with $\alpha_s = {}^{g^2}\!/_{4\pi}$. Overall, the scattering power of the medium is encoded into the transport coefficient $\hat{q} = m_D^2/\lambda = m_D^2\rho\sigma$, $\hat{q} \sim \mathcal{O}(\mathrm{GeV}^2/\mathrm{fm})$. In general, two different classes of energy loss can be defined (compare Figure 1.10).

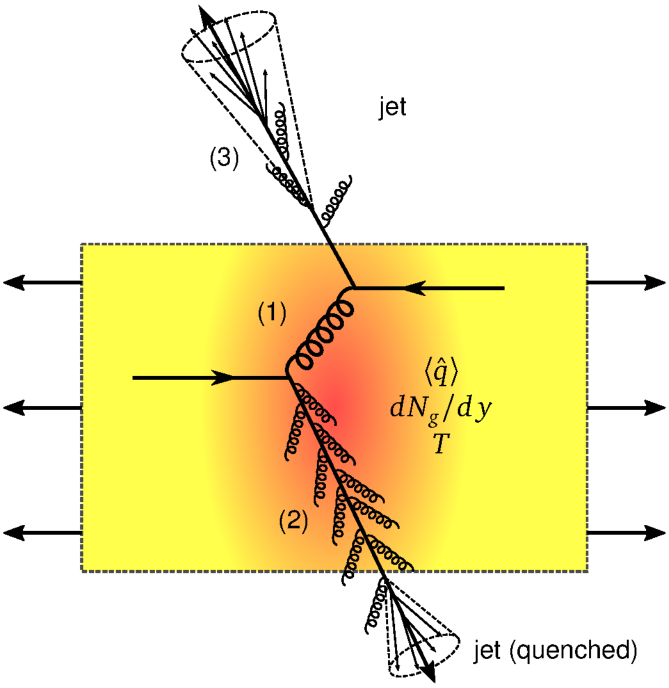

Figure 1.9.: Schematic jet quenching. Two partons originate from a hard scattering process (1), while one of the partons traverses the medium and loses energy to the medium by radiating out gluons (2), the other directly escapes into vacuum. In vacuum both partons radiate gluons before hadronising and forming jets. The medium is characterised by the transport coefficient $\langle\hat{q}\rangle$, the gluon density (dN_g/dy) and the temperature (T) [22].

The first one is the elastic (collisional) energy loss that arises from partons scattering elastically off colour charges present in the medium. The elastic energy loss is a superposition of individual scatterings and therefore it increases linearly with the distance travelled in the medium (L).

While in Bjorken's picture, the collisional energy-loss is the only contribution, it is now believed to only have a small impact compared to the energy loss by medium-induced soft gluon-radiation ("gluon-strahlung", inelastic energy loss) [27], which rises quadratically with L and is therefore expected to be the dominant process at large L at LHC.

In case of radiative energy loss, the thickness of the medium plays a significant role. For a medium thickness much smaller than the mean-free path, $L \ll \lambda$, a traversing parton is expected to undergo only one collision, here the energy loss can be described by a Bethe-Heitler (BH) like formalism.

$$\Delta E_{BH} \approx \alpha_s \hat{q} L^2 \ln(E/(m_D^2 L)) \tag{1.8}$$

For a thicker medium $(L \gg \lambda)$, the formation time of the radiated gluons gains influence on the energy loss, as multiple coherent scatterings might occur. The radiated gluons interfere destructively and thereby reduce the amount of radiated energy compared to the BH-regime. Due to their longer formation time[1], high energy (hard) gluons are stronger suppressed than soft gluons. This effect is referred to as the Landau-Pomeranchuk-Migdal (LPM) effect. In the LPM regime, the energy loss is modified to:

$$\Delta E_{LPM} \approx \alpha_s \hat{q} L^2 \tag{1.9}$$

for soft gluons with low energy ω ($\omega < \omega_c = {}^1\!/_2\, \hat{q} L^2$) and

$$\Delta E_{LPM} \approx \alpha_s \hat{q} L^2 \ln(E/(\hat{q}L)) \tag{1.10}$$

for hard gluons. In addition, the colour factors are different for gluons ($C_A = 3$) and quarks ($C_F = {}^4\!/_3$). Gluon jets are stronger suppressed than quark jets.

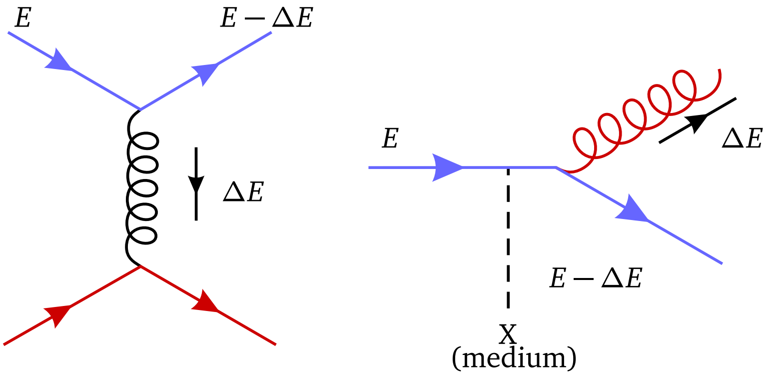

Figure 1.10.: Diagrams describing the two forms of energy loss a particle with the Energy E experiences. Left: Elastic (collisional) Right: Inelastic (radiative). [22]

For heavy quarks, the radiation of gluons is suppressed at angles smaller that the ratio of quark mass to its energy (M/E). This leads to a reduction of the total gluon radiation and is often referred to as "dead cone effect". For heavy quarks the collisional energy loss therefore becomes more important.

---

[1] The formation time $\tau \sim 2\omega/k_\perp^2$ with the energy ω and $k_\perp$ the transverse momentum of the radiation [25].

When investigating heavy-ion collisions to understand the properties of the QGP, it is important to keep in mind that the observables do not only depend on the created medium but can be influenced by differences in the incoming lead nucleus compared to a free proton. It is known, that the parton distribution functions in the nucleus (nPDFs) can be modified with respect to the PDFs in a proton. In order to quantify differences between the PDFs and nPDFs one best defines the ratio of the two:

$$R^a_{Pb}(x,Q^2) = \frac{f^a_{Pb}(x,Q^2)}{f^a_p(x,Q^2)} \tag{1.11}$$

Here, x is the parton momentum fraction and Q^2 is the four-momentum transfer squared. The PDF in protons is described by f^a_p where a is the parton species. In lead nuclei the PDF is modified to f^a_{Pb}. Fits for $R^a_{Pb}(x,Q^2)$ are shown in Figure 1.11. The calculations are based on a best fit to a large variety of experimental data reaching from deep inelastic electron scattering off nuclei to measurements of proton-gold collisions performed by the PHENIX collaboration at RHIC [28].

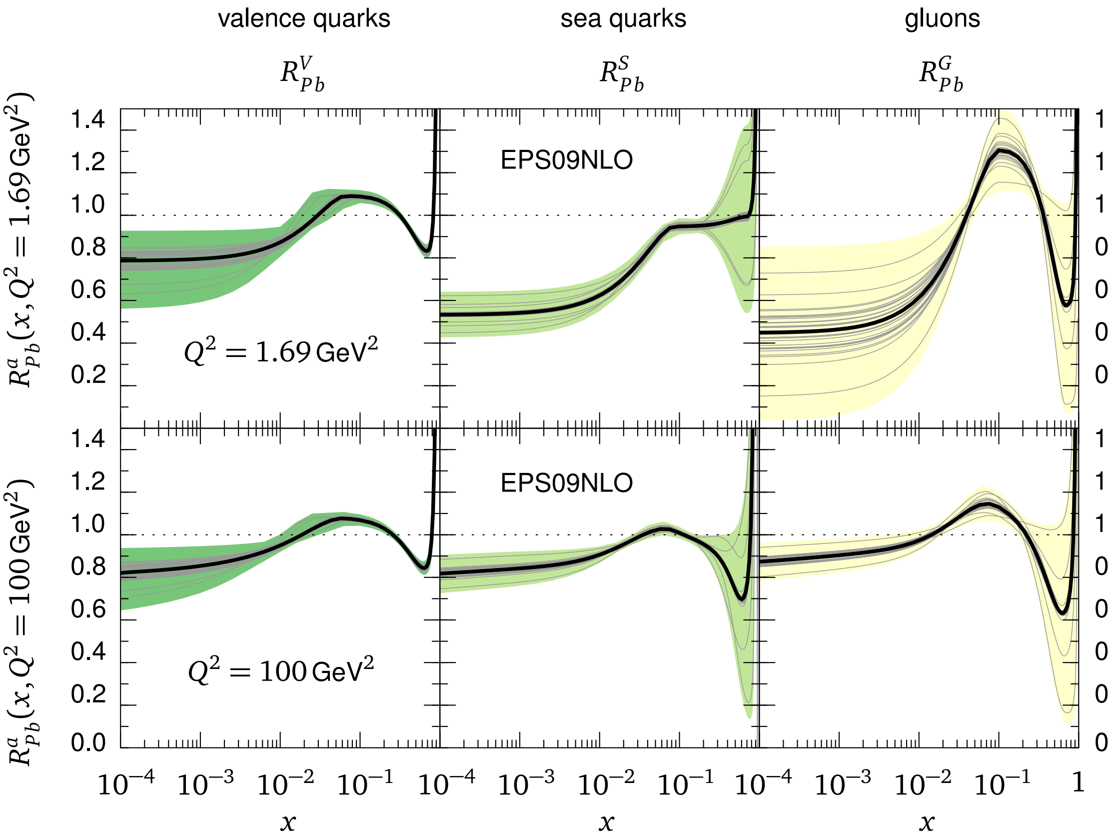

Figure 1.11.: The nuclear modification of parton distribution functions for different Q^2 (top, bottom) and for valence (left) and sea quarks (middle) as well as gluons (right) [28].

The nPDFs are calculated for the different constituents of the nucleus, valence and sea-quarks as well as for gluons. The nuclear modification of parton distributions depends on Q^2 and on x. Shadowing is driven by the most abundant partons at low x, the gluons. At high energies, the low x part of the PDF becomes dominant, and the parton distribution within the nucleon is dominated by gluons. At high enough densities the gluons overlap in phase-space and recombination becomes favourable, the gluon density saturates [29]. At midrapidity particle with Q^2 are produced by partons with $x \propto Q^2/\sqrt{s_{\mathrm{NN}}}$. Saturation effects affect low x gluons and should therefore be visible at low p_{T}.

At higher x, a gluon enhancement is seen in the nPDFs, this effect could be visible at higher p_{T}, and is often refered to as antishadowing.
One possibility to check for the role the nPDFs play, is investigating collisions of protons on nucleons (see section 2.4).

Another effect that is expected to emerge is the Cronin effect [30]. For the Cronin effect to appear, a parton performs an elastic collision before its inelastic hard process. This additional transverse momentum would be transferred to the p_{T} distribution of the created particles, shifting particles from low to an intermediate p_{T} range.

1.9 Bulk Particle Production

While hard particle production produces a spectral shape that is best described by a power-law behaviour, the shape of the spectrum at low transverse momenta can be described by a thermal (exponential) distribution. The measured identified particle yields however are best described if a blue-shift from a collective radial expansion is folded into the exponential spectra. This is known as the so-called blast wave parametrisation [31].
This radial flow is driven by the high pressure within the medium, which leads to radial expansion. In non-central collisions the medium possesses an initial spatial azimuthal asymmetry, leading to an anisotropic pressure gradient. This is translated into an anisotropic particle production [32]. From the bulk behaviour of the charged particle production medium properties such as the temperature at kinetic freeze-out, or the mediums shear viscosity can be derived.
The particle composition of the final state is well described by the thermal model, that uses three parameters: Volume, temperature and baryochemical potential. Remarkably not only light hadrons are described, but also strange hyperons and light nuclei [33].

1.10 Model Implementations

In the following, model calculations that incorporate the considerations made above are briefly presented. Though all models have been successfully describing physical observables in the past, they all differ in their ansatz. All models described derive the initial hard partons from pQCD cross sections, but only some include a dynamic medium, a running coupling constant α_s or collisional energy loss.

Vitev et al.

The calculations of Vitev et al. [34–36] include all medium effects into the quark-to-hadron splitting functions. They model the in-medium behaviour of the parton shower with a soft collinear effective theory (SCET) [37] with additional coupling to the medium by Glauber gluons exchanges SCET_G [38] that modify the fragmentation functions in the medium. In addition, the pQCD-based hard cross section used for pp is modified for the usage in heavy-ion collisions by adding initial state and cold-nuclear-matter effects, including Cronin and initial-state parton energy loss.
The medium properties enter the calculation in the form of scattering lengths for quarks and gluons.

Djordjevic et al.

The dynamical energy loss formalism employed by Djordjevic et al. [39, 40] uses the generic pQCD convolution that models the collision in three steps. The initial parton spectrum for the inital light quarks is extracted from Vitev et al. [41] an incorporates cold nuclear matter effects. Next, the partonic energy loss is estimated using both collisional and radiative energy loss. In addition, the calculations account for a dynamic medium with non-static scattering centres and include path length and multi-gluon fluctuations as well as a running coupling and a finite magnetic screening. The latter modifies the gluon-self energy of radiated and exchanged gluons and therefore influences the energy loss. The final step is the implementation of a parton-to-hadron fragmentation function, here DSS [42], is used for light hadrons.

CUJET

The CUJET3.0 model [43] aims at the simultaneous description of hard and soft physics. It is an extension of the pQCD-based CUJET2.0 model with additional suppression of quark and gluon degrees of freedom and the emergence of chromomagnetic monopoles. CUJET2.0 integrates local parton energy loss and hydrodynamic flow and models the radiative and collisional energy loss. The gluon bremsstrahlung is calculated via the DGLV opacity expansion. In CUJET, all thermodynamic properties are constrained by LQCD calculations.

Andrès et al.

The model of Andrès et al. [44] follows the formalism of quenching weights. Here, a local value for $\hat{q}_\mathrm{ideal} \sim 2\epsilon^{3/4}$ is derived from medium quantities, in particular the energy density ϵ, which is derived from hydrodynamical calculations. In order to fit these calculations to data, a free K-factor is introduced. It relates the $\hat{q}_\mathrm{ideal}$ to an effective jet-quenching parameter by $\hat{q} = K \cdot \hat{q}_\mathrm{ideal}$.
It was found previously that this factor is reduced at LHC energies compared to RHIC, and that it is independent of the collision centrality.

Higher-Twist Model

The higher-twist model implemented by Majumder and Shen [45] (HT-M) is a parameter-free calculation based upon a pQCD hard cross section and full factorisation. Parton-medium interaction is incorporated into medium-modified fragmentation functions based upon in-medium DGLAP equations. The jet transport parameter $\hat{q}$ depends on the local entropy density s, which is obtained from a $2+1$D viscous fluid dynamical simulation. In the Berkley-Wuhan (HT-BW) implementation, $\hat{q}$ is related to the local parton density in the QGP [46].

Bianchi et al.

The calculations of Bianchi et al. [47] are based on calculations by Majumder and Shen [45]. Here, high-p_T hadrons originate from the medium-modified fragmentation of hard partons. The transport coefficient $\hat{q}$ is related to the fluid dynamical simulations by scaling it with the temperature dependent entropy density. Bianchi et al. add an additional scaling of $\hat{q}$ with the energy scale of the jet. This is introduced by scattering of the hard jet-parton off Glauber gluons [38] radiated off the QGP.

Hard Thermal Loop

The McGill-AMY formalism (Arnold, Moore, Yaffe) [48] is based upon the definition of three distinct length scales. The characteristic behaviour of the constituents of the hot weakly coupled relativistic plasma are different for these scales. The first scale is the "hard" scale containing excitations with wave numbers (momenta) of $k \sim T$. For a weak coupling $g \ll 1$, these excitations travel trough the medium as free quasi-particles occasionally experiencing small-angle scatterings. Large-angle scatterings occur much less frequent.

The second scale is denoted as "soft", $k \sim gT$. At this scale ,the excitations interact with the plasma coherently. In order to apply pQCD at this scale, the coherent interactions have to be factorised into propagators and verticies. This procedure is known as the "hard-thermal-loop" (HLT). This "soft" scale dominates the large-angle scattering, while the small-angle scattering is dominated by g^2T, the "ultrasoft" scale. Here, perturbation theory can no longer be applied. Observables such as jet-quenching however, only depend on the scales of T and gT.

The MARTINI event generator [49] employs the McGill-AMY formalism to estimate the energy loss in a hydrodynamical medium. The initial hard collisions are generated using PYTHIA 8.1, which is also used for the implementation of the fragmentation.

2 Experimental Observations

2.1 Charged particle production

The production of charged particles is observed at different scales. At high p_{T}, hard processes such as jets are observed, while at low p_{T} the remnants of soft processes are found. These soft probes dominate the overall number of charged particles produced in the collision and can provide information on the medium. It is assumed that hard processes scale with the number of binary collisions (N_{coll}), while the production of soft particles is believed to scale with the number of participants (N_{part} see 1.6). The overall production of charged particles per $\langle N_{\mathrm{part}} \rangle$ is shown in Figure 2.1 left. The rise in charged-particle production with collision energy ($\sqrt{s_{\mathrm{NN}}}$) is found to follow a power law with a larger exponent for Pb–Pb than for pp. Figure 2.1 (right) shows the same quantity including further classes of collision centrality [50–54].
This behaviour is often associated with an increased contribution of hard processes. The different behaviour of pp an Pb–Pb indicates that a collision of lead ions is not a mere superposition of independent pp collisions.

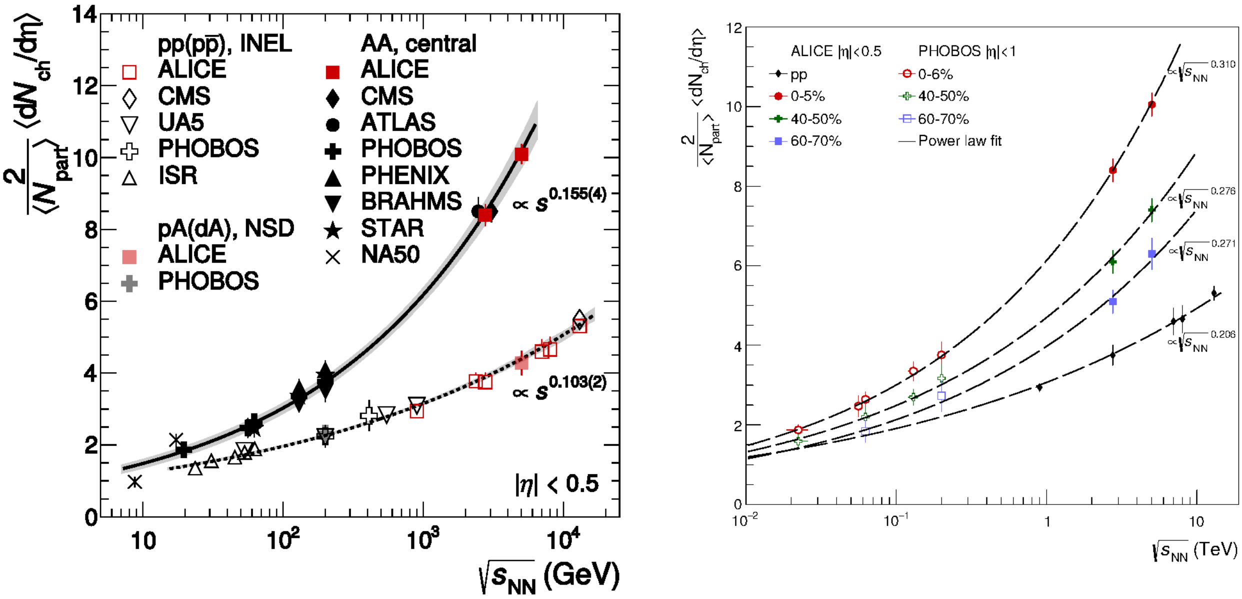

Figure 2.1.: The energy dependence of charged particle densities normalised to $\langle N_{\mathrm{part}} \rangle$ for different classes of centrality measured by PHOBOS and ALICE [50–54]. The fits for pp an Pb–Pb 0-5% are taken from [54]. A centrality dependent rise can be seen.

According to the Bjorken formula [55],

$$\epsilon_B = \frac{1}{\pi R^2 \tau_0} \cdot \left. \frac{dE_{\mathrm{T}}}{dy} \right|_{y=0}, \tag{2.1}$$

the energy density (ϵ_B) archived in the collision is related to the measured energy per unit of rapidity (dE_{T}/dy) around central rapidity. Here, R stands for the initial radius of the collision system and τ_0

for the formation time. In the transverse plane, the energy per unit of rapidity can be expressed as $dE_{\mathrm{T}}/d\eta\,(\,\mathrm{GeV}) \approx 1.25 \cdot d\mathrm{N}_{\mathrm{ch}}/d\eta$ [56].
With $R = (6.62{\pm}0.06)\,\mathrm{fm}$ [57] and τ_0 assumed to be at most $1\,\mathrm{fm}/c$, one can estimate the energy density. With the measurement, $d\mathrm{N}_{\mathrm{ch}}/d\eta = 1601 \pm 60$ for Pb–Pb at $\sqrt{s_{\mathrm{NN}}} = 2.76\,\mathrm{TeV}$ and $d\mathrm{N}_{\mathrm{ch}}/d\eta = 1943 \pm 54$ at $\sqrt{s_{\mathrm{NN}}} = 5.02\,\mathrm{TeV}$ [53, 54] one obtains:

$$\epsilon_B^{\mathrm{PbPb}}(2.76\,\mathrm{TeV}) = (14.5 \pm 0.6)\,\mathrm{GeV/\,fm^3}$$
$$\epsilon_B^{\mathrm{PbPb}}(5.02\,\mathrm{TeV}) = (17.6 \pm 0.6)\,\mathrm{GeV/\,fm^3}$$

For Xe–Xe ($R = (5.36 \pm 0.1)\,\mathrm{fm}$ $d\mathrm{N}_{\mathrm{ch}}/d\eta = 1167 \pm 24$ [58]), $\epsilon_B^{\mathrm{XeXe}}(5.44\,\mathrm{TeV}) = (16.2 \pm 0.7)\,\mathrm{GeV/\,fm^3}$ is found. These values are much larger than the LQCD estimation of the critical energy density $\epsilon_c = 1\,\mathrm{GeV/\,fm^3}$ [59].

2.2 Particle Spectra and the Nuclear Modification Factor

The measurement of the transverse momentum distribution of charged particles and their relative suppression in nucleus-nucleus (AA) collisions was one of the first pieces of evidence for the existence of the Quark Gluon Plasma at the Relativistic Hadron Collider (RHIC) at the Brookhaven National Lab [60, 61]. At the LHC, the momentum distributions were measured by ATLAS, CMS, and ALICE together spanning a range in p_{T} from 150 MeV/c up to 400 GeV/c [62–65]. While at low p_{T}, soft process play a dominant role in the particle production, the spectra is dominated by hard processes at higher p_{T}. Any medium modification to the particle production would affect the p_{T} distribution in Pb-Pb collisions compared to the distribution in pp collisions. A common way of analysing such a modification is through the nuclear modification factor defined as:

$$R_{\mathrm{AA}}(p_{\mathrm{T}}) = \frac{1}{\langle T_{\mathrm{AA}}\rangle} \frac{d^2N_{ch}^{AA}/d\eta dp_{\mathrm{T}}}{d^2\sigma_{ch}^{pp}/d\eta dp_{\mathrm{T}}} \tag{2.2}$$

Here N_{ch}^{AA} represents the multiplicity of charged particles in nucleus-nucleus (AA) collisions while σ_{ch}^{pp} describes the cross section in proton-proton (pp) collisions. $\langle T_{\mathrm{AA}}\rangle = \langle N_{\mathrm{coll}}\rangle/\sigma_{inel}$ is the nuclear overlap function which needs to be calculate with Glauber Model (see section 1.6). In the case of centrality dependent studies, T_{AA} is averaged over the centrality class.
If the nuclear modification factor is equal to unity ($R_{\mathrm{AA}} = 1$), no medium modification is present (binary collision scaling). A $R_{\mathrm{AA}} > 1$ would characterise an enhanced particle yield in Pb–Pb, while $R_{\mathrm{AA}} < 1$ indicates a suppressed yield of charged particles.
At RHIC the measurement of such a suppression of charged particle yields in Au–Au collisions was one of the key measurements providing evidence for the formation of the Quark Gluon Plasma [60, 61], Figure 2.2.
The measured R_{AuAu} shows a pronounced dependence on both centrality and transverse momentum. The largest suppression is found in central collisions. A p_{T} dependence is observed, showing only little suppression at low p_{T}, where scaling with the number of participants (N_{part}) is expected and an increased suppression for higher transverse momenta ($p_{\mathrm{T}} \approx 8\,\mathrm{GeV}/c$). When going from central to more peripheral collisions an increase in R_{AuAu} is observed reaching binary scaling in the most peripheral class of collisions.
With the start of the heavy-ion program at the LHC, collisions at an unprecedented energy of $\sqrt{s_{\mathrm{NN}}} = 2.76\,\mathrm{TeV}$ became available. The measurement of R_{PbPb} in Pb–Pb collisions confirmed the suppression at RHIC and could show that the suppression is present up to very high transverse momenta [62–64], see Figure 2.3.
The R_{PbPb} at $\sqrt{s_{\mathrm{NN}}} = 2.76\,\mathrm{TeV}$ shows the same dependence on centrality as was observed at lower energies. The suppression is the strongest for the most central collisions and becomes less for peripheral collisions. In central collisions R_{PbPb} reaches a minimum at p_{T} = 6 - 7 GeV/c of $R_{\mathrm{PbPb}} \sim 0.13$. Towards higher p_{T} suppression gets less, staying significant $R_{\mathrm{PbPb}} \sim 0.4$ even for the hightest $p_{\mathrm{T}} = 50\,\mathrm{GeV}/c$.

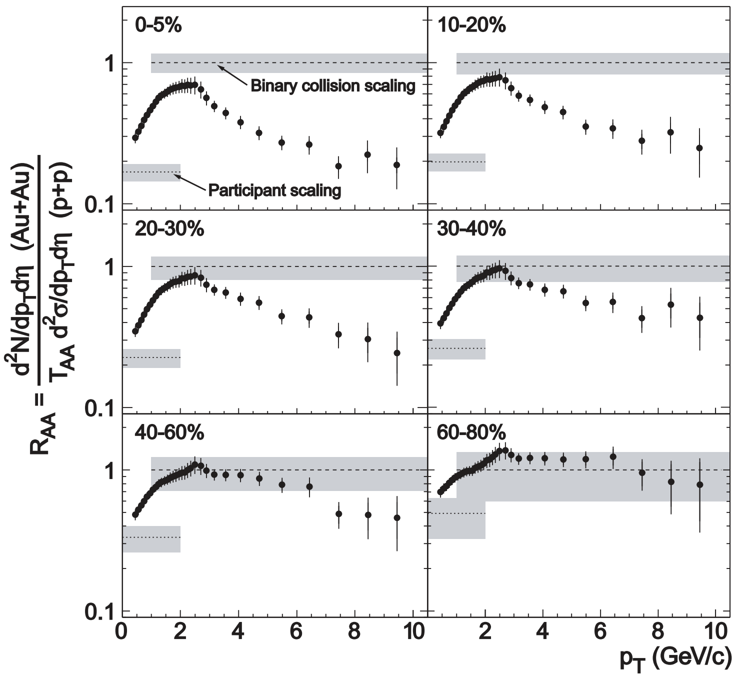

Figure 2.2.: R_{AuAu} measured in Au–Au collisions at $\sqrt{s_{\mathrm{NN}}}$ = 200 GeV in six classes of centrality measured by the STAR Collaboration [66].

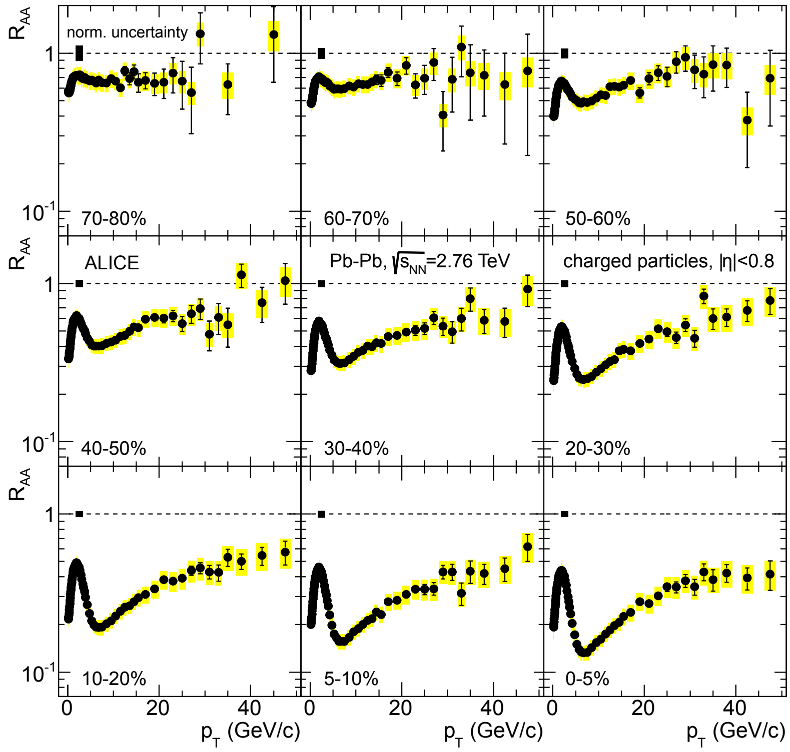

Figure 2.3.: R_{PbPb} measured in Pb–Pb collisions at $\sqrt{s_{\mathrm{NN}}} = 2.76$ TeV in nine classes of centrality [62].

2.3 Spectra of individual particle species

In addition to the inclusive measurement of charged particles, different particle species can be measured individually. Figure 2.4 shows the nuclear modification factor of the most abundant charged particles, pions ($\pi^{\pm}$), kaons ($\mathrm{K}^{\pm}$) and protons (p) and antiprotons ($\bar{\mathrm{p}}$) for Pb–Pb collisions at $\sqrt{s_{\mathrm{NN}}} = 2.76\,\mathrm{TeV}$. At high $p_{\mathrm{T}} > 10\,\mathrm{GeV}/c$, the yield of particles is suppressed independently of their species for central and peripheral collisions. At lower momenta, protons are less suppressed and the corresponding maximum of the R_{PbPb} is shifted towards higher p_{T}. This effect can be explained as protons are baryons while pions and kaons are mesons. Energy loss is not a phenomena of baryons of mesons but of individual partons. At freeze-out, when particles hadronize, thee quarks of similar momentum will form a baryon, while only two are needed to form a meson. Therefore baryons will have more momentum.

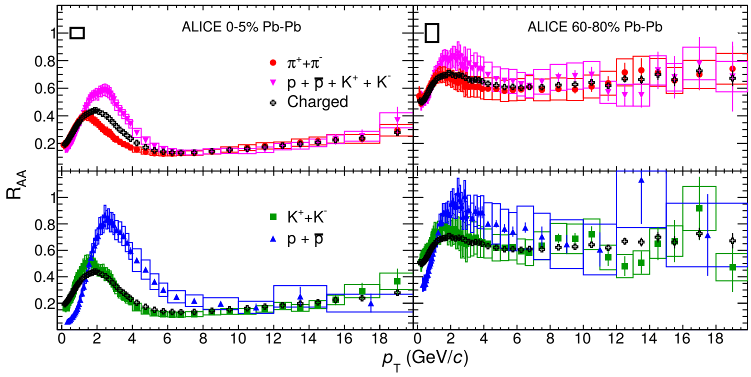

Figure 2.4.: R_{PbPb} measured in Pb–Pb collisions at $\sqrt{s_{\mathrm{NN}}} = 2.76\,\mathrm{TeV}$ for the most abundant particle species [67].

2.4 Collisions of Protons and Lead Ions

Collisions of protons and lead ions offer a unique possibility to study the initial stage effects discussed in section 1.8. The nuclear modification factor R_{pPb} is defined analogously to the R_{AA} in nucleus-nucleus collisions. In contrast to Pb–Pb collisions, the number of binary collisions in p–Pb is much lower, $\langle N_{\mathrm{part}}^{\mathrm{pPb}} \rangle = 7.9 \pm 0.6$ [68] as compared to $\langle N_{\mathrm{part}}^{\mathrm{PbPb}} \rangle^{0-5\%} = 385,1 \pm 4.3$ [62].
The R_{pPb} measurement with ALICE at $\sqrt{s_{\mathrm{NN}}} = 5.02\,\mathrm{TeV}$ [68] is shown in Figure 2.5.

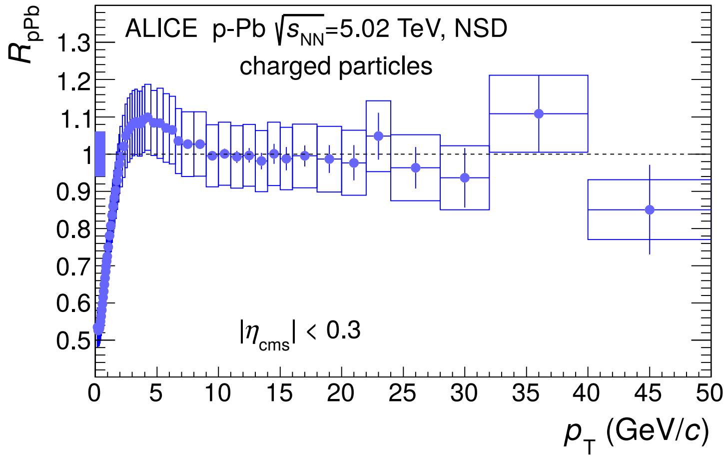

Figure 2.5.: R_{pPb} measured in p–Pb collisions at central rapidity [68].

The R_{pPb} is measured in its center-of-mass frame at central rapidity $|\eta_{cms}| < 0.3$. At $p_{\mathrm{T}} > 6\,\mathrm{GeV}/c$, R_{pPb} is consistent with unity, while at lower p_{T} deviations from unity can be seen. A Cronin-like enhancement at $p_{\mathrm{T}} \sim 4\,\mathrm{GeV}/c$ is not ruled out by the data, while at even lower p_{T}, N_{part}-scaling is present, with $R_{\mathrm{pPb}} \sim 0.5$. The binary scaling of charged-particle yields in p–Pb collisions, gives evidence, that the suppression found in Pb–Pb collisions originates from final-state effects and can be linked to the energy-loss of high-p_{T} partons in QGP.

2.5 Standard Candles

In contrast to jets, originating from strongly interacting partons, the electroweak gauge bosons do not interact with the medium. The $W^{\pm}$ and Z^0-bosons however have a lifetime shorter than the formation time of the QGP. However they can be reconstructed through their leptonic decays. Further evidence to the concept of N_{coll} scaling can therefore be found in the measurements of these probes. Figure 2.6 presents such measurement of direct photons [69] as well as $W^{\pm}$-bosons [70] and Z^0-bosons [71].

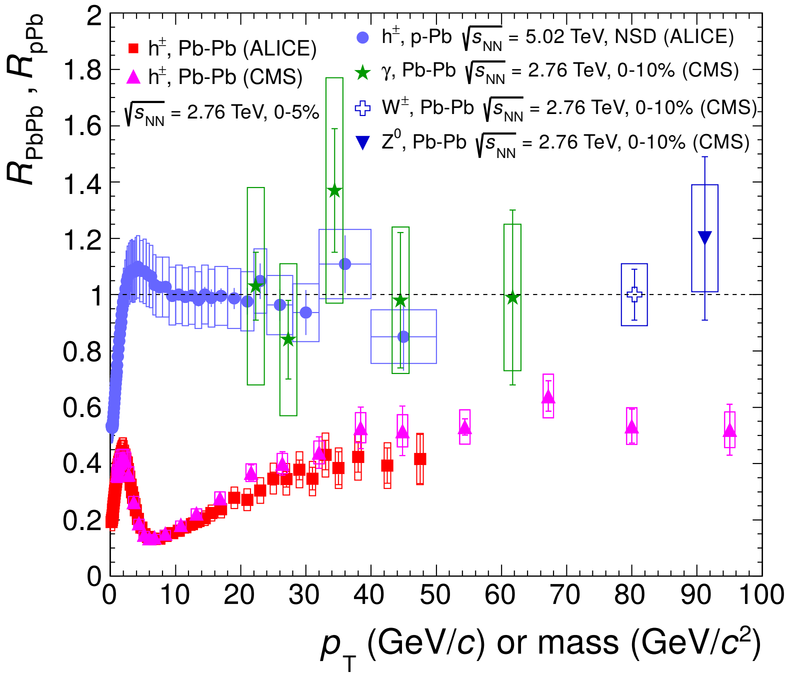

Figure 2.6.: Compilation of nuclear modification factors. The R_{pPb} of charged particles as well as the R_{PbPb} of $W^{\pm}$-bosons and Z^0-bosons and direct photos in central collisions is equal to unity, while the yield of charged hadrons in central Pb–Pb collisions is strongly suppressed. Figure published in [68].

It is found, that the production of electroweak gauge bosons in central heavy-ion collisions scales with the number of binary collisions (R_{PbPb} equal to unity). It is worth mentioning, that the production of the bosons in first order requires the partons to carry the electric or weak charge. Therefore they are only produced in collisions of quarks, as gluons only carry colour charges. While jets are more sensitive to the much larger gluon densities, heavy bosons probe the initial quark content.

2.6 Mean Transverse Momentum

Another way of characterising charged-particle production is by the observation of the mean transverse momentum $(\langle p_{\mathrm{T}} \rangle)$ of a collision. A special focus in this measurement lies on the behaviour of this observable in small collision systems. The $\langle p_{\mathrm{T}} \rangle$ as a function of $\mathrm{N_{ch}}$ in pp collisions at different center-of-mass energies is shown in the left panel of Figure 2.7. While only a small dependence on $\sqrt{s}$ was found, a monotonic rise of the $\langle p_{\mathrm{T}} \rangle$ with the number of produced charged particles is observed. In pp collisions, this result hints towards collective behaviours in the collision. Here collisions with a high number of charged particles are believed to originate from collisions with more than one parton-parton collision. If the resulting particles of these collision were to be fully independent, the $\langle p_{\mathrm{T}} \rangle$ would show a constant behaviour with increasing $\mathrm{N_{ch}}$.

A comparison of different collision systems reveals clear differences (Figure 2.7 right). While in Pb–Pb the $\langle p_{\mathrm{T}} \rangle$ is generally lower, it also shows a weaker dependence on the number of charged particles produced, though the range of $\mathrm{N_{ch}}$ shown is only including very peripheral collisions. In asymmetric collisions of proton and lead ions the $\langle p_{\mathrm{T}} \rangle$ shows a similar increase with $\mathrm{N_{ch}}$ for low number of charged particles, while towards higher $\mathrm{N_{ch}}$ the increase gets weaker and levels off.

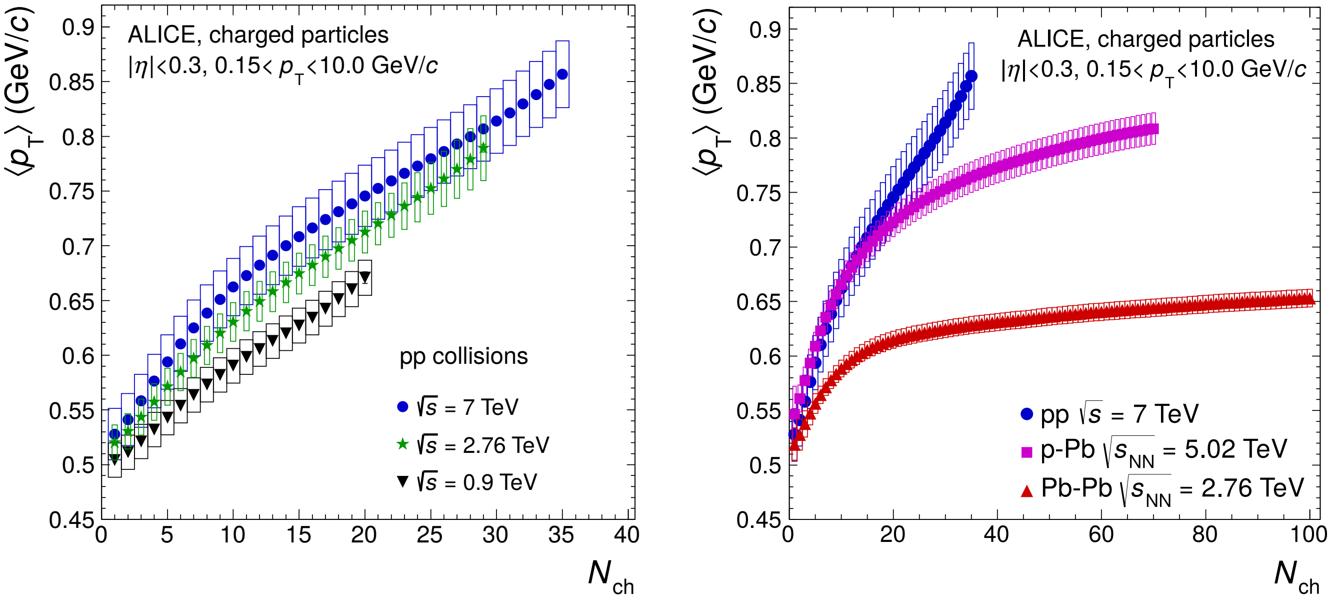

Figure 2.7.: Average transverse momentum $\langle p_{\mathrm{T}} \rangle$ as a function of charged-particle multiplicity $\mathrm{N_{ch}}$ in pp collisions at different collision energies (left) and in pp, p–Pb, and Pb–Pb collisions (right) [72].

2.7 Estimation of the Transport Coefficient

The nuclear modification factors from RHIC (Au–Au) and from LHC Run 1 (Pb–Pb) have led to the development of various different model calculations. As most of the models incorporate the jet-transport coefficient $\hat{q}$, a comparison of the models is possible. Such a survey study was done by the JET Collaboration [73], studying five different model calculations that succeed in describing both measured nuclear modification factors at RHIC and LHC.

Two of the models compared are based on Higher-Twist calculations while McGill-AMY and the MARTINI generator are based upon the Hard Thermal Loop approach. Further, the CUJET model is analysed (compare section 1.10).

All models account for the dynamic evolution of the medium but have different approaches to the energy loss. The hydrodynamic calculations done by the models fix an initial temperature of ∼ 370 MeV for RHIC and ∼ 470 MeV for LHC Run 1. Figure 2.8 shows scaled values for the jet transport coefficient $\hat{q}/T^3$

as a function of the medium's initial temperature T. The values quoted are calculations for a quark with an energy $E = 10\,\mathrm{GeV}$ at the centre of an AA collision at an initial time $\tau_0 = 0.6\,\mathrm{fm}/c$. The corresponding

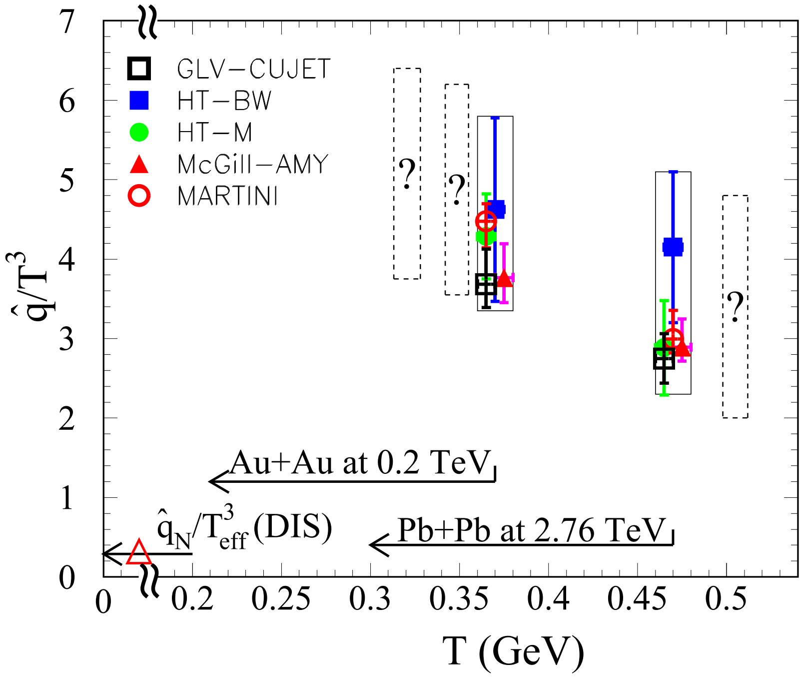

Figure 2.8.: The values for $\hat{q}$ obtained by various models. Dashed boxes indicate expectations for the upcoming data from the RHIC Beam-Energy Scan (BES) and for LHC Run 2. The red open triangle indicates the value of $\hat{q}_N$ for cold nuclei. [73].

values for $\hat{q}$ are,

$$\hat{q} \approx \begin{cases} 1.2 \pm 0.3\,\mathrm{GeV}^2/\mathrm{fm} & T = 370\,\mathrm{MeV}\ (\mathrm{RHIC}) \\ 1.9 \pm 0.7\,\mathrm{GeV}^2/\mathrm{fm} & T = 470\,\mathrm{MeV}\ (\mathrm{LHC\ Run\ 1}) \end{cases}. \tag{2.3}$$

The quoted uncertainties are the variations of the $\hat{q}$ values between the five different models studied. As a comparison, Figure 2.8 also shows the value for cold nuclei extracted from deep inelastic scattering experiments ($\hat{q}_N = 0.02\,\mathrm{GeV}^2/\mathrm{fm}$), which is orders of magnitude lower than the values from AA collisions.

3 The LHC and the ALICE detector

3.1 LHC

The Large Hadron Collider [74] is the world's largest particle collider built at the European Organization for Nuclear Research (CERN) in the border region of France and Switzerland close to Geneva. The LHC delivered first collisions in March 2010 and had its first data taking period (Run 1) until 2013 providing particle collisions with the highest collision energies ever achieved in a laboratory of $\sqrt{s} = 8\,\text{TeV}$ for proton-proton (pp) collisions. After two years of maintenance and upgrades the second data taking period (Run 2) started in 2015 with the first collision of protons at $\sqrt{s} = 13\,\text{TeV}$ as well as colliding lead ions (Pb–Pb) at $\sqrt{s_{\text{NN}}} = 5.02\,\text{TeV}$.

The LHC is constructed in a tunnel originaly dug for the Large Electron Positron Collider (LEP) 50—175 m below the surface with a circumference of 27 km. The collider consists of two beam pipes in which the beams travel in opposite directions. Both beams are bent by a total of 1232 common dipole magnets that provide fields with a magnetic field strength of 8.33 T. The magnetic field is generated by a current of 12000 A in the superconducting magnets, cooled by super fluid helium to 1.9 K. In addition 858 quadrupole and 6000 corrector magnets are needed to control and shape the beam. The two beam pipes cross at four interaction points, there the beams are brought to collision within the detectors. Even though the LHC was mainly designed to accelerate and collide protons, it is capable of providing collisions of heavy ions such as Lead (Pb–Pb) and Xenon (Xe–Xe). Besides symmetric collisions like Pb–Pb the accelerator facility also provided asymmetric collisions of protons and lead nuclei in Run 1 and Run 2.

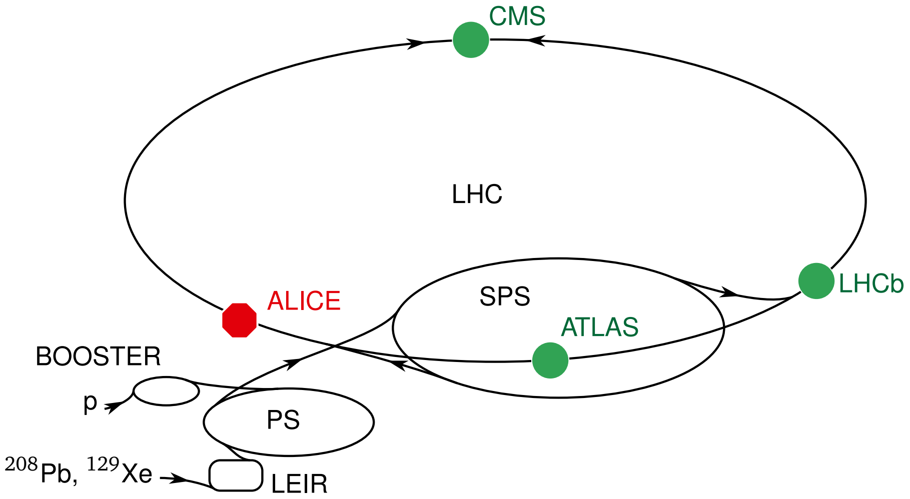

Figure 3.1.: Schematic view of the CERN accelerator facility. Adopted from [75].

The beams accelerated in the LHC are generated by the CERN accelerator complex shown in Figure 3.1. Lead ions are first accelerated by Linac 3 before being collected in the LEIR (Low Energy Ion Ring), where they are accelerated before they are injected into the PS (Proton Syncrotron) [76]. The PS again accumulates ions, before accelerating them and transferring the beams to the Super Proton Syncrotron (SPS). The steps of accumulating and acceleration are repeated again within the SPS before the Pb ions are injected into the LHC with a beam energy of 177 GeV/u (450 GeV for protons). This cycle is repeated to provide high beam intensities before accelerating the beams within the LHC, once accelerated the

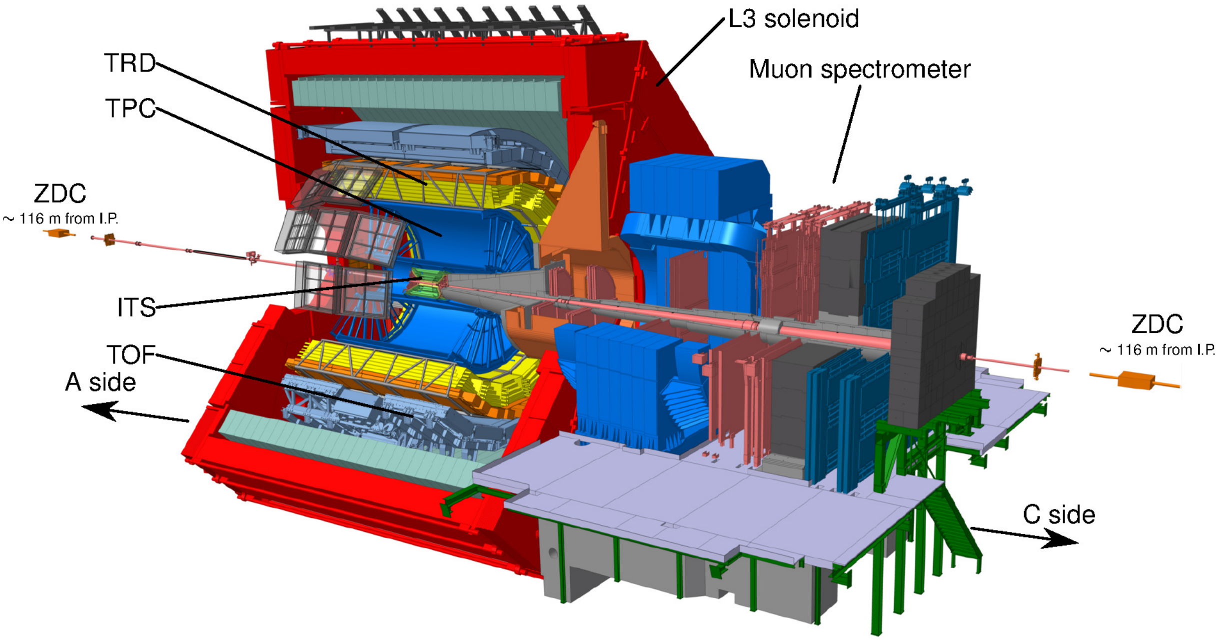

Figure 3.2.: Schematic view of the ALICE setup [80]

beams are brought to collision and are kept circulating until their intensity has decreased due to the collisions and beam loss. The process is repeated after one of theses fills has ended.
For protons the procedure is similar starting at Linac 2 and the Booster, before entering the PS.
Four large scale experiments are installed at the interaction points. CMS (Compact Muon Solenoid) and ATLAS (A Toroidal LHC ApparatuS) are dedicated to particle physics and discovered the Higgs Boson in 2012 [77, 78]. A continued focus is the detailed investigation of the Higgs Boson as well as the search for physics beyond the standard model. The LHCb experiment is committed to the study of the beauty (bottom) quark and could successfully discover a pentaquark state in 2015 [79].

3.2 ALICE

ALICE (A Large Ion Colliding Experiment) is commited to the study of heavy-ion collisions. While the other experiments are primarily designed for elemental collisions of protons, the design of ALICE is focused on the high track densities that occur in collisions of heavy ions. ALICE is composed of two parts, around the interaction point at central rapidity the so called central barrel detectors are installed within the large magnet that was previously used by the L3 experiment at LEP. In forward direction the muon spectrometer is installed which features its own dipole magnet.
The central barrel magnet provides a homogeneous solenoidal magnetic field (up to $B = 0.5\,\mathrm{T}$) parallel to the beam pipe within the magnet. Compared to the other LHC detectors it has a comparably low field strength, which enables ALICE to measure particles with a very low transverse momentum. Close to the interaction point the Inner Tracking System (ITS) is located. It consist of six layers of silicon detectors and is designed to provide excellent vertex resolution and tracking information close to the event vertex. The main tracking device of ALICE is the large Time Projection Chamber (TPC), a gaseous detector that provides precise tracking information and has outstanding particle identification (PID) capabilities. To larger radii the Transition Radiation Detector (TRD) and the Time Of Flight detector (TOF) complete the PID system.
To trigger events and to determine the event centrality in case of heavy ion collisions the V0 detectors are installed close to the interaction point in forward and backward direction.

Outside the main ALICE cavern 116 m away from the interaction point the Zero Degree Calorimeters (ZDC) are installed. This detector measures the energy of the spectators not taking part in the heavy-ion collision.

3.2.1 ITS

The Inner Tracking System [81] is placed in the centre of the detector setup around the beam pipe and consists of six layers of silicon detectors with radii between 39 mm and 430 mm (Figure 3.3). The inner radius is determined by the size of the beam pipe, while the outer radius is optimized for an efficient tracking in combination with the Time Projection Chamber. The main functions of the ITS are the improvement of the primary vertex and momentum resolution and the reconstruction of secondary vertices of heavy flavor and strange particle decays [82]. As the inner part of the ITS is mounted directly on the beam pipe, it has to withstand extreme particle densities of up to 100 particles per cm^2 for the innermost layer and about one particle per cm^2 for the outermost layer. These different radiation levels as well as technological and financial constraints lead to the application of different detector technologies in the individual layers of the ITS. The innermost layer is based on Silicon Pixel Detectors (SPD) which provide the high granularity necessary for an excellent precision in the determination of the track's distance of closest approach to the primary vertex (DCA). While the whole tracking covers rapidity of $|\eta| \leq 0.9$, the first layer of pixels covers $|\eta| \leq 1.75$. The third and fourth layer are based on Silicon Drift Detectors (SDD), while the two outermost layers contain double-sided Silicon micro-Strip Detectors (SSD) The four outer layers are read out analogously and can additionally be used to extend the particle identification (PID) capabilities of ALICE down to particles with a transverse momentum below 100 MeV/c. As ALICE has a focus on the measurement of low transverse momentum particles the material budget and radiation length of the Inner Tracking System is kept minimal. More information and plans for the upgrade can be found in [83].

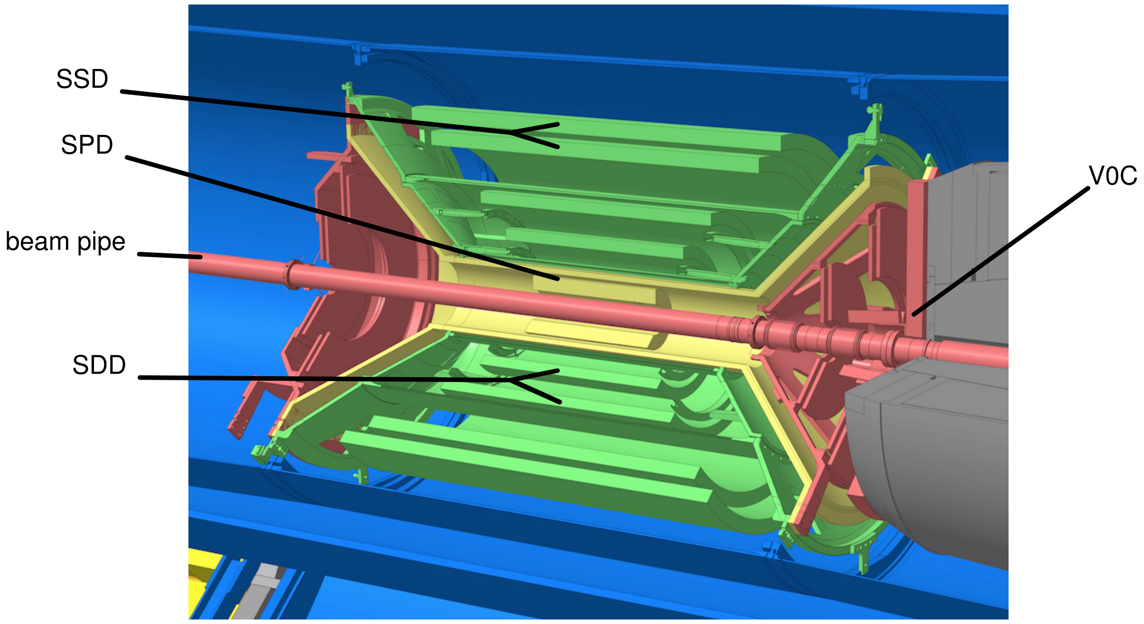

Figure 3.3.: Schematic view of the ITS [80]

3.2.2 TPC

The main tracking and particle identification device in ALICE is the Time Projection Chamber [84, 85], Figure 3.4. It is the largest TPC built and has the shape of a hollow cylinder that encapsulates the ITS. It has an inner radius of 848 mm, an outer radius of 2446 mm and a total length of 4994 mm covering a total active volume of 90 m^3. It covers the full azimuthal angle (ϕ) and $|\eta| < 0.9$ for tracks that fully cross the detector ($|\eta| < 1.5$ for tracks with 1/3 of their track length in the active region).

The active volume is divided by the large central electrode (at $z = 0$), which generates an electric field of 400 V/m pointing towards the electrode with a potential of -100 kV. The electric field is homogenized by the inner and outer field cage that employ resistor chains to reduce the voltage gradually.

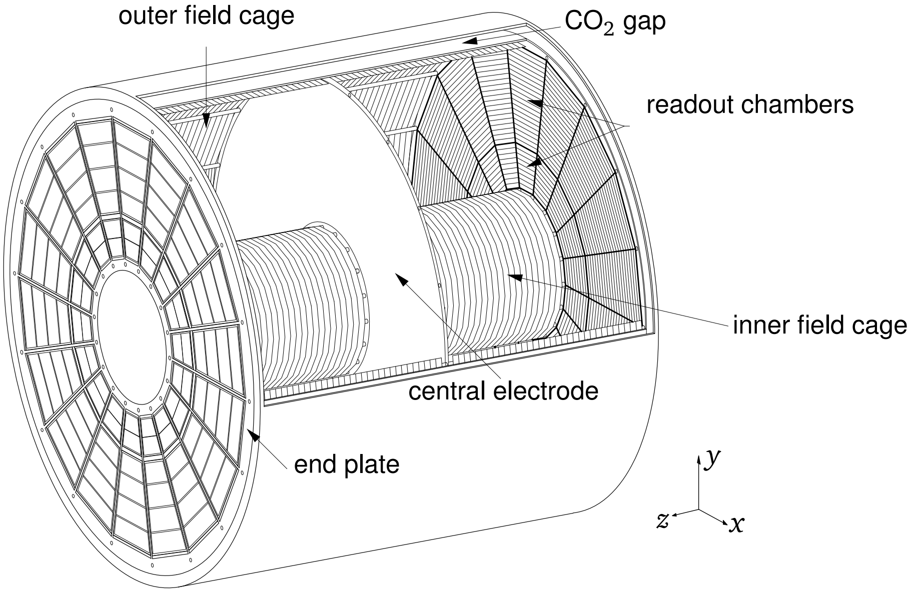

Figure 3.4.: Schematic view of the TPC [84] [86].

The TPC volume is filled with a detector gas, that is ionized by charged particles passing through. In addition the drift velocity ($\approx 2.6\ ^{cm}/_{\mu s}$) of electrons and ions has to be reasonable and also the chemical properties of the gas have to be taken into account in order to protect the sensitive detector. In Run 1 a gas mixture of 90 parts Ne, ten parts CO_2 and five parts N_2 was chosen. In the beginning of Run 2 a gas mixture containing Argon instead of Neon was chosen, as it generates more electrons during the ionization. The mixture has 88% Ar and 12% CO_2. Argon however has the disadvantage of a slower ion mobility which can lead to accumulation of space charge (see section 3.3.2), therefore later in Run 2 the gas was changed back to the Run 1 mixture.

The electrons created in the gas drift towards either end of the TPC where the detector readout is mounted. The end plates of the TPC are segmented into 18 trapezoidal sectors covering 20 degrees of azimuthal angle each. The end plates support the read out system which is segmented into the inner and outer readout chambers (IROC and OROC). In between two adjacent chambers a region without readout is located with a width in the azimuthal direction of 27 mm. The readout is carried out by multiwire proportional chambers, see Figure 3.5. The readout consist of three layers of wires and one layer of readout pads with an separation of 3 mm for OROCs (2 mm for IROCs). The first layer is the gating grid, its wires can be set to alternating potentials such that all electric field lines end at one of the wires. The gating grid is then closed and prevents electrons from passing into the amplification region and stops ions from drifting back in to the detection volume. For an open gating grid the wire potential is set to the potential of the surrounding field. The next layer with the cathode wires separate the amplification from the drift region. After passing the cathode wires the electrons generated by the track are accelerated in

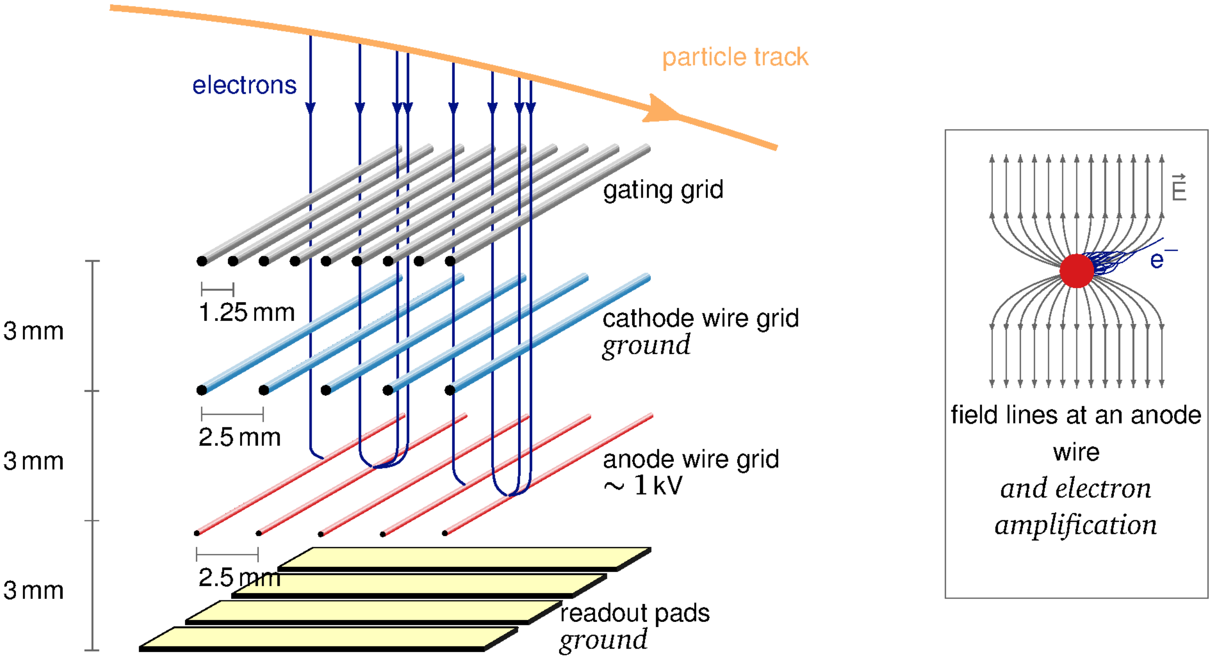

Figure 3.5.: Sketch of the readout system of the TPC. Dimensions given refer to an OROC. In an IROC the distance between pads and anode wires, as well as between anode and cathode wires is reduced to 2 mm. Figure adopted from [87]

the field created by the anode wires. The electric field responsible for the acceleration is the strongest close to the wires, and is high enough to generate avalanche electrons, thereby amplifying the signal. The electron avalanche induces a mirror charge in the readout pads which have a size of $4 \times 7.5\,\mathrm{mm}^2$ in the IROC while in the OROC the size changes to $6 \times 10\,\mathrm{mm}^2$ and $6 \times 15\,\mathrm{mm}^2$ for the outermost readout pads.

In total 159 rows with a total number of 557 568 readout pads provide the high granularity needed for a good track separation at the high track multiplicities achieved at ALICE ($dN_{\mathrm{ch}}/d\eta \approx 2000$ for central Pb–Pb collisions, compare section 2.1).

3.2.3 V0A & V0C

The VZERO (V0) [88,89] detectors are the main devices used for triggering and the determination of the collisions centrality (see section 3.5). The V0 detector consist out of two plates of plastic scintillator each segmented into 8 segments in azimuth and 4 rings in radial direction, read out by photomultiplier tubes. The detectors cover a rapidity range of ($2.8 > \eta > 5.1$) for V0A and ($-3.7 < \eta < -1.7$) for V0C. The V0A detector is located in positive z-direction about 340 cm away form the nominal interaction point while V0C is located in the negative z-direction only 90 cm away from the interaction point, as the space is shared with the absorber needed for the muon arm Figure 3.3.

3.3 Tracking and Vertexing

Finding tracks and extracting their physical quantities is a challenging task. The procedure of tracking is sketched in Figure 3.6, a detailed description of the tracking procedure can be found in [85](focus on TPC [90]).

Prior to the tracking procedure the raw input of each detector needs to be converted to clusters. This process is done for each detector separately, for the TPC it is either done offline which requires the storage

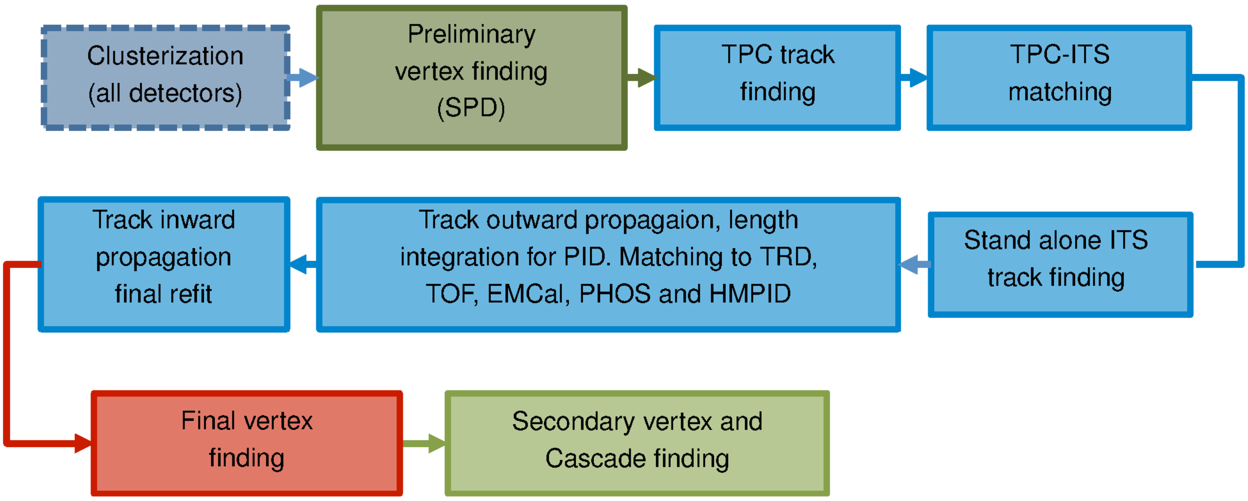

Figure 3.6.: Schematic outline of the tracking and reconstruction procedure in ALICE [85].

of all input data, or online by the High-Level Trigger (HLT). The HLT-clustering was commissioned during Run 1 and is used as a default in Run 2. It has the benefit, that a smaller fraction of data has to be stored.
The first step of tracking is the determination of the preliminary primary event-vertex. This is based on the two innermost layers (SPD) of the ITS, where found clusters are combined to tracklets. The vertex is assumed to be positioned at the point in which most of these tracklets converge.
The track finding then starts for the TPC at the largest radii, where track densities are the lowest. The TPC has 159 pad rows so a maximum of 159 clusters can be found per track. Track seeds are once constructed with two clusters and the previously found vertex, later with three clusters and without the vertex constraint. Those seeds are tracked inwards searching for the closest cluster within a proximity cut and updating the track at each iteration. Double counting of tracks is prevented by algorithms based on the fraction of shared clusters. The track is corrected for the particle's loss of energy in the drift gas by making a preliminary particle identification based on the specific energy loss in the gas (PID hypothesis). Once track propagation reaches the inner boundary of the TPC they become seeds for the tracking procedure in the ITS.
The ITS tracking starts with the propagation of the TPC seeds to the outermost layer. They are propagated inward and are updated at each step. A penalty factor on the track quality accounts for missing clusters in the ITS. As it is the case in the TPC, tracking in the ITS is performed with and without vertex constraint and tracks are checked for cluster sharing.
Clusters that were not attributed to TPC tracks are used in a ITS stand alone track finding. As low p_T tracks can be stopped by the detector material before reaching the TPC, the ITS extends the p_T reach downwards to 80 MeV/c.
As soon as the reconstruction reaches the innermost layer tracks are extrapolated and the distance of closest approach (DCA) to the preliminary vertex is determined.
Next all tracks are refitted in outward direction updating the track and the PID at each step. Once the outer boundary of the TPC is reached the tracks are matched to tracklets found in the TRD as well to signals in TOF and further detectors like EMCal, PHOS and HMPID. Finally a last refit is performed in inward direction and reconstructed tracks are used to determine the final primary vertex. In addition the tracks are searched for displaced vertices originating from decays of strange particles and for cascade decays. Fig. 3.7 shows the vertex resolution in the left panel. The resolution increases for heavier systems as higher particle multiplicities lead to a better constrained vertex. The right panel shows the resolution in inverse transverse momentum, as deduced from the tracking covariance matrix. The inverse-p_T resolution is connected to the relative p_T resolution via $\sigma_{p_\mathrm{T}}/p_\mathrm{T} = p_\mathrm{T} \cdot \sigma_{1/p_\mathrm{T}}$.

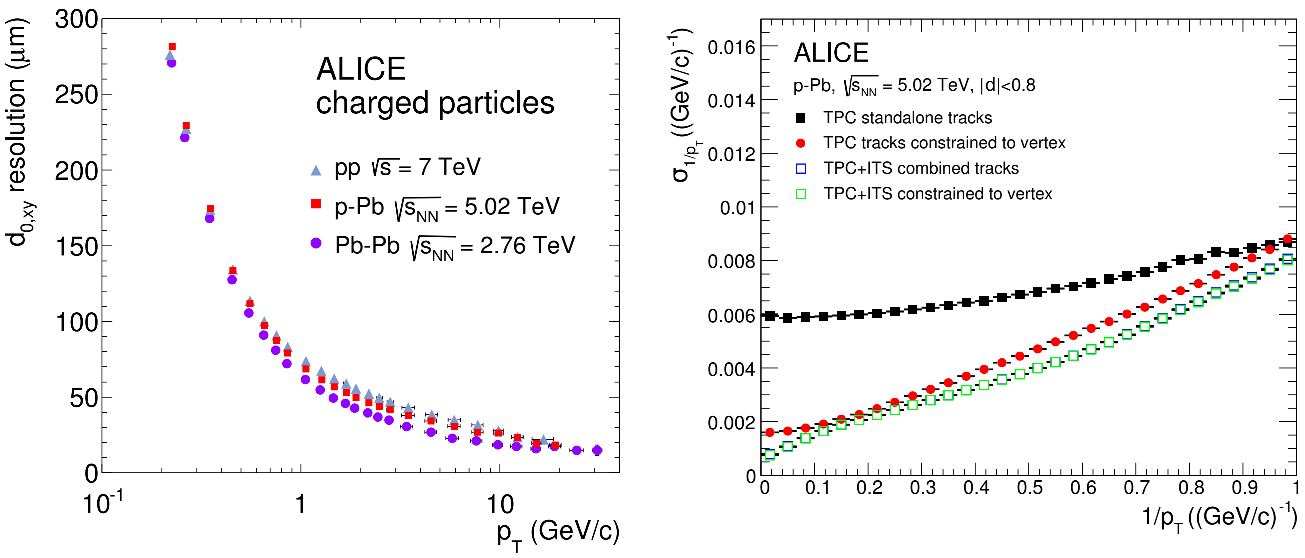

Figure 3.7.: Left: Resolution of the transverse distance to the primary vertex for all charged ITS–TPC tracks. Right: p_T resolution for standalone TPC and ITS–TPC matched tracks with and without constraint to the vertex [85].

3.3.1 Momentum Resolution

The transverse momentum is determined from the track radius $R = p_T/eB$. Here B is the magnetic field strength and p_T is the momentum component perpendicular to the magnetic field. This relation can be translated to [91]:

$$R = \frac{10}{3}\left(\frac{\mathrm{Tm}}{\mathrm{GeV}/c}\right)\frac{p_T}{B} \tag{3.1}$$

In this relation the transverse momentum p_T of the particle given in units of GeV/c and the magnetic field strength in T. A track with an momentum of 1 GeV/c perpendicular to the standard magnetic field of the L3 magnet ($B = 0.5\,\mathrm{T}$) therefore has an radius of $\sim 6.6\,\mathrm{m}$, which is already large compared to TPC's outer radius of $\sim 2.5\,\mathrm{m}$. Therefore it is more practical to calculate the momentum not by the track's radius, but by its sagitta, the maximum excursion of a piece of a circle over the corresponding chord $s = L^2/8R$ for $R >> L$.
The precision of the momentum-determination in the detector is constrained by two effects. At low p_T the multiple scattering of the particle itself in the detector material, and at high p_T by the finite spatial resolution within the detector. The spatial resolution is independent of the tracks momentum, but becomes significant at small values of the sagitta and thus higher momenta.

3.3.2 Space-Charge Distortions

With the change of the drift gas from Run 1 (Ne-CO_2-N_2) to Run 2 (Ar-CO_2) it was found that space charge was building up in the drift volume of the TPC. This leads to a distortion of the drift field, and therefore worsens the track reconstruction. These space charges are caused by ions that enter the drift volume. It was found that these ions originate from the gap in between the readout chambers, as the gating grid that prohibits ion backflow from within the amplification area is fully efficient. The amount of ions created increases with increasing interaction rate which results in larger distortions. As a consequence the charges are locally stable over longer periods of time which offers a possibility to correct for the distortion. It was also found, that space charges were already present during Run 1, though much smaller in magnitude. With the start of the data taking period in May 2017 the gas mixture used in Run 1 is used again and a reduction of distortions was observed while keeping the same interaction rate. A detailed description of the space-charges and their correction can be found in [86].

To correct the measured tracks for space-charge distortions a correction process based on the undistorted track hits in the TRD and ITS is used. This procedure is applied during the first reconstruction pass on special low multiplicity events and provides a correction map, that is itself applied to correct the tracks of all events, Figure 3.8 illustrates the procedure. In a first step a track finding similar to the standard procedure (section 3.3) but with relaxed tolerances on the track-to-cluster association in performed within the TPC. These TPC-tracks (blue) are used to find the corresponding hits within the ITS, TOF and TRD (red points).

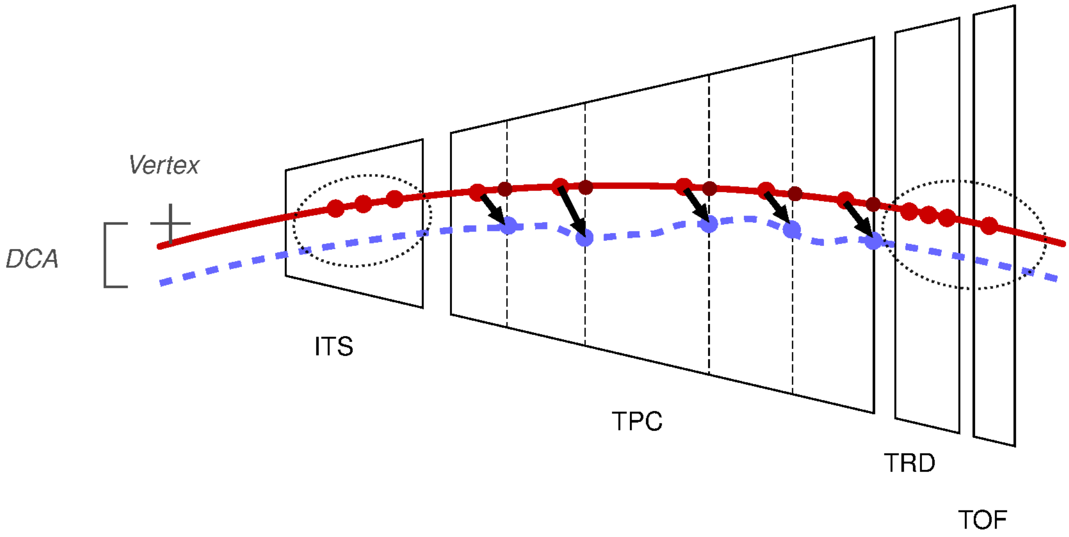

Figure 3.8.: Schematic view of a track passing through the detector's active area. The initial track (blue) is distorted within the TPC. Using ITS and TRD information the original track can be reconstructed (red) [86].

Next a track is constructed making use of only the information from these detectors (red), which is then used to estimate the undistorted track position along the pad rows (green). The difference between the distorted TPC-track and the estimated position based on the ITS-TRD-track is stored. After a clean up procedure these distortions are saved as a correction map, which is inverted and applied on the tracks of the following events. As the space charges fluctuate these procedure is repeated every 40 minutes. One way to verify the success of this method is by evaluating the distance of closed approach of a track to the vertex (DCA). The DCA for tracks with $p_{\mathrm{T}} > 2\,\mathrm{GeV}/c$ is shown in Figure 3.9, the DCA distribution of uncorrected tracks (blue) shows large deviations from zero which peaks at the sector boundaries. The distribution of the tracks after applying the correction maps are shown in red. It shows a clear improvement and demonstrates the success of the refitting procedure.

3.4 Differences Between Run 1 and Run 2

After the end of the first data-taking period (Run 1) in early 2013 the ALICE detector was maintained and improved. The LHC was also upgraded enabling the machine to deliver pp collisions at $\sqrt{s} = 13\,\mathrm{TeV}$ and Pb–Pb collisions at $\sqrt{s_{\mathrm{NN}}} = 5.02\,\mathrm{TeV}$, to achieve this a special focus lay on the performance of the magnets, that need to be operated with an increased electrical current.

On the detector a couple improvements were performed that influence the analysis. A large improvement was obtained by the repair of the SPD's cooling system. During Run 1 the performance of the SPD decreased as individual segments of the detector had to be turned off due to insufficient flow of the cooling liquid underneath the silicon pixels. The issue was found to be caused by the clogging of filters

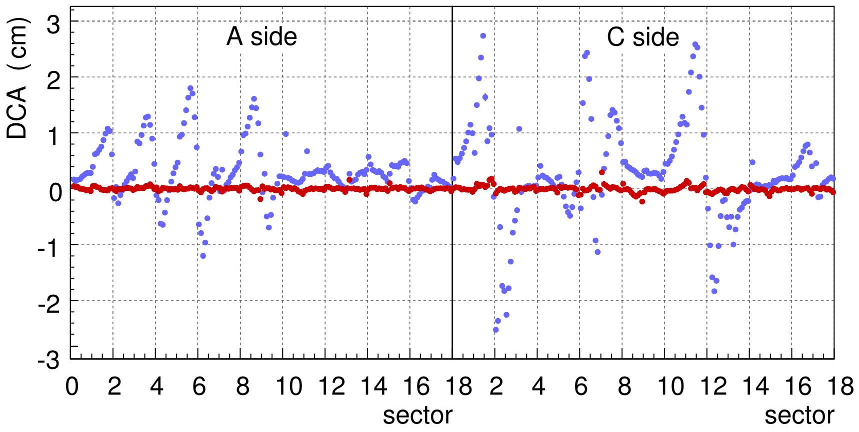

Figure 3.9.: The DCA for high-p_T tracks ($p_T > 2\,\mathrm{GeV}/c$) dependent on the sector measured in Pb-Pb at 4.5 kHz interaction rate. Results of reconstruction before (blue) and after (red) distortions correction described in the text are shown. Typically the distortions (large DCA) are the highest at the inner boundaries of the TPC. [86]

within the cooling system very close to the detector. The replacement of these filters was not feasible as all central-barrel detectors would have to be dismantled. Therefore the cooling pipes were freed using a drill, a challenging task, as the closest point of access was 4.5 m away from the clogged filters and the diameter of the cooling pipes is only 4 mm [92]. The cleaning proved to be successful and for Run 2 95% of the modules were fully performant.

Another major change was the change of the TPC detector gas from (Ne-CO_2-N_2) to (Ar-CO_2), that – in conjunction with an increased interaction rate – introduced the space-charge distortions described in section 3.3.2. The correction for the space-charge distortions is largely based on the transition-radiation detector (TRD) that is installed around the TPC and was fully installed during the shut-down that followed Run 1.

3.5 Centrality Determination

The collision's centrality is commonly described in terms of the percentage of the total geometric cross section. Typically events are classified by a centrality interval, in this analysis the most central class of collisions ranges from 0 to 5%. A detailed description of the centrality estimation is given in [57] with recent updates in [93]. Here only a short overview is given.

In ALICE, events are classified by their charged particle multiplicity in the V0 detectors (Figure 3.10, for V0 detectors see section 3.2.3). The method that proved to provide the most reliable signal is the combination from both V0 detectors, V0A and V0C, called V0M.

Centrality intervals are then defined by cuts in the V0M amplitude, shown in Figure 3.10 for Pb–Pb (left) and Xe–Xe (right).

The measured particle multiplicity is related to derived quantities such as the number of participating nucleons (N_{part}), the number of binary nucleon-nucleon collisions (N_{coll}) or the impact parameter (b) by a model calculation. Here a combination of a Glauber Monte Carlo simulation (see section 1.6) with a particle production model based on a non binomial distribution (NBD) is chosen.

The Glauber MC simulates the nuclei based on a Woods-Saxon potential with an radius of $R = (6.62 \pm 0.06)$ fm and a radius parameter $a = (0.546 \pm 0.010)$ fm for ^{208}Pb. The nucleons inside the nuclei are required to have an minimal hard-sphere exclusion distance of $d_{\mathrm{min}} = 0.4$ fm, so that no nucleons

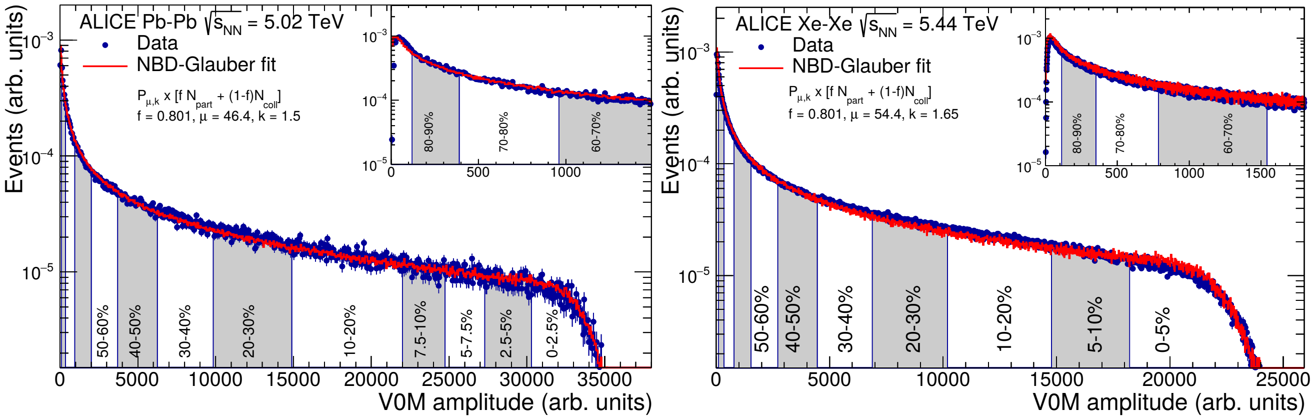

Figure 3.10.: The multiplicity distribution measured with the V0-detectors. The Glauber MC fit is shown as a red curve. The inset shows the distribution for peripheral collisions [93]

are closer than d_{min}. As this parameter is not known experimentally, it is varied within $\pm 0.4\,\text{fm}$ for the uncertainties. Collisions are then simulated by drawing a random impact parameter $0 \leq b \leq b_{\text{max}}$, where $b_{\text{max}} \simeq 20\,\text{fm} > 2R_{\text{Pb}}$. The maximum impact parameter is chosen such, that the probability of a collision becomes zero, if the distance between two nucleons of both nuclei becomes less than $d < \sigma_{\text{NN}}^{\text{inel}}/\pi$. Where $\sigma_{\text{NN}}^{\text{inel}}$ is the nucleon-nucleon cross-section typically estimated by interpolating pp-data and data from cosmic radiation at different collision energies. The cross-section chosen is $\sigma_{\text{NN}}^{\text{inel}} = 61.8 \pm 0.9\,\text{mb}$ for $\sqrt{s_{\text{NN}}} = 2.76\,\text{TeV}$, $\sigma_{\text{NN}}^{\text{inel}} = 67.6 \pm 0.6\,\text{mb}$ for $\sqrt{s_{\text{NN}}} = 5.02\,\text{TeV}$ and $\sigma_{\text{NN}}^{\text{inel}} = 68.4 \pm 0.5\,\text{mb}$ for Xe–Xe.
The charged particle multiplicity is simulated based on a negative binomial distribution $P_{\mu,k}(n)$ with a mean of μ and a width of k. The model assumes that the particle production originates from the so called ancestors, the number of ancestors in a collision is calculated from $N_{\text{ancestors}} = f N_{\text{part}} + (1-f) N_{\text{coll}}$ where soft interactions scale with N_{part} while the amount of hard interactions is realted to N_{coll}. Besides f the other free parameters are the parameters of the NBD, μ and k. This distribution is sampled $N_{\text{ancestors}}$ times for each simulated event in order to obtain the simulated V0M amplitude (Figure 3.10). A minimization procedure is applied in order to find the set of parameters that fit the measured distribution best.
In heavy-ion collisions at LHC energies the cross section for electromagnetic processes is very high, and thus the distribution of V0M amplitude is contaminated with events without hadronic interaction. Events with only electromagnetic processes however produce only very small multiplicities compared to events with hadronic interactions, consequently the contamination is present only at low V0M amplitude. In the same multiplicity range trigger inefficiencies and beam gas collisions can affect the analysis as well. As the Glauber MC only simulates hadronic interactions this effect can be judged by the agreement of simulation and data at low multiplicity. The effect of this background can be neglected for centralities in the range of 0–90%. The centrality classes are then defined by hard cuts on the simulated V0M amplitude in the range between 0–90%. In the determination of centrality this upper bound is referred to as the anchor point. The values of $\langle N_{\text{coll}} \rangle$, $\langle N_{\text{part}} \rangle$ as well as $\langle T_{\text{PbPb}} \rangle$ [93] are shown in Table 3.1.

Pb–Pb $\sqrt{s_{\mathrm{NN}}} = 2.76\,\mathrm{TeV}$

Centrality	$\langle N_{\mathrm{part}} \rangle$	$\langle N_{\mathrm{coll}} \rangle$	$\langle T_{\mathrm{PbPb}} \rangle$ [mb^{-1}]
0–5%	381.3 ± 1.3	1628 ± 71	26.35 ± 0.98
5–10%	329.2 ± 3.1	1276 ± 55	20.64 ± 0.77
10–20%	260.1 ± 1.8	897 ± 35	14.51 ± 0.49
20–30%	185.8 ± 2.0	543.7 ± 22	8.797 ± 0.32
30–40%	128.5 ± 1.7	313.3 ± 12	5.069 ± 0.18
40–50%	85.03 ± 1.4	168.5 ± 5.9	2.726 ± 0.09
50–60%	52.69 ± 1.3	83.1 ± 3.8	1.345 ± 0.058
60–70%	29.88 ± 1.1	37.13 ± 2.2	0.6008 ± 0.034
70–80%	15.13 ± 0.71	14.96 ± 0.9	0.242 ± 0.015

Pb–Pb $\sqrt{s_{\mathrm{NN}}} = 5.02\,\mathrm{TeV}$

Centrality	$\langle N_{\mathrm{part}} \rangle$	$\langle N_{\mathrm{coll}} \rangle$	$\langle T_{\mathrm{PbPb}} \rangle$ [mb^{-1}]
0–5%	383.6 ± 1.6	1777 ± 59	26.29 ± 0.81
5–10%	332.3 ± 2.4	1389 ± 50	20.55 ± 0.7
10–20%	263.0 ± 2.8	973.4 ± 37	14.4 ± 0.52
20–30%	188.2 ± 2.3	586.4 ± 20	8.675 ± 0.28
30–40%	130.7 ± 1.9	336.7 ± 12	4.98 ± 0.17
40–50%	86.51 ± 1.9	179.8 ± 7.1	2.659 ± 0.11
50–60%	53.77 ± 1.2	88.22 ± 3.1	1.305 ± 0.49
60–70%	30.51 ± 0.74	39.08 ± 1.6	0.5781 ± 0.025
70–80%	15.43 ± 0.49	15.57 ± 0.62	0.2303 ± 0.0096

Xe–Xe $\sqrt{s_{\mathrm{NN}}} = 5.44\,\mathrm{TeV}$

Centrality	$\langle N_{\mathrm{part}} \rangle$	$\langle N_{\mathrm{coll}} \rangle$	$\langle T_{\mathrm{XeXe}} \rangle$ [mb^{-1}]
0–5%	235.8 ± 1.5	948.9 ± 53	13.87 ± 0.78
5–10%	206.7 ± 1.8	737.3 ± 46	10.78 ± 0.67
10–20%	164.8 ± 2.0	510.6 ± 26	7.465 ± 0.52
20–30%	118.4 ± 2.7	302.8 ± 28	4.426 ± 0.42
30–40%	82.21 ± 2.8	171.3 ± 19	2.505 ± 0.28
40–50%	54.56 ± 2.5	91.81 ± 11	1.342 ± 0.17
50–60%	34.06 ± 2.1	46.04 ± 6.2	0.6731 ± 0.091
60–70%	19.72 ± 1.5	21.65 ± 2.9	0.3166 ± 0.043
70–80%	10.5 ± 0.78	9.515 ± 1.1	0.1391 ± 0.017

p–Pb $\sqrt{s_{\mathrm{NN}}} = 5.02\,\mathrm{TeV}$

Centrality	$\langle N_{\mathrm{part}} \rangle$	$\langle N_{\mathrm{coll}} \rangle$	$\langle T_{\mathrm{pPb}} \rangle$ [mb^{-1}]
0–100%	7.9 ± 0.6	6.9 ± 0.7	0.0983 ± 0.035

Table 3.1.: The mean N_{part}, N_{coll} and T_{AA} values for nine centrality classes of inelastic Pb–Pb and for minimum bias p–Pb collisions at $\sqrt{s_{\mathrm{NN}}} = 5.02\,\mathrm{TeV}$. The values and their uncertainties are obtained from Glauber Monte Carlo model calculations [93, 94].

4 Analysis

In the course of this thesis three different data sets have been analysed, the focus of the work however lies on the analysis of collisions of lead nuclei (^{208}Pb) at a collision energy of $\sqrt{s_{\rm NN}} = 5.02\,\text{TeV}$ that have been delivered by the LHC in November 2015. Even though the analysis methods presented in this chapter have been employed in previous publications [52,62,68,95,96] their quality has been improved resulting in a significant reduction of the systematic uncertainties. These improvements were first applied to the analysis of Pb–Pb at $\sqrt{s_{\rm NN}} = 5.02\,\text{TeV}$, that in turn required a reanalysis of the dataset of Pb–Pb collisions with a centre-of-mass energy of $\sqrt{s_{\rm NN}} = 2.76\,\text{TeV}$ recorded and published in 2010 [62, 95].
In 2017 the LHC was filled for the first time with xenon ions (^{129}Xe) and delivered collisions at $\sqrt{s_{\rm NN}} = 5.44\,\text{TeV}$ for a few hours. The following chapter focuses on the analysis of Pb–Pb collisions at $\sqrt{s_{\rm NN}} = 5.02\,\text{TeV}$. When necessary, differences to the other systems are pointed out, supporting figures can be found in appendix B.

4.1 Trigger

All of the data were taken with the minimum-bias (MB) trigger . It uses signals from the forward scintillator arrays (V0A and V0C), as well as the signal from the Silicon Pixel Detector (SPD). These signals are requested to be in coincidence with the bunch crossing at the ALICE interaction point. Collisions of lead ions at $\sqrt{s_{\rm NN}} = 2.76\,\text{TeV}$ were recorded in 2010. For these collisions triggering was performed by different combinations of hits in the SPD and V0C or V0A detector. All of these trigger scenarios however are fully efficient for the centrality range considered (0-80%), for details see [85]. For the measurements of Pb–Pb at $\sqrt{s_{\rm NN}} = 5.02\,\text{TeV}$ and Xe–Xe $\sqrt{s_{\rm NN}} = 5.44\,\text{TeV}$ these conditions were tightened to demand a signal in both V0A and V0C detectors.
In addition the offline event selection rejects beam induced backgroud as well as electromagnetic interactions. For this the timing signals of the V0A and V0C detectors are used. In addition timing signals in the ZDC detectors was used to reject electromagnetic contamination.

4.2 Simulation Tools

To correct the measurement for detector effects Monte-Carlo simulations are employed. To simulate the collision events the HIJING [97] event generator is used. HIJING models the nuclear geometry and follows the PYTHIA [98] model to simulate nucleon-nucleon interaction and the fragmentation process. It includes a schematic model of energy loss, but does not incorporate any model for final state interactions and hence does not reproduce any collective phenomena.
The particles of the simulated event are then propagated through a representation of the full ALICE detector, modeling the evolution of the particles and the detector response at each step using GEANT [99]. The simulated detector response is the used as input to the full ALICE reconstruction process as described in section 3.3.

4.3 Event Selection

To ensure uniform acceptance and reconstruction efficiency within the limited acceptance in pseudorapidity for tracks of $|\eta| < 0.8$, only events with a vertex position Z_v within ± 10 cm from the nominal interaction point ($Z_v = 0$) along the beam pipe are accepted, the vertex distribution of events and the η-distribution of single tracks is shown in Figure 4.1.

The primary event vertex is determined by tracks from the central barrel. The vertex is determined during reconstruction, once using the fully reconstructed tracks and once using only SPD tracklets (section 3.3). A few standard vertex cuts are applied on the Z_v^{SPD} reconstruction resolution, which is required to be better than 0.25 cm. Also the difference between track and SPD vertex needs to be $|Z_v^{\mathrm{Track}} - Z_v^{\mathrm{SPD}}| < 0.5$ cm. Events are characterised for their collision centrality based on the combined signal in the V0A and V0C detector (see section 3.5). Figure 4.2 shows the number of events in every class of centrality demonstrating the uniformity of the centrality selection up to the centrality of 80%. The total amount of events accepted for the three data samples is shown in Table 4.1.

	Events (Mio.)		
	Pb–Pb		Xe–Xe
$\sqrt{s_{\mathrm{NN}}}$	5.02 TeV	2.76 TeV	5.44 TeV
Before offline event selection	37.15	31.13	1.54
After Z_v-cut and within 0-80%	19.97	13.18	1.1

Table 4.1.: Number of events within $|Z_v| < 10$ cm and requiring a valid centrality.

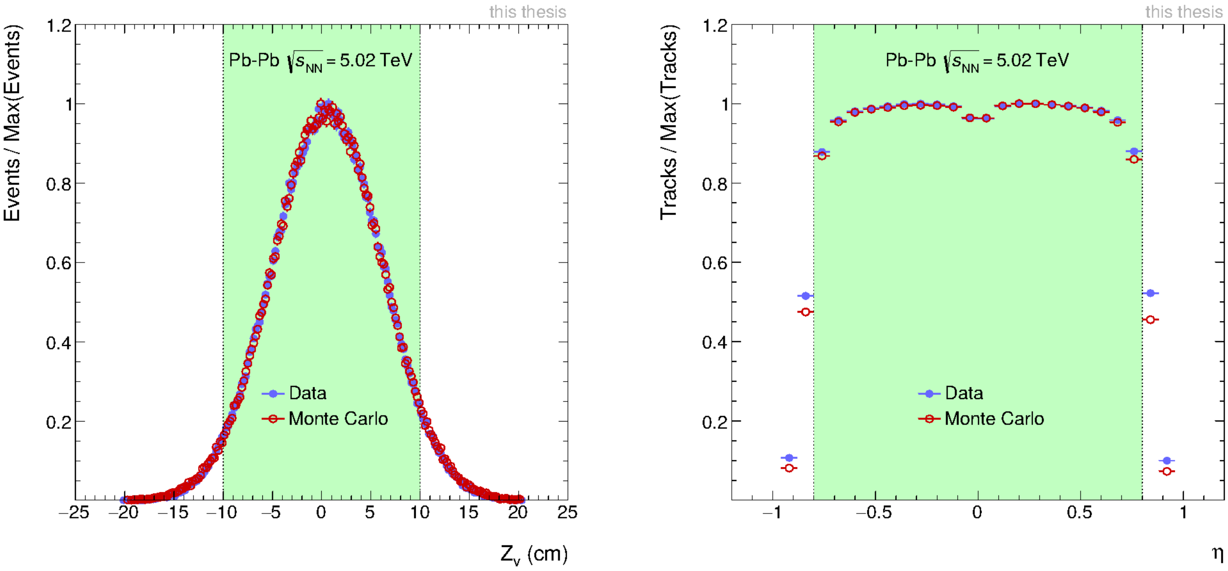

Figure 4.1.: The allocation of the primary event-vertex along the z-Axis (left), and distribution of track pseudorapidity (right). The accepted range is highlighted in green.

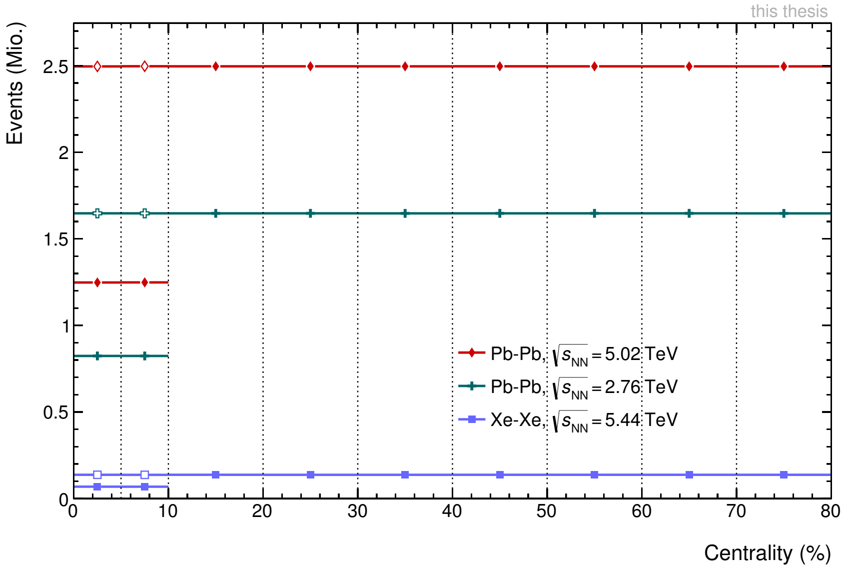

Figure 4.2.: Number of events per bin of centrality. Open symbols show the event count scaled by a factor of two to account for smaller bin width.

4.4 Definition of Primaries

In ALICE, a common definition of primary particles is used. It requires a particle to have a minimal lifetime long enough to be detectable by the detectors. The mean proper lifetime τ needs to be larger than $\tau_0 = 1\,\mathrm{cm}/c$. The mean proper lifetime of a particle species is the mean life time in the restframe of that particle. The value of τ_0 is motivated by the detector's capability to differentiate if a particle was created in the primary interaction or is the result of the decay of a particle with a lifetime shorter than τ_0. The common definition reads as follows [100]:

> *A primary particle is a particle with a mean proper lifetime τ larger than $1\,\mathrm{cm}/c$, which is either a) produced directly in the interaction, or b) from decays of particles with τ smaller than $1\,\mathrm{cm}/c$, restricted to decay chains leading to the interaction.*

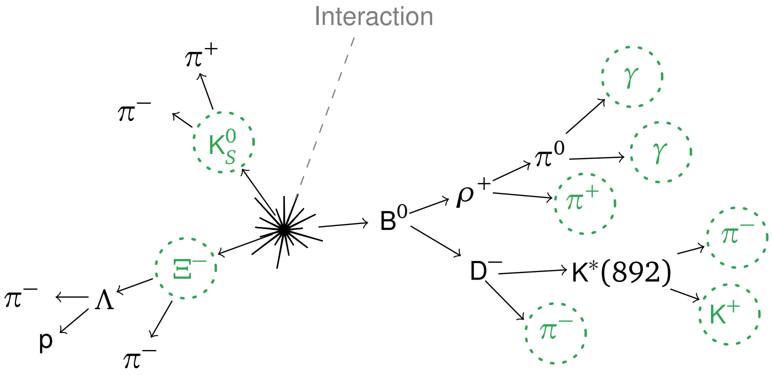

Figure 4.3.: Various decays. Particles defined as primaries are marked with circles. In both the Ξ^- and K_S decays, the initial particles are considered primary, since these particles are long-lived, while all the decay products are not considered primaries. In the B^0 decay chain, the π's, γ's, and the K^+ are all primary since they are the first long-lived particle in the decay chain leading back to the interaction. Figure and caption from [100].

Particles that are not primaries according to this definition are commonly denoted as secondaries. Apart from the decays of long lived ($\tau > 1\,\mathrm{cm}/\mathrm{c}$) particles, the interaction with detector material is a common source for such secondary particles. An illustration of different decays and the clasification of the resulting particles is given in Figure 4.3. In a previous version of a common ALICE definition, primary particles were defined as prompt particles produced in the collision, including decay products, except those from weak decays of strange particles. With the exception of the decay daughters of $\pi^{\pm}$ and $\mu^{\pm}$ (which rarely decay within in the ALICE acceptance) this definition is equivalent to the common definition quoted above.

4.5 Track Selection

The track selection is optimized for best track quality and small contamination from secondary particles while retaining a large efficiency for primary particles. Tracks are measured in the kinematic range $|\eta| < 0.8$ and $0.15 < p_{\mathrm{T}} < 50\,\mathrm{GeV}/c$. As in a heavy-ion (and pp as well) collision most particles are produced with $p_{\mathrm{T}} < 3\,\mathrm{GeV}/c$, quality can be favoured above quantity at low p_{T}, as their abundance is high. Due to an insufficient description of track variables in the Monte Carlo (MC) simulation the track selection contributes to the systematic uncertainties. Therefore selection criteria with a good MC description are favoured.

The track selection criteria, often called track cuts, are summarized in Table 4.2 for Pb–Pb collisions. (The distribution of the variables is compiled in appendix D.) The dataset of Xe–Xe collisions was taken with a reduced field strength of the main ALICE solenoid. This results in a modified track curvature for a given p_{T} and therefore cuts dependent on p_{T} are adjusted.

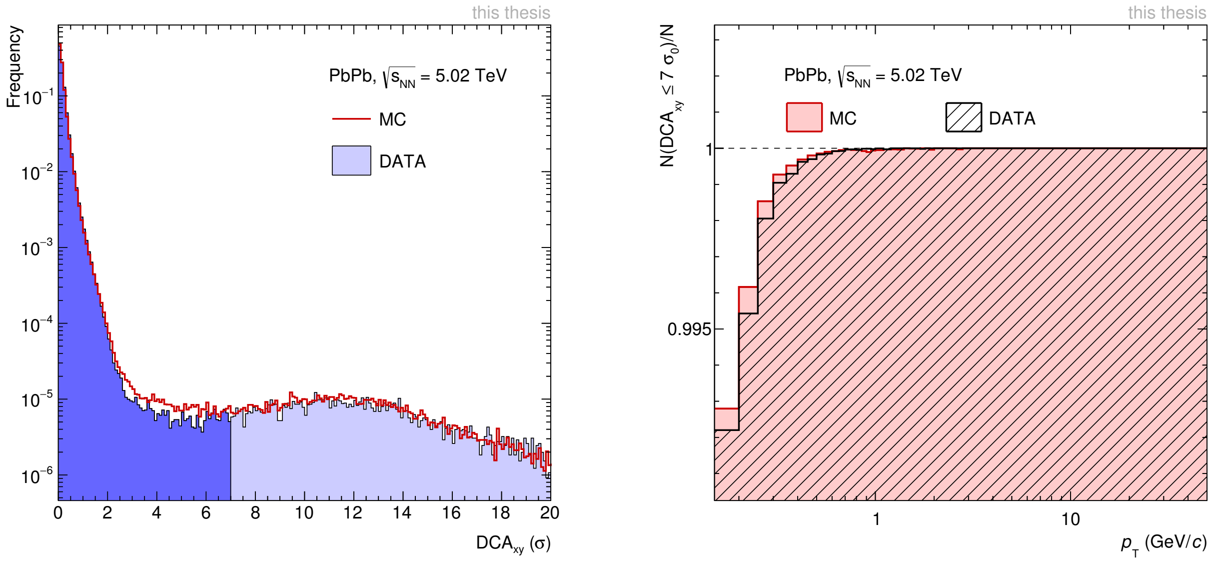

Figure 4.4.: The distribution of the track's distance of closest approach to the primary vertex in radial direction, DCA$_{xy}$ (left) and the impact of the cut on data and Monte Carlo (MC) simulation (right). The area highlighted in dark blue indicates the tracks passing this selection.

ITS Selection

The selection criteria applied on the ITS variables of the tracking mostly focus on achieving a good DCA resolution as well as a good p_{T}-resolution. This is accomplished by demanding at least one hit in the two inner layers of ITS, which have the best spatial resolution and are located close to the interaction point.

ITS Cuts		
DCA along z-axis	$\mathrm{DCA_z}$	$\leq 2\,\mathrm{cm}$
DCA in radial direction*	$\mathrm{DCA_{xy}}$	$\leq 7 \cdot \sigma_0$
χ^2 per ITS cluster	χ^2_{ITS}	≤ 36
ITS refit required		True
Require hit in the SPD		True
TPC Cuts		
Minimum length in active volume	L_{active}	130 cm
$1/p_{\mathrm{T}}$ dependence slope*	α_{slope}	1.5
Width of the exclusion zone	$W_{\mathrm{dead\text{-}zone}}$	3 cm
Minimum number of crossed rows	n_{rows}	$0.85\,L_{\mathrm{active}}$
Minimum number of TPC cluster	n_{cluster}	$0.7\,L_{\mathrm{active}}$
Crossed rows over findable cluster	$n_{\mathrm{rows}}/n_{\mathrm{findable}}$	≥ 0.8
Fraction of shared TPC clusters	$n_{\mathrm{shared}}/n_{\mathrm{cluster}}$	≤ 0.4
χ^2 per TPC cluster	χ^2_{TPC}	≤ 4
Reject kink daughters		True
TPC refit required		True
TPC-ITS Cuts		
χ^2 TPC constrained track vs. global track	$\chi^2_{\mathrm{TPC\text{-}ITS}}$	≤ 36

Table 4.2.: An overview of the track selection criteria used in the analysis. The criteria are not modified for different collision energies, however those marked by a star (*) had to be modified for the analysis of Xe–Xe collisions due to a reduced magnetic field strength.

Tracks are required to be part of the third track fitting and are rejected if the χ^2 per ITS cluster exceeds 36.

DCA Selection

On of the goals of the track selection is to achieve a high purity of primary particles in the selected sample. In this analysis selecting on the distance of track's closest approach to the vertex (DCA) is used to reduce the amount of contamination with secondary particles. Those originate primarily from the weak decay of strange particles and from particle interaction with the detector material and therefore the track is not related with the primary vertex resulting in a larger DCA. Two different DCA criteria are employed.

In the direction along the beam pipe ($\mathrm{DCA_z}$) is required to be less than 2 cm which is not very restrictive, while the cut on the DCA in radial direction is more restrictive and p_{T} dependent $\mathrm{DCA_{xy}}(p_{\mathrm{T}}) \leq 7\sigma_0(p_{\mathrm{T}})$. Here $\sigma_0(p_{\mathrm{T}}) = (26 + 50/(p_{\mathrm{T}} \text{ in } \mathrm{GeV}/c)^{1.01})\mu\mathrm{m}$ is an approximation for the standard deviation of the impact parameter resolution. For $\mathrm{B} = 0.2\,\mathrm{T}$ the standard deviation is estimated by $\sigma_0(p_{\mathrm{T}}) = (17 + 70/(p_{\mathrm{T}} \text{ in } \mathrm{GeV}/c)^{1.01})\mu\mathrm{m}$.

The cut becomes more and more restrictive towards high p_{T}, as the vertex resolution increases ($\mathrm{DCA_{xy}}(0.15\,\mathrm{GeV}/c) \leq 0.26\,\mathrm{cm}$, $\mathrm{DCA_{xy}}(1\,\mathrm{GeV}/c) \leq 0.05\,\mathrm{cm}$, $\mathrm{DCA_{xy}}(50\,\mathrm{GeV}/c) \leq 0.019\,\mathrm{cm}$ for Pb–Pb).

Geometric Length Selection

It is known that reconstruction efficiency of tracks in the TPC decreases at the edges of the TPC segments. This effect leads to an increase in the systematic uncertainty at intermediate transverse momentum ($p_{\mathrm{T}} \approx 1\,\mathrm{GeV}/c$ for $\mathrm{B} = 0.5\,\mathrm{T}$), as in this p_{T} range the curvature of the tracks means that a large fraction of the track length lies in between the sector boundaries. As tracks are not measured in between the sectors and as the measurement is less precise in the border regions, the overall track quality is reduced.

Therefore a new track cut based on the track's length in the TPC's active read-out area (L_{active}) was introduced. The parameters of this criterion allow for the definition of dead-area's width around the sector boundaries ($W_{\text{dead-zone}}$). The track length is calculated as the projection on the radial direction of the TPC. The maximum length a track can pass through the TPC is 160 cm. Most tracks achieve more than 140 cm as shown in Figure 4.5 left. To account for shorter track length at low p_{T} a p_{T}-dependent modification is applied $L^{\text{eff}}_{\text{active}}(p_{\text{T}}) = L^{\text{cut}}_{\text{active}} - |1/p_{\text{T}}|^{\alpha_{\text{slope}}}$. Tracks are accepted if $L_{\text{active}} > L^{\text{eff}}_{\text{active}}(p_{\text{T}})$. For the reduced magnetic field strength the slope dependence is changed to $\alpha_{\text{slope}} = 0.7$. In Figure 4.5 the affected momentum range can be seen. As the length in the active region of the TPC is determined based on geometrical considerations alone, the behaviour of the selection criteria can be simulated very well and uncertainties thus are very small.

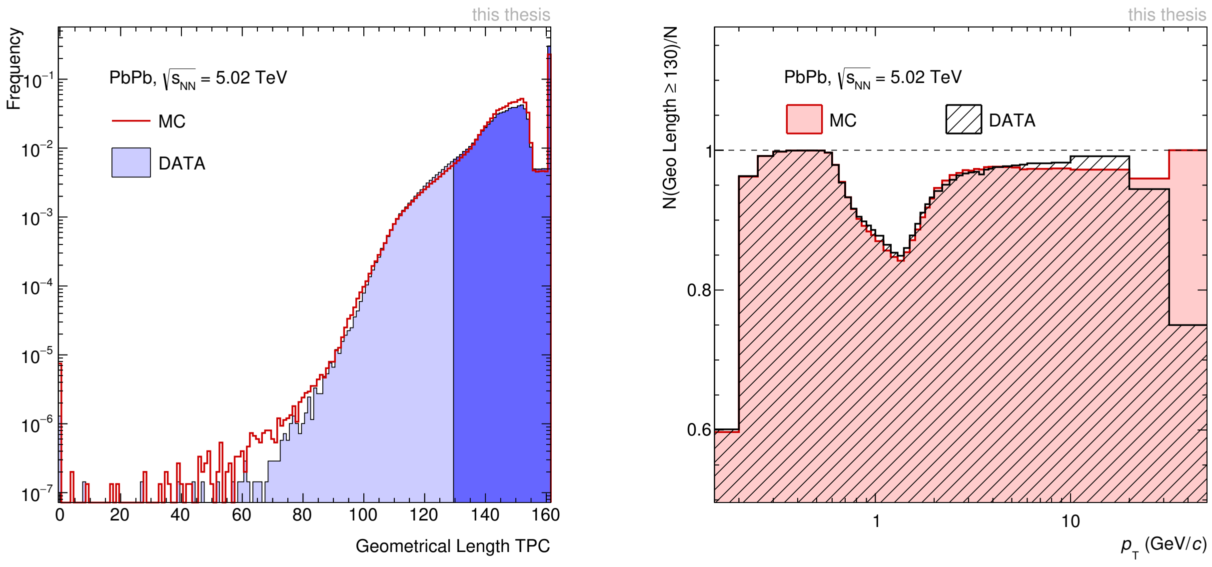

Figure 4.5.: The distribution of the track's length in the active volume (left). Note that most tracks go through the full TPC end are classified as tracks with $L_{\text{active}} = 160$ cm. The effect of this cut is the largest at $p_{\text{T}} \sim 1$ GeV/c as seen in the right figure.

Further TPC Selection Criteria

In addition to the selection on the length, a minimum number of crossed read-out rows (n_{rows}) is required (a maximum of 159 pad rows can be crossed). A read-out row counts as crossed, if a cluster was found in the pad row, or in the neighbouring two rows. This measure is applied as it accounts for missing clusters (with a sub-threshold signal). The minimal number of crossed rows required is set as $n_{\text{rows}} > 0.85 \cdot L^{\text{eff}}_{\text{active}}(p_{\text{T}})$. A minimum number of clusters found is required, it is set to $n_{\text{cluster}} > 0.7 \cdot L^{\text{eff}}_{\text{active}}(p_{\text{T}})$. The number of findable clusters n_{findable} is calculated from track properties, based on the maximal number of possible clusters, taking into account geometrical effects of dead read-out areas. The fraction of crossed rows to findable clusters is required to be at least 0.8.

Fake tracks, or tracks that are reconstructed multiple times, can be removed by requiring a maximum fraction of shared clusters over all clusters ($n_{\text{shared}}/n_{\text{cluster}}$). While n_{cluster} it the cluster count taken into account in the track fitting, n_{shared} counts all clusters assigned to more than one track. As not all clusters assigned to a track have to be taken into account for the fitting, the fraction of shared clusters can be larger than unity.

A minimal track quality is secured by requiring the TPC refit and by rejecting tracks with a $\chi^2_{\text{TPC}} \leq 4$.

Selection on $\chi^2_{\text{TPC-ITS}}$

One of the most sophisticated selection criteria is based upon the $\chi^2_{\text{TPC-ITS}}$, which is calculated from the five track parameters, taking into account their uncertainites. It removes tracks based on the difference between the χ^2 of the TPC track constrained to the primary vertex and the χ^2 of the global track. Its main purpose is to remove tracks with wrongly assigned ITS clusters or that scatter in the detector material between ITS and TPC.

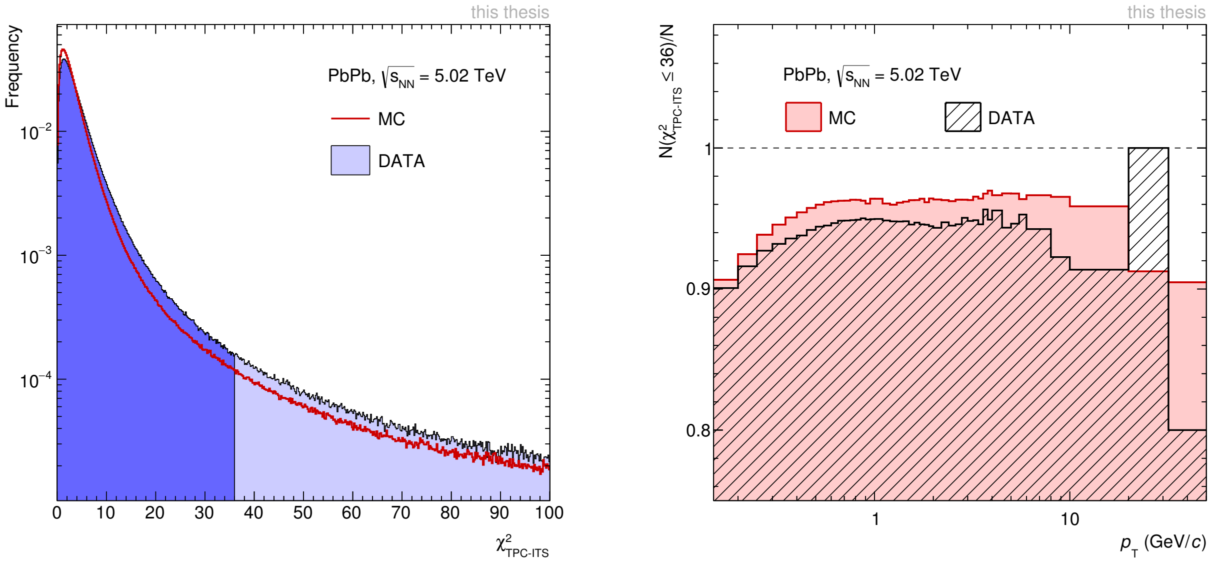

Figure 4.6.: The distribution of the track $\chi^2_{\text{TPC-ITS}}$ (left). For this cut the agreement of data and MC is worse than for other cuts.

4.6 Corrections

After track and event selection an uncorrected (raw) transverse-momentum distribution $y_{\text{raw}}(p_{\text{T}}, \eta)$ is obtained. This needs to be corrected for detector effects.

$$\begin{aligned} y_{\text{corrected}}(p_{\text{T}}, \eta) = & \times C_{\text{Acceptance}\times\text{efficiency}}(p_{\text{T}}) \cdot \alpha_{\text{Composition}}(p_{\text{T}}) \\ & \times (1 - C_{\text{Secondaries}}(p_{\text{T}}) \cdot \alpha_{\text{Sec.scaling}}(p_{\text{T}})) \\ & \times C_{p_{\text{T}}\text{-Resolution}}(p_{\text{T}}) \\ & \times y_{\text{raw}}(p_{\text{T}}, \eta) \end{aligned} \tag{4.1}$$

Three major corrections are applied to the raw spectra, first a correction for tracking inefficiency and holes it the detectors acceptance ($C_{\text{Acceptance}\times\text{efficiency}}$) is applied. Secondly secondary particles contaminating the spectra ($C_{\text{Secondaries}}$) are subtracted, this correction mainly effects the low-p_{T} range of the spectrum up to 2 GeV/c. The last correction is on the finite resolution of transverse momentum in the detector, that in conjunction with a steeply falling spectrum leads to an excess of high p_{T} tracks. While the p_{T}-resolution correction ($C_{p_{\text{T}}\text{-Resolution}}$) is based on data, the other two corrections are estimated by Monte-Carlo simulations. As simulation is not a fully correct reflection of the reality, the MC based corrections are matched to data. From this comparison reweighting factors ($\alpha_{\text{Composition}}$ and $\alpha_{\text{Sec.scaling}}$) are obtained that are applied to the corrections.

The correction for track loss caused by limited acceptance or tracking inefficiency is shown in Figure 4.7 left for both Pb–Pb datasets. The p_T-shape is generated by different effects: At low p_T the lower efficiency is caused by the strong curvature of tracks in the magnetic field and to the energy loss in the detector material. At intermediate p_T, the characteristic drop in efficiency around 1 GeV/c is caused primarily by the requirement of a minimal track length (L_{active}). At high p_T, the efficiency reaches a plateau, which resembles the maximal efficiency, before deceasing for even higher p_T. It has been suggested that this is related to jet structures, where tracks with a high p_T are produced as a part of a jet. The increased track density within the jet would lead to an reduced tracking efficiency.
The difference between efficiencies at $\sqrt{s_{\text{NN}}} = 5.02$ TeV and 2.76 TeV is caused by inactive channels in the SPD during Run 1 (compare section 3.4).

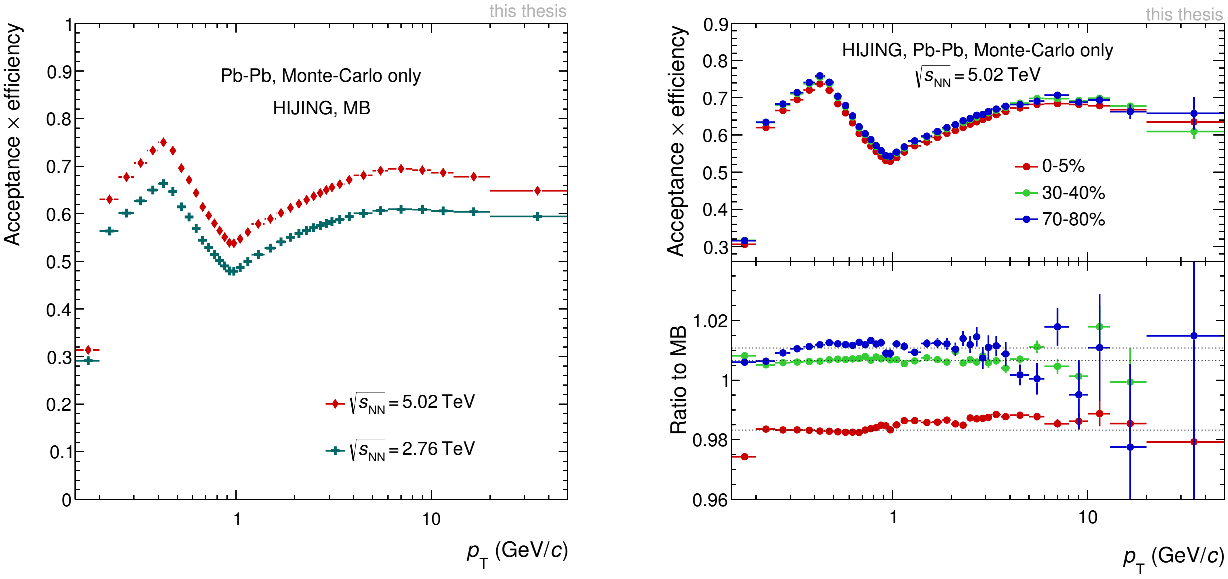

Figure 4.7.: The correction for acceptance and tracking inefficiency in Pb–Pb. The left figure shows the efficiency for the two different collision energies. The figure on the right shows the efficiency in dependence on the collision centrality (top panel) and their ratio to MB collisions (lower panel). Both figures show the efficiency without any data driven reweighting procedure applied.

Tracking Efficiency as a Function of Centrality

The ALICE detector is designed for high multiplicity, which results in an only small modification of the efficiency with centrality. Only for the most central collisions does the tracking efficiency deviate by more than 1% from the efficiency with no centrality selection applied. This is displayed in Figure 4.7. In order to reduce statistical fluctuation at high p_T, the efficiency from MB is scaled by a constant factor estimated from the ratio shown in the lower panel of Figure 4.7, the values are displayed in Table 4.3.

Centrality	0-5%	5-10%	10-20%	20-30%	30-40%
Ratio to MB	0.983	0.995	1.000	1.004	1.007
Centrality	40-50%	50-60%	60-70%	70-80%	
Ratio to MB	1.009	1.010	1.011	1.011	

Table 4.3.: The Ratios of centrality selected tracking efficiency to MB for Pb–Pb collisions at $\sqrt{s_{\text{NN}}} = 5.02$ TeV.

Particle Dependent Efficiency

Due to different lifetimes, different particle species have a different tracking efficiency. While pions ($\pi^\pm$) that dominate the charged particle spectrum have a lifetime of $c\tau_\pi = 7.8\,\mathrm{m}$ and thus rarely decay within the detector, kaons ($\mathrm{K}^\pm$) have a lifetime of $c\tau_\mathrm{K} = 3.7\,\mathrm{m}$ and therefore decay more frequently inside the detector. Track selection however discards tracks that are too short, so only kaons with an high enough momentum are tracked. The strongest deviation however is observed for strange hyperons. The lightest hyperons Σ^+ and Σ^- as well as their antiparticles have a very short decay length of only $c\tau_{\Sigma^+} = 2.4\,\mathrm{cm}$, $c\tau_{\Sigma^-} = 4.4\,\mathrm{cm}$. Therefore they are only tracked at $p_\mathrm{T} > 10\,\mathrm{GeV}/c$, albeit with low efficiency. Acceptance × efficiency for different particles is shown in Figure 4.8 (left).

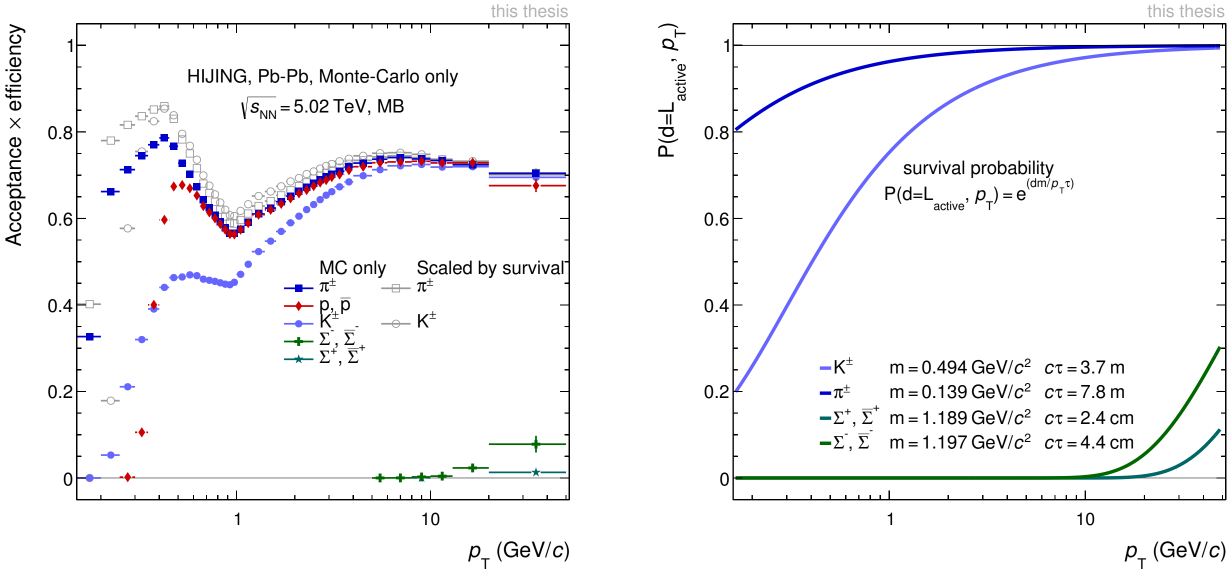

Figure 4.8.: The particle type dependent tracking efficiency (left) and the survival probability (right). The efficiencies for pions and kaons are shown scaled by the survival probability (open grey symbols) and unscaled (filled, coloured symbols).

To disentangle the different effects that influence the particle species dependent tracking efficiency one best investigates the probability of a particle reaching the outer boundaries of the TPC. The probability P that a particle with the mass m, a lifetime of τ and a transverse momentum p_T reaches the distance d before decaying is:

$$P(d, p_\mathrm{T}) = e^{-\frac{d \cdot m}{p_\mathrm{T} \cdot \tau}} \tag{4.2}$$

This survival probability is shown for different particle types in Figure 4.8 (right) for a distance $d = L_\mathrm{active}$. The left figure shows the tracking efficiency for pions and kaons scaled by their respective survival probability, indicated by the open grey symbols. While the tracking efficiency for pions and kaons differs much, the scaled tracking efficiencies are close. At high p_T the efficiencies for all particles but the strange hyperons overlap. The remaining differences result from differences of specific energy-loss in the detector gas, as well as different absorption in the detector material.

4.6.2 Particle Composition Correction

As the tracking efficiency is dependent on the particle type, the relative abundances of particle species plays an important role in the overall performance of the simulation. Fractions of the most abundant particles are shown in Figure 4.9. The relative abundances simulated by HIJING are dominated by pions,

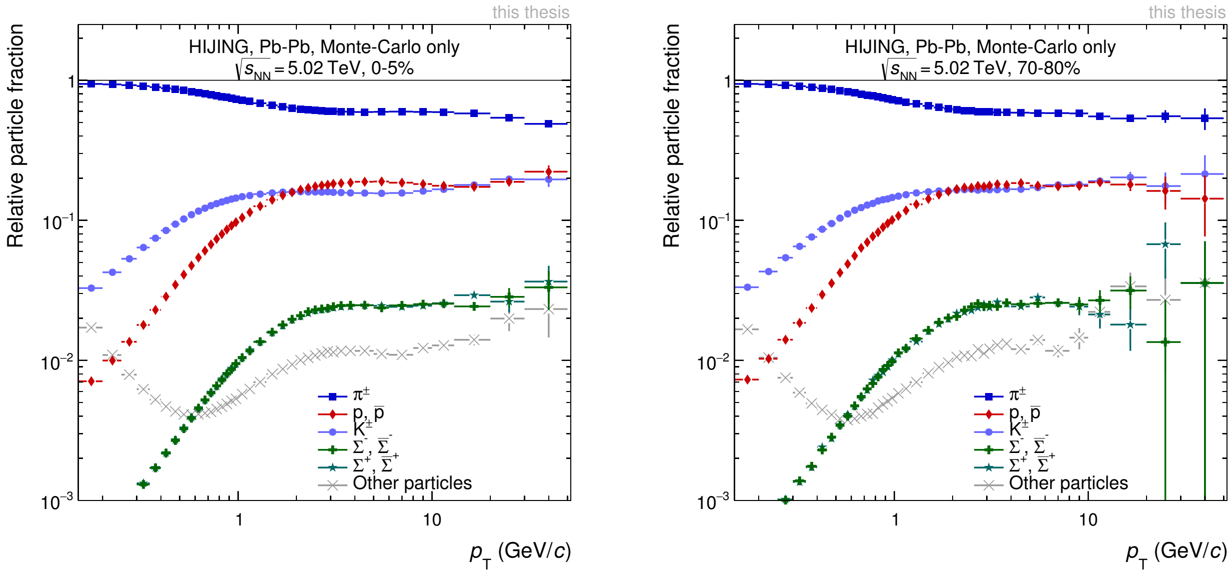

Figure 4.9.: Relative particle fractions for the most abundant particle species as generated by HIJING for central (left) and peripheral (right) collisions.

at low p_T. Other contributions are very small, while their contribution rises until a plateau is reached at $p_T \sim 2\,\mathrm{GeV}/c$. At high p_T, p, $\bar{p}$ and $K^{\pm}$ contribute with about 10-20%, while $\Sigma^{+}, \bar{\Sigma}^{-}$ and $\Sigma^{-}, \bar{\Sigma}^{+}$ amount up to 2-3%.

The influence of centrality on the simulated particle fractions is only small.

Relative Particle Abundances from Data

It has been observed that the event generators produce different relative abundances of particle species. In contrast to previous analyses of charged particle spectra this analysis benefits from the measurement of various identified particle spectra [67, 101, 102]. To compare the measured identified particle distributions with the relative abundances generated by the event generators the measurement needs to be extended to the same momentum range as the analysis. This extension is performed with the Bylinkin parametrization [103]. As no measurement of $\Sigma^{-}, \bar{\Sigma}^{+}$ and $\Sigma^{+}, \bar{\Sigma}^{-}$ exists, their p_T distribution is constructed based on the measured distributions of the neutral Λ-hyperon, which has equal strangeness and comparable mass ($m_{\Lambda} = 1.116\,\mathrm{GeV}/c^2$, $m_{\Sigma^+} = 1.189\,\mathrm{GeV}/c^2$, $m_{\Sigma^-} = 1.197\,\mathrm{GeV}/c^2$ [6]). In order to estimate the Σ-contribution, the Λ-spectrum is scaled by the ratios of the production cross-section for Σ-hyperon to the cross-section for Λ-hyperon, estimated by various event-generators and verified by expectations from the thermal model [20].

The resulting constructed particle fractions from data are shown in Figure 4.10. In particular the relative abundance of $\Sigma^{+}, \bar{\Sigma}^{-}$ and $\Sigma^{-}, \bar{\Sigma}^{+}$ is enhanced in comparison to the fraction from HIJING. Comparing the data based fractions one further observes that the amout of Σ-Baryons is strongly dependent on the centrality of the collision, this feature is related to the hydrodynamical evolution of the system, which is not included in HIJING.

Correction Factor

To correct the MC-only tracking efficiency for the inaccuracy of the relative particle fraction discussed above, the tracking efficiency is recalculated making use of the particle species dependent efficiencies and the relative abundances based on data. The resulting tracking efficiencies are presented in the top panel of Figure 4.11 for central and peripheral collisions. The lower panel presents the particle-species reweighting factor. This factor reaches up to 8% for central collisions while being much smaller for

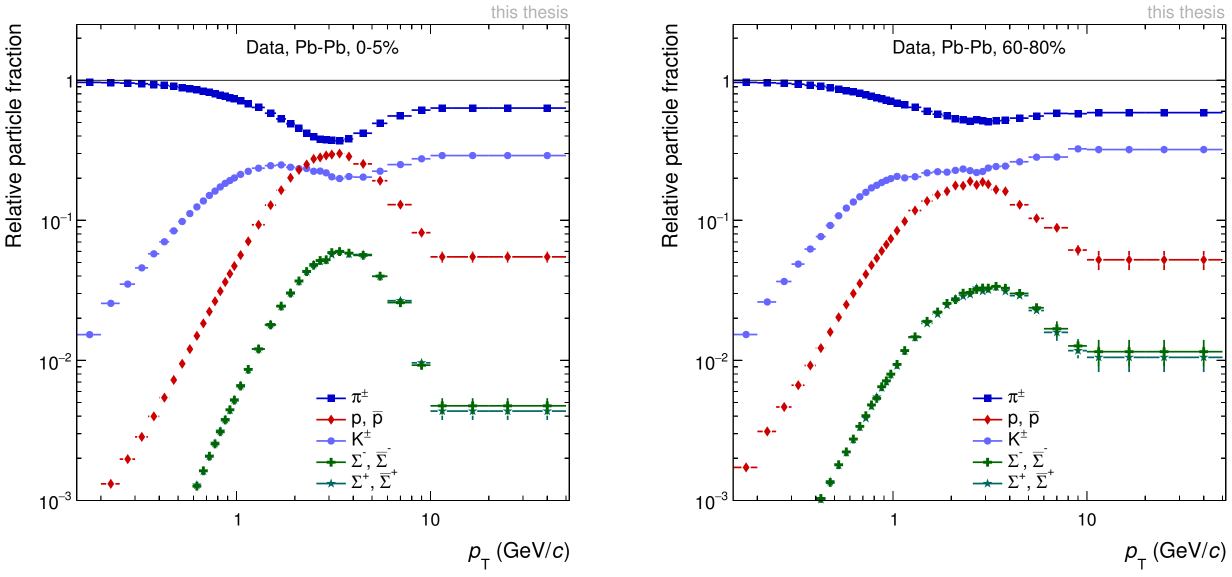

Figure 4.10.: Relative particle fractions for the most abundant particle species constructed from measurements in central (left) and peripheral (right) collisions.

peripheral collisions. This is a direct result of the behaviour of the strange baryons, that are strongly underestimated by HIJING simulations in central collisons. As statistics in the identified particle spectra but also in MC simulations is limited, the reweighting factor has to be calculated in wider centrality intervals that what is used in data.[2]

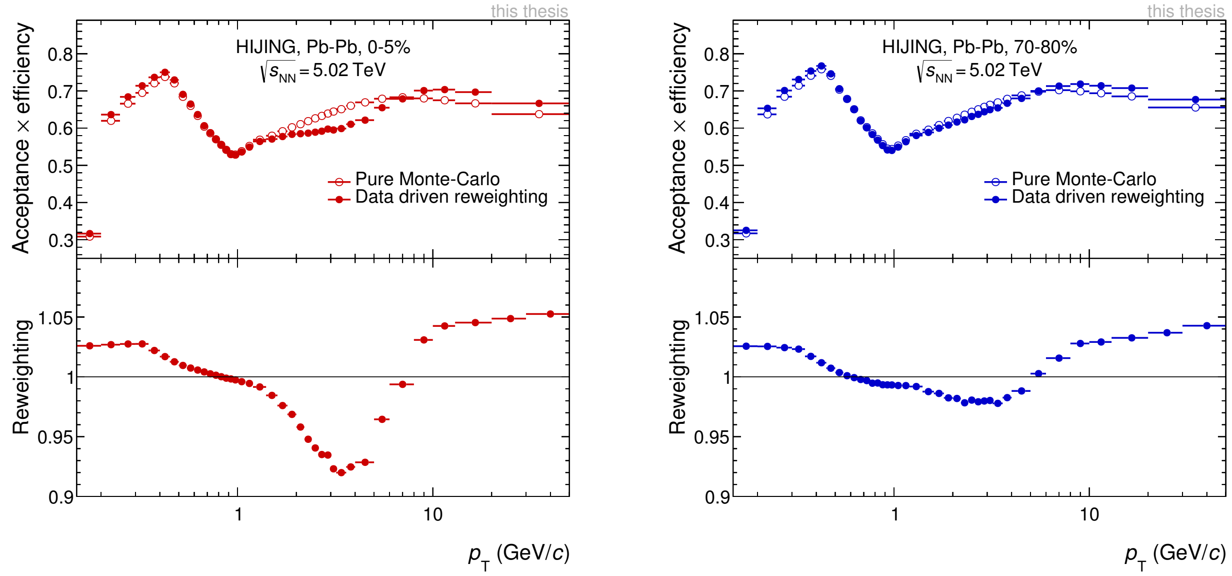

Figure 4.11.: The efficiency from pure MC (open symbols) and the efficiency after reweighting (filled symbols top panel) as well as the reweighting factor calculated (lower panel) for central (left) and peripheral collisions (right).

---

[2] Intervals used for the reweighting: 0–5%, 5–10%, 1–20%, 20–40%, 40–60%, 60–80%

In collisions of xenon nuclei the calculation of this reweighting factor is more difficult, as no measurement of the identified particle production in this collision system is presently available. The particle composition however is governed by the collision centrality and thus the system size. As xenon is smaller nucleus than lead, collisions with the same centrality do not have the same number of participants (N_{part}) or binary collisions (N_{coll}). In order to still perform the particle species reweighting, measured distributions of identified particles in Pb–Pb collisions with comparable values of N_{part} and $d\text{N}_{\text{ch}}/d\eta$ compared to Xe–Xe collisions are used. More details can be found in [104].

4.6.3 Efficiency at Reduced Magnetic Field

The collisions of xenon ions collected in October 2017 were taken with a reduced magnetic field of ALICE's solenoid magnet of $\text{B} = 0.2\,\text{T}$, in order to extend tracking and particle identification to the lowest possible momenta. A lower magnetic field leads to a reduced curvature of the tracks. At low track momentum this increases the reach, as fewer tracks are lost due to the strong curvature. The shape of the p_{T} dependent tracking efficiency is modified, especially, as selecting by the track's active length (L_{active}) depends on the momentum. Figure 4.12 (left) shows the efficiency for Pions ($\pi^{\pm}$) of the Xe–Xe data set taken with the reduced magnetic field. Using relation 3.1 relating the radius to the magnetic field it is possible to express the efficiency as a function of the track radius Figure 4.12 (right). Comparing the tracking efficiencies as a function of track radius a general similarity between the efficiencies can be observed. The minimum related to the tracks crossing the sector boundaries ($p_{\text{T}} \sim 1\,\text{GeV}/c$ for $\text{B} = 0.5\,\text{T}$) is found for tracks with a track radius $r_{\text{track}} \approx 6 - 7\,\text{m}$, independent of the tracks momentum. At low r_{track} the tracking efficiency is larger for the higher momentum in Pb–Pb collisions, as tracks with low p_{T} are impacted by the detector material more strongly. At high r_{track} the efficiencies diverge as a function of r_{track}, while the behaviour is similar for high p_{T}, suggesting that the drop of efficiency at high p_{T} is related to momentum and not to the radius.

It has to be noted, that the differences in the efficiency are also influenced by the exchange of detector gas, from $\text{Ar} - \text{CO}_2$ for Pb–Pb collisions to $\text{Ne} - \text{CO}_2$ for the Xe–Xe collisions.

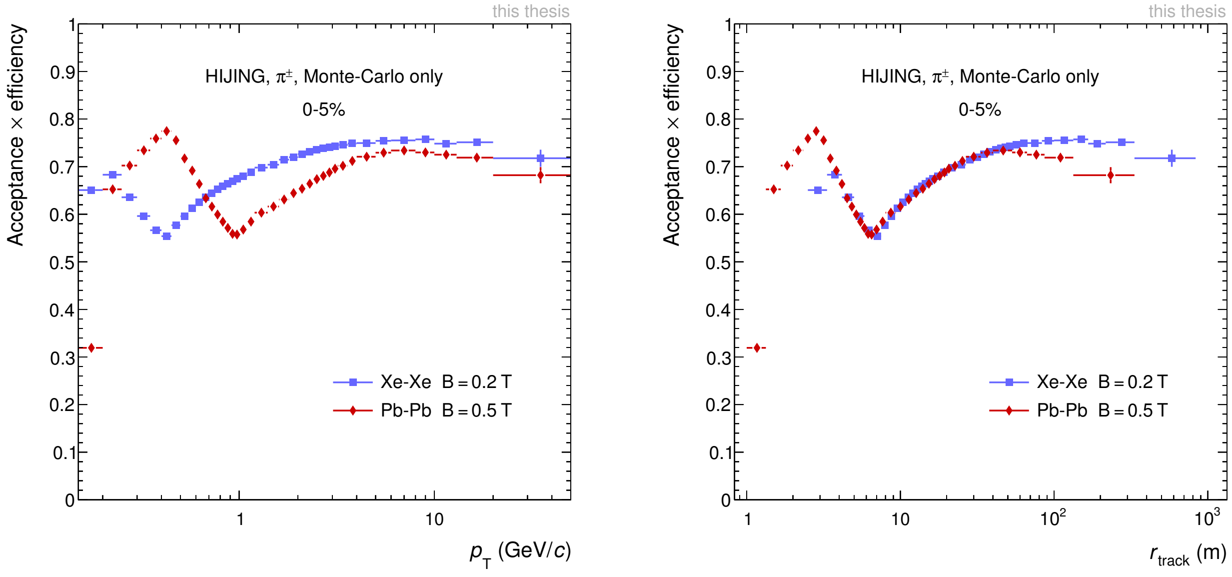

Figure 4.12.: The tracking efficiency for $\pi^{\pm}$ as a function of transverse momentum (right) and as a function of track radius (left) for Xe–Xe and Pb–Pb with different magnetic field strengths used in the ALICE solenoid. $\text{B} = 0.2\,\text{T}$ for Xe–Xe instead of the nominal $\text{B} = 0.5\,\text{T}$.

The uncorrected transverse momentum distribution contains a contribution from secondary particles (see section 4.4), which needs to be subtracted. The contamination stems from weak decays of particles produced in the initial collision, and also from interactions of primary particles in the detector material. Using Monte Carlo simulations, the contribution can be estimated, shown in Figure 4.13. At low p_{T}, the contamination is significant with more than 10%, while it decreases towards higher p_{T} and falls below 1% for $p_{\mathrm{T}} > 2\,\mathrm{GeV}/c$. This is caused by the steeply falling spectrum and the decay kinematics - a daughter particle carries only a fraction of the mother's p_{T}. The left plot shows the contamination obtained from simulation for Xe–Xe an Pb–Pb collisions at all collision energies analysed. The contamination shows no dependence on energy and is similar even though detector effects - and thus changes between Run 1 and Run 2 - are incorporated in the simulated contamination. An increased contamination in Xe–Xe collisions is most likely linked to the change in the magnetic field, as the DCA-resolution decreases for smaller track radii. The dependence of the secondary particle contamination on the collision centrality is significant (Figure 4.13 right). At low transverse momenta, the contamination in central collisions is almost twice as large as in peripheral collisions. This reflects the suppression of strangeness production in small systems. At high p_{T}, the difference between the contamination in central and peripheral collisions vanishes. Here, the contamination is very low and governed by remnants of particle interactions with detector material.

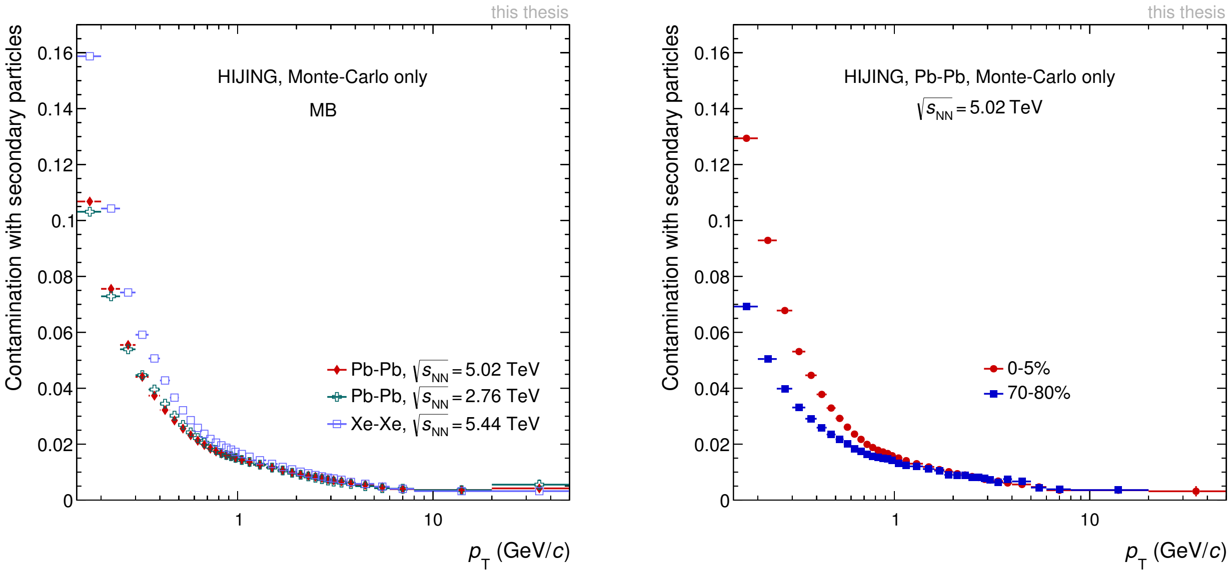

Figure 4.13.: The contamination with secondary particles for all three datasets analysed (left) and for two different classes of centrality (right). While only a small influence of the collision energy is observed, the dependence on centrality is significant.

Monte-Carlo Scaling

As discussed in section 4.6.1, Monte-Carlo event-generators fail at describing the particle fractions accurately, the amount of secondary particles is no exception. In this analysis, the true fraction of secondary particles in data is obtained by examining the DCA_{xy} distributions of tracks. The underlying assumption is, that both types of secondary particles, the decay daughters as well as the remnants of detector interactions have an origin separated from the primary event vertex and thus have a modified DCA_{xy} distribuion. Especially the width of the distribution should be affected. In Figure 4.14 this distribution is shown for Pb–Pb (left) and Xe–Xe collisions (right) for both data and simulation (HIJING). In simulation it is possible to separate the contributions from primary and secondary particles (and further from decays or material interaction). As can be seen from the distributions for secondaries and primary particles, the distribution of primary particles has a sharp peak at $\mathrm{DCA}_{xy} = 0$. The width of the DCA_{xy} distribuion is much larger for secondary particles.

In order to estimate the amount of secondary and primary particles in data, a linear combination of both templates from MC is compared to the distribution in data. A minimization procedure optimizes the relative weights in order to find the optimal relation. In Xe–Xe it was feasible to perform this procedure not only with two templates (primary and secondary particles), but with three, splitting the contribution of secondaries to further differentiate between particles originating from decays and material interactions. The lower panel of Figure 4.14 shows the ratio of these template-fits to data.

As the selection criteria are chosen such that the contamination with secondary particles is minimal the criteria have to be loosened to obtain a sufficient amount of secondaries. Therefore no cut on the DCA_{xy} nor on the $\chi^2_{\text{TPC-ITS}}$ are applied.

The procedure described above is performed for different ranges of p_{T}. As statistics in the simulation is limited, the number of p_{T} intervals is limited. In total the true fraction of secondaries is calculated in three intervals of p_{T} (Figure 4.15). The ratio of the true amount of secondaries in data to the amount in MC is calculated and used to scale the contamination factor. To account for limited statistics the correction factor is linearly interpolated in between the bin centres. The scaled correction factors and the scaling factors are shown in Figure 4.16

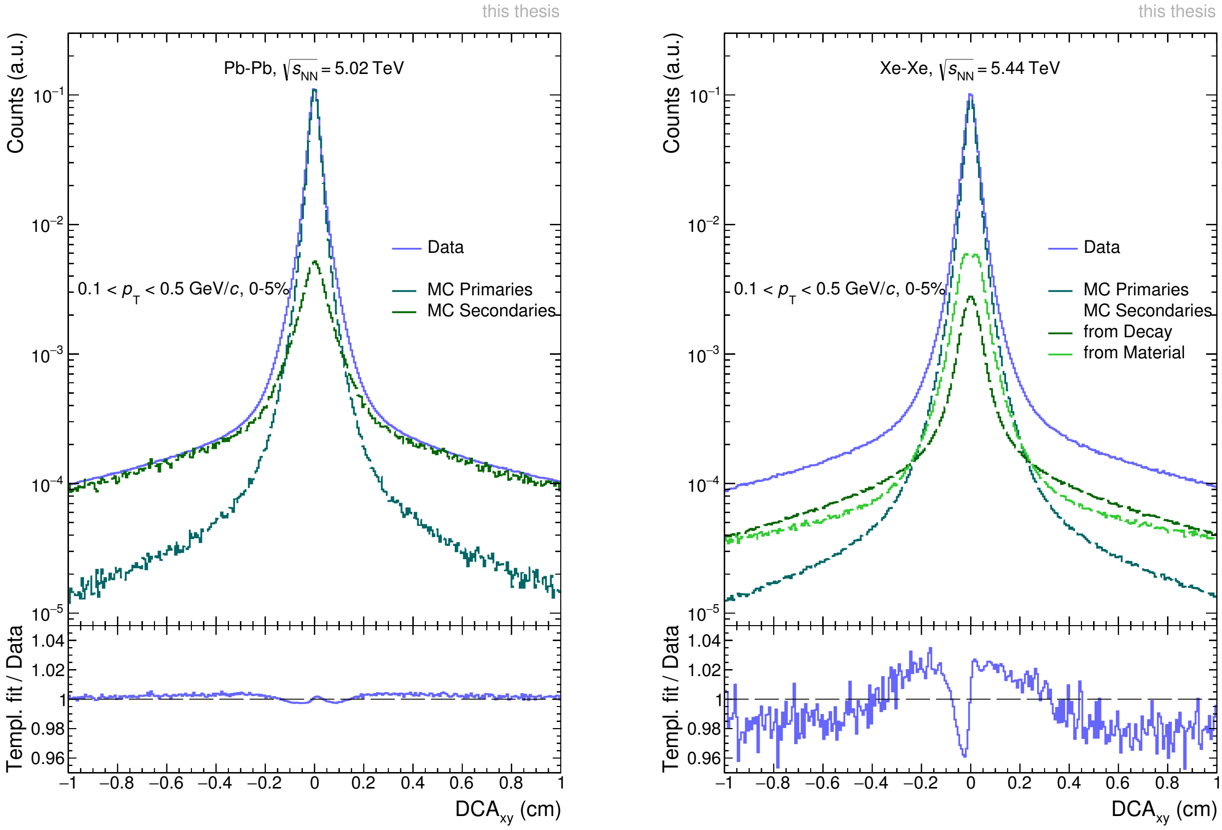

Figure 4.14.: The DCA_{xy} distributions for Pb–Pb (left) and Xe–Xe (right). The distributions are shown for the most central (0–5%) collisions and for a transverse momentum of $0.1 < p_{\mathrm{T}} < 0.5\,\mathrm{GeV}/c$. In Pb–Pb two templates are chosen for the fit, while in Xe–Xe three templates were feasible. The lower panel shows the ratio of the fit to the data.

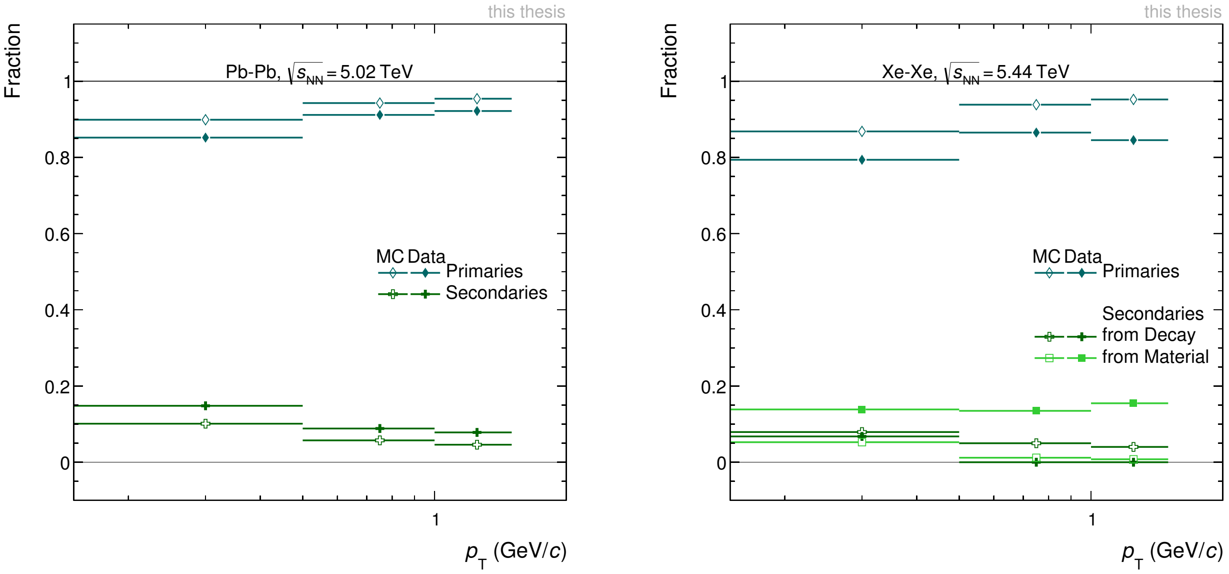

Figure 4.15.: The fractions of primaries and secondaries for different p_T bins. In Pb–Pb collisions two templates were used, in Xe–Xe collisions three templates were feasible.

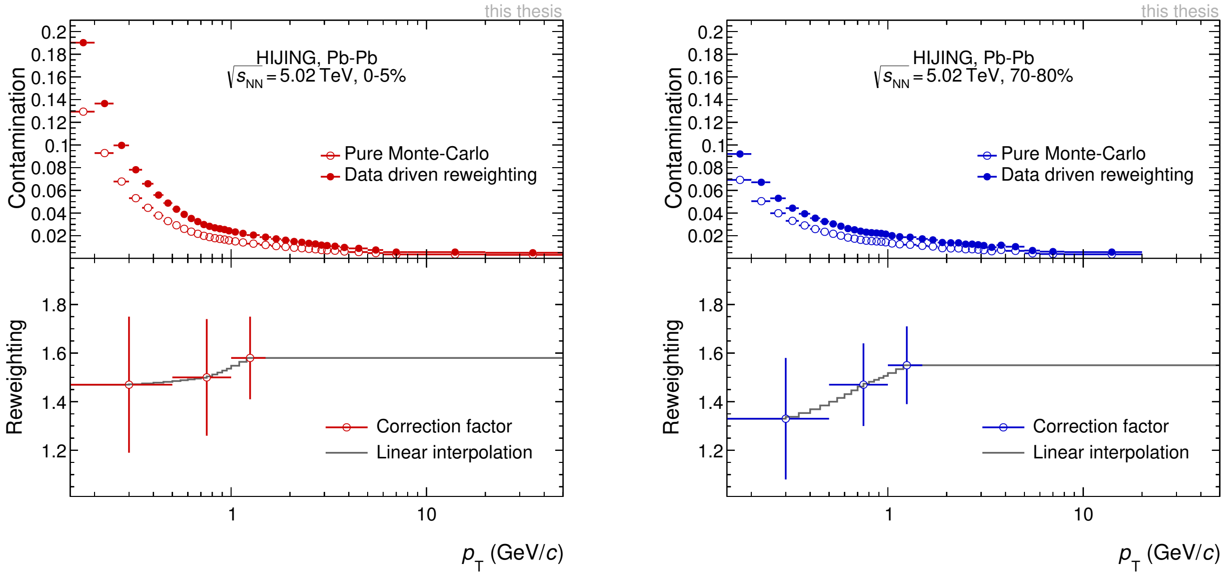

Figure 4.16.: The contamination with secondary particles for central (left) and peripheral collisions (right). The upper panel shows the contamination subtracted from the uncorrected momentum distribution. The contribution estimated by pure Monte Carlo is shown with open symbols. The contamination after rescaling is shown with filled symbols. The lower panel shows the reweighting factor estimated by template fits to the DCA$_{xy}$ distribution in data (coloured symbols), and the linear interpolation used to scale the contamination (grey line).

4.6.5 Transverse Momentum Resolution

As discussed in section 3.3.1, the resolution of the transverse-momentum determination can not be neglected at high p_{T}, as tracks get less curved. Even thought the momentum resolution is symmetric and the momentum of a track with a given p_{T} is over and underestimated in equal parts, the steeply falling shape of the transverse momentum distribution gives rise to an effect on the distribution itself. This results in an artificial hardening of the spectra, as more low p_{T} tracks are shifted to high p_{T} than vice-versa.

The resolution of the transverse momentum is estimated during the tracking and reconstruction procedure for each track individually. Figure 4.17 shows the distribution track p_{T} and the corresponding relative momentum-resolution $\sigma_{p_{\mathrm{T}}}/p_{\mathrm{T}}$. While most tracks have a good resolution in the proximity of the lower bound discussed in section 3.3.1, other tracks have a significantly worse resolution. This is a result of the tracking performance. At high p_{T} the length of track is crucial and therefore tracks that have only one hit in the SPD are distinct from tracks with two hits in the SPD. Tracks with only one hit in the SPD can be found in a second band at worse resolution at $p_{\mathrm{T}} \approx 10\,\mathrm{GeV}/c$. At low p_{T} tracks are shorter and the momentum resolution is worsened by particle species dependent multiple scattering.

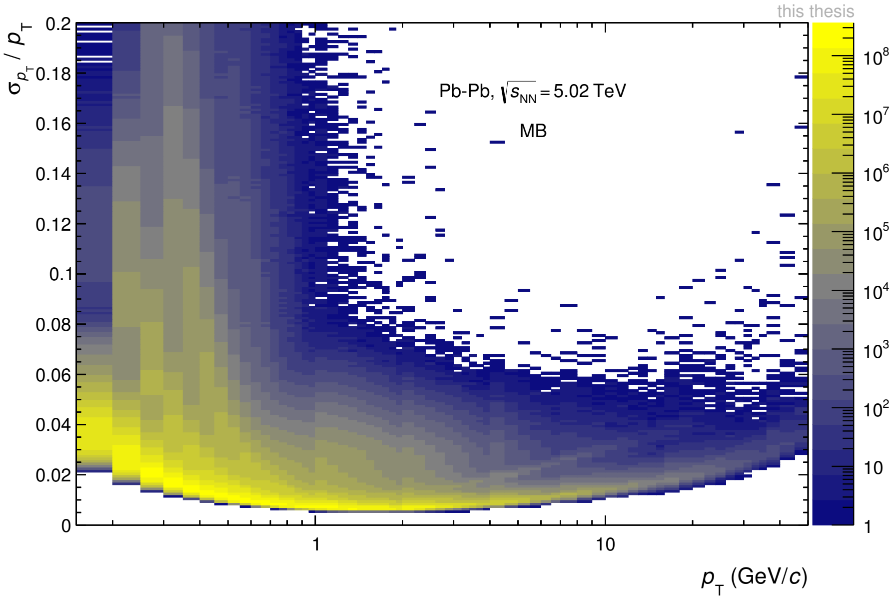

Figure 4.17.: The distribution of relative momentum-resolution in dependence of the track p_{T}. Most tracks have a good resolution while the lower bound of the relative momentum resolution increases at high and low p_{T}, as discussed in section 3.3.1.

An additional contribution to the p_{T} resolution is given by the different tracking performance of tracks from positively and negatively charged particles. In the ALICE coordinate-system a negative value of $1/p_{\mathrm{T}}$ stands for tracks with negative charge. When fitting the track $1/p_{\mathrm{T}}$ distribution it is expected to find the minimum at zero but instead a shifted minimum is found, see Figure 4.18. This shift ($\Delta_{1/p_{\mathrm{T}}}$) is found to be dependent of the azimuthal angle ϕ, and amounts in the mean to $0.0004\,c/\mathrm{GeV}$ with an RMS of $0.0003\,c/\mathrm{GeV}$. To account for this effect, the RMS is quadratically added to the resolution.

To estimate the effect of finite momentum resolution on the spectra, the distribution is first parametrised in the region above $10\,\mathrm{GeV}/c$ by a power-law. In an unfolding procedure a value of p_{T} is randomly picked from the parametrisation before it is smeared with an random choice based on a Gaussian distribution with a mean of zero and a width sampled from the relative momentum resolution displayed in Figure 4.17. The distribution with the applied smearing is compared to the original unsmeared distribution. The ratio of the two is then applied to the distribution as a correction factor for tracks with $p_{\mathrm{T}} > 10\,\mathrm{GeV}/c$

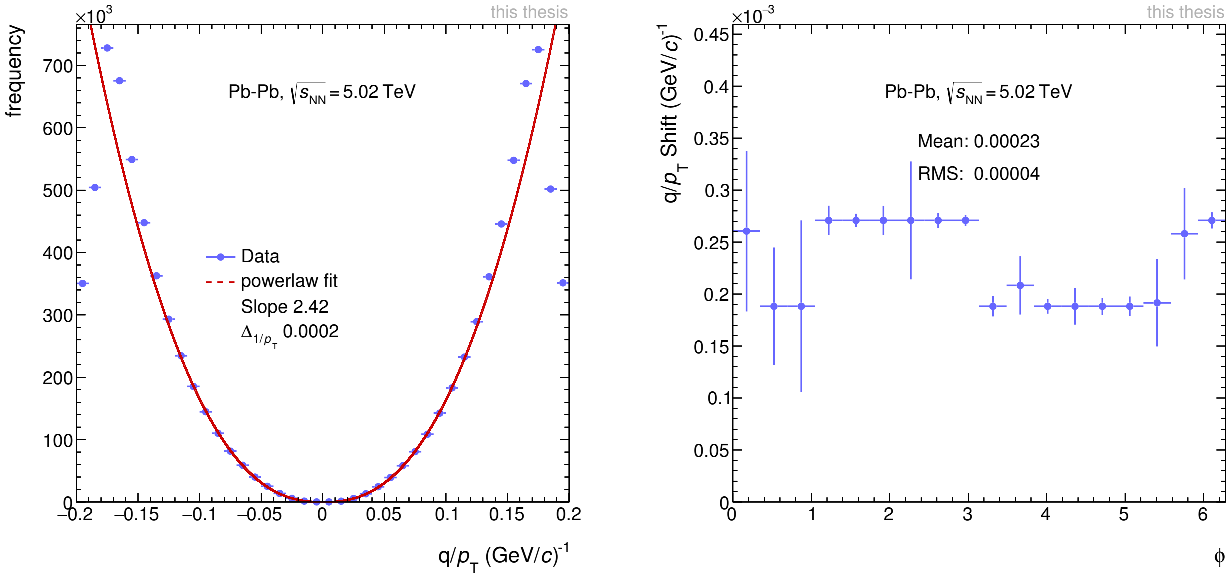

Figure 4.18.: The distribution of q$/p_{\mathrm{T}}$ of tracks, the minimum is determined by fitting a powerlaw and a shift of $\Delta_{1/p_{\mathrm{T}}} = 0.0002\,c/\mathrm{GeV}$ is found for all tracks. The shift is dependent on the azimuthal angle in the TPC.

(Figure 4.19). Although no centrality dependence of the relative momentum resolution is found, the correction factor gains a dependence on collision centrality, as the spectra in central collisions are less steep than in peripheral collisions. Central collisions therefore are less affected by the the p_{T}-resolution correction than peripheral collisions. In Pb–Pb at $\sqrt{s_{\mathrm{NN}}} = 5.02\,\mathrm{TeV}$, the correction factor varies between 1% at $p_{\mathrm{T}} = 50\,\mathrm{GeV}/c$ for central and 2% for peripheral collisions (Figure 4.19). For Xe–Xe collisions the strength of the resolution correction is increased, as the high-p_{T} degradation of the momentum res-

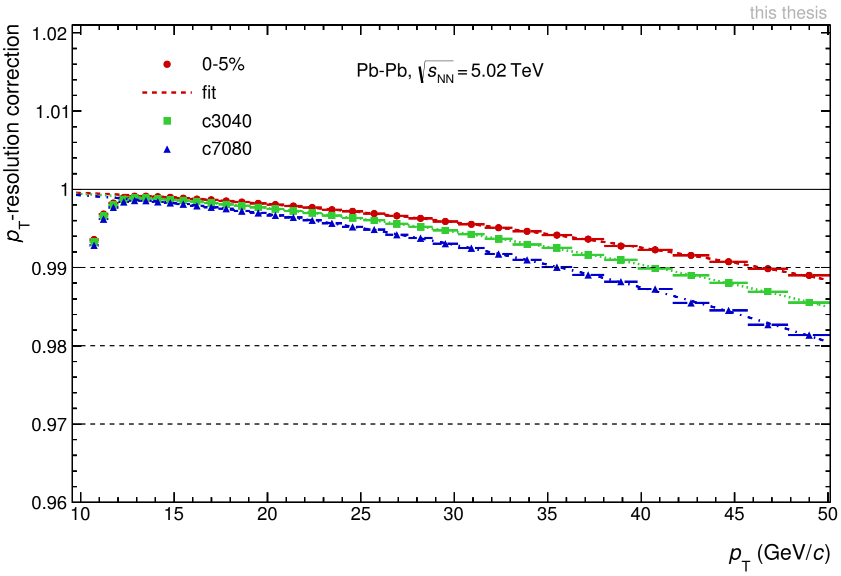

Figure 4.19.: The p_{T} dependent correction factor to account for finite p_{T}-resolution. The correction applied depends on the hardness of the spectrum. As steepness increases for peripheral collisions the correction becomes larger.

olution becomes relevant at lower p_{T}, due to the lower magnetic field strength. Here it reaches 3% for central and 4% for peripheral collisions at $p_{\mathrm{T}} = 50\,\mathrm{GeV}/c$.

4.7 Systematic Uncertainties

The systematic uncertainties are described in this section. The contributions are introduced by assumptions made during the analysis and the corrections performed. The selection criteria for tracks and events are well motivated but numerical values for selection criteria are partially arbitrary. The correction for the tracking inefficiency is largely based on Monte-Carlo simulations which needs to be validated. The corrections based on data – secondary scaling and particle composition correction – include fits and extrapolations that are varied to estimate their contributions. In addition, the data the correction is based on contains systematic uncertainties that need to be propagated. A summary of the uncertainties on the transverse momentum distributions is shown in Table 4.4, their dependence on p_{T} are shown in Figure 4.20. Even though the analysis procedure is identical, the uncertainties differ between the data sets analysed. This is a result of different detector and reconstruction performance at the time of data taking.

Source of Uncertainty	**Uncertainty in %**					
	Pb–Pb, $\sqrt{s_{\mathrm{NN}}} = 5.02\,\mathrm{TeV}$		Pb–Pb, $\sqrt{s_{\mathrm{NN}}} = 2.76\,\mathrm{TeV}$		Xe–Xe, $\sqrt{s_{\mathrm{NN}}} = 5.44\,\mathrm{TeV}$	
	0–5%	70–80%	0–5%	70–80%	0–5%	70–80%
Event selection	0.14	0.13	1.45	1.46	0.22	0.83
Track selection	1.46 / 4.82	0.58 / 3.53	1.69 / 1.48	1.59 / 1.26	1.58 / 1.19	0.95 / 0.99
Secondary particles	1.69 / 0	0.88 / 0	1.43 / 0	1.02 / 0	1.39 / 0	0.61 / 0
Particle composition	0.32 / 0.44	0.32 / 0.54	0.30 / 0.49	0.30 / 0.60	0.31 / 0.52	0.33 / 0.58
Tracking efficiency	0.83 / 0.35	1.04 / 0.17	0.44 / 0.90	0.70 / 1.08	1.86 / 0.37	2.16 / 0.57
Material budget	0.32 / 0.13		0.32 / 0.13		0.32 / 0.13	
p_{T} resolution	0 / 0.065	0 / 1.00	0 / 0.54	0 / 1.57	0 / 0.48	0 / 0.93
Interaction rate	0.39 / 1.56	0.39 / 1.56	-		-	
Total p_{T} dependent	2.54 / 5.11	1.66 / 4.03	2.77 / 2.38	2.59 / 2.77	3.07 / 1.44	2.67 / 2.10
Anchor point	0.06	3.50	0.06	3.59	0.06	3.24

Table 4.4.: Contributions to the overall systematic uncertainty. The numbers are averaged in the p_{T} intervals from 0.2-0.5 GeV/c (left) and 40-50 GeV/c (right). For the total, all contributions are added in quadrature.

4.7.1 Event Selection

For heavy-ion collisions more central than 80%, the trigger and vertex determination are considered to be fully efficient, thus the only uncertainty on the selection of events is imposed by the selection on the vertex position along the beam pipe (Z_{v}).
To estimate the uncertainty, the selection of the vertex position along the beam pipe (Z_{v}) is varied from the nominal $\pm 10\,\mathrm{cm}$ to $\pm 5\,\mathrm{cm}$, $\pm 20\,\mathrm{cm}$ in both analysis of data and in simulation later used for the correction. The full analysis is performed with the varied selection criteria and the resulting spectra are compared to the spectra obtained with the nominal value of Z_{v}. The ratio was found to be independent of p_{T} and is therefore approximated with a constant for the whole range of p_{T}. In the case of Xe–Xe and Pb–Pb collisions at $\sqrt{s_{\mathrm{NN}}} = 5.02\,\mathrm{TeV}$ the uncertainty is small ($< 1\%$), while it is larger $\sim 1.5\%$ for Pb–Pb collisions at $\sqrt{s_{\mathrm{NN}}} = 2.76\,\mathrm{TeV}$.
f

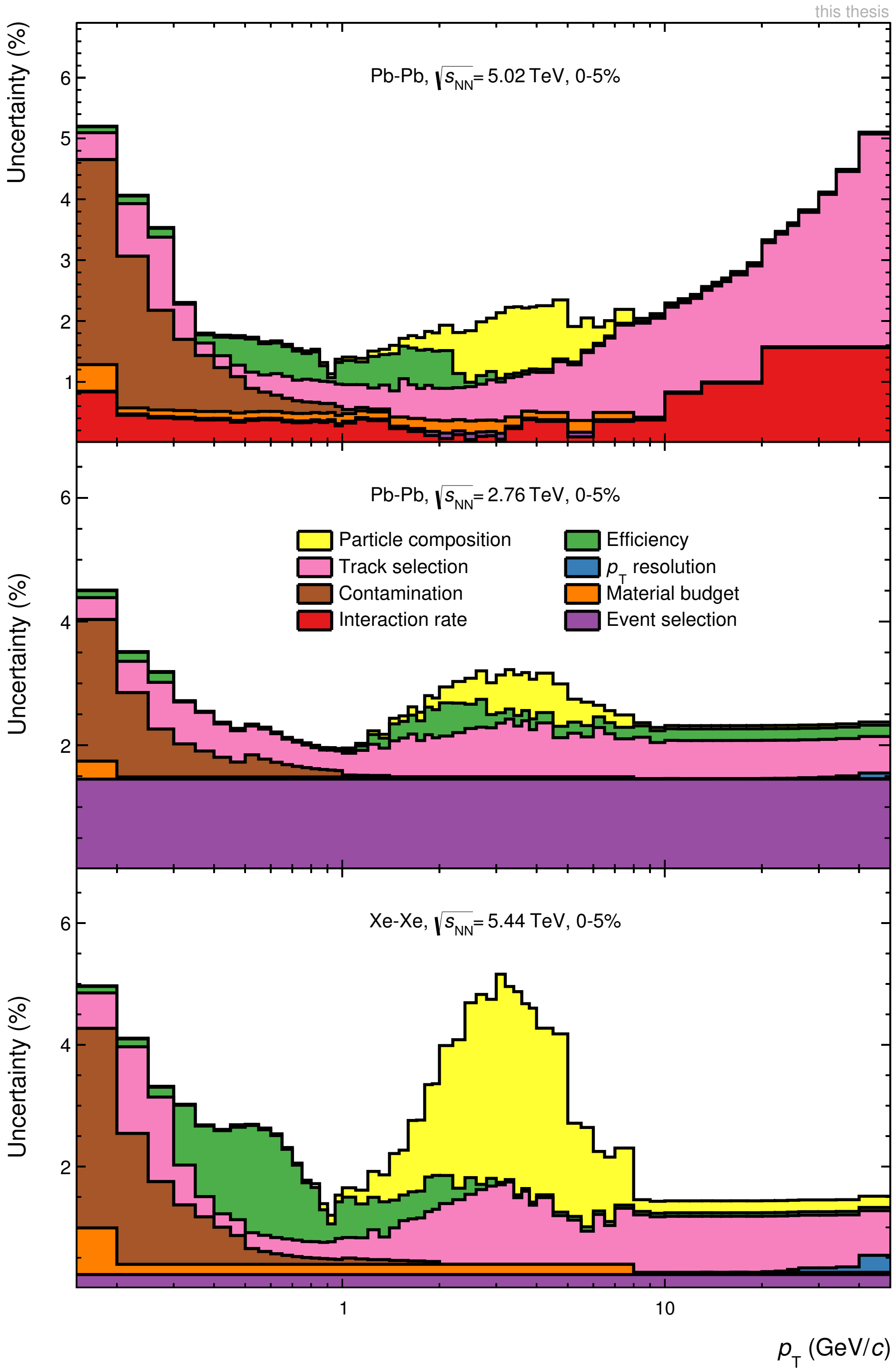

Figure 4.20.: An overview of the p_T dependent systematic uncertainties in all data sets analysed. Each line shows the quadratic sum of the lines below. Even though the contributions are estimated in the same way the amount of uncertainties varies for the data sets. For Pb–Pb at $\sqrt{s_{NN}} = 5.02$ TeV the overall uncertainty is dominated by the contribution of the track selection at high p_T. Also it has an additional contribution from a varying interaction rate, which is not present in the other data sets. (Compare Figure C.1 for more peripheral collisions.)

4.7.2 Anchor Point

In the centrality estimation (section 3.5), the anchor point is defined as the amplitude of the V0 detector equivalent to a certain percentile of the hadronic cross section. It determines the absolute scale of the centrality. In this analysis the anchor point is set to $(90 \pm 0.5)\%$. The systematic uncertainty of the p_{T} spectra that is due to centrality selection was estimated moving the anchor point by its assigned uncertainty of 0.5% and recalculating the centrality boundaries accordingly. The uncertainty is estimated from the variation of the resulting p_{T} distributions and amounts to $\sim 0.06\%$ for central (0-5%) and $\sim 3.5\%$ for peripheral collisions (70-80%) for all collision systems. As this uncertainty is independent of transverse momentum it is applied as a normalisation uncertainty.

4.7.3 Track Selection

Track selection criteria	**Nominal**	**Variations**	
DCA$_z$	2 cm	1 cm	5 cm
DCAxy	$7\sigma_0$	$4\sigma_0$	$10\sigma_0$
χ^2_{ITS}	36	25	49
Hit in the SPD	required	not required	
$n_{\mathrm{rows}}/n_{\mathrm{finable}}$	0.8	0.7	0.9
$n_{\mathrm{shared}}/n_{\mathrm{cluster}}$	0.4	0.2	1
χ^2_{TPC}	4	3	5
L_{active}	130 cm	120 cm	140 cm
$W_{\mathrm{dead\text{-}zone}}$	3 cm	2 cm	3 cm
$\chi^2_{\mathrm{TPC\text{-}ITS}}$	36	25	49

Table 4.5.: The variation of the track selection criteria.

The selection of the values for the track-selection citeria is driven by the knowledge of the tracking and detector performance. But regardless on how well each selection value is motivated the choice of a given value bears an uncertainty. To account for this, the selection criteria were varied in reasonable ranges and the whole analysis up to the fully corrected spectra was performed using the modified track selection in data as well as in the simulation. The resulting transverse-momentum distributions are compared to the spectra obtained with nominal selection. For each bin the larger of the two ratios of spectra (modified / nominal) is assigned as the uncertainty related to this criteria. At large p_{T} the ratio is parametrised to minimise the sensitivity of systematic uncertainties on statistical fluctuations. Figure 4.21 shows this procedure for the two dominant contributions in Pb–Pb collisions at $\sqrt{s_{\mathrm{NN}}} = 5.02\,\mathrm{TeV}$, χ^2_{TPC} and $\chi^2_{\mathrm{TPC\text{-}ITS}}$. The contribution from the selection on χ^2_{TPC} is significant at low p_{T} and shows fluctuations at high p_{T}. In order to avoid statistical fluctuation in the estimation of the systematic uncertainties, the behaviour at high p_{T} is approximated by a constant function. The lower boundary for this procedure is indicated by a vertical dashed line in Figure 4.21. The constant function was chosen for all contributions in all systems studied. The only exception to this is the contribution of $\chi^2_{\mathrm{TPC\text{-}ITS}}$, which shows an increasing behaviour towards high p_{T}. At high p_{T} the contribution is again parametrised, but here an exponentially increasing function was chosen. This feature is only observed for this selection criterion and only in Pb–Pb collisions at $\sqrt{s_{\mathrm{NN}}} = 5.02\,\mathrm{TeV}$, for the other datasets analysed a constant behaviour at high p_{T} is found.

For each bin in p_{T} the uncertainties of all track selection criteria were then added up in quadrature. In Figure 4.22 the summed systematic uncertainties and their individual contributions are presented for two different collision centralities. The impact of the high track density in the TPC on the fitting

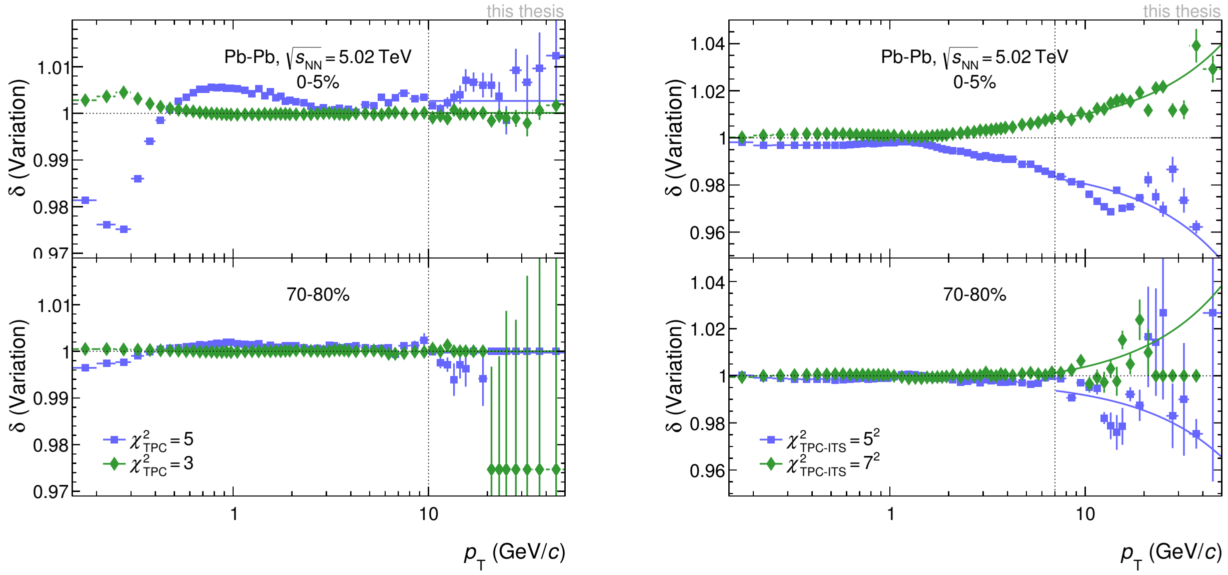

Figure 4.21.: The ratio of the modified to the nominal spectra under change of the track selection criteria that dominate the track selection uncertainty in Pb–Pb at $\sqrt{s_{\mathrm{NN}}} = 5.02$ TeV. At high p_{T} the ratio is fitted to reduce the impact of low statistics on the systematic uncertainties. The lower limit of the fit is indicated by the dashed line.

Track	**Uncertainty in %**					
Selection	Pb–Pb, $\sqrt{s_{\mathrm{NN}}} = 5.02$ TeV		Pb–Pb, $\sqrt{s_{\mathrm{NN}}} = 2.76$ TeV		Xe–Xe, $\sqrt{s_{\mathrm{NN}}} = 5.44$ TeV	
Criteria	0–5%	70–80%	0–5%	70–80%	0–5%	70–80%
DCA$_z$	<0.01 / <0.01	<0.01 / <0.01	<0.01 / <0.01	<0.01 / <0.01	<0.01 / <0.01	<0.01 / <0.01
DCAxy	0.30 / 0.06	0.30 / 0.06	0.35 / 0.55	0.35 / 0.55	0.18 / 0.26	0.18 / 0.26
χ^2_{ITS}	<0.01 / 0.01	<0.01 / 0.01	0.02 / 0.01	0.02 / 0.01	0.01 / 0.02	0.01 / 0.02
Hit in the SPD	0.09 / 0.03	0.09 / 0.03	0.24 / 0.06	0.24 / 0.06	0.55 / 0.30	0.55 / 0.30
$n_{\mathrm{rows}}/n_{\mathrm{findable}}$	0.25 / 0.17	0.24 / 0.88	0.08 / 1.06	0.32 / 1.10	0.15 / 0.07	0.08 / 0.10
$n_{\mathrm{shared}}/n_{\mathrm{cluster}}$	0.08 / 0.31	0.05 / 0.21	0.36 / 0.16	0.21 / 0.04	0.08 / 0.62	0.04 / 0.31
χ^2_{TPC}	1.19 / 0.27	0.12 / 0.03	1.42 / 0.62	1.41 / 0.20	1.21 / 0.18	0.56 / <0.01
L_{active}	0.27 / 0.21	0.27 / 0.21	0.20 / 0.04	0.20 / 0.04	0.21 / 0.26	0.21 / 0.26
$W_{\mathrm{dead\text{-}zone}}$	0.20 / 0.23	0.20 / 0.23	0.15 / 0.11	0.15 / 0.11	0.22 / 0.13	0.22 / 0.13
$\chi^2_{\mathrm{TPC\text{-}ITS}}$	0.31 / 4.79	0.13 / 3.39	0.65 / 0.58	0.17 / 0.08	0.30 / 0.85	0.16 / 0.80
Total	1.46 / 4.82	0.58 / 3.53	1.69 / 1.48	1.59 / 1.26	1.58 / 1.18	0.95 / 0.99

Table 4.6.: Contributions to the systematic uncertainty of the track selection. The numbers are averaged in the p_{T} intervals from 0.2-0.5 GeV/c (left) and 40-50 GeV/c (right). For the total, all contributions are added in quadrature.

performance can be seen at low p_{T}, where the contribution from the χ^2_{TPC} reduces from more than 2% in central to less than 1% in peripheral collisions.

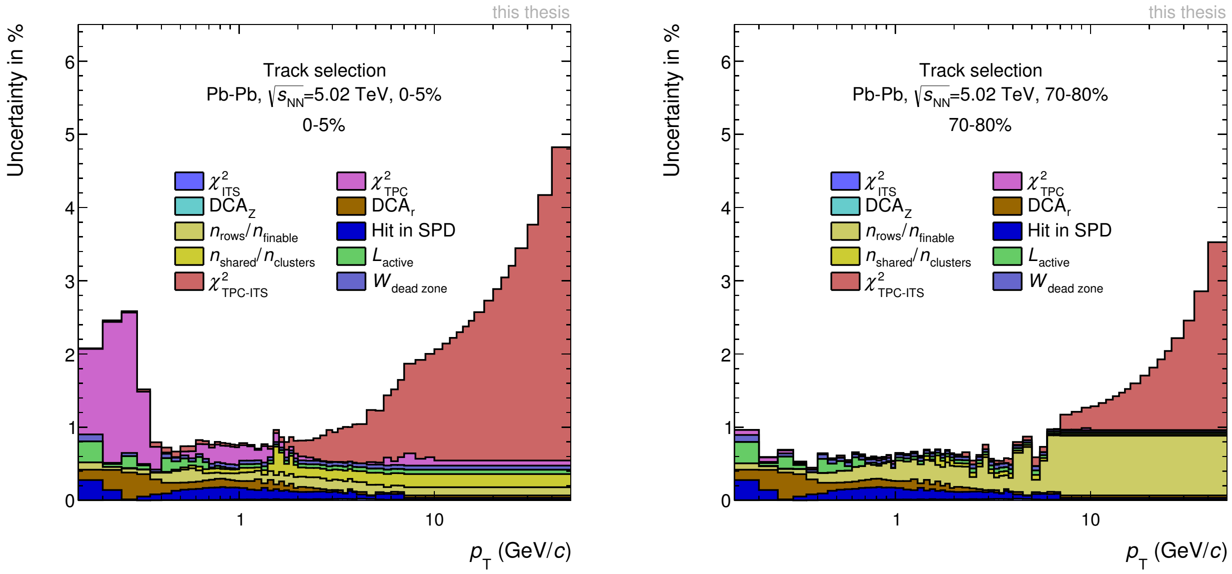

Figure 4.22.: The p_T dependence contribution to the systematic uncertainty of the track selection criteria employed in this analysis.

4.7.4 Particle Composition Correction

The particle composition correction is based on measured data and a set of assumptions, all of which contribute to the systematic uncertainties. First, the influence of systematic uncertainties of the measured particle distributions need to be evaluated. To account for this, the measured transverse momentum distribution were varied within their uncertainties, propagating the change in the correction factor as uncertainty. As the contribution of $\Sigma^+, \bar{\Sigma}^-$ and $\Sigma^-, \bar{\Sigma}^+$ are estimated based on the measurement of Λ-Baryons, an additional 20% uncertainty is added to this contributions. The contribution of the remaining MC-only particles is varied by 30%. In central Pb–Pb collisions, the quadratic sum of theses variations amounts for an uncertainty of up to 3%, while in peripheral collisions the magnitude is at the level of 2%.

Another notable contribution to the overall uncertainty is the effect of the parametrisation to low and high p_T. In the calculation of the correction factor, this parametrisation and extrapolation to low p_T is performed using a Bylinkin function. To estimate the systematic uncertainties a modified Hagedorn function [105] is used as an alternative parametrisation. In addition also the p_T in which the parametrisation is performed is modified. The uncertainty of the parametrisation towards low p_T is however found to be small (0.5%).

At high p_T ($> 10\,\text{GeV}/c$) a different assumption is made, here the relative contributions of the particle species is kept constant. The contribution to the uncertainties is estimated by moving the lower range of the constant fractions to $p_T = 8\,\text{GeV}/c$ and $12\,\text{GeV}/c$, which results in an uncertainty of 1% in peripheral and central collisions.

The separate contributions are summed up quadratically and included in the overall systematic uncertainty, the contribution of the particle composition correction is shown in Figure 4.23.

To calculate the correction in Xe–Xe collisions, a matching centrality interval in Pb–Pb collisions at $\sqrt{s_{NN}} = 2.76\,\text{TeV}$ is required. The uncertainty of this selection is estimated by comparing the correction factor obtained for the selected centrality interval with the neighbouring more peripheral interval.

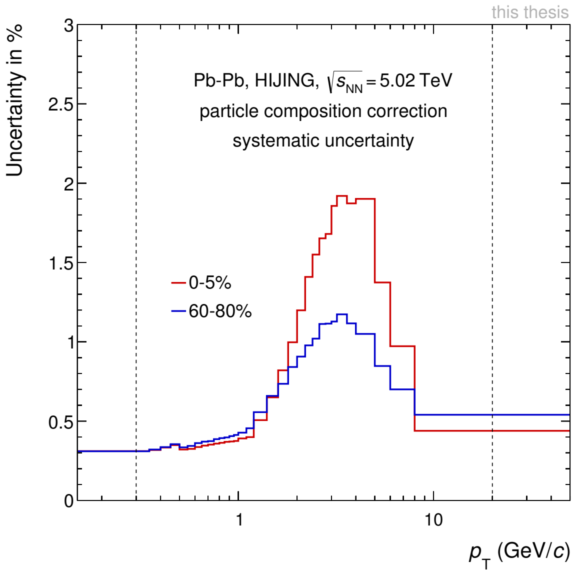

Figure 4.23.: The p_T dependence of the uncertainty of the particle composition correction. The uncertainty dominates at $p_T \approx 3\,\text{GeV}/c$ where the correction factor is the largest due to the more abundant strange baryons in data with respect to MC.

4.7.5 Contamination with Secondary Particles

The uncertainties of the scaling factor used to correct the MC-only secondary contamination correction are driven by two components. The first component is the quality of the template fits. Here the RMS of the differences between fit and data are considered as an contribution to the uncertainties. The second component is estimated by changing the number of templates used. For Pb–Pb collisions, where two templates were used as default, the difference between two and three templates is added to the uncertainties. In case of Xe–Xe collisions the difference to two templates is used. The uncertainties of the correction factor are shown in the lower panels of Figure 4.16. In order to propergate these uncertainties to the transverse momentum distribution, the scaling factor is moved up and down by the uncertainties and the correction is applied to the uncorrected spectra. The ratio of the spectra with the modified scaling factor, to the spectra with the unmodified scaling, is taken into account as uncertainty of the secondary correction. The contribution is significant for low p_T, reaching $\sim$ 4% at $0.2\,\text{GeV}/c$. Towards high p_T, the contribution falls quickly, so the uncertainty is negligible for $p_T > 1\,\text{GeV}/c$.

4.7.6 Transverse Momentum Resolution Correction

The p_T-resolution correction is obtained by an unfolding procedure based on a power-law parametrisation of the corrected p_T distribution. To estimate the influence of this parametrisation, the lower fit boundaries have been varied from its nominal $10\,\text{GeV}/c$ to $8\,\text{GeV}/c$ and $12\,\text{GeV}/c$. The correction factor obtained with the varied fit ranges is compared to the nominal correction, the attributed uncertainty is displayed in Figure 4.24. The other contribution to the uncertainty stems from the additional smearing that is applied. To estimate the effect, the correction factor is calculated without the application of the extra smearing factor. Both contributions are found to be independent of the selected centrality, and are added up in quadrature. The overall uncertainty for Pb–Pb is below 0.1% but nevertheless taken into account. For the data set of Xe–Xe collisions measured with a reduced magnetic field, the uncertainty is larger, but still only reaching up to 0.5% for high p_T. In peripheral collisions the contribution is increased due to a steeper spectrum. Here, the uncertainty amounts up to 1% at $p_{\mathrm{T}} = 50\,\mathrm{GeV}$ in peripheral Xe–Xe collisions and 0.15% in peripheral Pb–Pb collisions.

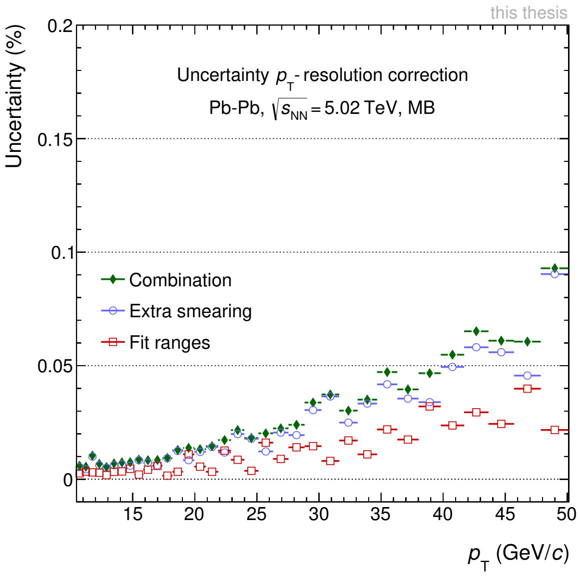

Figure 4.24.: p_{T} dependence of the uncertainty related to the momentum resolution correction. Two contributions are taken into account. The smaller one is related to the variation of the fit ranges, the larger one stems from the additional smearing applied. Overall the contribution is below 0.1%.

The raw spectra are corrected for tracking inefficiency based on MC simulations. As no direct estimation of the uncertainty is possible, the description of a different quantity that can be determined in MC and data is exploited. As this proxy the fraction of tracks reconstructed only with information from TPC to tracks with additional hits in ITS, the matching efficiency $\epsilon_{\text{matching}}$ is chosen. This quantity is shown as a function of transverse momentum in Figure 4.25.

$$\epsilon_{\text{matching}}(p_{\text{T}}) = \frac{dN_{\text{TPC+ITS}}/dp_{\text{T}}}{dN_{\text{TPC-only}}/dp_{\text{T}}} \tag{4.3}$$

The sample of tracks that are reconstructed only employing TPC (TPC-only) information is selected by applying the following selection criteria: TPC refit, $|\text{DCA}_z| < 3.2\,\text{cm}$, $|\text{DCA}_r| < 2.4\,\text{cm}$, number of crossed rows in the TPC $n_{\text{rows}} > 120$, ratio of crossed rows over findable clusters in the TPC $n_{\text{rows}}/n_{\text{findable}} > 0.8$, fraction of shared TPC clusters $n_{\text{shared}}/n_{\text{cluster}} < 0.4$, χ^2 per TPC cluster $\chi^2_{\text{TPC}} < 4$.
For TPC-ITS combined tracks the following criteria are in addition applied: ITS refit and a hit in the first or second layer of the SPD.
The TPC-ITS sample is therefore a subsample of the TPC-only sample. As no ITS information is used,

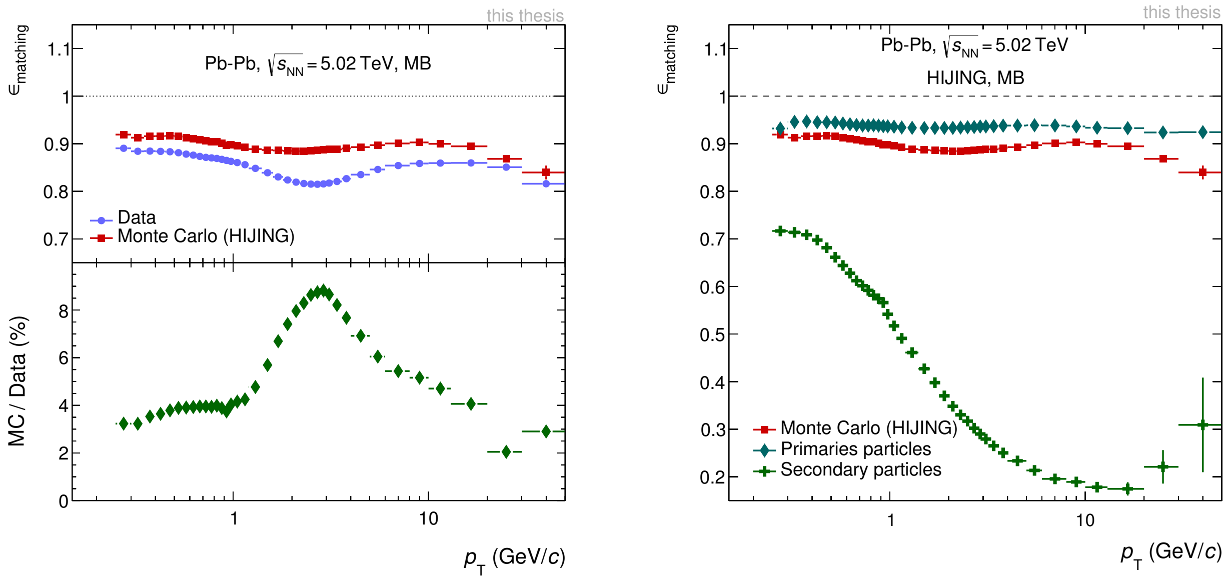

Figure 4.25.: Matching efficiency in data and pure MC is shown in the top panel of the left figure. The lower panel shows discrepancy of data and MC. The discrepancy is due to a different matching efficiencies for primary and secondary particles and an inaccurate description of their relative fractions in MC. The matching efficiency for primary and secondary particles is shown in the right panel.

data taken a high interaction rate is strongly in contaminated with pile up. To prevent an artificial worsening of the systematic uncertainty a track-by-track pile-up rejection based on the expected time difference of bunch-crossing and a signal in the time of flight (TOF) detector is applied.
The ratio of matching efficiencies obtained in data and MC is sensitive to an inaccurate description of the true efficiency.

$$\text{Unc}(p_{\text{T}}) = \left|1 - \frac{\epsilon^{\text{MC}}_{\text{matching}}(p_{\text{T}})}{\epsilon^{\text{Data}}_{\text{matching}}(p_{\text{T}})}\right| \tag{4.4}$$

The deviation of this ratio from unity has been used as the uncertainty on the tracking efficiency in previous publications (lower panel of Figure 4.25 left). The large discrepancy of data and pure MC is due to an inaccurate description of secondary particle production in MC. As discussed in section 4.6.4 secondary particles (from decays of strange hadrons and detector interaction) are more abundant in data as compared to MC. The magnitude of this effect is enlarged for TPC-only tracks, as the selection criteria on DCA have been relaxed. Secondary particles have a very low matching efficiency with respect to primary particles shown in the right panel of Figure 4.25. For primary particles the matching efficiency is close to 95% while the efficiency for secondary particles quickly decreases with p_{T} and reaches a minimum of about 10%.

In section 4.6.4 a method to estimate the true fractions of secondary particles in data, based on template fits to the DCA$_r$ distribution has been introduced. This procedure is again utilized to estimate the amount of secondaries with the selection criteria used in the TPC-only sample. The MC matching efficiency is then constructed by scaling primary and secondary particle matching efficiency according to the true fractions of secondaries found in data. After this rescaling the agreement of the matching efficiencies in data and MC is greatly improved (see Figure 4.26), with a remaining difference of about 1-1.5%, which is assigned as systematic uncertainty.

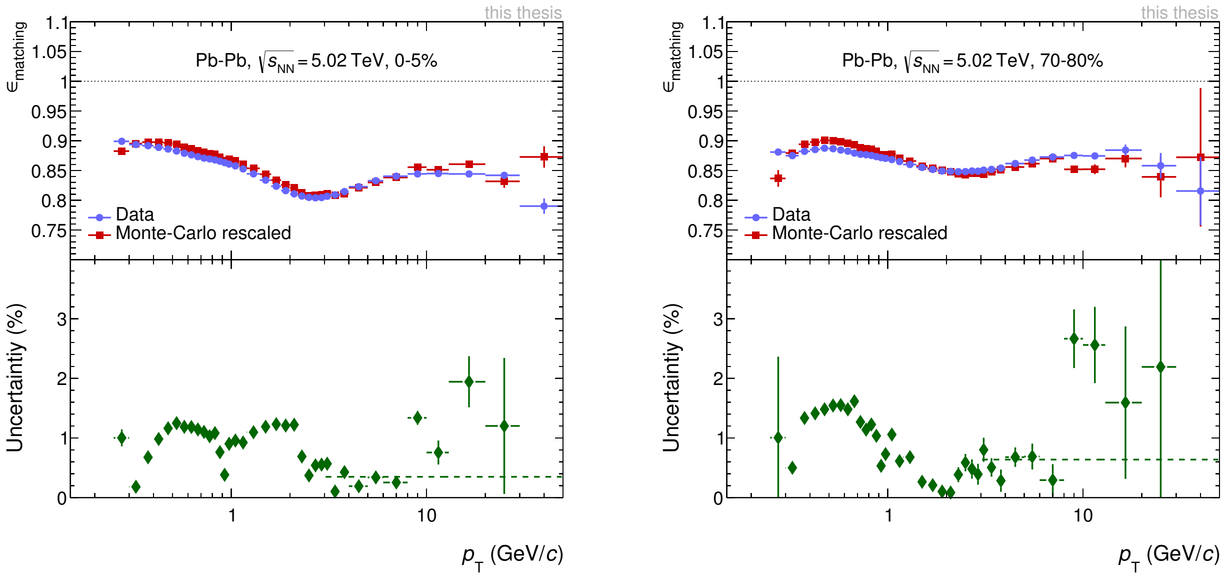

Figure 4.26.: The ratio of the efficiencies for data and the reweighted MC.

In case of Xe–Xe collisions the reweighting is not as successful as in Pb–Pb and the uncertainty is $\sim$ 3% for low and $\sim$ 1% at high p_{T}.

4.7.8 Material Budget

As the correction depends on a detector simulation within the GEANT framework, the description of the detector material is a potential source of an uncertainty. In the past the uncertainty of the GEANT simulation was estimated by varying the material budget in the simulation by ±7% [96]. There an uncertainty of 1.5-0.2% was estimated. The analysis of photon conversions could however provide a better constraint for the material budget of only ±4.5% [85]. So far the simulation with a smaller variation has not been repeated, thus the uncertainty found previously is scaled by a factor of 4.5/7. This uncertainty is applied to all collisions systems.

4.7.9 Influence of the Interaction Rate

The data set of Pb–Pb at $\sqrt{s_{\mathrm{NN}}} = 5.02\,\mathrm{TeV}$ was taken at various interaction rates, spanning between 1.34 kHz and 6.87 kHz. As the detector performance depends on the interaction rate, the influence on the measurement is not negligible. This effect is investigated by splitting the complete sample of runs taken into two classes of interaction rate. A high interaction rate sample containing runs taken at a rate above 4.5 kHz and a low interaction rate sample with runs taken a rate of 2.5 kHz and less. The interaction rate of the runs is shown in Figure 4.27 left. The characteristic shape of the interaction rate vs. run is given by the decreasing intensity during a fill cycle. The uncorrected spectra of theses three classes are shown in the top panel of Figure 4.27 right. While the uncorrected spectra of the two samples significantly differ from a spectra calculated using all the runs of the period, the difference is lower when the corrected spectra are compared (lower panel of Figure 4.27 right). To account for the remaining influence of the interaction rate, the deviation of the low interaction-rate class to the whole period is taken into account as a p_{T}-dependent uncertainty.

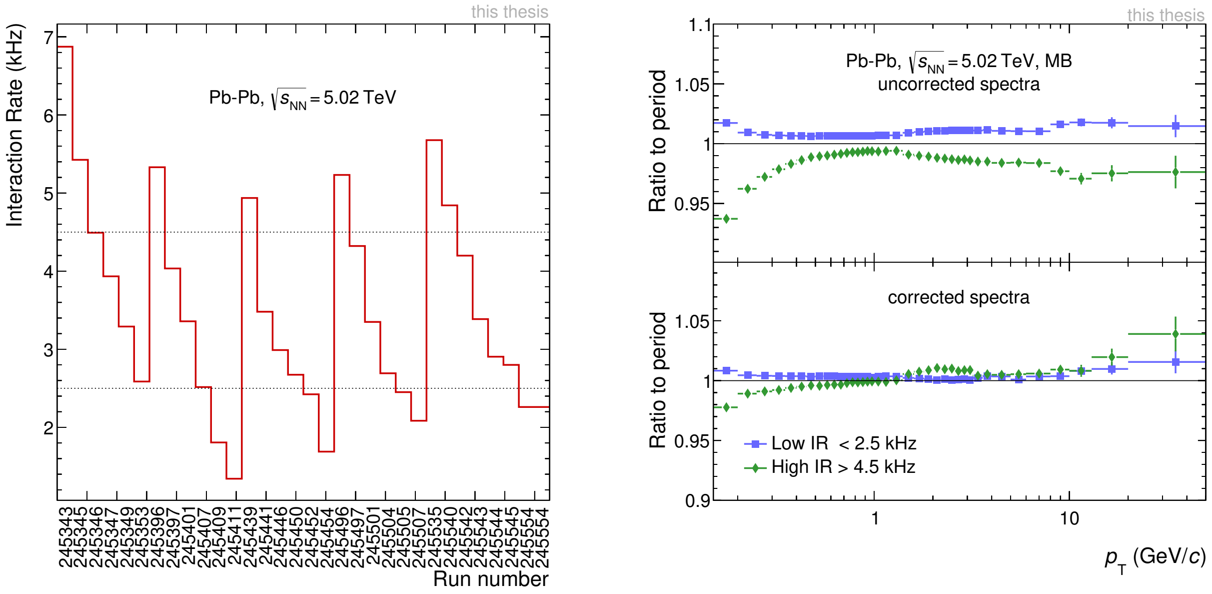

Figure 4.27.: The interaction rate (IR) of the runs used in the analysis of Pb–Pb collisions with $\sqrt{s_{\mathrm{NN}}} = 5.02\,\mathrm{TeV}$ (left). The horizontal lines indicate the separation of the sample into three classes in interaction-rate. The figure on the right shows the ratio of the high and low IR sample to the full data sample for uncorrected spectra (top) and corrected spectra (lower panel).

5 pp Reference

The measurement of the charged-particle production in pp collisions is not only a baseline measurement needed for the determination of the nuclear modification factor, but provides insights into particle production and it challenges our understanding of collective behaviour.

5.1 Measurement of Transverse-Momentum Distributions in pp Collisions

During its first two running periods, the LHC provided a wide range of collision energies of pp collisions. Most notably the baseline for the R_{AA} at $\sqrt{s_{\mathrm{NN}}} = 2.76\,\mathrm{TeV}$, but also collisions at $\sqrt{s} = 0.9, 7, 8\,\mathrm{TeV}$ were recorded during Run 1 [96]. Until Run 2 no measurement of pp at $\sqrt{s} = 5.02\,\mathrm{TeV}$ was performed.

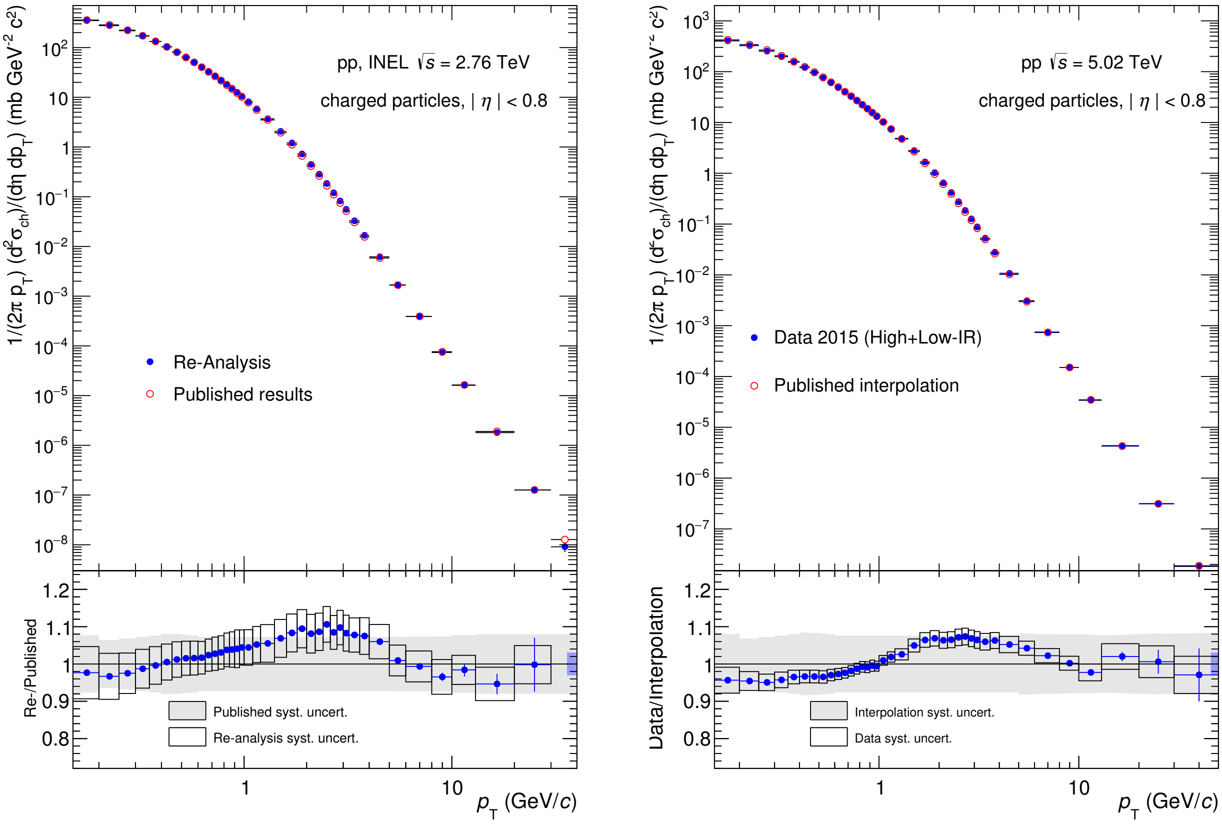

Figure 5.1.: The measured cross sections for charged-particle production in pp collisions at $\sqrt{s} = 2.76\,\mathrm{TeV}$ (left) and $\sqrt{s} = 5.02\,\mathrm{TeV}$ (right). The lower panel of the left figure shows the ratio of the cross section used in this analysis to one from a previous publication [96]. The lower panel of the right figure shows the ratio of the measured cross section to an interpolated cross section used for the determination of R_{pPb} [68, 106], as no measurement of pp at $\sqrt{s} = 5.02\,\mathrm{TeV}$ was availiable at that time.

Therefore, a pp reference for the determination of the R_{pPb} at $\sqrt{s_{\mathrm{NN}}} = 5.02\,\mathrm{TeV}$ [68, 106] had to be constructed otherwise during Run 1 [96]. This reference was built assuming a power-law dependence of the charged-particle yield for a given transverse momentum below $p_{\mathrm{T}} < 5\,\mathrm{GeV}/c$. The interpolation of cross sections at $\sqrt{s} = 2.76\,\text{TeV}$ and $\sqrt{s} = 7\,\text{TeV}$ was used. For higher momenta the measurement at $\sqrt{s} = 7\,\text{TeV}$ was scaled down by a factor obtained from NLO calculations. In addition the constructed reference was smoothed at high p_{T} to reduce statistical fluctuations, using a power-law function.

During Run 2 a sample of pp collisions at $\sqrt{s} = 5.02\,\text{TeV}$ was recorded. The measured production cross section for charged particles is shown in Figure 5.1 (right). The measurement was performed in the kinematic range of $150\,\text{MeV}/c \leq p_{\mathrm{T}} < 50\,\text{GeV}/c$ for particles with a pseudorapidity of $|\eta| < 0.8$. The results are compared to the interpolation used during Run 1. The comparison confirms that the procedure used in the interpolation describes the physics well. Especially at high and low p_{T} interpolation and measurement agree well, while at intermediate p_{T} a clear difference can be seen. This difference, still covered by the systematic uncertainties, originates from the correction for inaccurate particle composition in the Monte Carlo generators (section 4.6.2).

The measurement is compared to predictions from the EPOS LHC event generator [107], which incorporates collective effects, and PYTHIA 8 [98] with the Monash-2013 tune [108] including colour reconnection in Figure 5.2. Both event generators describe the p_{T} distribution similarly well at both energies, reproducing the spectral shape within 20%.

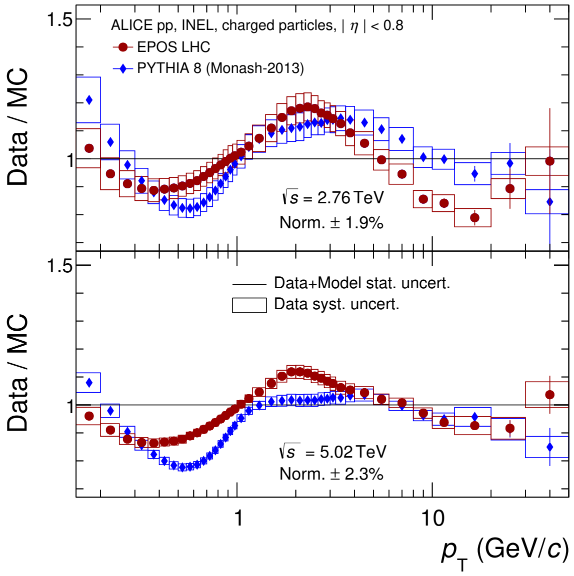

Figure 5.2.: Comparison of the charged-particle transverse-momentum spectra measured in pp collisions to model calculations, for $\sqrt{s} = 2.76\,\text{TeV}$ (top) and $\sqrt{s} = 5.02\,\text{TeV}$ (bottom). The statistical uncertainties of the data and model calculations are added in quadrature. The boxes represent the systematic uncertainties of the data [109].

The new analysis strategies described before were also applied to the measurement of the transverse-momentum distributions in pp collisions. In addition to the analysis of events with the new collision energy, also the data sample at $\sqrt{s} = 2.76\,\text{TeV}$ has been reanalysed. The result of this measurement is shown in Figure 5.1 (left), it is compared with the published result. While the new measurement confirms the published results, the information on the particle fractions gained during Run 1 leads to an enhancement at intermediate p_{T}. Compared to the results at $\sqrt{s} = 5.02\,\text{TeV}$ the systematic uncertainties at $\sqrt{s} = 2.76\,\text{TeV}$ are larger. This is related to a different performance of the detectors and is also observed in Pb–Pb. In the previous publications of R_{AA} the reference was smoothed, to account for statistical uncertainties using a power-law dependence of the transverse-momentum distribution at high p_{T}. This procedure however is not applied in the measured R_{AA} shown in the following section, which is compensated by a coarser binning at high p_{T}. With the help of a van der Meer scan [110] the measured transverse-momentum distribution can be translated into a momentum differential cross section.

5.2 Construction of a pp Reference at $\sqrt{s} = 5.44\,\mathrm{TeV}$

To calculate the nuclear modification factor of charged particles in Xe–Xe collisions recorded at $\sqrt{s_{\mathrm{NN}}} = 5.44\,\mathrm{TeV}$, a pp reference at the same collision energy is needed. To obtain a reference, two methods have been implemented. The default procedure assumes a power-law dependence of the cross section at a fixed p_{T}. This is also the method employed before to generate the pp-reference at $\sqrt{s} = 5.02\,\mathrm{TeV}$ before a measurement at that collision energy became possible. An example of this interpolation can be see in Figure 5.3 (left). The top panel shows the default interpolation making use of the measurements at $\sqrt{s} = 5.02\,\mathrm{TeV}$ and $\sqrt{s} = 7\,\mathrm{TeV}$. The lower panel shows the same calculation performed using the measurement at $\sqrt{s} = 2.76\,\mathrm{TeV}$ instead of the one at $\sqrt{s} = 5.02\,\mathrm{TeV}$. Both methods are in good agreement within 5%. In addition, the measurement at $\sqrt{s} = 7\,\mathrm{TeV}$ was not corrected for inaccurate particle composition in the MC simulation. Therefore, the interpolation has been done without particle composition correction for $\sqrt{s} = 5.02\,\mathrm{TeV}$ as well.

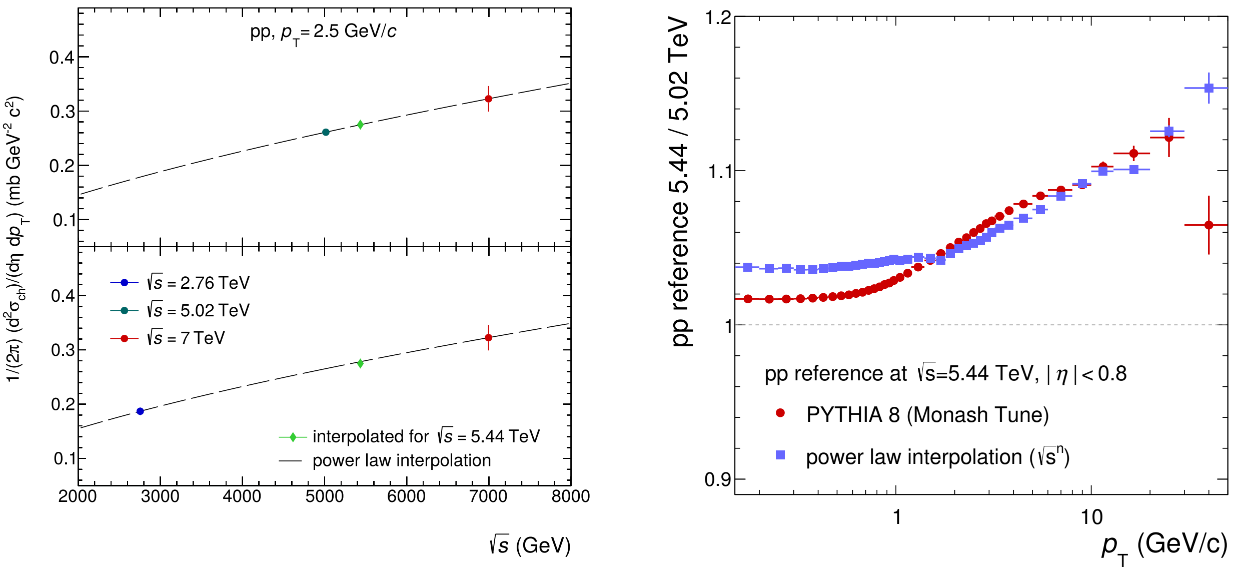

Figure 5.3.: Left: The power-law interpolation used to construct the pp reference at $\sqrt{s} = 5.44\,\mathrm{TeV}$. Both panels show the interpolation for the same exemplary value of p_{T}. The top panel shows the default interpolation between $\sqrt{s} = 5.02\,\mathrm{TeV}$ and $\sqrt{s} = 7\,\mathrm{TeV}$, the lower panel the interpolation between $\sqrt{s} = 2.76\,\mathrm{TeV}$ and $\sqrt{s} = 7\,\mathrm{TeV}$. Right: The scaling factors from $\sqrt{s} = 5.02\,\mathrm{TeV}$ to $\sqrt{s} = 5.44\,\mathrm{TeV}$ are derived from power law interpolation and model comparison [109].

The other possibility to construct a reference out of the transverse-momentum distributions generated by event generators such as PYTHIA 8 or EPOS. Two sets of events were generated with both generators, at $\sqrt{s} = 5.02\,\mathrm{TeV}$ and at $\sqrt{s} = 5.44\,\mathrm{TeV}$.

The ratios of $\sqrt{s} = 5.02\,\mathrm{TeV}$ to $\sqrt{s} = 5.44\,\mathrm{TeV}$ obtained from all three methods are compared with each other in Figure 5.3(right). While differences are visible between the power-law interpolation and the generator based methods at low p_{T}, the overall agreement is good with a maximal deviation of 2%.

The systematic uncertainty of the constructed pp reference is estimated by adding two contributions linearly. For each p_{T} interval the systematic uncertainties between $\sqrt{s} = 5.02\,\mathrm{TeV}$ and $\sqrt{s} = 7\,\mathrm{TeV}$ are interpolated. In addition the maximum deviation of the power-law method to either model calculations of 2% is added independently of the momentum.

6 Results

6.1 Transverse Momentum Distributions in Collisions of Pb nuclei

The transverse momentum distribution of primary charged particles in Pb–Pb collisions is shown in Figure 6.1 for collision energies of $\sqrt{s} = 2.76\,\text{TeV}$ (left panel) and $\sqrt{s} = 5.02\,\text{TeV}$ (right panel). The yields are presented as the double differential charged-particle yields normalised to the number of events, for nine bins of centrality. In addition, the yields for pp and p–Pb collisions at $\sqrt{s} = 5.02\,\text{TeV}$ are presented. For better visibility the yields of Pb–Pb collisions are scaled. The lower panels show the systematic uncertainties for selected yields. At $\sqrt{s_{\text{NN}}} = 2.76\,\text{TeV}$ the uncertainties are dominated by the contribution of the event selection, while the uncertainties at $\sqrt{s} = 5.02\,\text{TeV}$ are driven by the secondary correction at low p_{T} and by track selection at high p_{T}. In peripheral collisions of lead ions the resulting spectra exhibits a similar p_{T} dependence as the yield in pp collisions. For more central collisions the spectrum is progressively depleted above $p_{\text{T}} = 5\,\text{GeV}/c$ with respect to peripheral collisions.

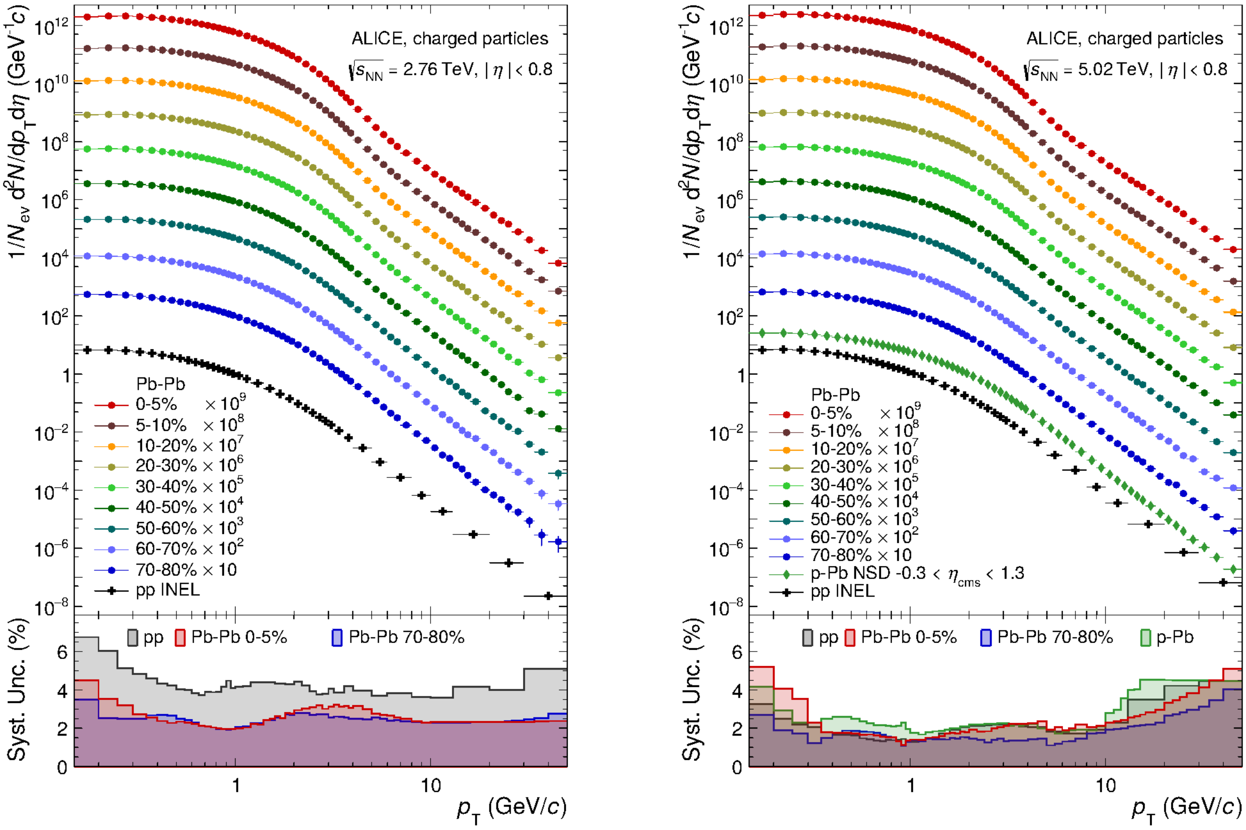

Figure 6.1.: The transverse-momentum distribution of charged particles measured in Pb–Pb collisions at $\sqrt{s} = 2.76\,\text{TeV}$ (left) and $\sqrt{s} = 5.02\,\text{TeV}$ (right). For better visibility the yields are scaled. Additionaly the yields of pp and p–Pb collisions are shown for the same centre-of-mass energy. The lower panels of the figures show the systematic uncertainties for selected yields. Published in [109].

6.2 Ratio of Yields (5.02 TeV/2.76 TeV)

The evolution of the charged-particle distribution with increasing collision energy is investigated by determining the ratio between measured yields at both energies. The ratios are shown in Figure 6.2 and they demonstrate a similar trend for all centralities in Pb–Pb and also for pp collisions. At low p_{T}, the value of the ratio is ~ 1.24, as expected from the already observed increased charged-particle production [54].

Towards higher p_{T}, the ratios increase monotonously, showing the significantly increased charged-particle production at high p_{T} (harder spectrum) with increasing centre-of-mass energy. At high p_{T}, the ratio in central collisions seems to indicate a less pronounced increase at high p_{T} than in pp, while for peripheral collisions the hardening shows the same magnitude as in pp collisions. This difference between peripheral and central collisions might indicate a stronger energy loss in central collisions at $\sqrt{s} = 5.02\,\mathrm{TeV}$ compared to $\sqrt{s} = 2.76\,\mathrm{TeV}$.

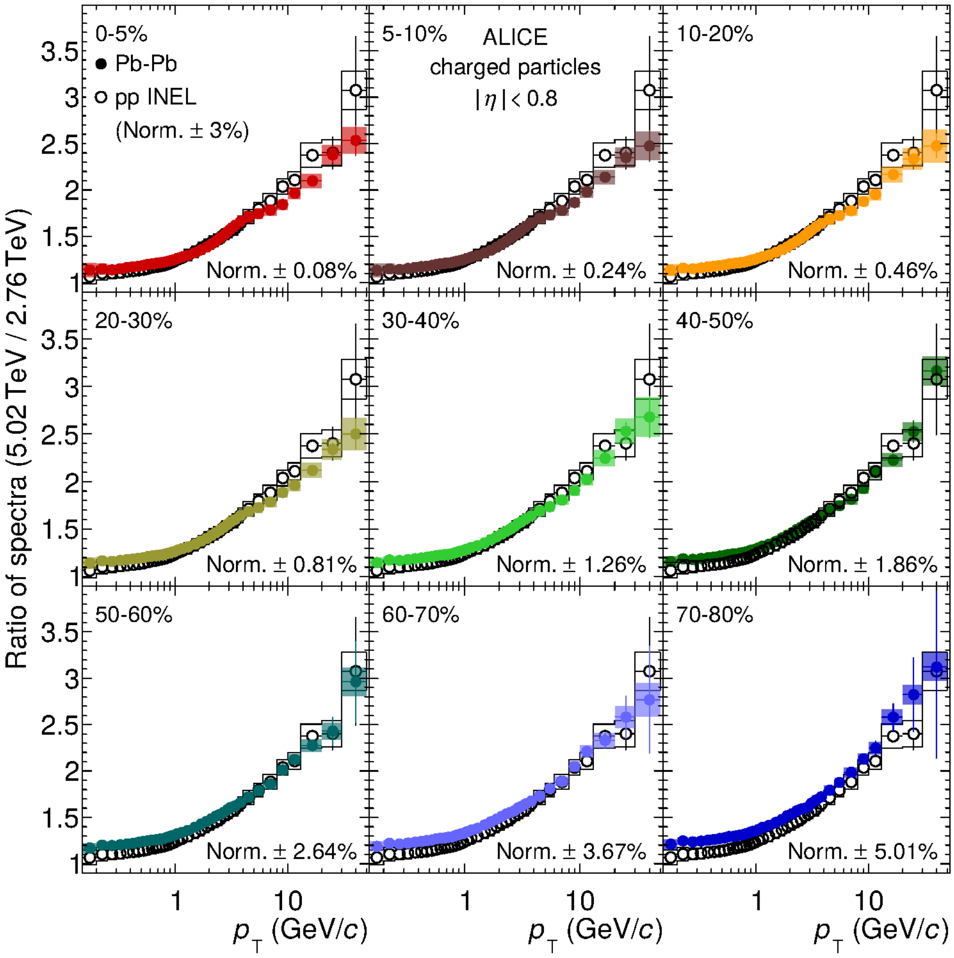

Figure 6.2.: The ratio of charged particles yields in Pb–Pb collisions at $\sqrt{s_{\mathrm{NN}}} = 5.02\,\mathrm{TeV}$ to yields at $\sqrt{s_{\mathrm{NN}}} = 2.76\,\mathrm{TeV}$. Filled symbols show Pb–Pb for different classes of centrality, while open symbols show the same value in pp. The normalisation uncertainties are quoted for each centraltiy.Published in [109].

6.3 Ratio of ratios (Pb–Pb/pp)

The evolution of the ratios is further compared by calculating the double ratio of the centrality dependent ratios in Pb–Pb to the ratio in pp (RR_{PbPb}) (Figure 6.3). Two different observations can be made, first the level of the RR_{PbPb} in peripheral collisions is higher than the RR_{PbPb} in central collisions. This is unexpected as the increase of charged particle production in central collisions is larger with respect to peripheral collisions, as shown in section 2.1. The p_{T} independent RR_{PbPb} can also be calculated from the charged particle production measured independently based on the ITS [51–54]. The estimation from this measurement is shown as a dotted line at low p_{T} in Figure 6.3; it agrees with the p_{T} dependent measurement for low p_{T}. The reversed level is therefore not only seen in the measurement of charged particle spectra. It is however within systematic uncertainties.

The level aside, the RR_{PbPb} in central collisions shows a decreasing trend and a value below unity for $p_{\mathrm{T}} > 5\,\mathrm{GeV}/c$, while in peripheral collisions the RR_{PbPb} shows no such decreasing trend. This might be related to parton energy loss in central collisions, that leads to a reduced hardening of the charged particle yield.

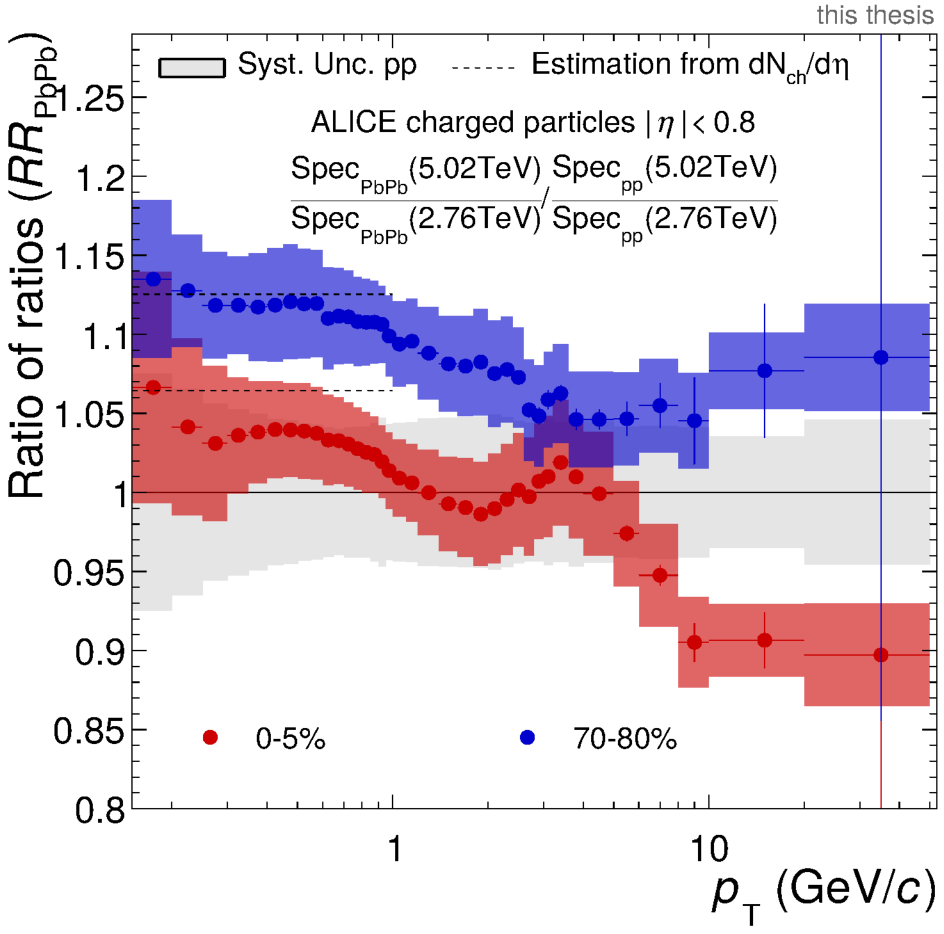

Figure 6.3.: The double ratio of spectra at two energies in Pb–Pb to pp. The filled symbols are calculated from data presented in this work, while the dotted lines are calculated from independently measured charged particle densities [51–54]. The coloured boxes show the systematic uncertainties in the measurement of Pb–Pb while the grey band around unity indicates the uncertainties of the measurement at pp.

6.4 Nuclear Modification Factor in Pb–Pb Collisions

The nuclear modification factors as a function of p_{T} for nine centrality intervals are shown in Figure 6.4. Filled symbols present the measurement at $\sqrt{s_{\mathrm{NN}}} = 5.02\,\mathrm{TeV}$, the open symbols display the reanalysis at $\sqrt{s_{\mathrm{NN}}} = 2.76\,\mathrm{TeV}$. The normalisation uncertainties, originating from centrality selection as well as from the determination of T_{PbPb}, are shown as boxes around unity at low p_{T}. Both measurements exhibit similar features, with only moderate suppression ($R_{\mathrm{PbPb}} \sim 0.6 - 0.7$) for peripheral collisions (70–80%) and a pronounced minimum of $R_{\mathrm{PbPb}} < 0.2$ at $p_{\mathrm{T}} \sim 6 - 7\,\mathrm{GeV}/c$ for central collisions. Towards higher $p_{\mathrm{T}} > 7\,\mathrm{GeV}/c$ a significant rise of the nuclear modification factor can be observed. Remarkably both measurements of R_{PbPb} indicate the same suppression in central and semi-central collisions. In peripheral collisions a slightly weaker suppression at $\sqrt{s} = 5.02\,\mathrm{TeV}$ can not be ruled out. In conjunction with the hardening of spectra for higher centre-of-mass energies, similar nuclear modification factors hint towards a stronger energy loss in a hotter and denser medium.

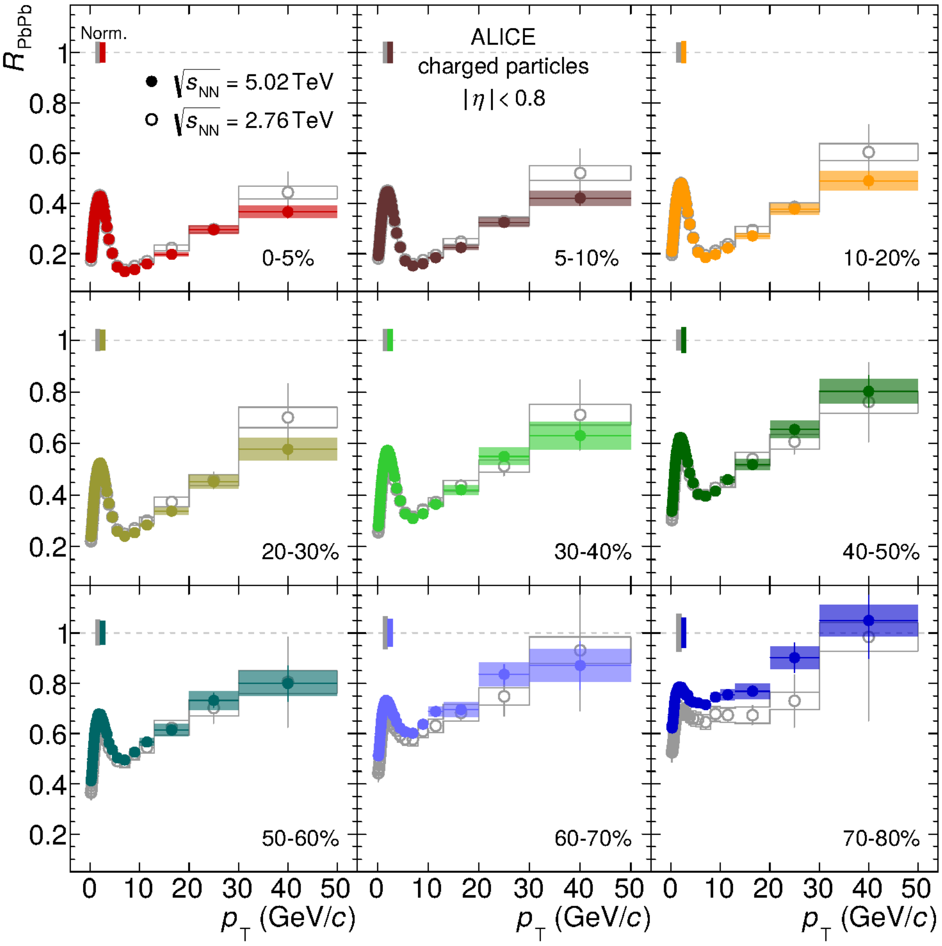

Figure 6.4.: Nuclear modification factors in Pb–Pb collisions at $\sqrt{s} = 5.02\,\mathrm{TeV}$ (filled symbols) and $\sqrt{s} = 2.76\,\mathrm{TeV}$ (open symbols) for nine classes of centrality. The normalisation uncertainty is shown as boxes around unity at low p_{T}. Published in [109].

The previously published measurement of the nuclear modification factor in p–Pb collisions has been repeated including the improved methods developed for the analysis of Pb–Pb and pp collisions. In addition, the constructed pp reference used in the previous publications [68] was made obsolete by the measurement of pp collisions at $\sqrt{s} = 5.02\,\text{TeV}$. Both the improved techniques as well as the measured pp reference reduce the systematic uncertainties on the R_{pPb} significantly, as visible in Figure 6.5. While

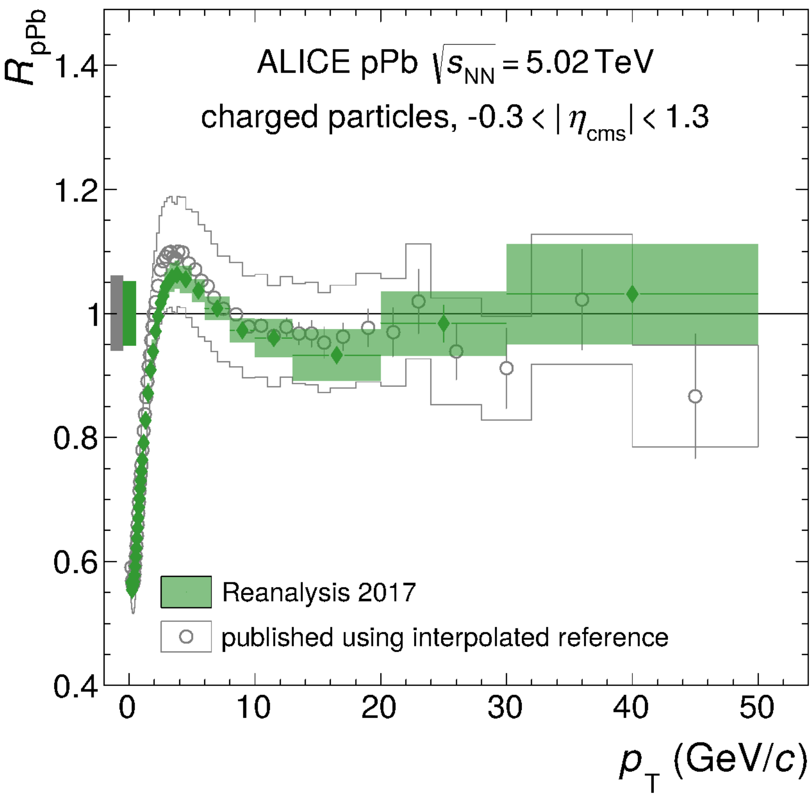

Figure 6.5.: The p_{T}-dependent nuclear modification factor in p–Pb collisions. The filled symbols show the R_{pPb} with the improved analysis methods presented in this work, as published in [109]. Open symbols show R_{pPb} as presented in a previous publication [68].

the enhancement around $p_{\text{T}} \approx 5\,\text{GeV}/c$ is confirmed with the reduced uncertainties a possible $R_{\text{pPb}} < 1$ for $12\,\text{GeV}/c < p_{\text{T}} < 30\,\text{GeV}/c$ is not excluded by the data.

The observed enhanced charged-particle yield, often referred to as a Cronin-like enhancement [30], is likely to be dominated by an increased yield of protons in p–Pb compared to pp collisions [111]. A R_{pPb} around unity proves that the observed modifications of the charged yield in heavy-ion collisions are not caused by initial state effects.

6.6 Nuclear Modification Factor Comparison to CMS

The results obtained in this analysis are compared to published results by the CMS collaboration [65] in Figure 6.6. Compared to ALICE, CMS can operate at a significantly higher interaction rate as the detector is largely based on fast calorimeters and silicon trackers. This results in a much higher number of events, which together with a sophisticated trigger system leads to an extended range towards high p_{T}. In addition, a higher magnetic field strength improves the p_{T}-resolution at high p_{T}, at the cost of a reduced capability at low p_{T} [112].

The measured R_{PbPb} shows a good agreement for the momentum reach covered by both experiments. While the results presented in this work reach $p_{\mathrm{T}} = 50\,\mathrm{GeV}/c$, CMS shows a continuous rise of R_{PbPb} with increasing R_{PbPb}, reaching $R_{\mathrm{PbPb}} \approx 0.8$ for $p_{\mathrm{T}} > 100\,\mathrm{GeV}/c$. The measured R_{pPb} for both experiments

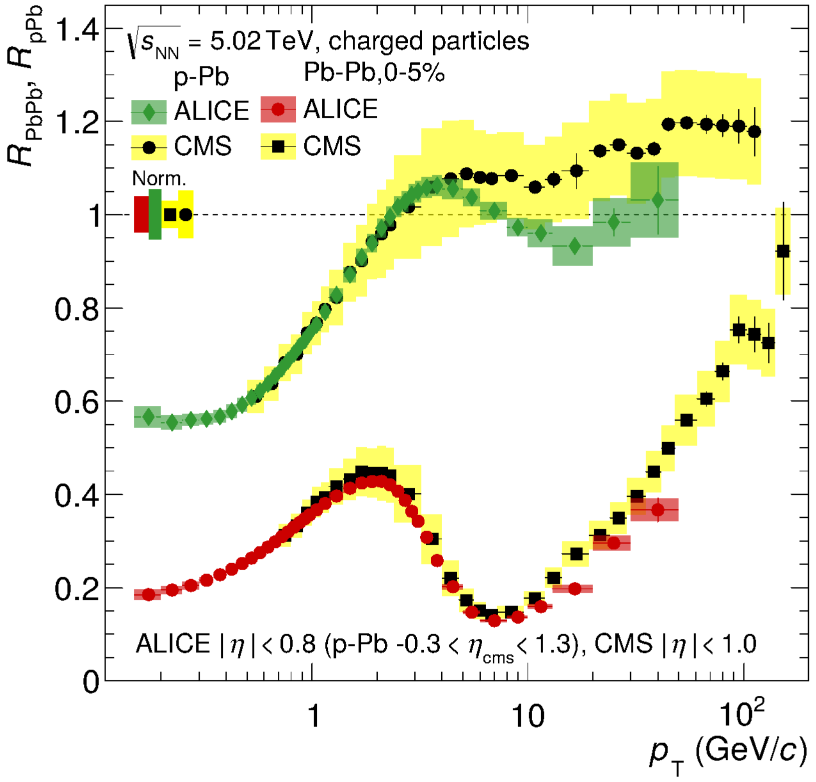

Figure 6.6.: The R_{PbPb} measured in this work and the R_{pPb} compared to the nuclear modification factors published by the CMS collaboration [65].Published in [109].

rely on a measured pp reference spectrum and show a good agreement for $p_{\mathrm{T}} < 10\,\mathrm{GeV}/c$ while the R_{pPb} presented in this work is compatible with unity at high p_{T}, the measurement by the CMS collaboration shows an departure of unity for high p_{T}, which however can at present not be ruled out by the ALICE data.

The transverse momentum distributions in collisions of xenon ions is shown in the top panel of Figure 6.7 for all nine classes of centrality together with the pp-reference spectrum. This is obtained by scaling the interpolated differential cross section (section 5) by a Glauber MC calculation of the nucleon-nucleon cross section in pp [113]. The lower panel shows the systematic uncertainty in Xe–Xe collisions for two centrality classes and the uncertainty of the pp-reference. The systematic uncertainties of spectra in Xe–Xe are dominated by the contribution of the secondary scaling (DCA$_r$-template fits) at low p_{T} and by the contribution of the tracking efficiency at intermediate $p_{\mathrm{T}} \sim 2-3\,\mathrm{GeV}/c$. As for the pp-reference, the uncertainties are largely dominated by the interpolation procedure and hence are larger with respect to Xe–Xe collisions. In peripheral collisions the spectra in Xe–Xe collision show a p_{T}-dependence comparable to pp. For more central collisions an increase of the yield of high p_{T} particles can be observed. In peripheral collisions, the spectra are limited by statistical precision and therefore not shown up to the highest p_{T}.

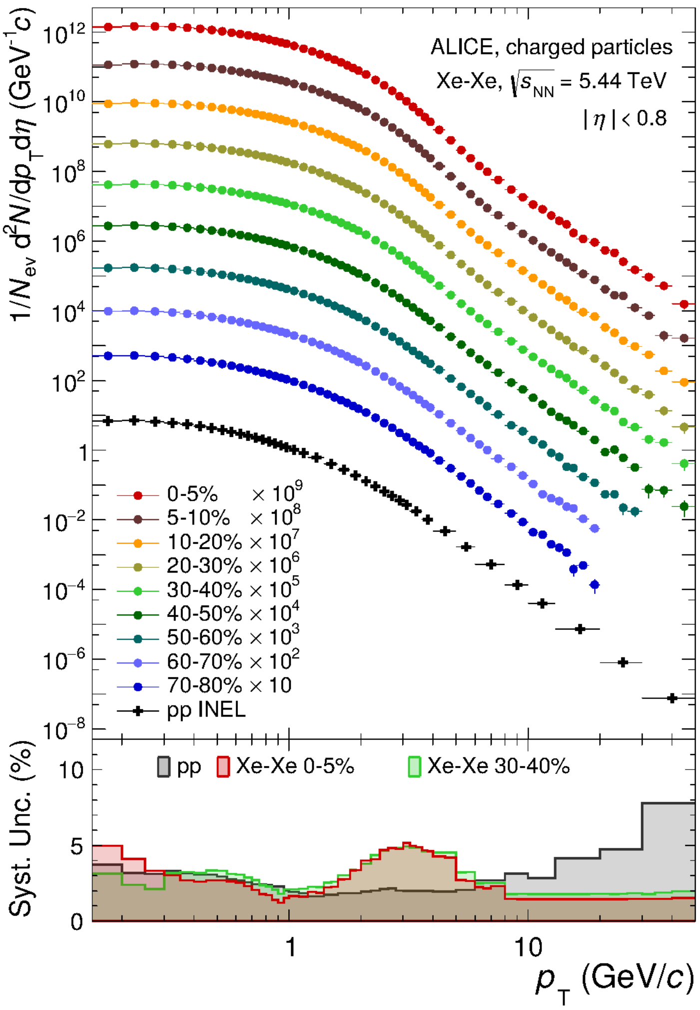

Figure 6.7.: Transverse momentum distribution of charged particles measured in Xe–Xe collisions at $\sqrt{s} = 5.44\,\mathrm{TeV}$. The yields are scaled for better visibility. Yields of peripheral collisions exhibit low statistical precision towards high p_{T}. The lower panel shows the systematic uncertainties for selected yields [114].

Nuclear Modification Factor

The nuclear modification factor as a function of p_T is shown in Figure 6.8. Here, R_XeXe is constructed using the interpolated pp-reference at $\sqrt{s} = 5.44\,\mathrm{TeV}$ (described in chapter 5) and using the values for the nuclear thickness function $\langle T_\mathrm{XeXe}\rangle$ from Table 3.1. The values for R_XeXe are compared to the Pb–Pb collisions in the corresponding classes of centrality. The normalisation uncertainty is shown as boxes around unity at low p_T. They stem from the uncertainty in the centrality selection as well as from uncertainties in the determination of $\langle T_\mathrm{XeXe}\rangle$. The uncertainty of the nuclear thickness function is larger in Xe–Xe than in Pb–Pb collisions, because the nuclear-charge-density distribution of the deformed ^{129}Xe nucleus is known with less precision [58]. In general, the behaviour and shape of R_XeXe are comparable to the shape and behaviour of R_PbPb, namely a stronger suppression in central and a weaker suppression in more peripheral events. A difference in the magnitude of this suppression is observed for all centralities and for the full momentum range. Nevertheless the strongest suppression by a factor of 6 occurs at $p_\mathrm{T} \sim 6-7\,\mathrm{GeV}/c$. This is the same momentum range where the strongest suppression occurs in Pb–Pb collisions. While R_XeXe and R_PbPb are similar for central collisions, the suppression in peripheral collisions is much weaker in Xe–Xe than in Pb–Pb. This difference of suppression at the same centrality class can

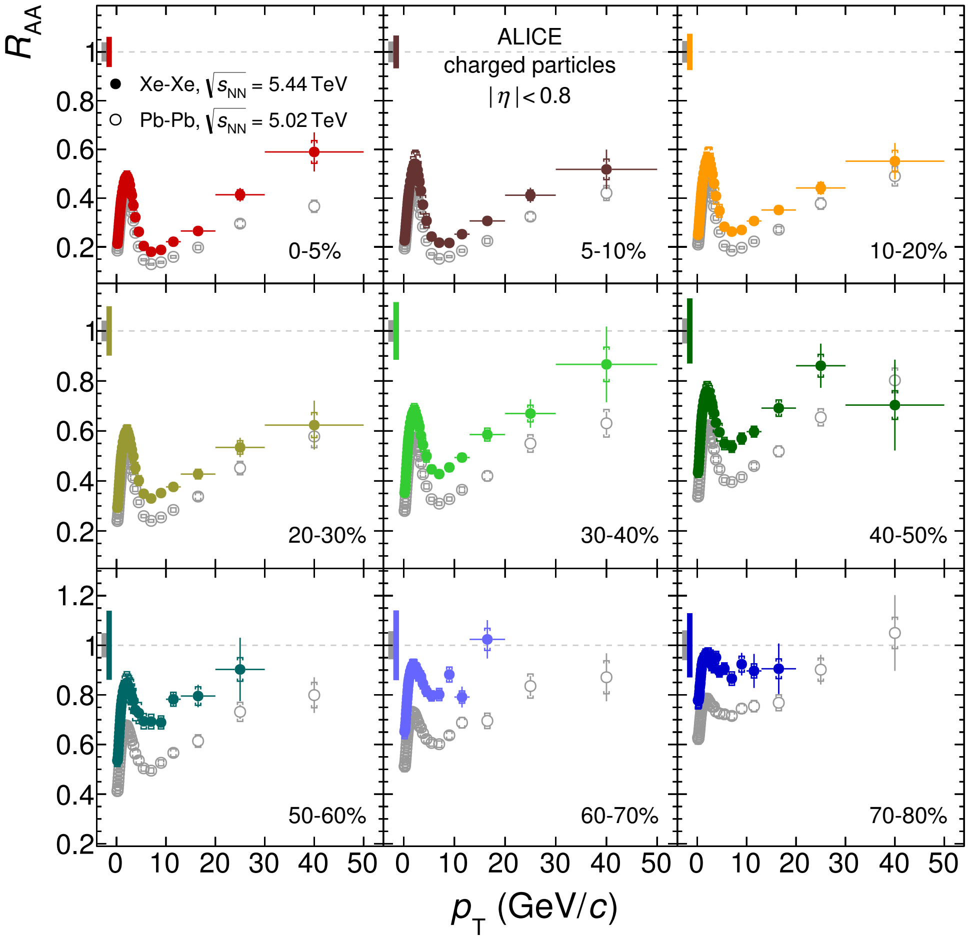

Figure 6.8.: The nuclear modification factors in collisions of Xenon nuclei compared to the R_PbPb measured in Pb–Pb (grey, open symbols). In Xe–Xe collisions, R_XeXe shows a similar behaviour with a maximal suppression for $p_\mathrm{T} \sim 6-7\,\mathrm{GeV}/c$ and a rise in R_XeXe for higher p_T. In peripheral collisions R_XeXe is larger than R_PbPb indicating a reduced suppression within the same class of centrality. The values for $\langle N_\mathrm{coll}\rangle$ for the different collision systems are however not comparable within centrality intervals [114].

be attributed to the respectively larger path length in Pb–Pb collisions.

It has to be noted that the same class of centrality in these different systems does not imply similar collision geometry which results in a significant difference between R_{XeXe} and R_{PbPb}, as seen in the comparison. In fact, N_{coll} and N_{part} differ in the same class of centrality for the two collision systems, as can be seen in Table 3.1.

Therefore, a comparison of the different R_{AA} not in terms of centrality but in terms of energy density is favourable. Such comparisons are done with the $\langle d\mathrm{N}_{\mathrm{ch}}/d\eta\rangle$ as a measure of the system size and are shown in the following section.

6.8 Comparison of Results from Pb–Pb and Xe–Xe

As seen in the previous section, the nuclear modification factors of Xe–Xe and Pb–Pb collisions show significant differences, especially in peripheral collisions. This is attributed to the larger path length in Pb–Pb collisions, leading to a larger suppression compared to Xe–Xe collisions in the same class of centrality. In central Pb–Pb collisions high numbers of binary nucleon-nucleon collisons are reached $\langle N_{\mathrm{coll}}\rangle^{0-5\%}_{\mathrm{PbPb}} = 1777 \pm 59$. In Xe–Xe these values are much lower $\langle N_{\mathrm{coll}}\rangle^{0-5\%}_{\mathrm{XeXe}} = 948.9 \pm 75$, comparable to

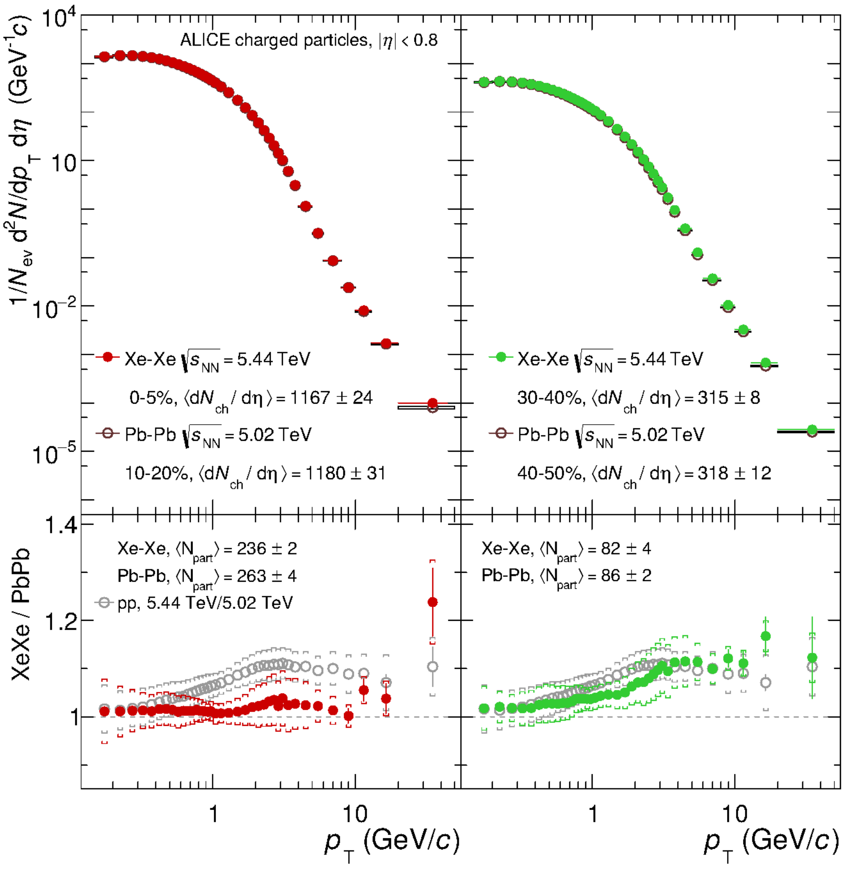

Figure 6.9.: Comparison of transverse-momentum distributions in Xe–Xe (filled symbols) and Pb–Pb (open symbols) in centrality classes with a comparable value of $\langle d\mathrm{N}_{\mathrm{ch}}/d\eta\rangle$. In the lower panels the ratio Xe–Xe/Pb–Pb is compared to the ratio of interpolated and measured pp reference at $\sqrt{s} = 5.44\,\mathrm{TeV}$ and $\sqrt{s} = 5.02\,\mathrm{TeV}$ [114].

10–20% central Pb–Pb collisions $\left(\langle N_{\text{coll}}\rangle^{10-20\%}_{\text{PbPb}} = 973.4 \pm 37\right)$.
A measure of the collision's energy density is given by the $d\text{N}_{\text{ch}}/d\eta$ measurement. This value has been determined within the ALICE collaboration based on measurements in the ITS [53, 54, 58].
In Figure 6.9, the spectra of Xe–Xe and Pb–Pb collisions are compared directly for similar values of $\langle d\text{N}_{\text{ch}}/d\eta\rangle$. The magnitude and shape of the spectra in 0–5% most central Xe–Xe collisions is remarkably well matched by the spectra of 10–20% most central Pb–Pb collisions at lower p_{T} ($< 10\,\text{GeV}/c$). In this momentum range the expansion of the system is driven by fluid dynamics. At higher p_{T}, the charged particle yield in 0–5% most central Xe–Xe collisions exceeds the yield in 10–20% central Pb–Pb collsions. This is attributed to the higher collision energy that results in a harder spectrum, which is also found in pp. For comparison, the lower panel of Figure 6.9 shows the ratio of spectra in Xe–Xe to Pb–Pb collisions (coloured) together with the ratio of the interpolated cross section in pp collisions at $\sqrt{s} = 5.44\,\text{TeV}$ to the measurement at $\sqrt{s} = 5.02\,\text{TeV}$.
In semi-central collisions (Figure 6.9 right) differences between Xe–Xe and Pb–Pb collisions are not limited to high p_{T}, but are increasing with p_{T}. At high p_{T} the differences amount to 10–15%.

The nuclear modification factor as a function of $d\text{N}_{\text{ch}}/d\eta$ is shown in Figure 6.10. It is evaluated in three different ranges of transverse momentum (low/medium/high) for all measured collisions systems. The ranges are chosen such that they cover the local maximum at low p_{T} ($p_{\text{T}} = 1-4\,\text{GeV}/c$), the momentum range of strongest suppression ($p_{\text{T}} = 5-8\,\text{GeV}/c$) and the range of rising R_{AA} ($p_{\text{T}} = 10-20\,\text{GeV}/c$). In Pb–Pb collisions, much higher values of $d\text{N}_{\text{ch}}/d\eta$ are achieved with respect to Xe–Xe. For low p_{T}, where the system is governed by collective expansion, the nuclear modification factor of Xe–Xe and Pb–Pb collisions converge for high $d\text{N}_{\text{ch}}/d\eta$. A collision energy dependence with $R_{\text{PbPb}}(2.76\,\text{TeV})$ consistently below $R_{\text{PbPb}}(5.02\,\text{TeV})$ can be observed independently of $d\text{N}_{\text{ch}}/d\eta$. As the charged particle yield in the p_{T} interval considered is governed by radial flow, the energy dependence of the R_{PbPb} is related to the increase in collision energy. The relative increase of R_{XeXe} at low $d\text{N}_{\text{ch}}/d\eta$ might be linked to a different, more compact, shape of the collision region, which in turn results in an increased radial flow.
At high p_{T}, a striking agreement of R_{AA} is found for Xe–Xe and Pb–Pb collisions at both collision energies measured for $\langle d\text{N}_{\text{ch}}/d\eta\rangle > 400$. In this high transverse momentum region, the yield of charged particles is governed by partonic energy loss in the deconfined medium.

In a simplified model of radiative energy loss (compare section 1.7), the energy loss depends quadratically on the path length and linearly on the density of (coloured) scattering centres.

$$\Delta E \propto \rho_c L^2. \tag{6.1}$$

In heavy-ion collisions, the generated medium is dominated by gluons. The density of scattering centres can thus be estimated based on the energy density:

$$\rho_c \approx \rho_g \approx \epsilon \tag{6.2}$$

As discussed in section 2.1, the charged-particle density can be used as a measure for the energy density $\epsilon \propto 1.25/(\pi R^2 \tau) \cdot d\text{N}_{\text{ch}}/d\eta$ [56]. For central collisions, the path length a high-p_{T} parton travels through the medium is proportional to R. It then follows:

$$\Delta E \propto \frac{1}{\pi R^2 \tau} \cdot \left\langle \frac{d\text{N}_{\text{ch}}}{d\eta} \right\rangle \cdot R^2 \propto \left\langle \frac{d\text{N}_{\text{ch}}}{d\eta} \right\rangle. \tag{6.3}$$

In peripheral collisions – low values for $d\text{N}_{\text{ch}}/d\eta$ – the argumentation of $L \sim R$ no longer holds, also the overall yield might be influenced by a larger contribution from binary nucleon-nucleon collisions in the corona of the collision [115]. In the corona, binary nucleon nucleon collisions are expected to provide a yield comparable to pp or p–Pb collisions, as the medium densities reached are much lower than in the core of the collision, while binary nucleon nucleon collisions in the core of the heavy-ion collision contribute to physical effects such as flow and partonic-energy loss. The relative contribution from the core are expected to dominate the charged particle yields for all but peripheral collisons.

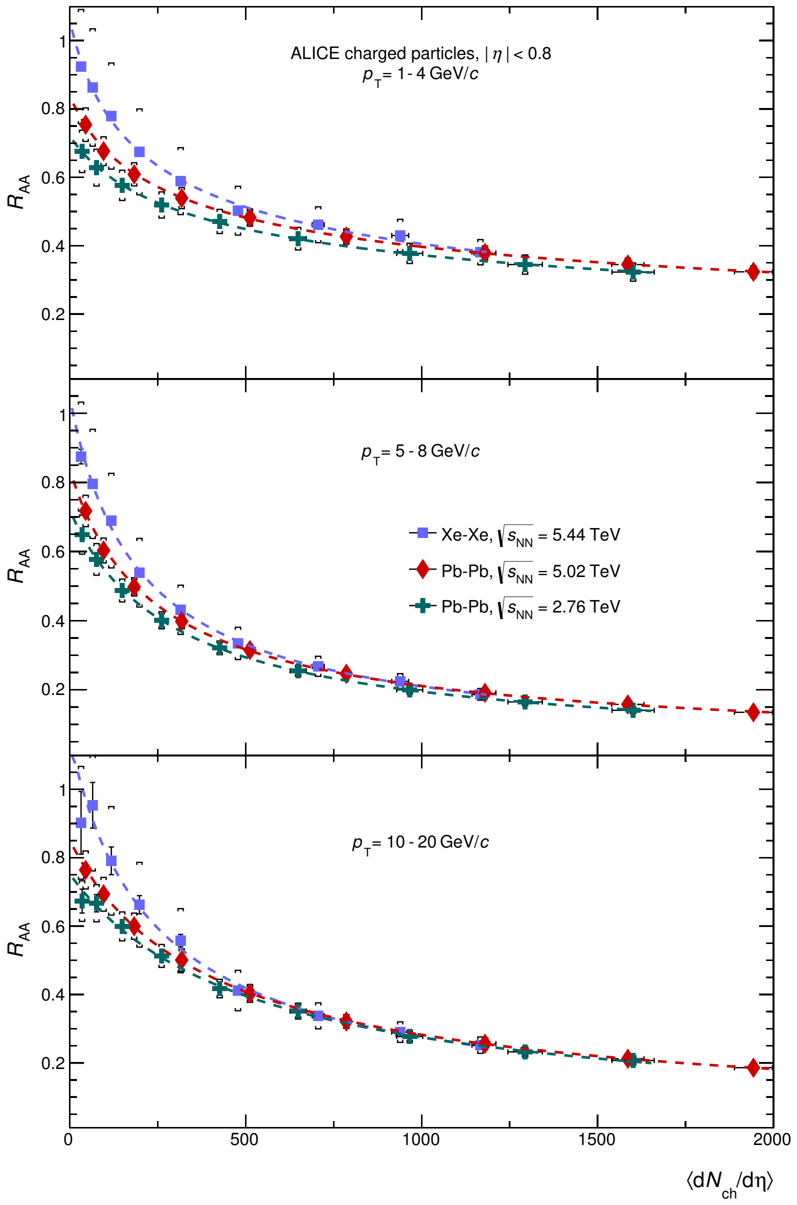

Figure 6.10.: The nuclear modification factors in Xe–Xe and Pb–Pb integrated in three p_T intervals as a function of $\langle d\mathrm{N}_{ch}/d\eta \rangle$ [114].

6.9 Nuclear Modification Factor Comparison to Theory

The measured nuclear modification factor for 0–5% centrality is compared to model predictions in Figure 6.11. The underlying concepts of the models are described in section 1.10. All models describe the key features of the data. The calculations by Vitev et al., Djordjevic et al. and CUJET 3.0 describe the data quantitatively well. The upper and lower boundaries are obtained by the variation of input parameters, such as the coupling strength which Vitev et al. assume to be $g = 1.9 \pm 0.1$.
The K factor fit of Andrés et al. predicts a $\sim$ 15% larger suppression at $\sqrt{s_{\mathrm{NN}}} = 5.02\,\mathrm{TeV}$ when not including data at this energy into the fit. Bianchi et al. overestimate the R_{PbPb}.

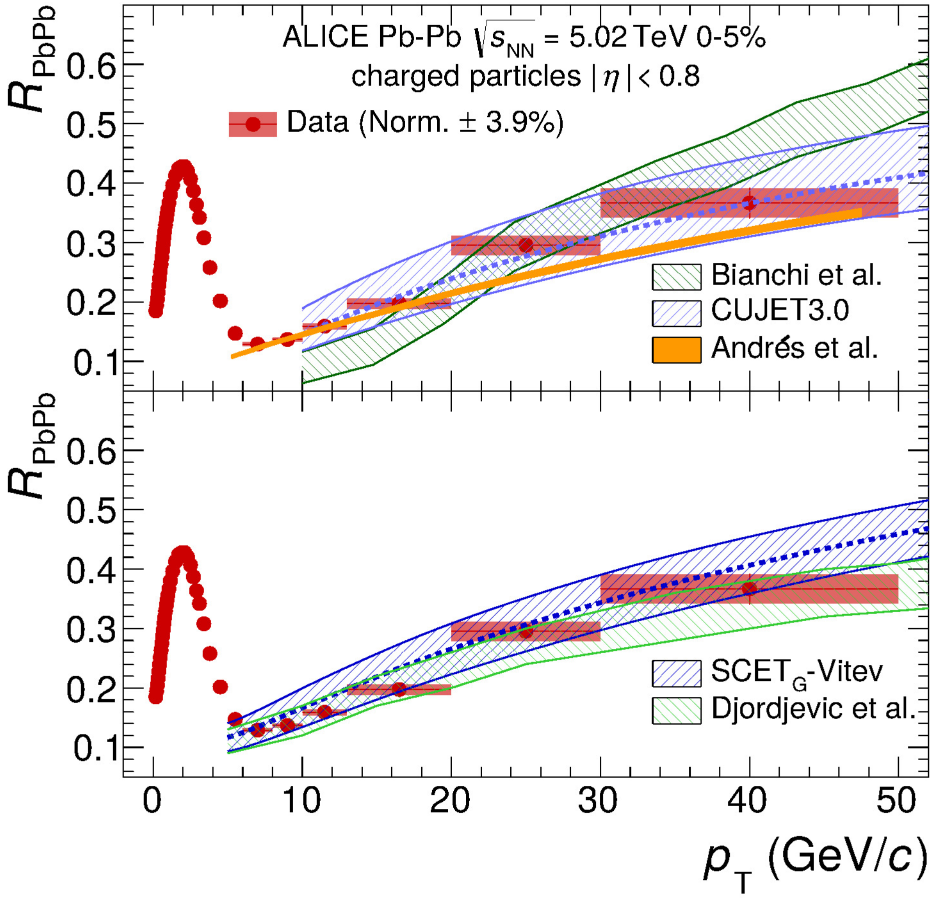

Figure 6.11.: The nuclear modification factor of charged particles in 0–5% most central Pb–Pb collisions at $\sqrt{s} = 5.02$ TeV in comparison to model calculations [36, 40, 43, 44, 47]. Figure published in [109].

6.10 Mean Transverse Momentum

It is possible to calculate the mean transverse momentum $(\langle p_T \rangle)$ from the transverse-momentum distribution. This allows for a comparison with previously published measurements [72] (compare section 2.6). The $\langle p_T \rangle$ is calculated in two different momentum ranges, from 150 MeV/c to 10 GeV/c and with an extrapolation down to $p_T = 0$, respectively. Without extrapolation, the $\langle p_T \rangle$ is the mean of the measured momentum distribution. The individual contributions of the p_T-dependent systematic uncertainties as discussed in section 4.7 are propagated to $\langle p_T \rangle$ by shifting the measured distribution to the extremes of each of the individual contribution. The individual differences to the unshifted $\langle p_T \rangle$ are added quadratically. While statistical uncertainties are negligible, systematic uncertainties range up to 0.7% for central Pb–Pb collisions. The largest uncertainties are found for Pb–Pb at $\sqrt{s_{NN}} = 5.02$ TeV, where the systematic uncertainties show the strongest dependence on p_T. The values for $\langle p_T \rangle$ without an extrapolation are summarised in Table 6.1.

To extrapolate the momentum distribution down to $p_T = 0$ the spectral shape is parametrised using a Hagedorn function [105]:

$$\mathrm{Yield}(p_T) = \alpha \frac{p_T^2}{\sqrt{m_\pi^2 + p_T^2}} \left(\frac{1 + p_T}{\gamma} \right)^{-\beta} \tag{6.4}$$

Centrality	$\langle p_{\mathrm{T}} \rangle^{5.44\,\mathrm{TeV}}_{\mathrm{XeXe}}$ (GeV/c)	$\langle p_{\mathrm{T}} \rangle^{5.02\,\mathrm{TeV}}_{\mathrm{PbPb}}$ (GeV/c)	$\langle p_{\mathrm{T}} \rangle^{2.76\,\mathrm{TeV}}_{\mathrm{PbPb}}$ (GeV/c)
0–5%	0.732 ± 0.005	0.729 ± 0.005	0.696 ± 0.004
5–10%	0.740 ± 0.005	0.731 ± 0.005	0.698 ± 0.003
10–20%	0.734 ± 0.004	0.732 ± 0.004	0.698 ± 0.003
20–30%	0.721 ± 0.003	0.728 ± 0.004	0.694 ± 0.003
30–40%	0.714 ± 0.003	0.720 ± 0.003	0.686 ± 0.003
40–50%	0.701 ± 0.002	0.706 ± 0.003	0.673 ± 0.003
50–60%	0.688 ± 0.002	0.691 ± 0.003	0.658 ± 0.002
60–70%	0.671 ± 0.002	0.672 ± 0.002	0.640 ± 0.002
70–80%	0.654 ± 0.002	0.654 ± 0.002	0.623 ± 0.002

Table 6.1.: $\langle p_{\mathrm{T}} \rangle$ calculated from the spectra of Xe–Xe $\sqrt{s} = 5.44\,\mathrm{TeV}$ without extrapolation. The shown uncertainties are systematic, while statistical uncertainties are negligible.

The function's parameters are fitted to the distribution in the range of $150\,\mathrm{MeV}/c < p_{\mathrm{T}} < 1\,\mathrm{GeV}/c$. The mean transverse momentum of the function in its fit range is added to the $\langle p_{\mathrm{T}} \rangle$ from the measurement weighted by their integrals. The statistical uncertainty of the extrapolation is calculated from the uncertainties of the function's parameters. The systematic uncertainty of the procedure is estimated by two contributions. First the fit range of the Hagedorn function is changed to $150\,\mathrm{MeV}/c < p_{\mathrm{T}} < 500\,\mathrm{MeV}/c$ taking into account the deviation of $\langle p_{\mathrm{T}} \rangle$ to the previous calculation. Additionally, the range in which the fit is considered is changed to $0 < p_{\mathrm{T}} < 200\,\mathrm{MeV}/c$, evaluating the histograms from $200\,\mathrm{MeV}/c < p_{\mathrm{T}} < 10\,\mathrm{GeV}/c$. In total, the statistical uncertainties are negligible, i.e. below 0.05% in peripheral and below 0.01% in central collisions. The systematic uncertainties range between and 0.6% (peripheral) and 0.8% (central) when using the extrapolation. The values for $\langle p_{\mathrm{T}} \rangle$ with extrapolation are listed in Table 6.2.
Figure 6.12 (left) shows the calculated $\langle p_{\mathrm{T}} \rangle$ with the interplation to $p_{\mathrm{T}} = 0$ as a function of the collision centrality. For all three collision systems analysed in this work the $\langle p_{\mathrm{T}} \rangle$ in peripheral collisions is lower than in central collisions as it is expected from an increased radial flow in central collisions. An increase of $\langle p_{\mathrm{T}} \rangle$ with collision energy is seen independently of collision centrality. This is not unexpected as the ratio of spectra shows an increased particle production at higher p_{T}. However the increase of $\langle p_{\mathrm{T}} \rangle$ can not only be attributed to a hardening of particle production at high p_{T}, as it is also present when limiting the p_{T} range of the $\langle p_{\mathrm{T}} \rangle$ calculation to $0 - 3\,\mathrm{GeV}/c$, as seen in Figure 6.12 (right). This shows, that the spectra at high p_{T} does not significantly contribute to the $\langle p_{\mathrm{T}} \rangle$. The larger $\langle p_{\mathrm{T}} \rangle$ at higher collision energy can therefore be attributed to a larger radial flow. The values for $\langle p_{\mathrm{T}} \rangle$ in Xe–Xe and Pb–Pb collisions at $\sqrt{s_{\mathrm{NN}}} = 5.02\,\mathrm{TeV}$ are similar with a maximal difference $< 2\%$. In order to draw any conclusion from this observation one would need to disentangle the effects of increased collision energy, different initial energy densities as well as different pressure gradients. These effects could be studied further with the help of identified particle spectra. Model calculations show small differences in $\langle p_{\mathrm{T}} \rangle$ of identified particles ($\pi^{\pm}$, $\mathrm{K}^{\pm}$ and $\mathrm{p}, \bar{\mathrm{p}}$) between Xe–Xe and Pb–Pb collisions [116].

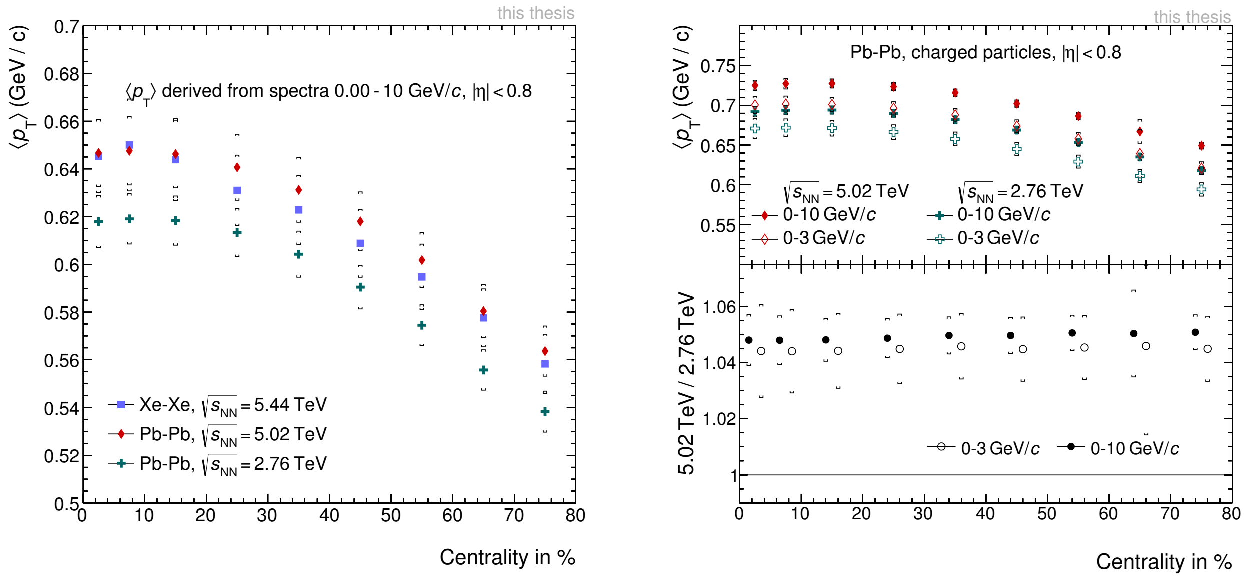

Figure 6.12.: The centrality dependence of $\langle p_T \rangle$ for all three systems analysed (left). The figure on the right, displays the dependence of $\langle p_T \rangle$ in Pb–Pb collisions on centre-of-mass energy for two different ranges of p_T.

Centrality	$\langle p_T \rangle^{5.44\,\text{TeV}}_{\text{ex. XeXe}}$ (GeV/c)	$\langle p_T \rangle^{5.02\,\text{TeV}}_{\text{ex. PbPb}}$ (GeV/c)	$\langle p_T \rangle^{2.76\,\text{TeV}}_{\text{ex. PbPb}}$ (GeV/c)
0–5%	0.728 ± 0.005	0.725 ± 0.006	0.692 ± 0.005
5–10%	0.735 ± 0.006	0.727 ± 0.006	0.694 ± 0.004
10–20%	0.730 ± 0.005	0.727 ± 0.005	0.694 ± 0.004
20–30%	0.717 ± 0.004	0.723 ± 0.004	0.690 ± 0.004
30–40%	0.710 ± 0.004	0.716 ± 0.004	0.682 ± 0.004
40–50%	0.697 ± 0.003	0.702 ± 0.004	0.669 ± 0.004
50–60%	0.684 ± 0.003	0.686 ± 0.004	0.653 ± 0.004
60–70%	0.667 ± 0.003	0.667 ± 0.004	0.635 ± 0.004
70–80%	0.649 ± 0.003	0.649 ± 0.004	0.618 ± 0.004

Table 6.2.: $\langle p_T \rangle$ derived from transverse momentum distributions with an additional extrapolation to $p_T = 0$. The shown uncertainties are systematic, while statistical uncertainties are negligible.

6.11 Calculation of $dN_{ch}/d\eta$ from Spectra

The charged-particle multiplicity $dN_{ch}/d\eta$ has been measured independently of this analysis using only information from the Inner Tracking System [53, 54]. This measurement provides an independent reference to compare the analysis to. In order to determine the $dN_{ch}/d\eta$ from the measured particle distribution, the integral of the distribution is calculated. Starting from $p_T = 150\,\text{MeV}/c$ up to $p_T = 50\,\text{GeV}/c$, this can be directly calculated from the measurement, the uncertainty is obtained by shifting the distribution by their total systematic uncertainty. This is a conservative approach since not all contributions are correlated. To account for particles with a momentum below $p_T = 150\,\text{MeV}/c$, a Hagedorn function [105] is used to parametrise the yield in the range of $0.15\,\text{GeV}/c < p_T < 1\,\text{GeV}/c$ (as was done for the determination of $\langle p_T \rangle$). The uncertainty of the extrapolation procedure is estimated by varying the lower fit ranges to $0.2\,\text{GeV}/c$ and the upper range to $3\,\text{GeV}/c$ and taking the maximum deviation of each variation. The values of $dN_{ch}/d\eta$ determined from the p_T distribution after extrapolation are compared to the published values in Figure 6.13 for Pb–Pb and Figure 6.14 for Xe–Xe. The calculated

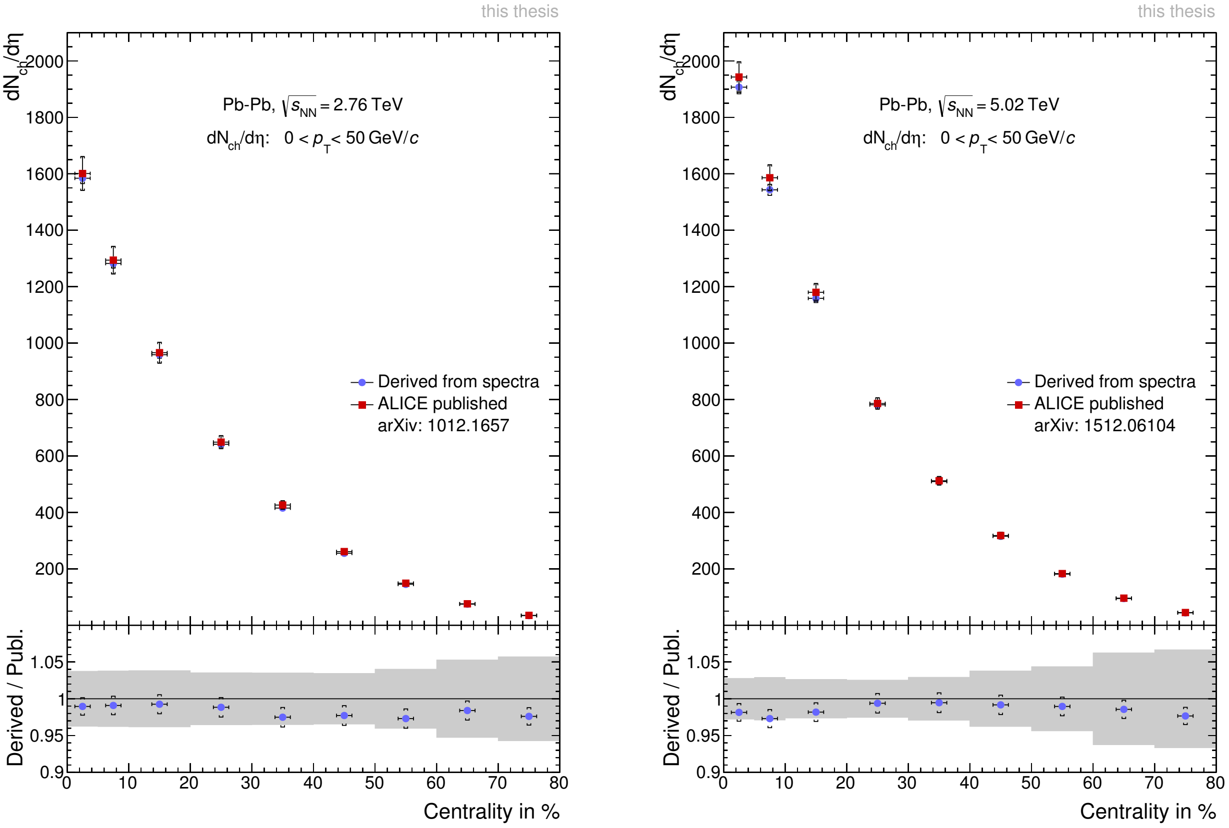

Figure 6.13.: $dN_{ch}/d\eta$ for Pb–Pb collisions, the grey band the in lower panel represents the systematic uncertainties of the published data [53, 54].

values for $dN_{ch}/d\eta$ derived from this analysis are lower than those published for Pb–Pb and above for Xe–Xe collisions. Given that these are independent measurements, the two measurement agree well with a maximum deviation of 5%, within systematic uncertainties.

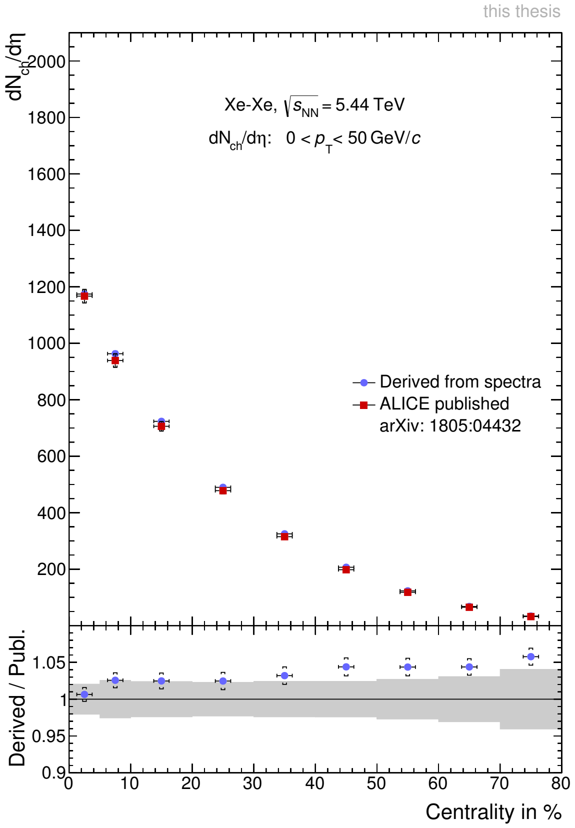

Figure 6.14.: $dN_{ch}/d\eta$ for Xe–Xe collisions, the grey band in the lower panel represents the systematic uncertainties of the published data [58].

7 Summary and Conclusion

Within this thesis, ultrarelativistic heavy-ion collisions at the LHC were analysed with ALICE. Not only a new regime of collision energy was studied in collisions of lead ions, but for the first time different ions - xenon - were brought to collision. Transverse-momentum distribution for inclusive primary charged particles were measured at midrapidity ($|\eta| < 0.8$) and $0.15 < p_{\mathrm{T}} < 50\,\mathrm{GeV}/c$ for nine classes of collision centrality in Pb–Pb and Xe–Xe collisions. Pb–Pb collisions were analysed with centre-of-mass energies per nucleon pair at $\sqrt{s_{\mathrm{NN}}} = 2.76\,\mathrm{TeV}$ and $\sqrt{s_{\mathrm{NN}}} = 5.02\,\mathrm{TeV}$, Xe–Xe collisions at $\sqrt{s_{\mathrm{NN}}} = 5.44\,\mathrm{TeV}$.

New and improved methods for the analysis led to a significant reduction by a factor of two in the systematic uncertainties compared to previous results. An improved reconstruction and the successful treatment of space-charge distortions in the TPC provide the basis for this work. The introduction of a new track selection criteria based on the track length in the active TPC read-out area reduces systematic uncertainties as it is described well in Monte Carlo (MC) simulations.

The correction for tracking inefficiency and detector acceptance is known to depend on the particle species present in the data sample. This analysis benefits from the measurements during Run 1, that make the recalculation of the tracking efficiency based on the measured p_{T} distributions of identified particles possible. For central collisions in Pb–Pb, this particle-composition correction amounts up to 10%.

The second largest correction to the charged particle yield is the correction for the contamination by secondary particles that stem from decays and interactions in the detector material. The amount of secondaries present in data and MC is estimated by examining the distribution of the track's distance of closest approach to the event vertex. MC simulations underestimate the secondary contamination by up to $\sim 50\%$ and are corrected for this effect.

For all collision systems the distributions are steeply falling at high p_{T}, while the slope is less steep for more central collisions.

Collision energy effects on the p_{T} distributions were studied for Pb–Pb collisions. The ratio of particle yields at $\sqrt{s_{\mathrm{NN}}} = 5.02\,\mathrm{TeV}$ to those at $\sqrt{s_{\mathrm{NN}}} = 2.76\,\mathrm{TeV}$ reveal a surprisingly comparable behaviour for all centralities and even when compared to pp collisions. While at low p_{T} the increase in particle yield is moderate, the increase at high p_{T} is larger. As expected, the particle production by hard processes increases stronger with collision energy than the production through soft processes.

Using the measured p_{T} differential cross section of primary particles in pp collision at $\sqrt{s} = 2.76\,\mathrm{TeV}$ and $\sqrt{s} = 5.02\,\mathrm{TeV}$, the nuclear modification factors (R_{AA}) are calculated for Pb–Pb. For Xe–Xe a power-law based interpolation is used to construct a pp reference at $\sqrt{s} = 5.44\,\mathrm{TeV}$. Nuclear modification factors of all collision systems show similar features. The least suppression is found in peripheral collisions, where in addition only little p_{T} dependence is observed. With increasing centrality, the suppression increases as well, while developing a characteristic p_{T} dependence. A minimum in R_{AA} is found at $p_{\mathrm{T}} \sim 6-7\,\mathrm{GeV}/c$ with $R_{\mathrm{AA}} \approx 0.13$ for most central collisions of Pb–Pb at $\sqrt{s_{\mathrm{NN}}} = 5.02\,\mathrm{TeV}$. Towards higher p_{T} the R_{AA} features a linear increase while still showing a significant suppression at $p_{\mathrm{T}} = 50\,\mathrm{GeV}/c$ ($R_{\mathrm{AA}} \approx 0.4$).

For central Pb–Pb collisions, the R_{AA} stays constant when increasing the collision energy to $\sqrt{s_{\mathrm{NN}}} = 5.02\,\mathrm{TeV}$. Having in mind the increase in yield at high p_{T}, an energy independent R_{AA} requires an increase in parton energy loss. This suggests a hotter and denser medium with a longer lifetime.

A direct comparison of R_{AA} in Pb–Pb and Xe–Xe as a function of centrality reveals similar features, even though the nuclei have different sizes, and thus the system is different for the same class of collision centrality. The nuclear modification factors are compared as a function of $d\mathrm{N}_{\mathrm{ch}}/d\eta$ for different p_{T} intervals. At low p_{T}, a scaling is found for Xe–Xe and Pb–Pb collisions at similar collision energies, while the R_{AA} for Pb–Pb collisions at $\sqrt{s_{\mathrm{NN}}} = 2.76\,\mathrm{TeV}$ is consistently lower. This behaviour can be attributed to an increase of radial flow with collision energies. At high transverse momenta, where energy loss dominates the yield of charged particles, a scaling of R_{AA} with $d\mathrm{N}_{\mathrm{ch}}/d\eta$ is found for all collision systems, including the result at the lower energy. This behaviour is consistent with a L^2 path length dependence of the partonic energy loss within the medium.

From the measured transverse momentum distributions, the mean transverse momentum and the charged particle density per unit of rapidity is calculated. The latter is compared to an independent measurement of $d\mathrm{N}_{\mathrm{ch}}/d\eta$ and shows a good agreement. The $\langle p_{\mathrm{T}} \rangle$ in Pb–Pb collisions increases with increasing collision energy. For all systems studied peripheral events exhibit a lower $\langle p_{\mathrm{T}} \rangle$ than central events.

The R_{AA} in Pb–Pb at $\sqrt{s_{\mathrm{NN}}} = 5.02\,\mathrm{TeV}$ has been compared to model calculations based on different formulations of energy loss. All models succeed in describing the shape of the R_{AA}, within their uncertainties.

The measurements presented in this thesis benefit largely from measured transverse momentum distributions of identified particles. In future, this analysis would benefit from further measurements at $\sqrt{s_{\mathrm{NN}}} = 5.02\,\mathrm{TeV}$, but especially of a measurement of $\Sigma^-, \bar{\Sigma}^+$ and $\Sigma^+, \bar{\Sigma}^-$.

The path length dependence of the energy loss could be studied in more detail, by determining the R_{AA} for the same $d\mathrm{N}_{\mathrm{ch}}/d\eta$ instead of collision centrality. As the systematic uncertainties in R_{XeXe} are driven by the shape of the ^{129}Xe nucleus a future measurement could benefit from a different isotope of xenon with better known geometry. The most control over the size and the average path length in the system is achieved in central collisions. With the collisions of different nuclei the path-length dependence of the energy loss could be studied in more detail.

Appendices

A Results

A.1 Comparison of nuclear modification factor

The nuclear modification factor measured in Pb–Pb and Xe–Xe collisions as a function of $\langle N_{\mathrm{coll}} \rangle$ and $\langle N_{\mathrm{part}} \rangle$ in Figure C.3. While at low p_{T} a scaling with N_{part} for high $\langle N_{\mathrm{part}} \rangle$ is observed (left figure, top panel), no scaling is found for higher p_{T}. At high p_{T}, the R_{AA} seems to scale better with $\langle N_{\mathrm{coll}} \rangle$, (right figure, lower panel). As discussed in section 3.5 the charged particle production is related to the weighted sum of N_{part} and N_{coll}. At low p_{T} charged particle production is dominated by soft processes, that scale with N_{part}, while hard processes scale with N_{coll}. Those dominate the charged particle yield at high p_{T}.

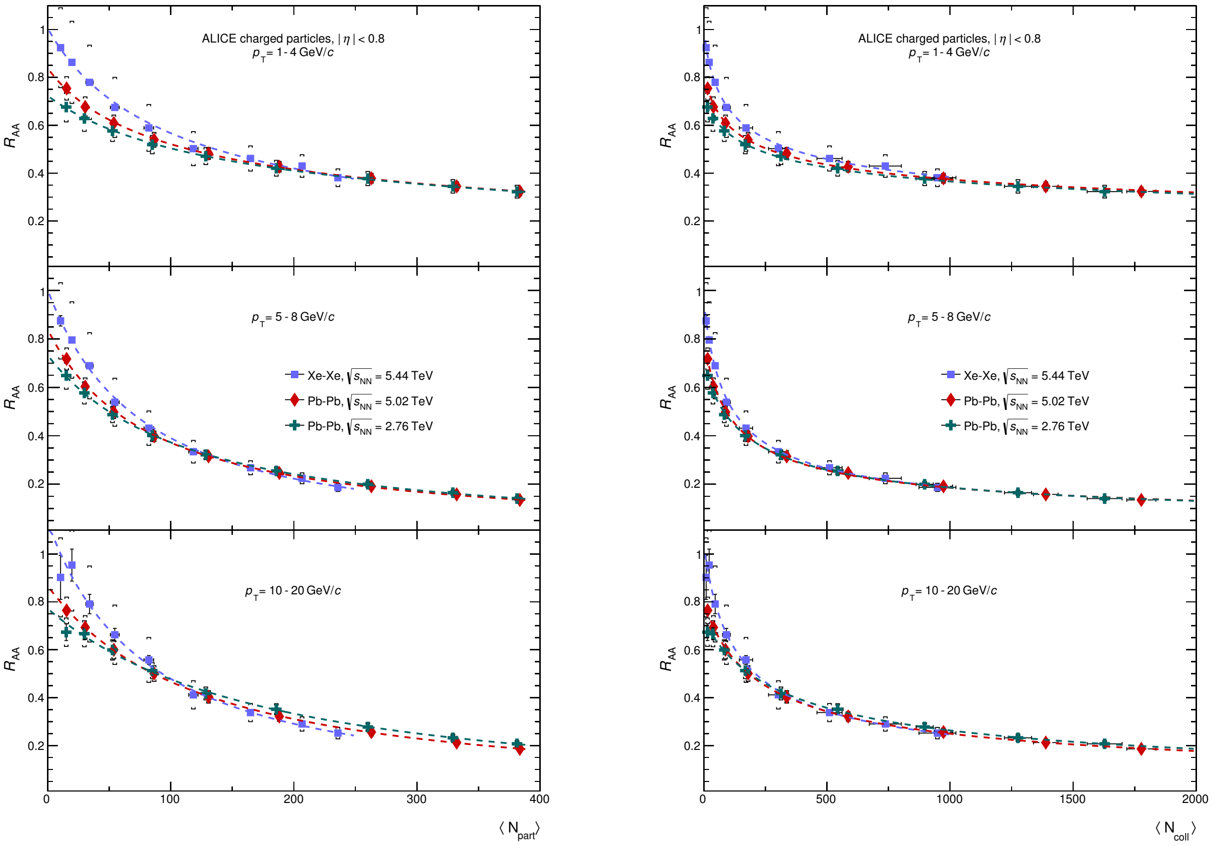

Figure A.1.: Comparison of the nuclear modification factor in Xe–Xe and Pb–Pb collisions integrated over identical regions in p_{T} as a function of $\langle N_{\mathrm{part}} \rangle$ (left) and $\langle N_{\mathrm{coll}} \rangle$ (right).

A.2 Extrapolation to higher transverse momenta

A.2.1 Extrapolating the Reference to High Transverse Momenta

The coarse binning as well as the range in p_{T} of the nuclear modification factor presented, is largely motivated by the limited statistics of the data set of pp collision at $\sqrt{s} = 5.02\,\mathrm{TeV}$. To overcome this limitation it is possible to approximate the behaviour of the pp reference at high p_{T} by a fit to the reference. As a parametrisation a Hagedornfunction [105] has been choosen as shown in Figure A.2 left. The function is fitted to a finer binned distribution in the range $6\,\mathrm{GeV}/c < p_{\mathrm{T}} < 50\,\mathrm{GeV}$. To estimate the systematic uncertainty of the fit, the reference is shifted by its systematic uncertainty and again fitted by the same function. The difference of these fits is then added quadratically to the uncertainty of the last bin for the extrapolation for $p_{\mathrm{T}} > 50\,\mathrm{GeV}/c$. Figure A.2 right shows a comparison of interpolation to measurements published by CMS [65]. A difference of $\sim 7\%$ is observed for high p_{T}.

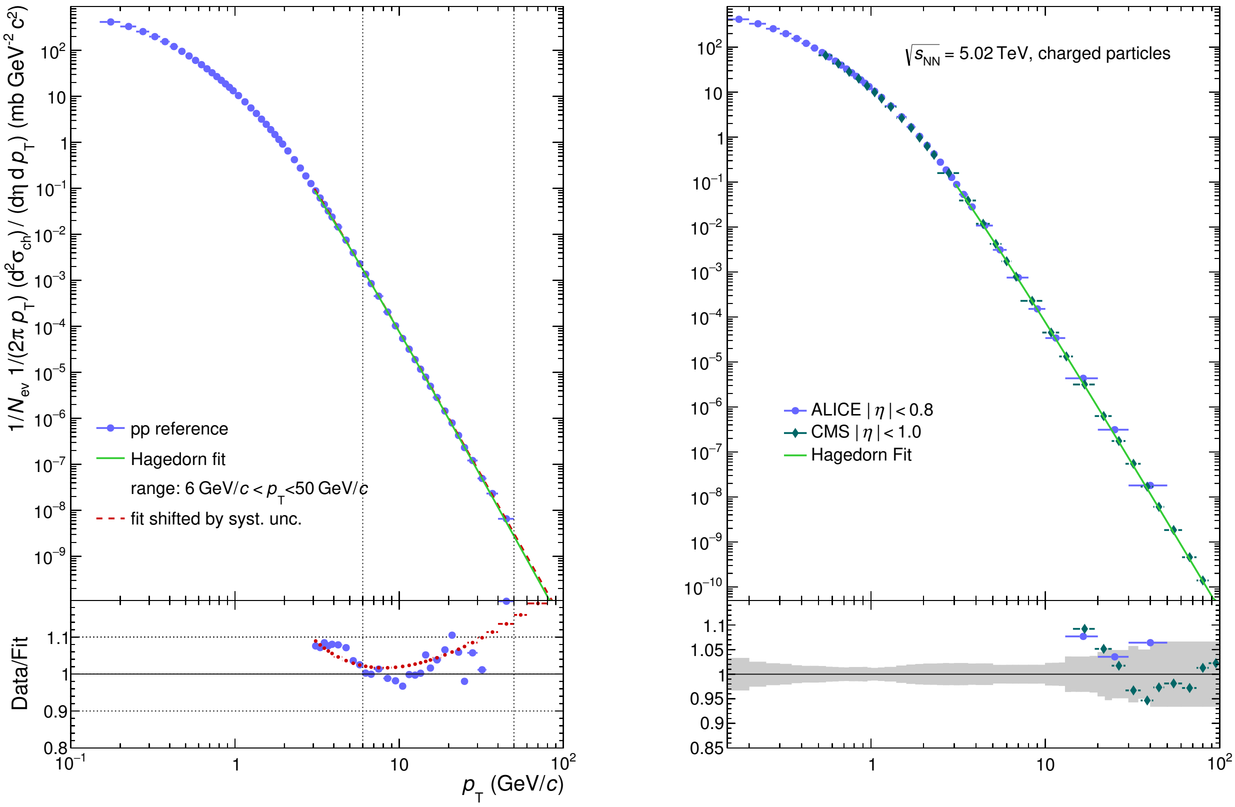

Figure A.2.: Left: A finer binned version of the pp reference with a Hagedorn function fitted to the high p_{T} slope. The lower panel shows the ratio of data to the fit, as well as the ratio of a fit to the pp reference shifted by its systematic uncertainties. Right: The fit compared to the pp reference of ALICE, and CMS [65]. The grey band shows the attributed systematic uncertainties up to very high p_{T}.

A.2.2 Nuclear Modification Factor in Pb–Pb Collisions with Extrapolated pp Reference

With the help of the interpolated reference (section A.2.1), a nuclear modification factor can be calculated up to $p_{\mathrm{T}} = 100\,\mathrm{GeV}/c$, as shown in Figure A.3. The interpolated nuclear modification factor is compared to the original measurement. While in central collisions the statistics allows for the calculation of a R_{PbPb}, the uncertainties increase towards peripheral collisions. In central collisions, the increasing trend of R_{PbPb} seems to continue to higher p_{T}. In more peripheral collisions, a saturation of the R_{PbPb} can not be ruled out.

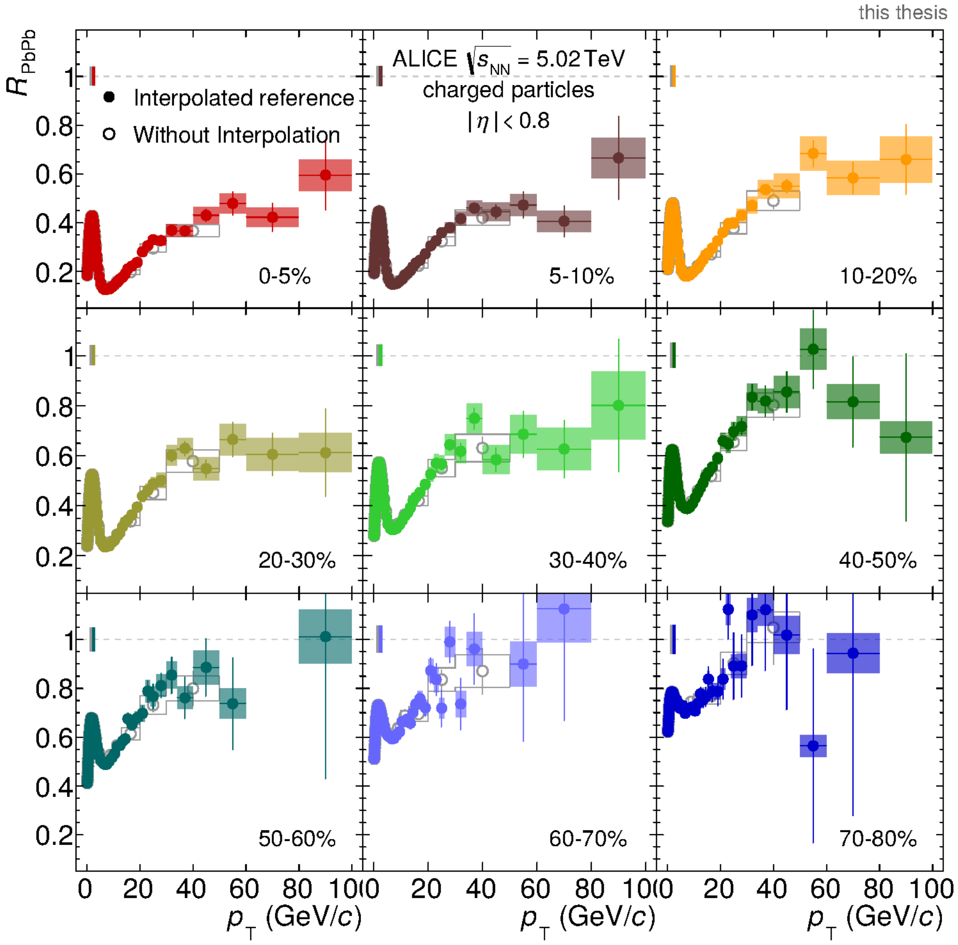

Figure A.3.: The p_{T}-dependent nuclear modification factor derived with the inter- and extrapolated pp reference.

B Analysis

B.1 Tracking Efficiency

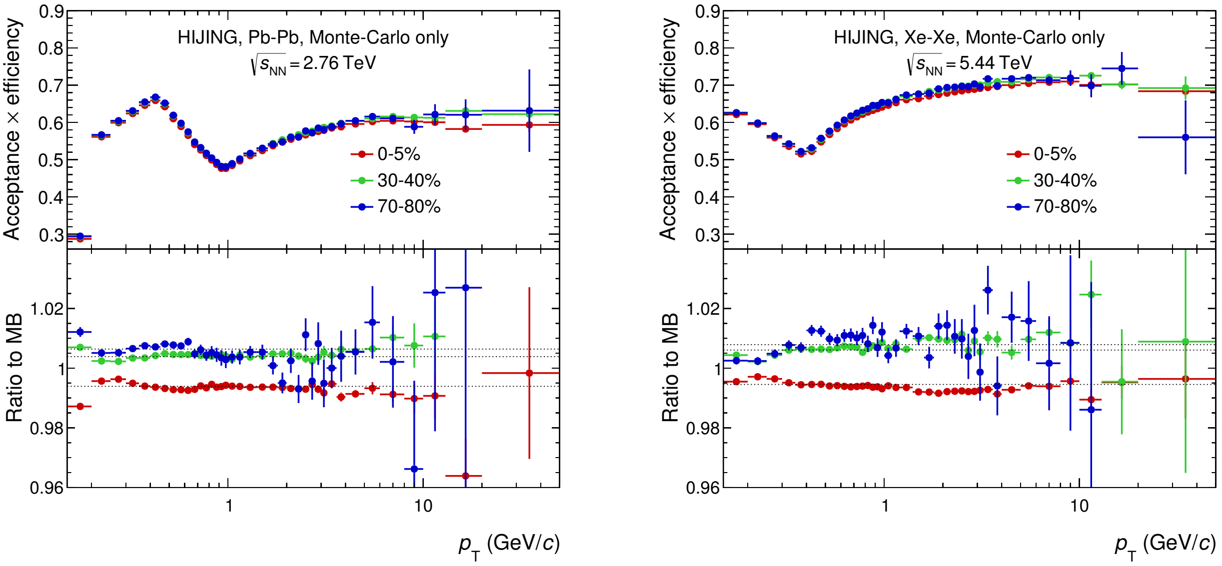

Figure B.1.: The tracking efficiency for different bins of centrality in Pb–Pb collisions at $\sqrt{s_{NN}} = 2.76$ TeV(left) and Xe–Xe collisions at $\sqrt{s_{NN}} = 5.44$ TeV

Centrality	0-5%	5-10%	10-20%	20-30%	30-40%
Ratio to MB	0.994	0.998	0.999	1.002	1.004
Centrality	40-50%	50-60%	60-70%	70-80%	
Ratio to MB	1.005	1.006	1.006	1.006	

Table B.1.: The Ratios of centrality selected tracking efficiency to MB for Pb–Pb at $\sqrt{s_{NN}} = 2.76$ TeV.

Centrality	0-5%	5-10%	10-20%	20-30%	30-40%
Ratio to MB	0.995	1.001	1.003	1.005	1.006
Centrality	40-50%	50-60%	60-70%	70-80%	
Ratio to MB	1.007	1.008	1.008	1.008	

Table B.2.: The Ratios of centrality selected tracking efficiency to MB Xe–Xe at $\sqrt{s_{NN}} = 5.44$ TeV.

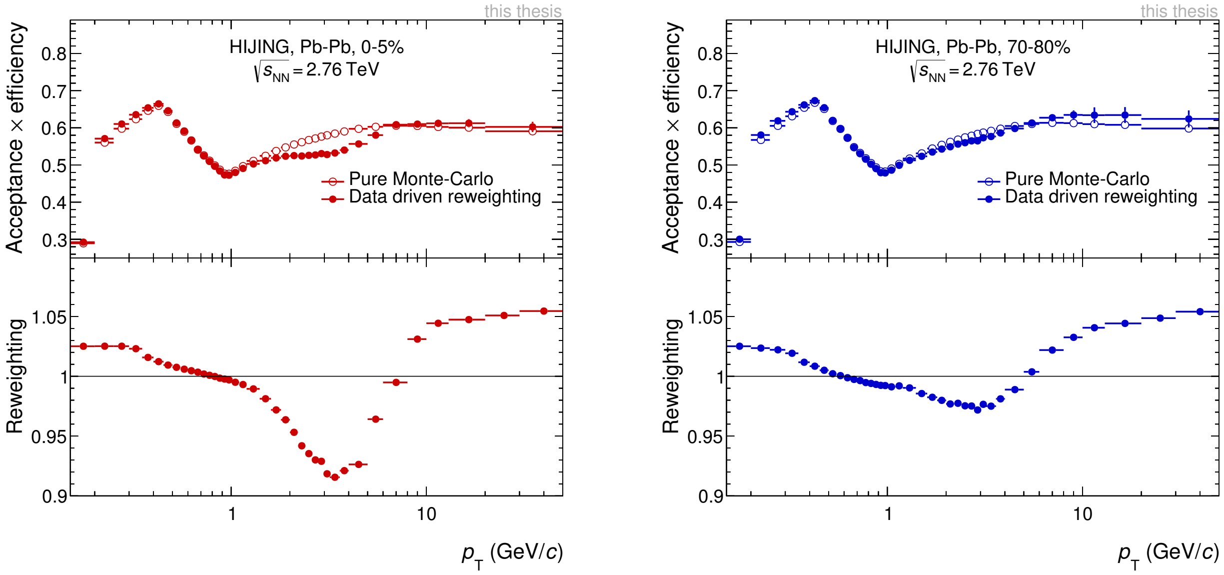

Figure B.2.: The efficiency from pure MC (open symbols) and the efficiency after reweighting (filled symbols top panel) as well as the reweighting factor calculated (lower panel) for central (left) and peripheral collisions (right). Pb–Pb collisions at $\sqrt{s_{NN}} = 2.76$ TeV.

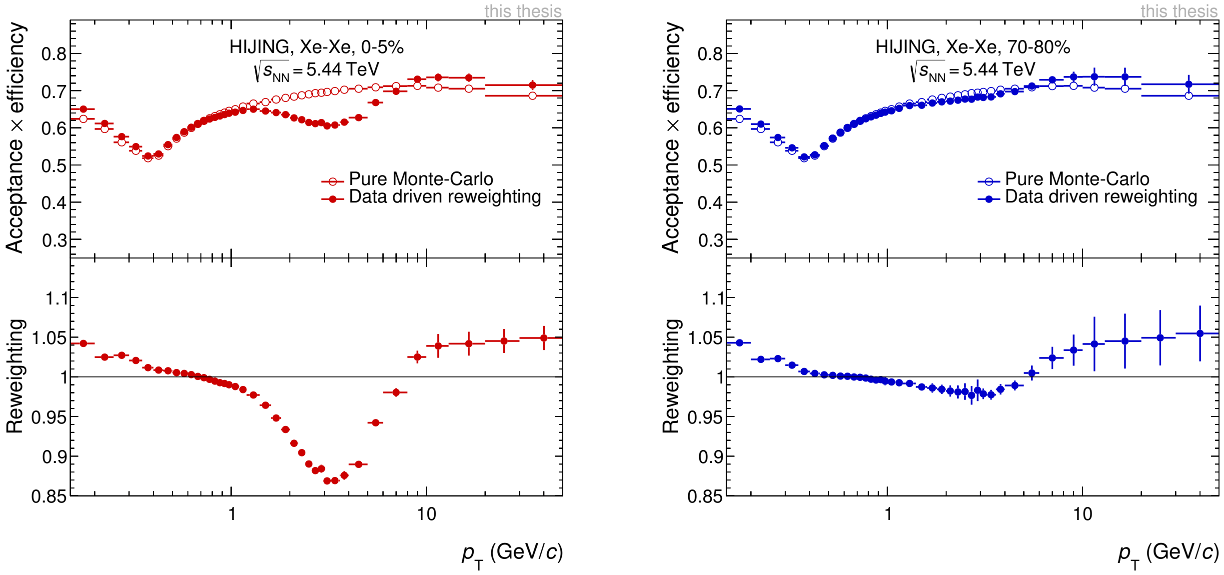

Figure B.3.: The efficiency from pure MC (open symbols) and the efficiency after reweighting (filled symbols top panel) as well as the reweighting factor calculated (lower panel) for central (left) and peripheral collisions (right). Xe–Xe collisions at $\sqrt{s_{NN}} = 5.44$ TeV.

B.2 Secondary Contamination

The contamination with secondary particles for central (left) and peripheral collisions (right) is shown in Figure B.4 and Figure B.5. The upper panel shows the contamination subtracted from the uncorrected momentum distribution. The contribution estimated by pure Monte Carlo is shown with open symbols. The contamination after rescaling is shown with filled symbols. The lower panel shows the reweighting factor estimated by template fits to the DCA$_{xy}$ distribution in data (coloured symbols), and the linear interpolation used to scale the contamination (grey line).

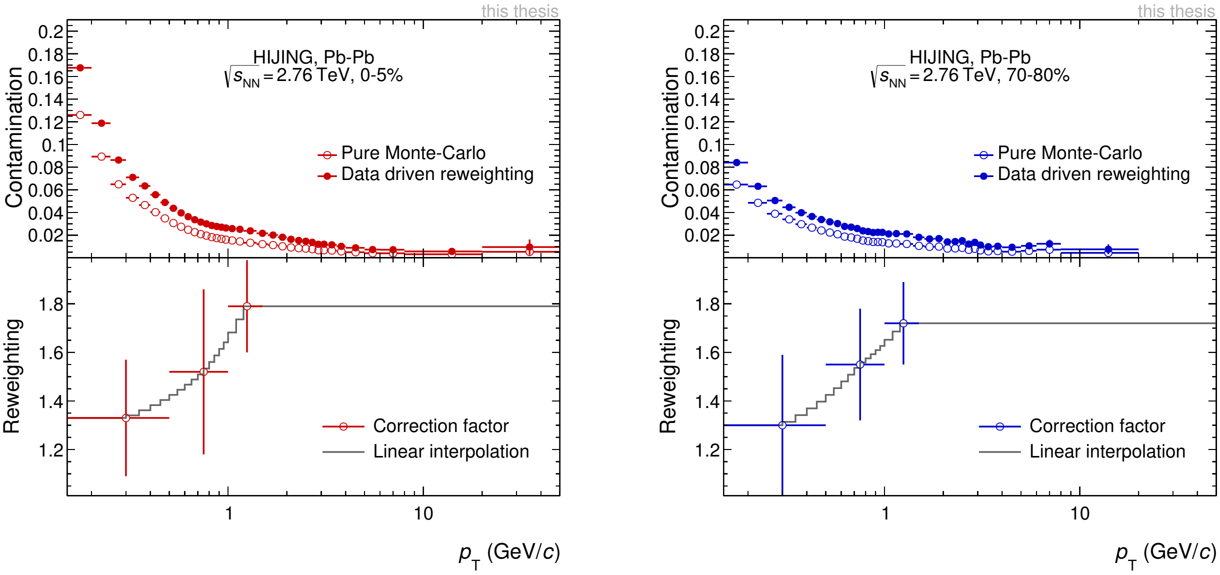

Figure B.4.: Pb–Pb collisions at $\sqrt{s_{NN}} = 2.76$ TeV.

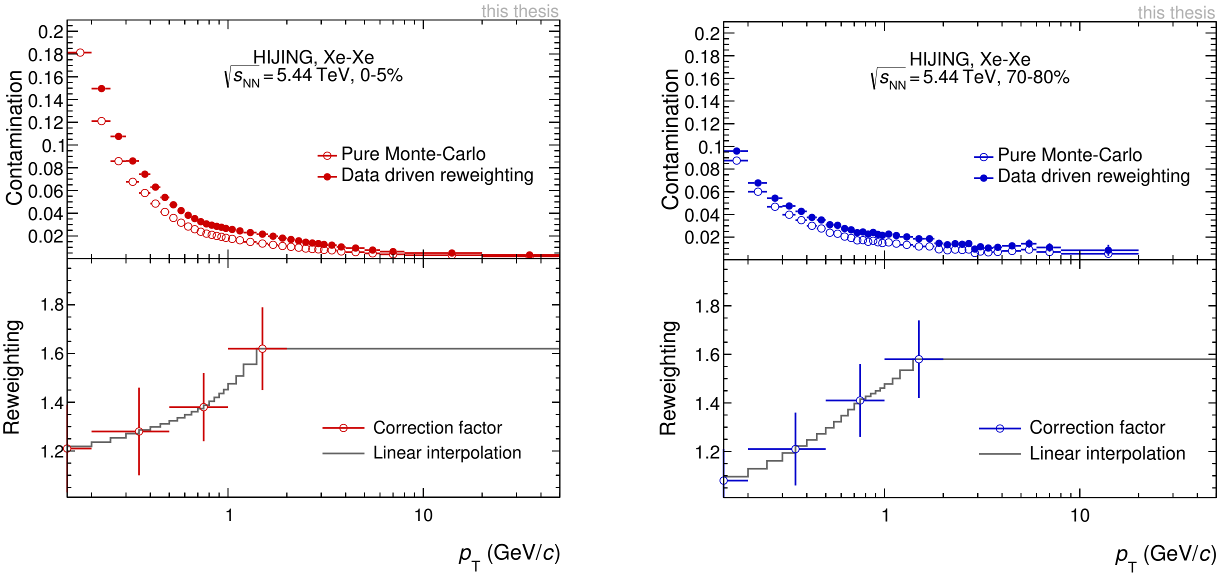

Figure B.5.: Xe–Xe collisions at $\sqrt{s_{NN}} = 5.44$ TeV.

C Systematic Uncertainties

The systematic uncertainties for all systems, as shown in Figure 4.20 is displayed below for 30–40% and 70–80% most central collisions.

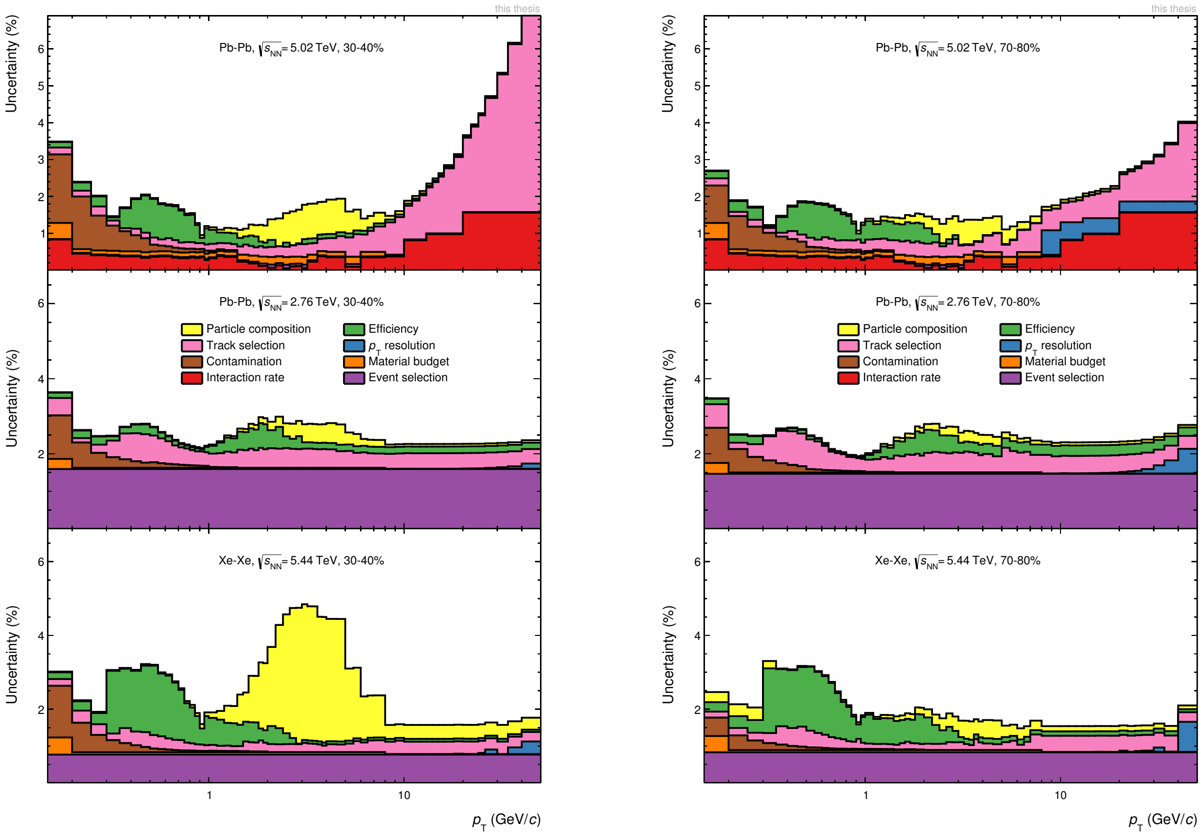

Figure C.1.: An overview of the p_T dependent systematic uncertainties in all data sets analysed. Each line shows the quadratic sum of the lines below. Even though the contributions are estimated in the same way the amount of uncertainties varies for the data sets. For Pb–Pb at $\sqrt{s_{NN}} = 5.02$ TeV the overall uncertainty is dominated by the contribution of the track selection at high p_T. Also it has an additional contribution from a varying interaction rate, which is not present in the other data sets.

C.1 Track Selection

Pb–Pb 2.76 TeV

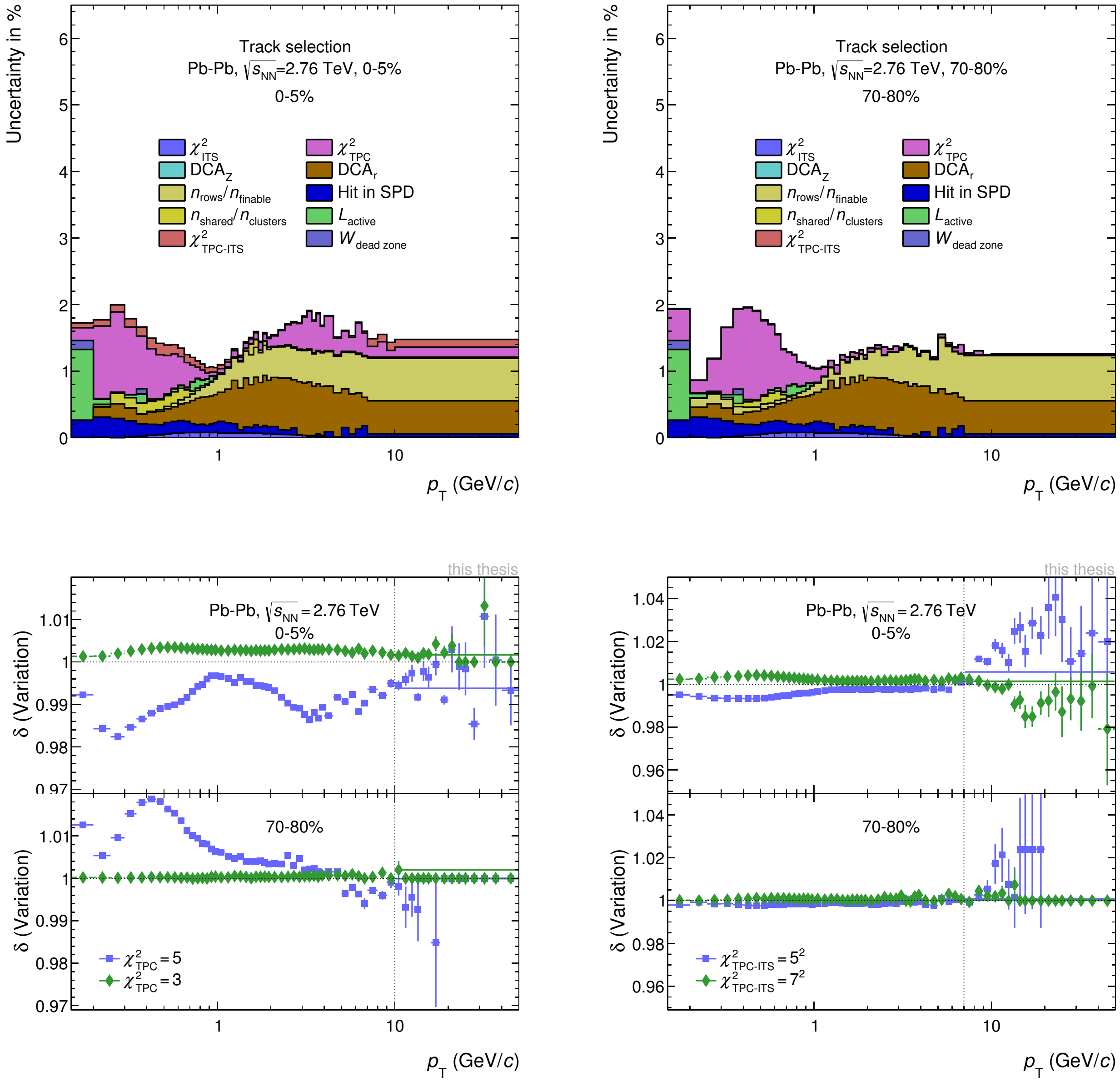

Figure C.2.: Comparison of the nuclear modification factor in Xe–Xe and Pb–Pb collisions integrated over identical regions in p_T as a function of N_{coll} (left) and (N_{part}).

Xe–Xe 5.44 TeV

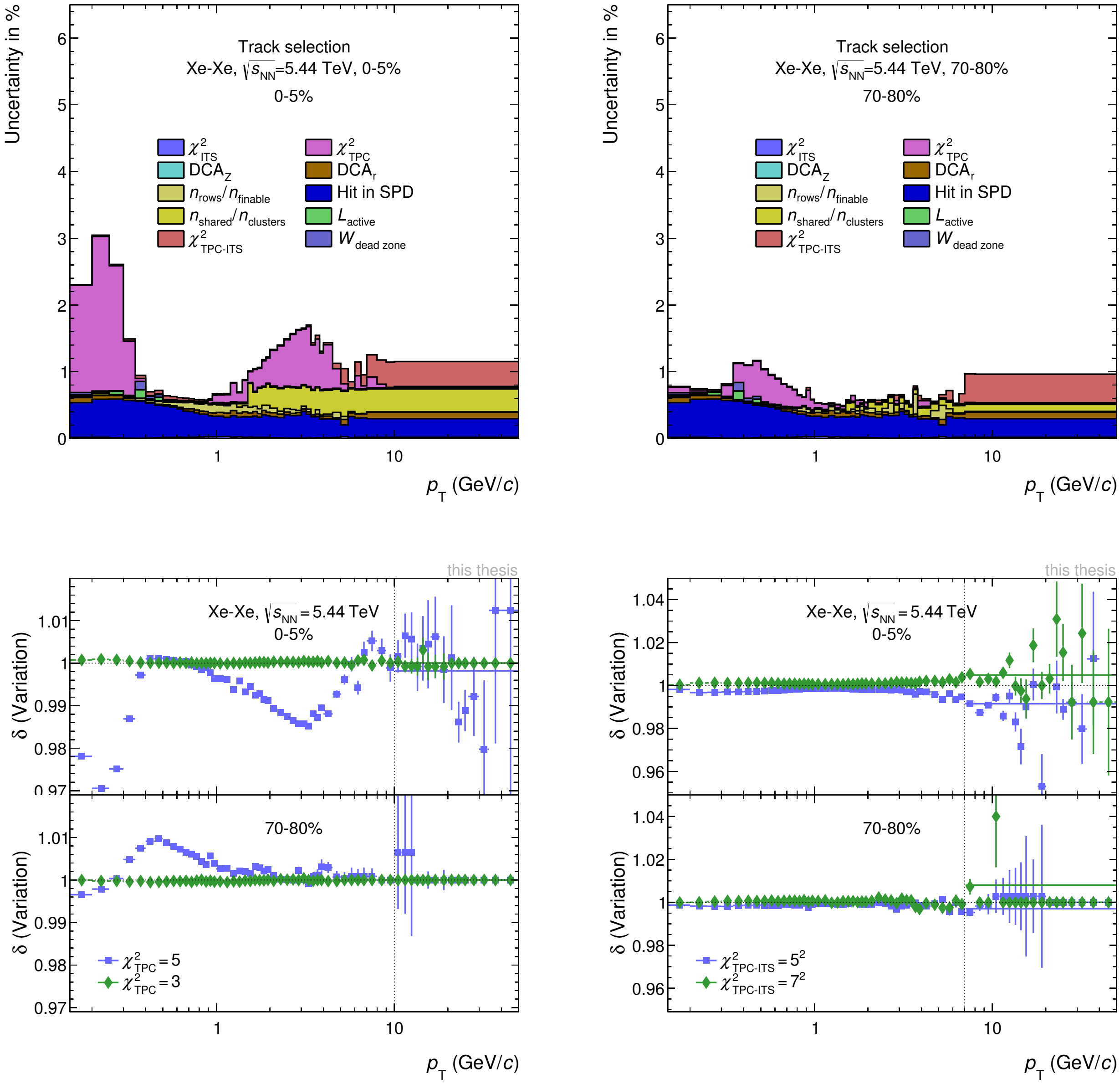

Figure C.3.: Comparison of the nuclear modification factor in Xe–Xe and Pb–Pb collisions integrated over identical regions in p_T as a function of N_{coll} (left) and (N_{part}).

D Track Selection Criteria

In the following, the distributions of variables the track selection relies on is shown. For each variable the distribution, the ratio of rejected tracks in both MC and data, as well as the agreement of data and MC is shown.

D.1 Pb–Pb 5 TeV

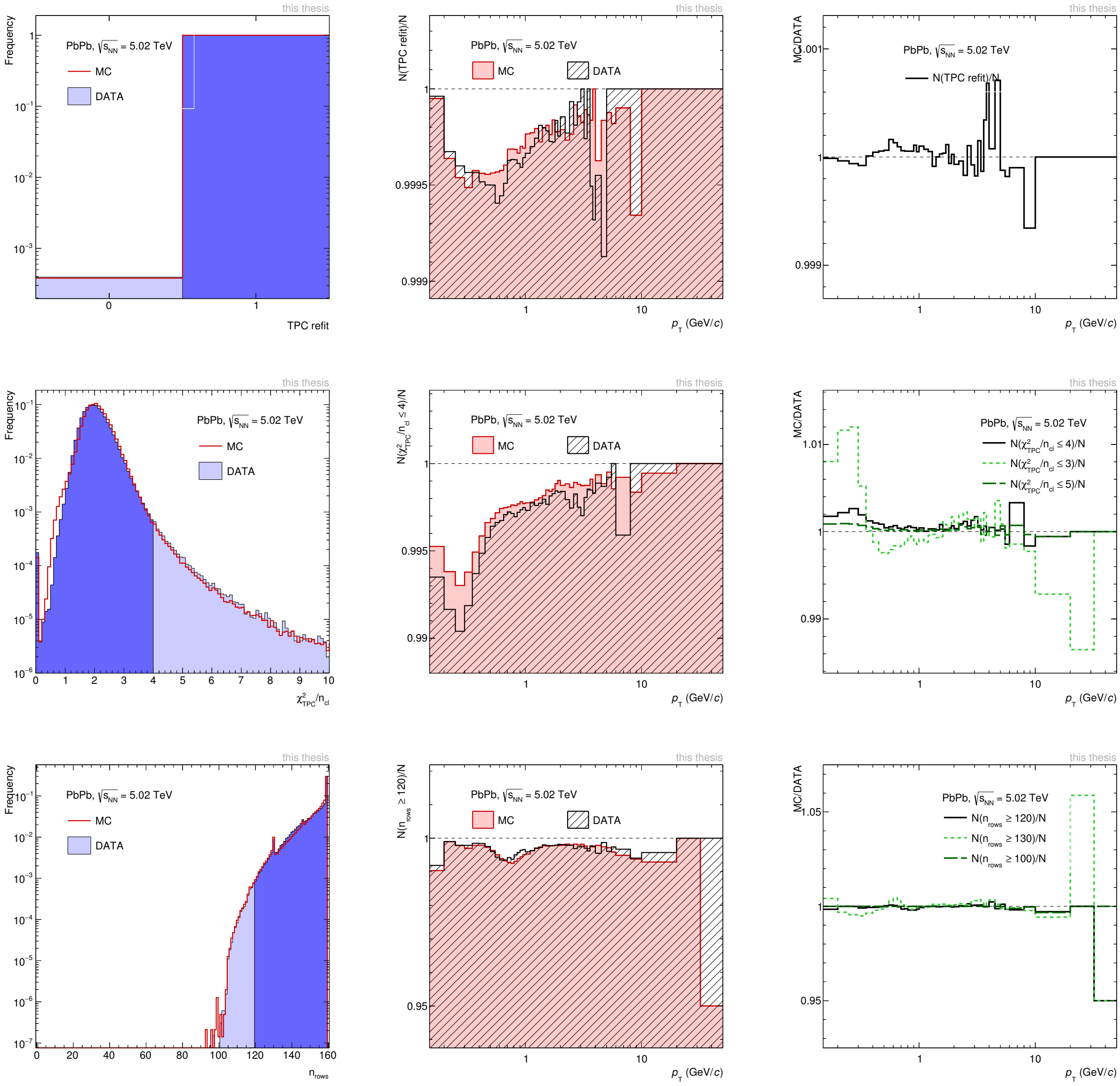

Figure D.1.: Track selection variables in Pb–Pb at $\sqrt{s_{NN}} = 5.02$ TeV.

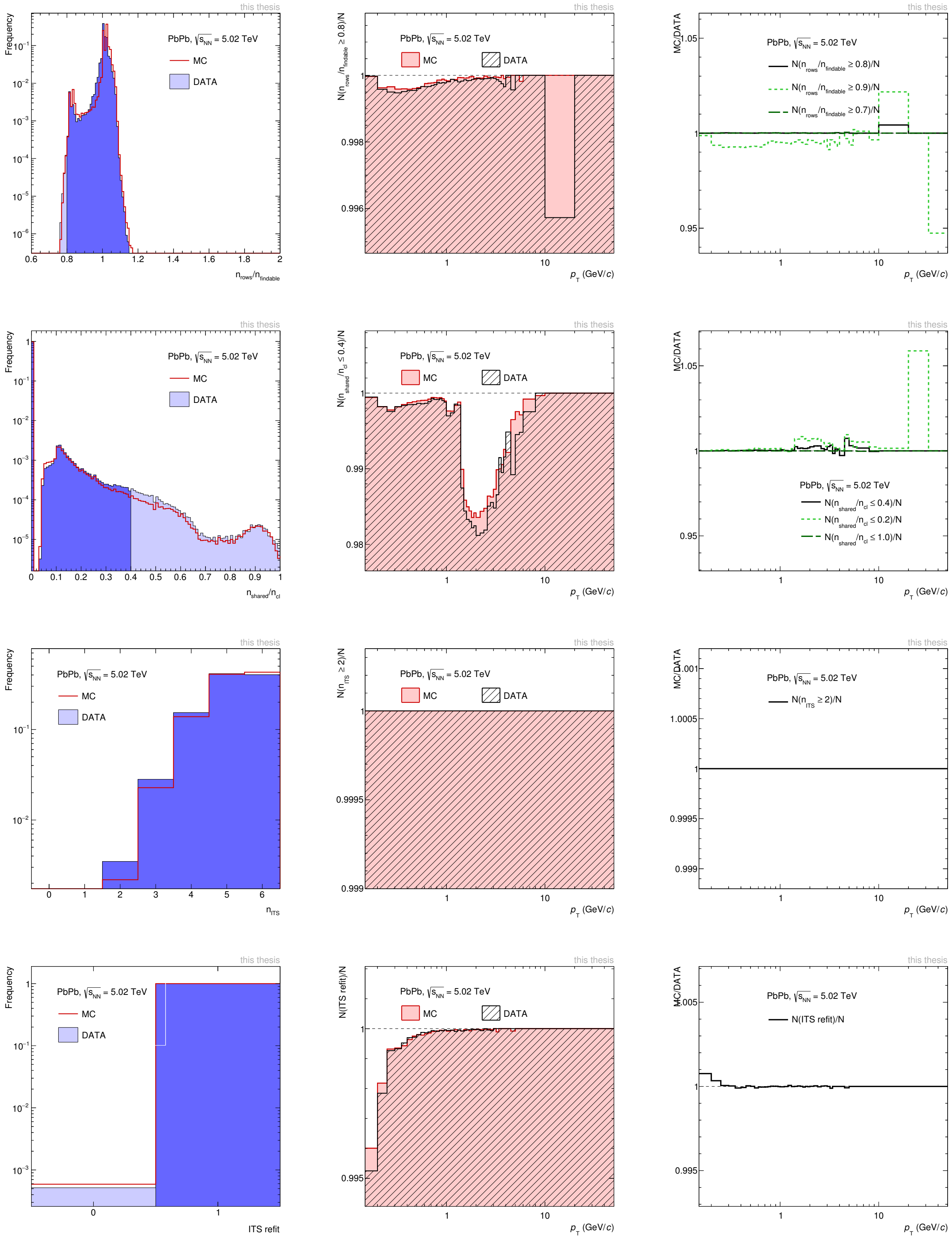

Figure D.2.: Track selection variables in Pb–Pb at $\sqrt{s_{NN}} = 5.02\,\text{TeV}$.

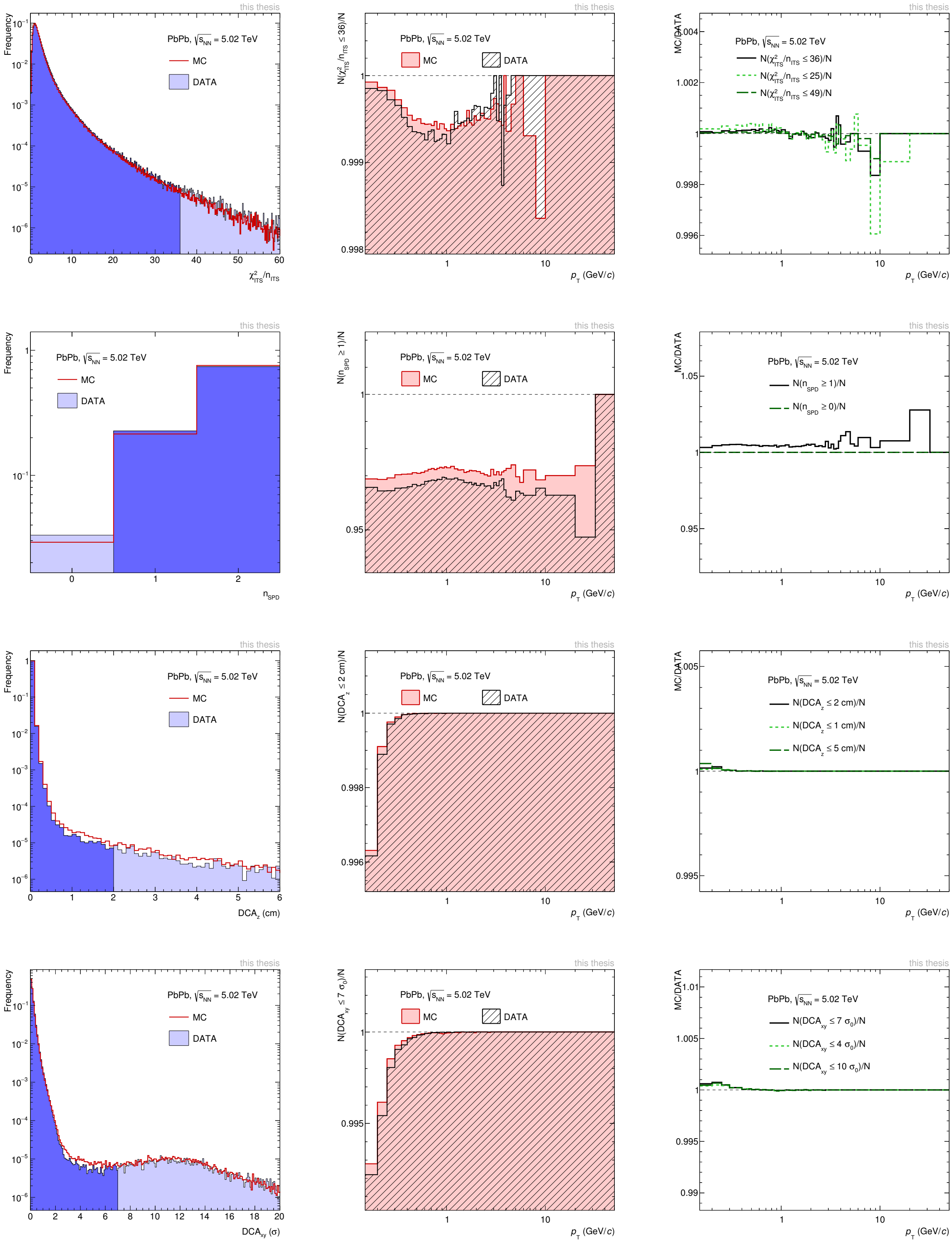

Figure D.3.: Track selection variables in Pb–Pb at $\sqrt{s_{\mathrm{NN}}} = 5.02$ TeV.

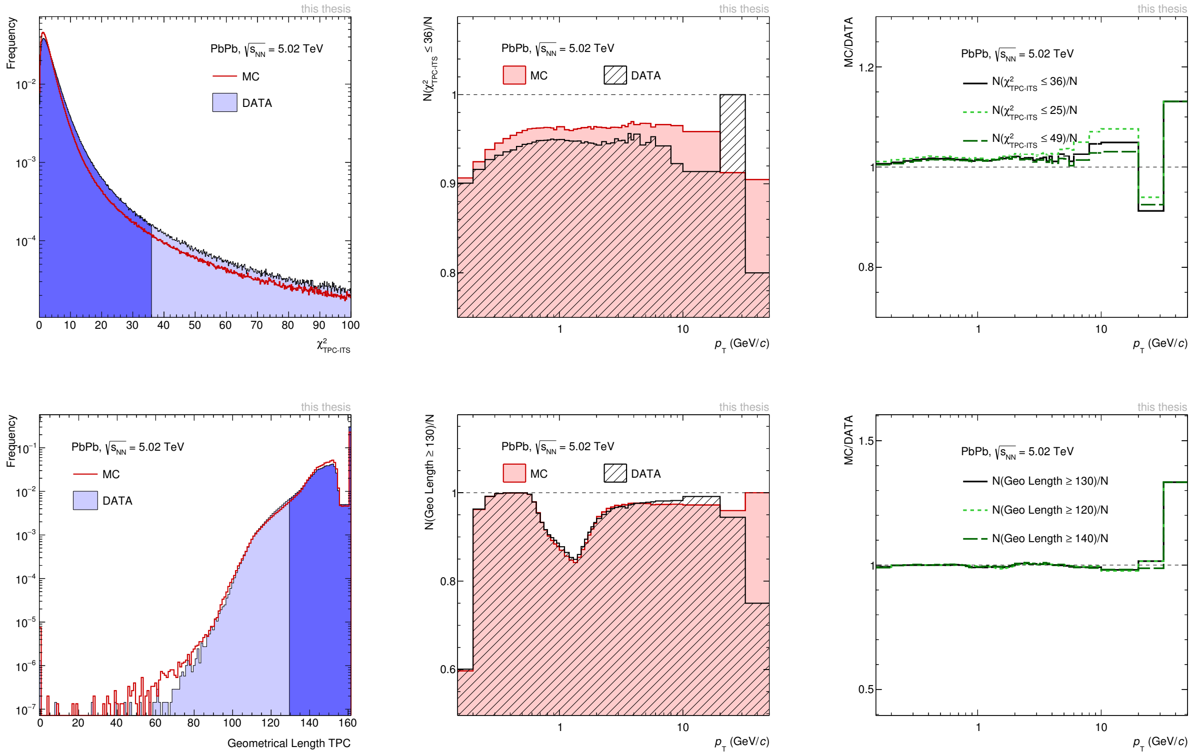

Figure D.4.: Track selection variables in Pb–Pb at $\sqrt{s_{NN}} = 5.02\,\mathrm{TeV}$.

D.2 Pb–Pb 2 TeV

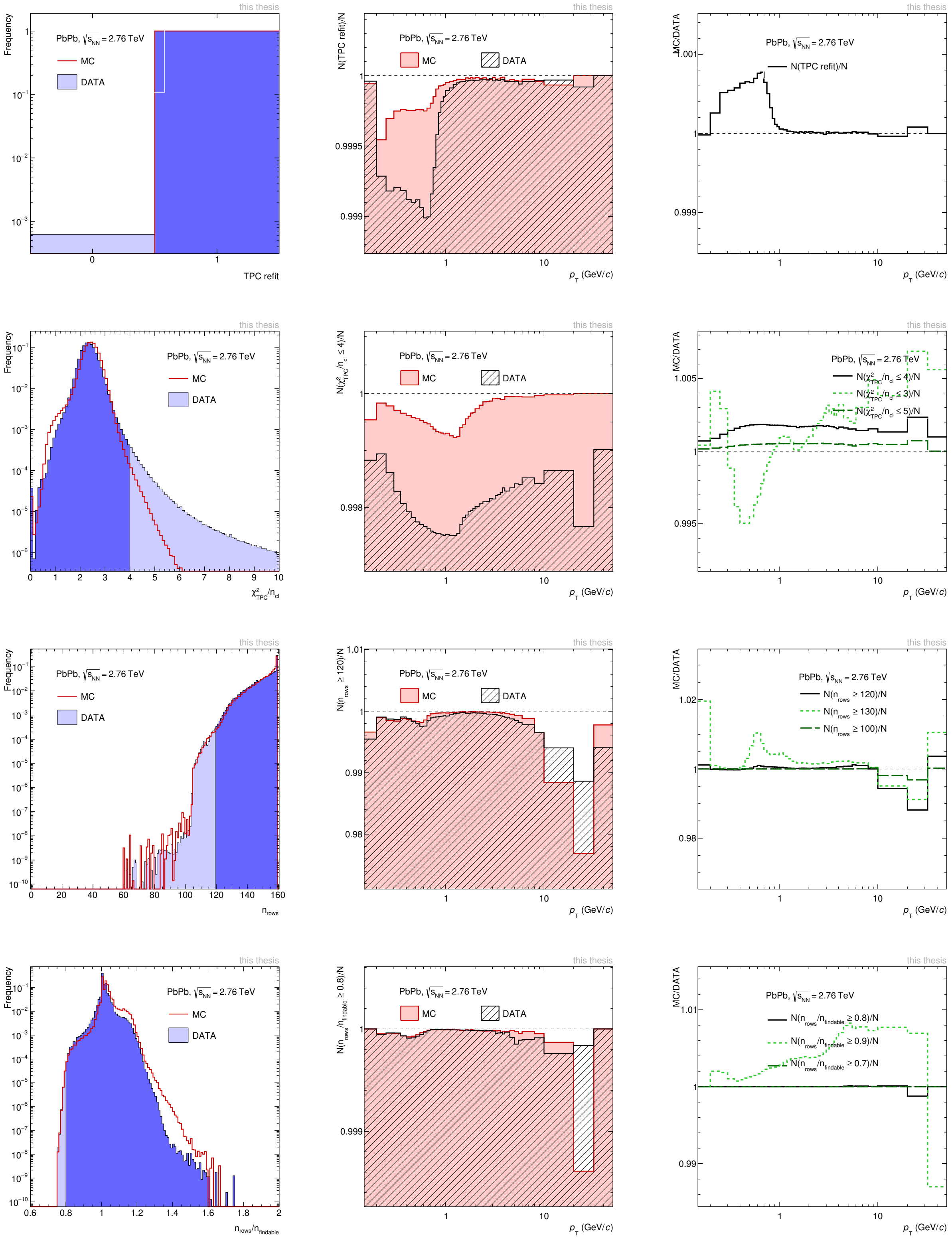

Figure D.5.: Track selection variables in Pb–Pb at $\sqrt{s_{NN}} = 2.76$ TeV.

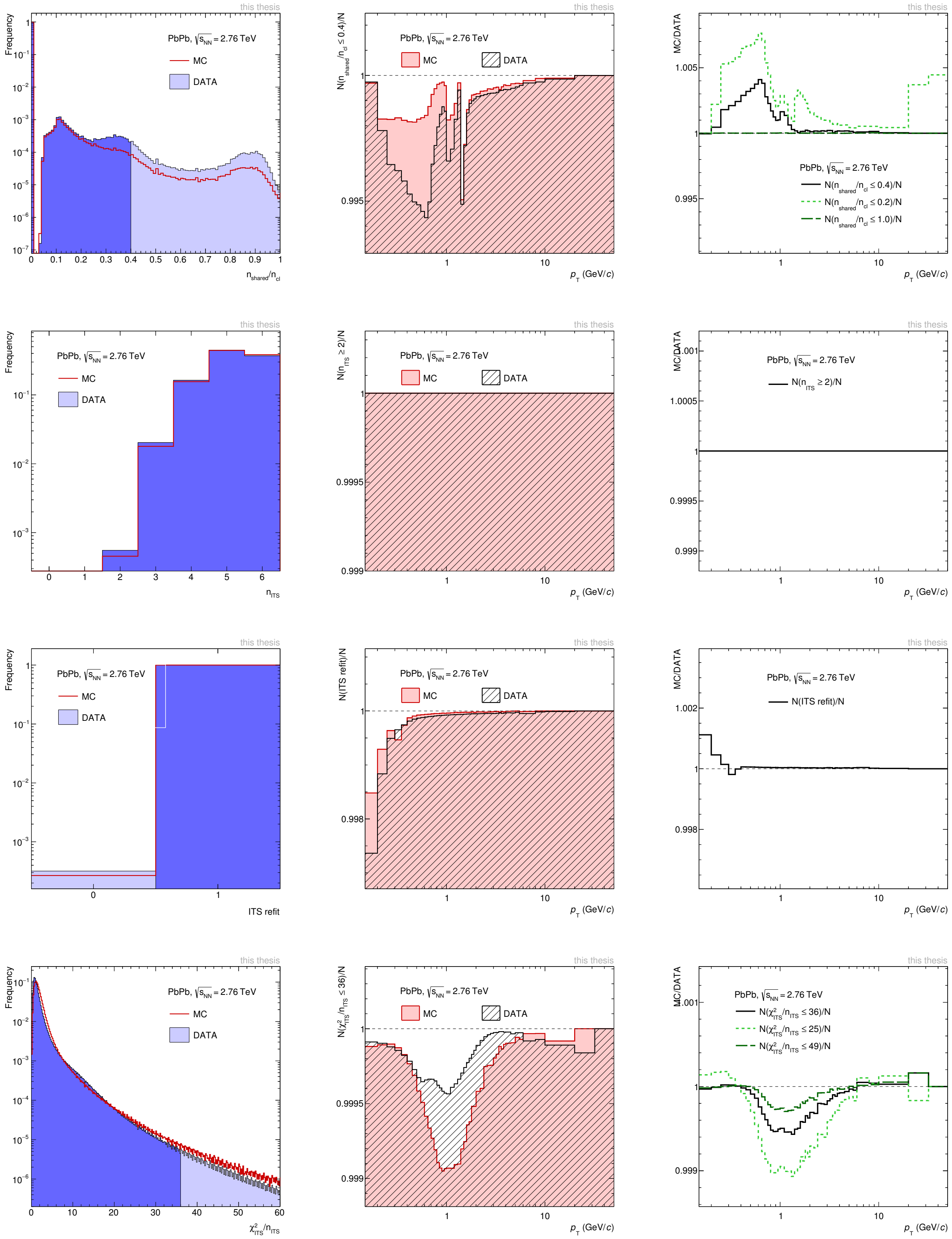

Figure D.6.: Track selection variables in Pb–Pb at $\sqrt{s_{NN}} = 2.76\,\text{TeV}$.

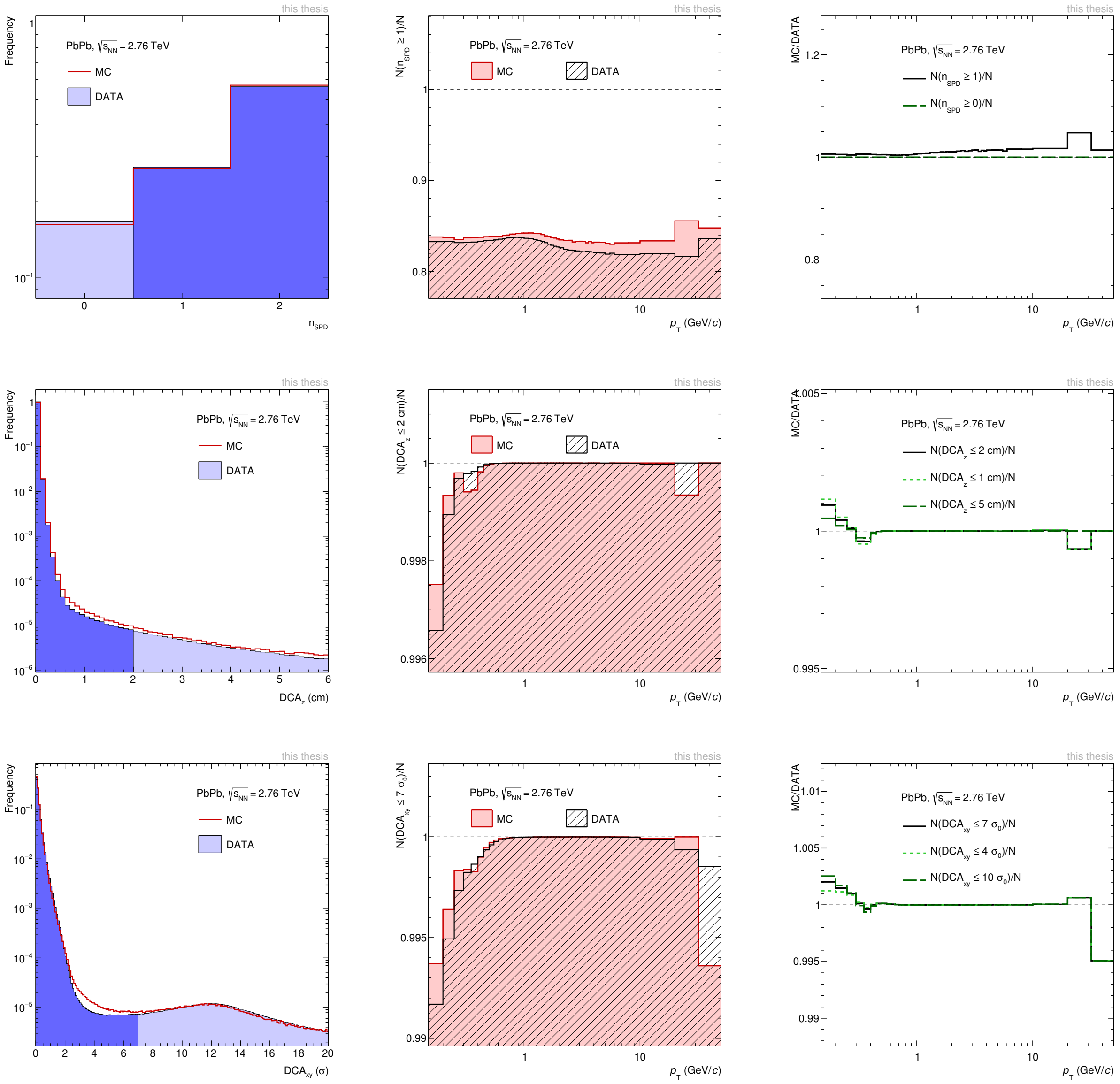

Figure D.7.: Track selection variables in Pb–Pb at $\sqrt{s_{NN}} = 2.76$ TeV.

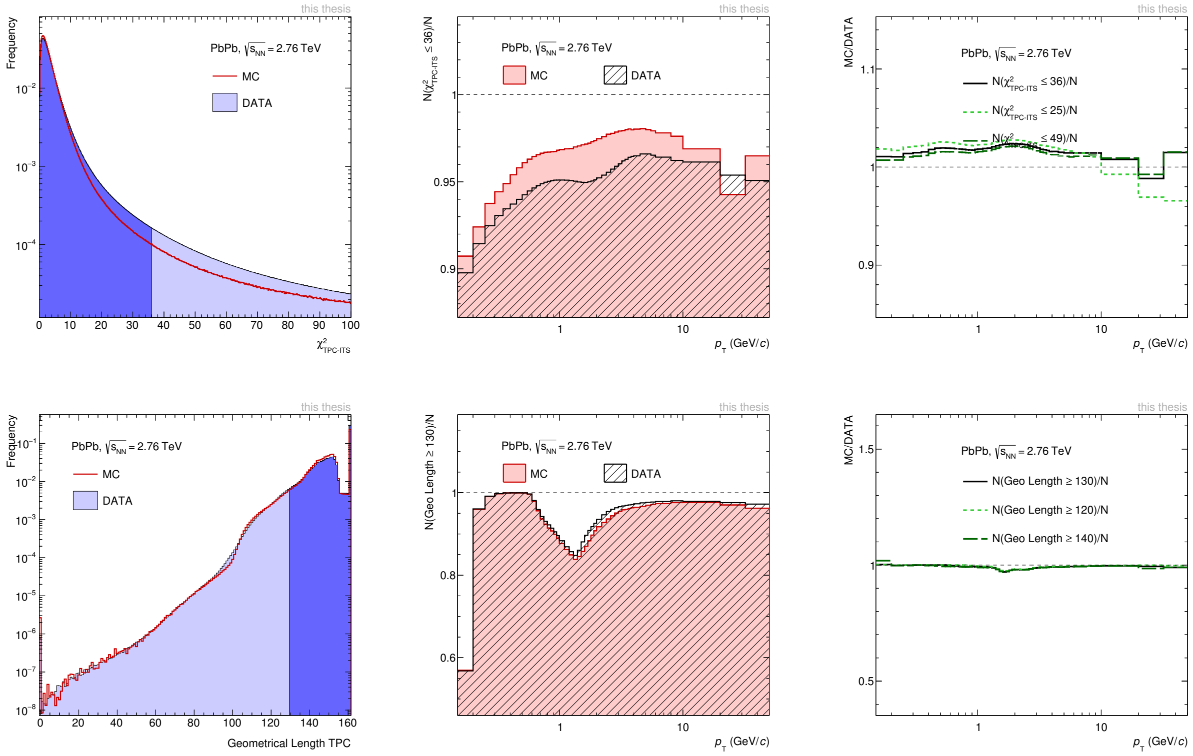

Figure D.8.: Track selection variables in Pb–Pb at $\sqrt{s_{NN}} = 2.76$ TeV.

D.3 Xe–Xe 5 TeV

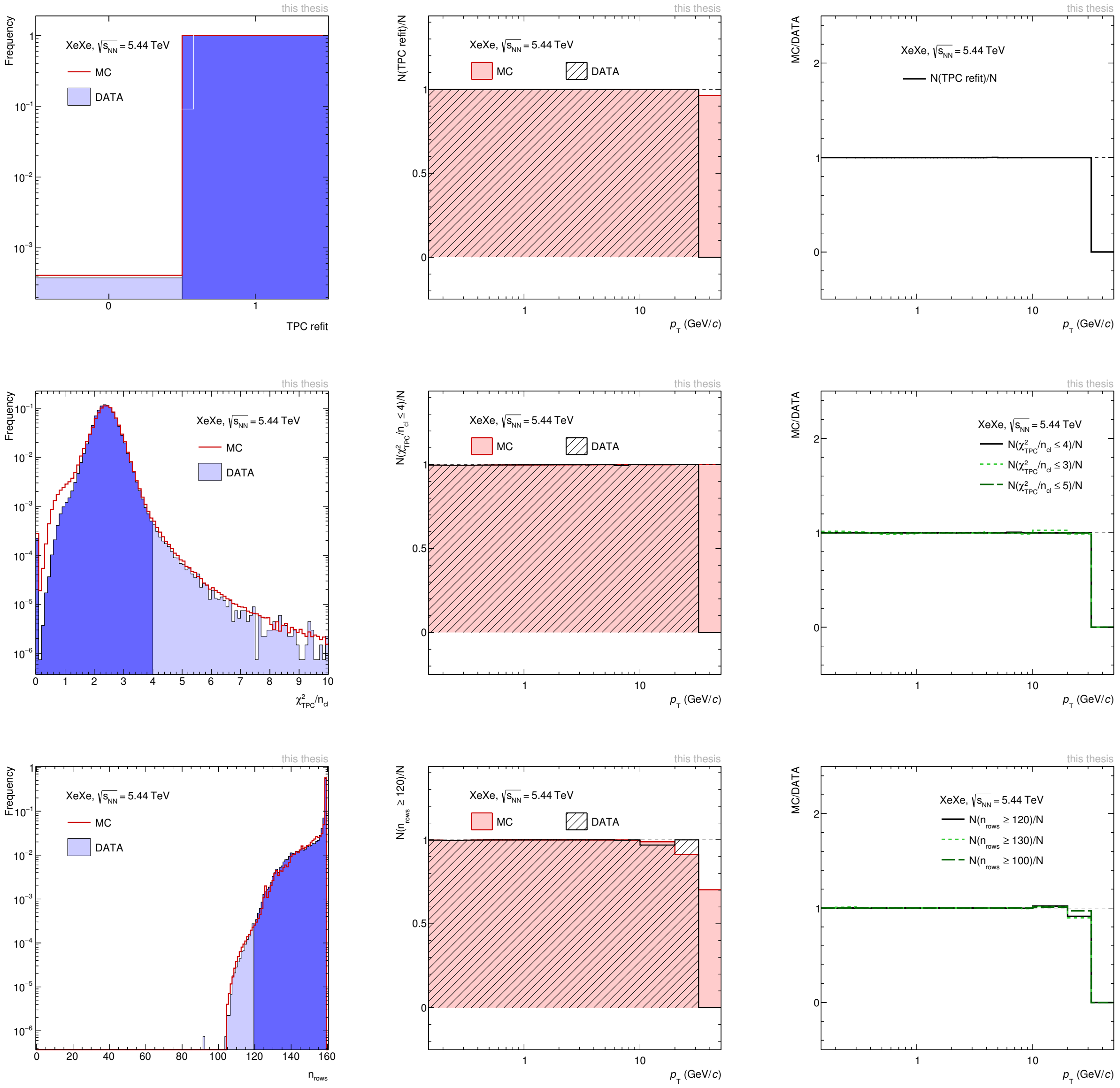

Figure D.9.: Track selection variables in Xe–Xe at $\sqrt{s_{NN}} = 5.44$ TeV.

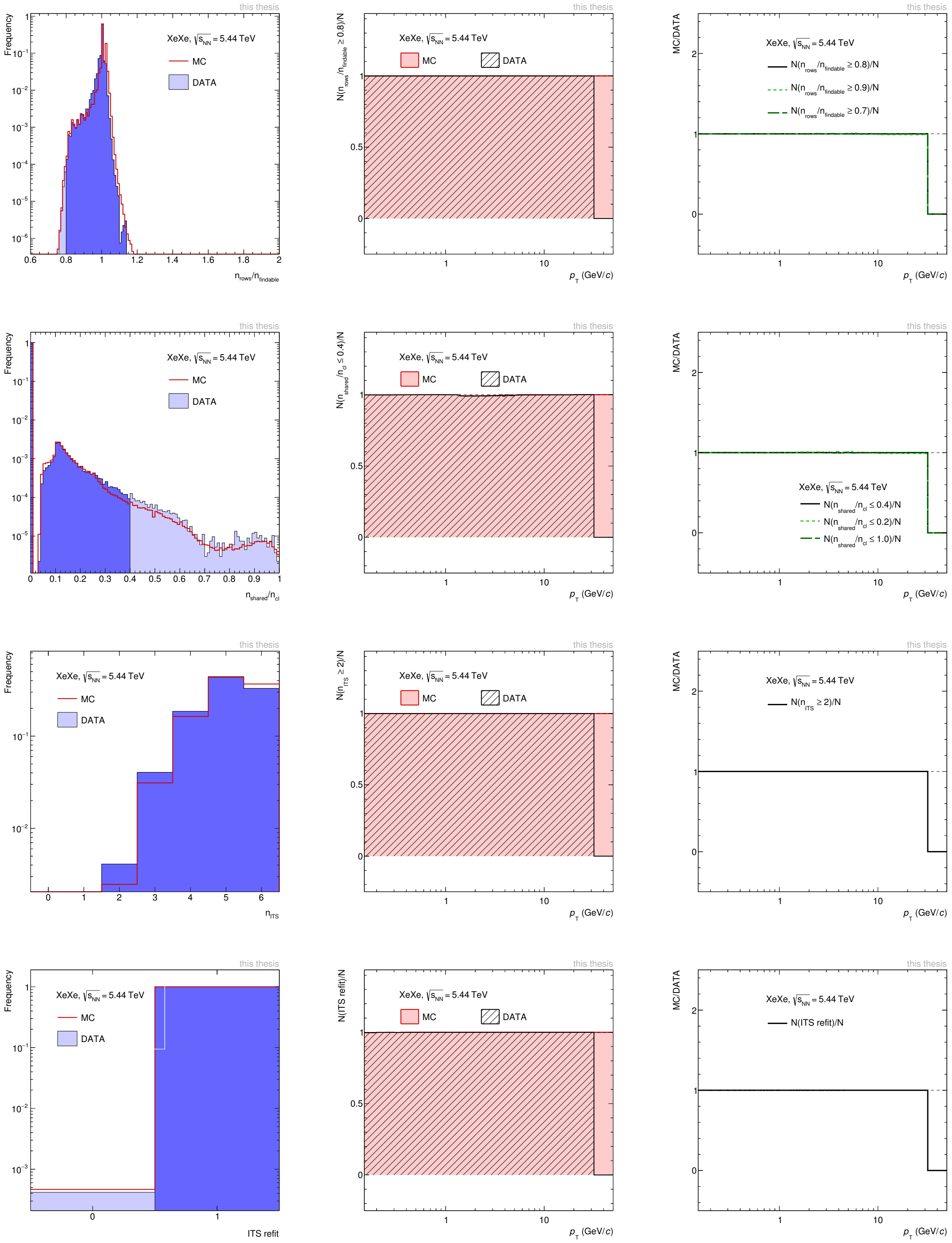

Figure D.10.: Track selection variables in Xe–Xe at $\sqrt{s_{NN}} = 5.44\,\text{TeV}$.

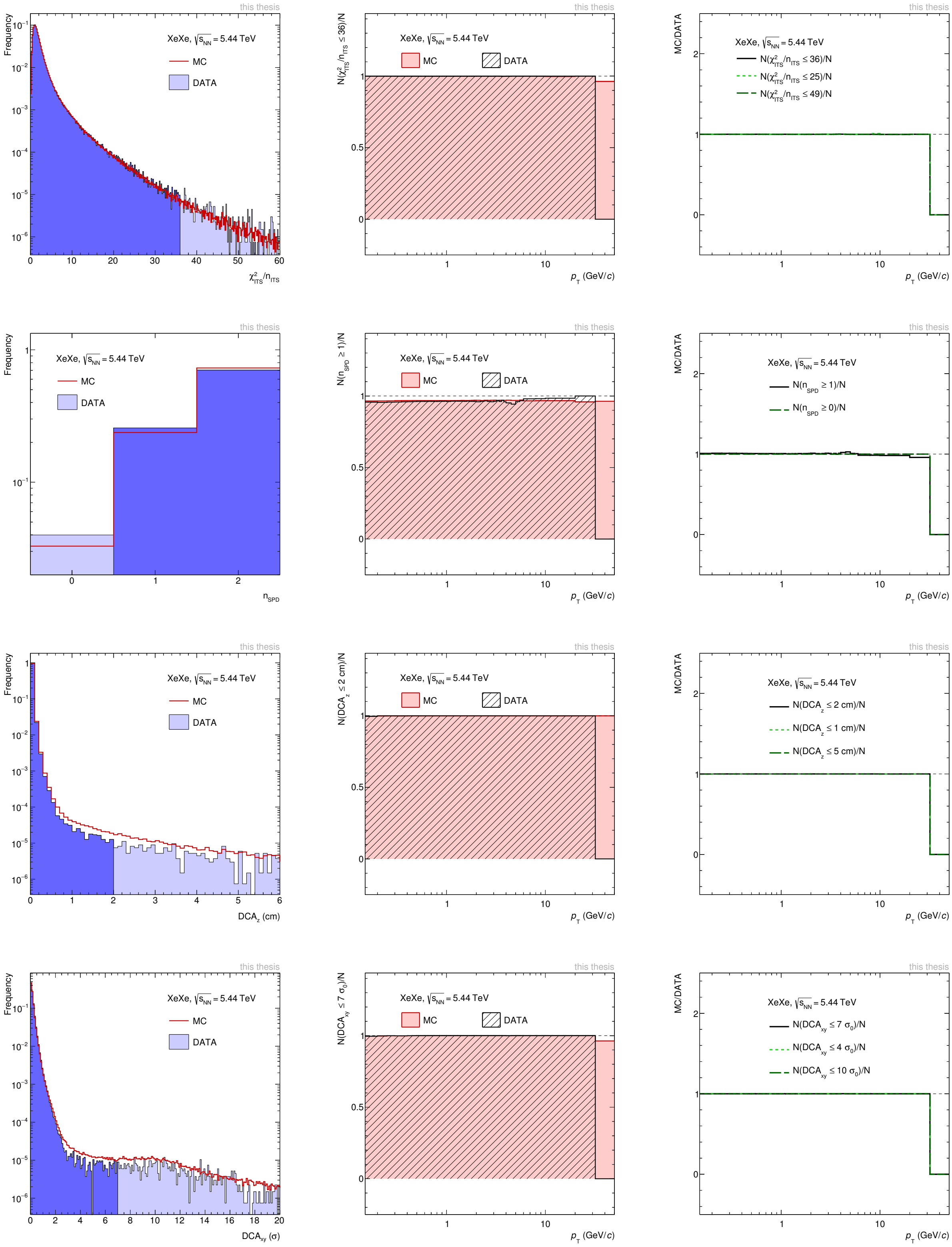

Figure D.11.: Track selection variables in Xe–Xe at $\sqrt{s_{NN}} = 5.44$ TeV.

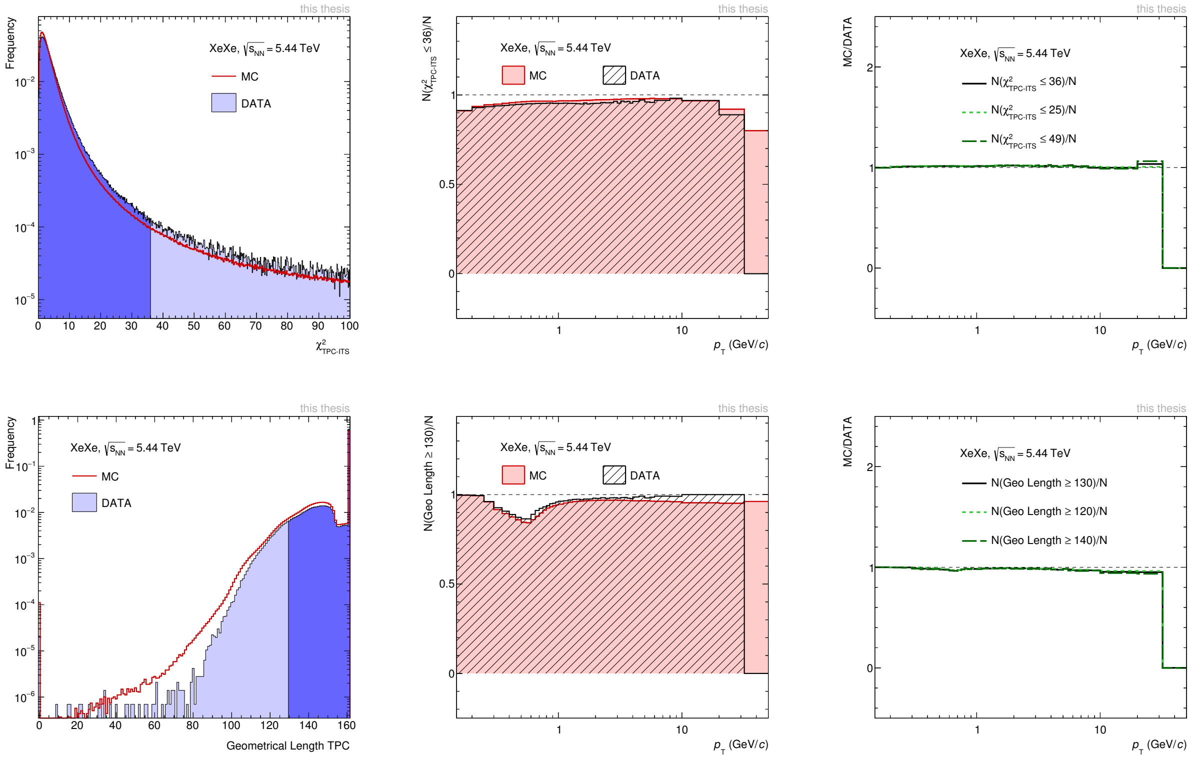

Figure D.12.: Track selection variables in Xe–Xe at $\sqrt{s_{NN}} = 5.44\,\text{TeV}$.

Acknowledgements

After finishing the thesis, I would like to give thanks to the people that not only helped me with the work, but also made the experience so memorable. First and foremost I would like to thank my supervisor Dr. Anton Andronic, for introducing me to the field of heavy-ion physics and for his catching enthusiasm. I would like to thank Dr. Silvia Masciocchi for welcoming me into her group and taking care of the bureaucracy when needed.

Also I would like to thank Dr. Jacek Otwinowski, Dr. Kai Schweda, Dr. Marian Ivanov, Dr. Michael Knichel, Dr. Federica Sozzi, Edgar Perez-Lezama, Patrick Huhn and Michael Habib for the common effort that has been a big part of the work done.

I also want to thank Dr. Ralf Averbeck, Kai, Michael and Anton for proofreading my thesis.

For their hospitality in México I want to thank Prof. Dr. Guy Paic, Dr. Antonio Ortiz, Omar Vasquez and Sergio Iga.

I'm especially greatfull to Edgar, Lukas Kreis, Steffen Weber, Tona Jimenez-Bustamante and Michael Habib for sharing the office in late hours and making the experience so memorable. Also, I would like to give thanks to the whole group for the wonderful atmosphere and for discussions during lunch and coffee breaks.

Bibliography

[1] Bjorken, J., Energy loss of energetic partons in quark - gluon plasma: Possible extinction of high p_T jets in hadron–hadron collisions, Preprint **FERMILAB-PUB-82-059-THY** (1982).

[2] M. Thomson, Modern Particle Physics (Cambridge University Press, 2013).

[3] Eichten, E. and Gottfried, K. and Kinoshita, T. and Kogut, J. and Lane, K. and Yan, T., Spectrum of Charmed Quark-Antiquark Bound States, Phys. Rev. Lett. 34 (1975) 369.

[4] Bazavov, A. et al., Nonperturbative QCD Simulations with 2+1 Flavors of Improved Staggered Quarks, Rev. Mod. Phys. 82 (2010) 1349, 0903.3598.

[5] Parisi, G. and Petronzio, R. and Rapuano, F., A measurement of the string tension near the continuum limit, Physics Letters B 128 (1983) 418 .

[6] Patrignani, C. et al., Review of Particle Physics, Chin. Phys. C40 (2016) 100001.

[7] Gwenlan, C., Combined HERA Deep Inelastic Scattering Data and NLO QCD Fits, Nucl.Phys.Proc.Suppl. 191 (2009) 5, 0902.1807.

[8] Dokshitzer, Y., Calculation of the Structure Functions for Deep Inelastic Scattering and e+ e- Annihilation by Perturbation Theory in Quantum Chromodynamics., Sov. Phys. JETP 46 (1977) 641, [Zh. Eksp. Teor. Fiz.73,1216(1977)].

[9] Gribov, V. and Lipatov, L., Deep inelastic e p scattering in perturbation theory, Sov. J. Nucl. Phys. 15 (1972) 438, [Yad. Fiz.15,781(1972)].

[10] Altarelli, G. and Parisi, G., Asymptotic Freedom in Parton Language, Nucl. Phys. B126 (1977) 298.

[11] Satz, H., Color Screening in SU(N) Gauge Theory at Finite Temperature, Nucl. Phys. A418 (1984) 447C.

[12] Collins, J. C. and Perry, M. J., Superdense Matter: Neutrons or Asymptotically Free Quarks?, Phys. Rev. Lett. 34 (1975) 1353.

[13] Andronic, A. and Braun-Munzinger, P., Ultrarelativistic nucleus-nucleus collisions and the quark gluon plasma, Lect. Notes Phys. 652 (2004) 35, hep-ph/0402291.

[14] Karsch, F., Lattice QCD at high temperature and density, Lect. Notes Phys. 583 (2002) 209, hep-lat/0106019.

[15] Karsch, F. and Laermann, E., Thermodynamics and in medium hadron properties from lattice QCD, (2003), hep-lat/0305025.

[16] Bazavov, A. et al., Equation of state in (2+1)-flavor QCD, Phys. Rev. D90 (2014) 094503, 1407.6387.

[17] The STAR Collaboration, An Experimental Exploration of the QCD Phase Diagram: The Search for the Critical Point and the Onset of De-confinement, (2010), 1007.2613.

[18] Ablyazimov, T. et al., Challenges in QCD matter physics –The scientific programme of the Compressed Baryonic Matter experiment at FAIR, The European Physical Journal A 53 (2017) 60.

[19] Braun-Munzinger, P. and Redlich, K. and Stachel, J., Particle production in heavy ion collisions, (2003) 491, nucl-th/0304013.

[20] Andronic, A. and Braun-Munzinger, P. and Stachel, J., Thermal hadron production in relativistic nuclear collisions: The Hadron mass spectrum, the horn, and the QCD phase transition, Phys. Lett. B673 (2009) 142, 0812.1186, [Erratum: Phys. Lett.B678,516(2009)].

[21] Strickland, M., Anisotropic Hydrodynamics: Three lectures, Acta Phys. Polon. B45 (2014) 2355, 1410.5786.

[22] d'Enterria, D., Jet quenching, Landolt-Bornstein 23 (2010) 471, 0902.2011.

[23] E. Iancu, Proceedings, 40th International Symposium on Multiparticle Dynamics (ISMD 2010): Antwerp, Belgium, September 21-25, 2010, pp. 411–437, 2011, 1105.0751.

[24] Liu, F. and Liu, S., Quark-gluon plasma formation time and direct photons from heavy ion collisions, Phys. Rev. C89 (2014) 034906, 1212.6587.

[25] Qin, G. and Wang, X., Jet quenching in high-energy heavy-ion collisions, Int. J. Mod. Phys. E24 (2015), 1511.00790.

[26] Miller, M. and Reygers, K. and Sanders, S. and Steinberg, P., Glauber modeling in high energy nuclear collisions, Ann. Rev. Nucl. Part. Sci. 57 (2007) 205, nucl-ex/0701025.

[27] Mehtar-Tani, Y., Theoretical Developments in QCD Jet Energy Loss, Nucl. Phys. A956 (2016) 168, 1602.01047.

[28] Eskola, K. and Paukkunen, H. and Salgado, C., EPS09: A New Generation of NLO and LO Nuclear Parton Distribution Functions, JHEP 04 (2009) 065, 0902.4154.

[29] Gelis, F., Color Glass Condensate and Glasma, Int. J. Mod. Phys. A28 (2013) 1330001, 1211.3327.

[30] Cronin, J. W. and Frisch, H. J. and Shochet, M. J. and Boymond, J. P. and Piroué, P. A. and Sumner, R. L., Production of hadrons at large transverse momentum at 200, 300, and 400 GeV, Phys. Rev. D 11 (1975) 3105.

[31] Schnedermann, E. and Sollfrank, J. and Heinz, U., Thermal phenomenology of hadrons from 200-A/GeV S+S collisions, Phys. Rev. C48 (1993) 2462, nucl-th/9307020.

[32] The ALICE Collaboration, Elliptic flow of charged particles in Pb-Pb collisions at 2.76 TeV, Phys.Rev.Lett. 105 (2010) 252302, 1011.3914.

[33] Andronic, A. and Braun-Munzinger, P. and Stachel, J., Hadron production in central nucleus-nucleus collisions at chemical freeze-out, Nucl. Phys. A772 (2006) 167, nucl-th/0511071.

[34] Kang, Z. and Lashof-Regas, R. and Ovanesyan, G. and Saad, P. and Vitev, I., Jet quenching phenomenology from soft-collinear effective theory with Glauber gluons, Phys. Rev. Lett. 114 (2015) 092002, 1405.2612.

[35] Chien, Y. and Emerman, A. and Kang, Z. and Ovanesyan, G. and Vitev, I., Jet Quenching from QCD Evolution, Phys. Rev. D93 (2016) 074030, 1509.02936.

[36] Vitev, I., SCET for jet physics in the vacuum and the medium, Nuclear and Particle Physics Proceedings 289-290 (2017) 59 , 8th International Conference on Hard and Electromagnetic Probes of High Energy Nuclear Collisions.

[37] Bauer, C. and Fleming, S. and Luke, M., Summing Sudakov logarithms in B —> X(s gamma) in effective field theory, Phys. Rev. D63 (2000) 014006, hep-ph/0005275.

[38] Idilbi, A. and Majumder, A., Extending Soft-Collinear-Effective-Theory to describe hard jets in dense QCD media, Phys. Rev. D80 (2009) 054022, 0808.1087.

[39] Djordjevic, M. and Djordjevic, M., Predictions of heavy-flavor suppression at 5.1 TeV Pb + Pb collisions at the CERN Large Hadron Collider, Phys. Rev. C92 (2015) 024918, 1505.04316.

[40] Djordjevic, M. and Blagojevic, B. and Zivkovic, L., Mass tomography at different momentum ranges in quark-gluon plasma, Phys. Rev. C94 (2016) 044908, 1601.07852.

[41] Kang, Z. and Vitev, I. and Xing, H., Nuclear modification of high transverse momentum particle production in p+A collisions at RHIC and LHC, Phys. Lett. B718 (2012) 482, 1209.6030.

[42] de Florian, D. and Sassot, R. and Stratmann, M., Global analysis of fragmentation functions for pions and kaons and their uncertainties, Phys. Rev. D75 (2007) 114010, hep-ph/0703242.

[43] Xu, J. and Liao, J. and Gyulassy, M., Bridging Soft-Hard Transport Properties of Quark-Gluon Plasmas with CUJET3.0, JHEP 02 (2016) 169, 1508.00552.

[44] Andrés, C. and Armesto, N. and Luzum, M. and Salgado, C. and Zurita, P., Energy versus centrality dependence of the jet quenching parameter $\hat{q}$ at RHIC and LHC: a new puzzle?, Eur. Phys. J. C76 (2016) 475, 1606.04837.

[45] Majumder, A. and Shen, C., Suppression of the High p_T Charged Hadron R_{AA} at the LHC, Phys. Rev. Lett. 109 (2012) 202301, 1103.0809.

[46] Wang, X. and Guo, X., Multiple parton scattering in nuclei: Parton energy loss, Nucl. Phys. A696 (2001) 788, hep-ph/0102230.

[47] Bianchi, E. and Elledge, J. and Kumar, A. and Majumder, A. and Qin, G. and Shen, C., The x and Q^2 dependence of $\hat{q}$, quasi-particles and the JET puzzle, (2017), 1702.00481.

[48] Arnold, P. and Moore, G. and Yaffe, L., Photon emission from ultrarelativistic plasmas, JHEP 11 (2001) 057, hep-ph/0109064.

[49] Schenke, B. and Gale, C. and Jeon, S., MARTINI: An Event generator for relativistic heavy-ion collisions, Phys. Rev. C80 (2009) 054913, 0909.2037.

[50] The PHOBOS Collaboration, Phobos results on charged particle multiplicity and pseudorapidity distributions in Au+Au, Cu+Cu, d+Au, and p+p collisions at ultra-relativistic energies, Phys. Rev. C83 (2011) 024913, 1011.1940.

[51] The ALICE Collaboration, Charged-particle multiplicities in proton–proton collisions at $\sqrt{s} = 0.9$ to 8 TeV, Eur. Phys. J. C77 (2017) 33, 1509.07541.

[52] The ALICE Collaboration, Pseudorapidity and transverse-momentum distributions of charged particles in proton–proton collisions at $\sqrt{s} = 13$ TeV, Phys. Lett. B753 (2016) 319, 1509.08734.

[53] The ALICE Collaboration, Centrality dependence of the charged-particle multiplicity density at mid-rapidity in Pb-Pb collisions at $\sqrt{s_{NN}} = 2.76$ TeV, Phys. Rev. Lett. 106 (2011) 032301, 1012.1657.

[54] The ALICE Collaboration, Centrality dependence of the charged-particle multiplicity density at midrapidity in Pb-Pb collisions at $\sqrt{s_{\mathrm{NN}}} = 5.02$ TeV, Phys. Rev. Lett. 116 (2016) 222302, 1512.06104.

[55] Bjorken, J., Highly relativistic nucleus-nucleus collisions: The central rapidity region, Phys. Rev. D 27 (1983) 140.

[56] The CMS Collaboration, Measurement of the Pseudorapidity and Centrality Dependence of the Transverse Energy Density in Pb-Pb Collisions at $\sqrt{s_{\mathrm{NN}}} = 2.76$ TeV, Phys. Rev. Lett. 109 (2012) 152303.

[57] The ALICE Collaboration, Centrality determination of Pb–Pb collisions at $\sqrt{s_{NN}} = 2.76$ TeV with ALICE, Phys. Rev. C88 (2013) 044909, 1301.4361.

[58] The ALICE Collaboraion, Centrality and pseudorapidity dependence of the charged-particle multiplicity density in Xe–Xe collisions at $\sqrt{s_{\mathrm{NN}}} = 5.44$ TeV, (2018), 1805.04432.

[59] Borsányi, S. and Fodor, Z. and Hoelbling, C. and Katz, S. and Krieg, S. and Szabó, K., Full result for the QCD equation of state with 2+1 flavors, Phys. Lett. B 730 (2014) 99 .

[60] The PHENIX Collaboration, Suppression of hadrons with large transverse momentum in central Au+Au collisions at $\sqrt{s_{NN}} = 130$-GeV, Phys. Rev. Lett. 88 (2002) 022301, nucl-ex/0109003.

[61] The STAR Collaboration, Centrality dependence of high p_T hadron suppression in Au+Au collisions at $\sqrt{s}_{NN} = 130$-GeV, Phys. Rev. Lett. 89 (2002) 202301, nucl-ex/0206011.

[62] The ALICE Collaboration, Centrality Dependence of Charged Particle Production at Large Transverse Momentum in Pb–Pb Collisions at $\sqrt{s_{\mathrm{NN}}} = 2.76$ TeV, Phys. Lett. B720 (2013) 52, 1208.2711.

[63] The CMS Collaboration, Study of high-pT charged particle suppression in PbPb compared to pp collisions at $\sqrt{s_{NN}} = 2.76$ TeV, Eur. Phys. J. C72 (2012) 1945, 1202.2554.

[64] The ATLAS Collaboration, Measurement of charged-particle spectra in Pb+Pb collisions at $\sqrt{s_{\mathrm{NN}}} = 2.76$ TeV with the ATLAS detector at the LHC, JHEP 09 (2015) 050, 1504.04337.

[65] The CMS Collaboration, Charged-particle nuclear modification factors in PbPb and pPb collisions at $\sqrt{s_{\mathrm{N\,N}}} = 5.02$ TeV, JHEP 04 (2017) 039, 1611.01664.

[66] The STAR collaboration, Transverse momentum and collision energy dependence of high p(T) hadron suppression in Au+Au collisions at ultrarelativistic energies, Phys. Rev. Lett. 91 (2003) 172302, nucl-ex/0305015.

[67] The ALICE Collaboration, Production of charged pions, kaons and protons at large transverse momenta in pp and Pb–Pb collisions at $\sqrt{s_{\mathrm{NN}}} = 2.76\,$TeV, Phys, Lett. B 736 (2014) 196 .

[68] The ALICE Collaboration, Transverse momentum dependence of inclusive primary charged-particle production in p-Pb collisions at $\sqrt{s_{\mathrm{NN}}} = 5.02$ TeV, Eur. Phys. J. C74 (2014) 3054, 1405.2737.

[69] The CMS Collaboration, Measurement of isolated photon production in pp and PbPb collisions at $\sqrt{s_{NN}} = 2.76$ TeV, Phys. Lett. B710 (2012) 256, 1201.3093.

[70] The CMS Collaboration, Study of W boson production in PbPb and pp collisions at $\sqrt{s_{NN}} = 2.76$ TeV, Phys. Lett. B715 (2012) 66, 1205.6334.

[71] The CMS collabortation, Study of Z boson production in PbPb collisions at $\sqrt{s_{NN}} = 2.76$ TeV, Phys. Rev. Lett. 106 (2011) 212301, 1102.5435.

[72] The ALICE Collaboration, Multiplicity dependence of the average transverse momentum in pp, p-Pb, and Pb-Pb collisions at the LHC, Phys. Lett. B727 (2013) 371, 1307.1094.

[73] Burke, K. et al., Extracting the jet transport coefficient from jet quenching in high-energy heavy-ion collisions, Phys. Rev. C90 (2014) 014909, 1312.5003.

[74] (ed.) Evans and (ed.) Bryant, LHC Machine, JINST 3 (2008) S08001.

[75] Overview of the Cern Accelerator complex, `http://images.netzwelt.de/article/2011/nutzer-ab-sofort-experimente-rund-lhc-unterstuetzen-bild-cern7069.jpg` (2013).

[76] M. Benedikt et al., LHC Design Report v.3 : the LHC Injector ChainCERN Yellow Reports: Monographs (CERN, Geneva, 2004).

[77] The ATLAS Collaboration, . The ATLAS Collaboration, Observation of a new particle in the search for the Standard Model Higgs boson with the ATLAS detector at the LHC, 2012, arXiv: 1207.7214.

[78] The CMS Collaboration, S.e.a. Chatrchyan, Observation of a new boson at a mass of 125 GeV with the CMS experiment at the LHC, 2012, arXiv: 1207.7235.

[79] The LHCb Collaboration, Observation of $J/\psi p$ Resonances Consistent with Pentaquark States in $\Lambda_b^0 \to J/\psi K^- p$ Decays, Phys. Rev. Lett. 115 (2015) 072001, 1507.03414.

[80] The ALICE Collaboration, ALICE figure repository, `https://aliceinfo.cern.ch` (2018).

[81] The ALICE Collaboration, ALICE Inner Tracking System (ITS): Technical Design Report, (1999).

[82] The ALICE Collaboration, The ALICE experiment at the CERN LHC, Journal of Instrumentation 3 (2008) S08002.

[83] The ALICE Collaboration, Technical Design Report for the Upgrade of the ALICE Inner Tracking System, (2013).

[84] Alme, J. et al., The ALICE TPC, a large 3-dimensional tracking device with fast readout for ultra-high multiplicity events, Nuclear Instruments and Methods in Physics Research A 622 (2010) 316, 1001.1950.

[85] The ALICE Collaboration, Performance of the ALICE Experiment at the CERN LHC, Int. J. Mod. Phys. A29 (2014) 1430044, 1402.4476.

[86] The ALICE Collaboration, Space-charge distortion measurements and their calibration in the ALICE TPC, To be published (2018).

[87] Schäfer, O., Layout of gas amplification and read-out with proportional wires, `https://www.lctpc.org/sites/sites_custom/site_lctpc/content/e8/e46/e21014/Wirereadout_eng.jpg` (2006).

[88] . The ALICE Collaboration, ALICE forward detectors: FMD, TO and VO: Technical Design Report (CERN, Geneva, 2004), Submitted on 10 Sep 2004.

[89] The ALICE collaboration, Performance of the ALICE VZERO system, JINST 8 (2013) P10016.

[90] Ivanov, M. and Belikov, I. and Hristov, P. and Šafařík, K., Track reconstruction in high density environment, Nuclear Instruments and Methods in Physics Research Section A: Accelerators, Spectrometers, Detectors and Associated Equipment 566 (2006) 70 , TIME 2005.

[91] W. Blum, W. Riegler and L. Rolandi, Particle Detection with Drift ChambersParticle Acceleration and Detection (Springer Berlin Heidelberg, 2008).

[92] D. Colella, 24th International Workshop on Vertex Detectors (VERTEX2015), p. 3, 2015.

[93] The ALICE Collaboration, Centrality determination in heavy-ion collisions, ALICE-PUBLIC-2017-XXX (2017).

[94] The ALICE Collaboration, Centrality dependence of particle production in p-Pb collisions at $\sqrt{s_{\rm NN}} = 5.02$ TeV, Phys. Rev. C91 (2015) 064905, 1412.6828.

[95] The ALICE Collaboration, Suppression of Charged Particle Production at Large Transverse Momentum in Central Pb-Pb Collisions at $\sqrt{s_{NN}} = 2.76$ TeV, Phys. Lett. B696 (2011) 30, 1012.1004.

[96] The ALICE Collaboration, Energy Dependence of the Transverse Momentum Distributions of Charged Particles in pp Collisions Measured by ALICE, Eur. Phys. J. C73 (2013) 2662, 1307.1093.

[97] Wang, X. and Gyulassy, M., HIJING: A Monte Carlo model for multiple jet production in p p, p A and A A collisions, Phys.Rev. D44 (1991) 3501.

[98] Sjostrand, T. and Mrenna, S. and Skands, P., A Brief Introduction to PYTHIA 8.1, Comput. Phys. Commun. 178 (2008) 852, 0710.3820.

[99] R.e.a. Brun, GEANT Detector Description and Simulation Tool (CERN Program Library Long Write-up W5013, 1994).

[100] The ALICE Collaboration, The ALICE definition of primary particles, ALICE-PUBLIC-2017-005 (2017).

[101] The ALICE Collabortation, K^0_S and Λ Production in Pb-Pb Collisions at $\sqrt{s_{\mathrm{NN}}} = 2.76\,\mathrm{TeV}$, Phys. Rev. Lett. 111 (2013) 222301.

[102] The ALICE Collaboration, Centrality dependence of the nuclear modification factor of charged pions, kaons, and protons in Pb–Pb collisions at $\sqrt{s_{\mathrm{NN}}} = 2.76\,\mathrm{TeV}$, Phys. Rev. C 93 (2016) 034913.

[103] Bylinkin, A. and Chernyavskaya, N. and Rostovtsev, A., Predictions on the transverse momentum spectra for charged particle production at LHC-energies from a two component model, The European Physical Journal C 75 (2015) 166.

[104] H. P., Datenbasierte Effizienzkorrektur zum Nachweis geladener Teilchen im ALICE Experiment, Master's thesis, Johann Wolfgang Goethe-Universität Frankfurt am Main, 2017.

[105] Hagedorn, R., Multiplicities,p_T distributions and the expected hadron → quark-gluon phase transition, La Rivista del Nuovo Cimento (1978-1999) 6 (1983) 1.

[106] The ALICE Collaboration, Transverse momentum distribution and nuclear modification factor of charged particles in p-Pb collisions at $\sqrt{s_{NN}} = 5.02$ TeV, Phys. Rev. Lett. 110 (2013) 082302, 1210.4520.

[107] Pierog, T. and Karpenko, Iu. and Katzy, J. M. and Yatsenko, E. and Werner, K., EPOS LHC: Test of collective hadronization with data measured at the CERN Large Hadron Collider, Phys. Rev. C92 (2015) 034906, 1306.0121.

[108] Skands, P. and Carrazza, S. and Rojo, J., Tuning PYTHIA 8.1: the Monash 2013 Tune, Eur. Phys. J. C74 (2014) 3024, 1404.5630.

[109] The ALICE Collaboration, Transverse momentum spectra and nuclear modification factors of charged particles in pp, p-Pb and Pb-Pb collisions at the LHC, (2018), 1802.09145.

[110] The ALICE Collaboration, ALICE luminosity determination for pp collisions at $\sqrt{s} = 5$ TeV, ALICE-PUBLIC-2016-005 (2016).

[111] The ALICE Collaboration, Multiplicity Dependence of Pion, Kaon, Proton and Lambda Production in p-Pb Collisions at $\sqrt{s_{NN}} = 5.02$ TeV, Phys. Lett. B728 (2014) 25, 1307.6796.

[112] The CMS Collaboration, The CMS experiment at the CERN LHC, Journal of Instrumentation 3 (2008) S08004.

[113] Loizides, C. and Kamin, J. and d'Enterria, D., Precision Monte Carlo Glauber predictions at present and future nuclear colliders, (2017), 1710.07098.

[114] The ALICE Collaboraion, Transverse momentum spectra and nuclear modification factors of charged particles in Xe-Xe collisions at $\sqrt{s_{\mathrm{NN}}} = 5.44$ TeV, (2018), 1805.04399.

[115] Werner, K., Core-corona separation in ultra-relativistic heavy ion collisions, Phys. Rev. Lett. 98 (2007) 152301, 0704.1270.

[116] Giacalone, G. and Noronha-Hostler, J. and Luzum, M. and Ollitrault, J., Hydrodynamic predictions for 5.44 TeV Xe+Xe collisions, (2017), 1711.08499.

[117] Gronefeld, J., The nuclear modification of charged particles in Pb-Pb at $\sqrt{s_{\mathrm{NN}}} = 5.02\,\mathrm{TeV}$ measured with ALICE, (2016), 1609.07334.

Curriculum Vitae

Julius Maximilian Gronefeld
March 3rd 1988, Bonn-Bad Godesberg, Germany

Education

October 2016	Awarded with Giersch-Excellence-Grant 2016
Since Feb 2015	Member of HGS-HIRe - Helmholtz Graduate School for Hadron and Ion Research
Since Feb 2015	PhD Student Physics, GSI Helmholtzzentrum Darmstadt Thesis: “Transverse Momentum Distributions and Nuclear Modification Factors in Heavy-Ion Collisions with ALICE at the LHC” Advisor: Prof. Dr. Anton Andronic
March 2014	Master of Science, Physics, Techinische Universität Darmstadt Thesis: “Transverse Momentum Distribution and Nuclear Modification Factors in p-Pb Collisions with ALICE and the LHC” Average grade: 1.60
April 2012	Bachelor of Science, Physics, Techinische Universität Darmstadt Thesis: “Influence of Electrolyte Concentration on Growth, Cristal Orientation and Seebeck-Coefficient of Bi_2Te_3 Nanowires” Average grade: 2.68
June 2008	Civil service at the university’s child hospital, Universiät Bonn
June 2007	Abitur, Friedrich-Ebert-Gymnasium, Bonn Major: Physics & History Average grade: 1.90

International Experience

2004	School year at the Hesston High School in Kansas
2014	Cycle journey from Darmstadt to Bangkok through Europe, central and eastern Asia
2017	Two months at the University of Mexico City (UNAM)

Publications with significant contribution

- *ALICE Collaboration*, "Transverse momentum spectra and nuclear modification factors of charged particles in pp, p–Pb and Pb–Pb collisions at the LHC", arXiv:1802.09145 (2018) [109].
- *J. Gronefeld for the ALICE Collaboration*, "The nuclear modification of charged particles in Pb–Pb at $\sqrt{s_{\rm NN}} = 5.02\,\rm TeV$ measured with ALICE", arXiv:1609.07334 [117].
- *ALICE Collaboration*, "Pseudorapidity and transverse-momentum distributions of charged particles in proton–proton collisions at $\sqrt{s} = 13$ TeV", Phys. Lett. B 753 (2016) 319, arXiv:1509.08734 [52].
- *ALICE Collaboration*, "Centrality dependence of particle production in p-Pb collisions at $\sqrt{s_{\rm NN}} = 5.02\,\rm TeV$", Phys. Rev. C91 (2015) no.6, 064905, arXiv:1412.6828 (2014) [94].
- *ALICE Collaboration*, "Transverse momentum dependence of inclusive primary charged-particle production in p–Pb collisions at $\sqrt{s_{\rm NN}} = 5.02\,\rm TeV$ ", Eur. Phys. J. C 74, 3054 (2014) [68].

Talks and posters

- Charged particle spectra in Pb–Pb collisions and nuclear modification factors at $\sqrt{s_{\rm NN}} = 5.02\,\rm TeV$ measured with ALICE, talk, QCD Challenges from pp to AA, Puebla, 2017
- Transverse momentum distribution and the nuclear modification factors of charged particles in Pb–Pb collisions at $\sqrt{s_{\rm NN}} = 5.02\,\rm TeV$, poster, Quark Matter, Chicago, 2017
- New results related to hard probes in Pb–Pb at $\sqrt{s_{\rm NN}} = 5.02\,\rm TeV$ with ALICE, talk, LHCP, Lund, 2016
- Charged-particle distributions in Pb–Pb collisions at $\sqrt{s_{\rm NN}} = 5.02\,\rm TeV$, talk, DPG Spring meeting, Darmstadt, 2016
- Charged-hadron spectra and energy loss, talk, Arbeitstreffen Kernphysik Schleching, 2016
- Transverse momentum distribution of charged particles in pp collisions at $\sqrt{s} = 13\,\rm TeV$ with ALICE at the LHC, poster, Quark Matter, Kobe, 2015
- Transverse momentum distributions of charged particles in p–Pb collisions with ALICE at the LHC, talk, DPG Spring meeting, Frankfurt, 2014

Erklärung zur Dissertation

Hiermit versichere ich, die vorliegende Dissertation ohne Hilfe Dritter nur mit den angegebenen Quellen und Hilfsmitteln angefertigt zu haben. Alle Stellen, die aus Quellen entnommen wurden, sind als solche kenntlich gemacht. Diese Arbeit hat in gleicher oder ähnlicher Form noch keiner Prüfungsbehörde vorgelegen.

Darmstadt, den 09. April 2018

(Julius Gronefeld)